



The  
University  
Of  
Sheffield.

**The Viability of Image Registration as a Method for the  
Quantification of Displacement in Penetrating Impact  
Experiments**

**By:**

Edward A Cramphorn

**Supervisors:**

Dr Zeike A Taylor

Dr Matt Carre

A thesis submitted in partial fulfilment of the requirements for the degree of  
Doctor of Philosophy

The University of Sheffield  
Faculty of Engineering  
School (or Department) of Mechanical Engineering

Submission Date

**11/10/2018**



The  
University  
Of  
Sheffield.

**The Viability of Image Registration as a Method for the  
Quantification of Displacement in Penetrating Impact  
Experiments**

**By:**

Edward A Cramphorn

A thesis submitted in partial fulfilment of the requirements for the degree of  
Doctor of Philosophy

The University of Sheffield  
Faculty of Engineering  
School (or Department) of Mechanical Engineering

Submission Date

11/10/2018

# **Thesis Corrections Undertaken**

Please find below a short outline of all the corrections that have been recommended by the in the examiners report alongside specific recommendations contained in the examiners' feedback.

## **Recommended thesis corrections**

1. *As all testing is at relatively low speed (<100 m/s rather than >1000 m/s), the title should be modified to replace “penetrating ballistic” with “low velocity”.*

This recommendation has been taken into account and the title was modified to “*Penetrating Projectile Impacts*” as this is a true description of the work undertaken in this thesis. As the lower velocity used was a result of testing and research undertaken during the thesis, this title better describes the work undertaken while addressing the valid comment that the final penetrating projectile impact testing was performed at a relatively lower speed than traditional ballistic testing.

2. *Language, grammar and typographical errors should be eliminated. While some of these are identified in the marked-up theses, there are others. Therefore, the document should be edited carefully and thoroughly before resubmission.*

It was highlighted that the quality of the English in the thesis was of a poor standard. So to address this, extra care has been taken throughout to ensure that the presentation and English is of the expected standard alongside ensuring consistency in layout and in typography throughout.

3. *Review comments made in the marked-up theses and adjust text to address points raised.*

The thesis has been modified to address the specific comments and points raised in both examiners' annotated thesis copies. This has meant that many areas of the thesis have been expanded to address the comments to overcome the short comings identified or to provide better clarity on specific points. This has resulted in a large expansion of the thesis across all the chapters and was one of the significant part of the correction process (Word count increased from 50000 to 70000).

4. *Ensure that figures are reproduced clearly in print and add labels to explain key features.*

All figures have been produced to the highest quality possible and all legends have been expanded to better explain what is shown in the image.

5. *Explain non-standard words e.g. medical terms in Chapter 2 and image processing terms in Chapter 3 and 5. Also reconsider the use of the term “artefact” throughout the thesis as is used to mean different things.*

Throughout the thesis, care has been taken to address the use of specialist words by ensuring that the first usage coincides with an explanation of the meaning. As identified by the examiners, the word artefact was being used to express multiple different concepts. The text has been altered to enhance clarity. In the thesis, artefact now specifically refers to unusual or erroneous behaviour of image registration with anomalies now being used to refer to experimental data that shows behaviour that

was not as expected or has presented an unusual response. In all other cases, the thesis explicitly refers to the point being discussed, for example optical distortions that are encountered during filming.

6. *Provide justification for choices made. Include an explanation of preliminary studies, which were completed but are currently not presented, that have been used to define the final experimental methods.*

Specifically in relation to Chapter 6, an entire new subsection has been added that clearly states the range of explorative and proof of concept tests that were undertaken to explore or define the experimental arrangement. This can be found in Section 6.3 Explorative Testing. In Chapters 3 and 5, in line with the comments provided in the examiners' thesis corrections, any explorative testing or justifications for research choices have been added where appropriate or expanded to better reflect the actual work undertaken.

7. *Remove section 2.4.1 as the hand grenade is not a good justification for the selected fragment. A 6mm ball bearing is a standard type for this test (most common fragment in personnel-borne IEDs).*

As suggested, the section was changed to reflect the examiners' comments while also expanding the reasoning to include the epidemiology that has been seen in the medical literature which investigates such injuries. However to allow the analytical study to be undertaken, it was still necessary to define how a charge mass was derived; please see Section 2.4.1 for full details.

8. *Explain the details of the finite-element model (for example, element type formulation and calculation procedure) used and discuss the benefits of alternative material models.*

The relevant section (3.2.7) has been expanded to contain in depth description of the computational model, including both its construction and use. This is in sufficient enough detail to allow another researcher to undertake the work. The discussion of other material models has been expanded in Section 3.2.1 and the justification for the specific material model used has been made clearer in Section 3.2.2.

9. *Explain the contribution of the collaborator involved with finite element work before FE results are presented.*

To aid and ensure that clarity is maintained throughout the work as advised, these contributions have been clearly stated at the beginning of the relevant sections. Section 3.2 and 5.4.9.

10. *Rewrite section 1.3 to define aims and objectives in a clearer way.*

As suggested, the objectives and the specific goal of each of the chapters are clearly stated and context given to aid in understanding to make it clearer to the reader.

11. *Enhance the content of Chapter 2 by referring to commercially available textbooks on explosive ordnance and commercial materials.*

The referencing and content throughout the chapters have been enhanced through rewriting and the use of available references that explore explosive ordnance, such as IEDs structure and how they are used or deployed.

*12. Re organise chapters for greater coherency: currently chapter 3 contains the theory of image registration and Chapter 5 its principal application- this separation is rather unhelpful. On the other hand Chapter 4 and 6 have the relevant background included at the beginning.*

The chapters are distinct as this allows for the best exploration of the theory of image registration and the different usage of image registration. However as highlighted, the current arrangement does not aid the coherency of the thesis. As such, Chapter 3 and 4 have been swapped, so Chapter 4 explores the theory and previous usage of image registration and Chapter 5 explores how it can be applied the testing arrangement and laying out the method being proposed in this thesis.

*13. Re-organise the content of Section 4.1 to achieve a better match to the material discussed. Consider including ballistic soap (plastic behaviour) and Permagel (improved clarity). Make a more comprehensive note of the work on ballistic gel by Jussilla (ref 147) and include some basic material properties.*

The sections have been renamed to ensure clarity is maintained while still drawing the distinction between the surrogates that are derived from organic or inorganic material. These are distinct from the use of cadaveric tissue as in the literature, these are distinct lines drawn between these differently derived surrogates. In line with the examiners' suggestion where appropriate, more detailed information from the work that Jussilla (ref) has undertaken was added while also including PERMA-GEL and Ballistic Soap on the examiners' recommendation.

As indicated where possible, material parameters or models used and the specific tissue that these relate to have been given.

*14. The results highlight problems with the procedures used for the experiments and subsequent image registration. However, as the candidate still holds the view that the approach could be made to work, the future work section should be extended to explain clearly, how this could be achieved. The level of detail provided, and the reasons for each activity, should be adequate for a different researcher to devise a test and evaluation plan that can justify the expected success of the approach.*

In line with the examiners' comments, Section 7.3 has been greatly expanded. This now includes two distinct proposals. Firstly, a proposed outline of possible future research to modify the image registration method to address the short comings that have been identified, such as the optical distortion that resulted from the sample movement and multi-planar motion. The second recommends changes to the experimental arrangement to improve the grid pattern insertion and filming arrangements. It should be noted that this section now strongly recommends the main focus of any future work should be on exploring the use of 3D imaging and image registration.

# **Abstract**

Experimental characterisation of tissue deformations associated with penetrating impact of fragments from explosive devices is challenging. Whereas experiments involving ballistic gelatine tissue simulants enable direct visualisation of deformation patterns, quantification of these deformations remains difficult. This thesis investigates the use of image registration for this purpose.

Image registration methods optimise alignment of corresponding structures in image pairs, and in the process estimate the deformation fields that best achieve this. In the current context, it is hypothesised that registration of consecutive images from videos of gelatine penetration events can enable the corresponding gelatine deformation fields to be estimated.

Three main activities were undertaken towards validation of this hypothesis: the proposed registration approach was tested on a series of synthetic images emulating the types of deformations expected in penetration events; the approach was then tested on images derived from a carefully controlled indentation experiment, in which a block of gelatine was deformed quasi-statically with a rigid indenter while the resulting deformation was filmed; and finally it was tested on video footage from projectile penetration experiments, in which metal projectiles were fired into blocks of gelatine and filmed with a high speed video camera.

A series of complementary studies was also undertaken in support of these experiments. Firstly, to better understand the parameters of real penetration scenarios, the fragment generation and flight behaviour of a typical explosive device were analysed. Secondly, to improve understanding of the material behaviour of the test gelatine, mechanical characterisation tests were undertaken, and a visco-hyperelastic constitutive model was proposed.

The individual registration operations themselves appeared to perform well, in the sense that initially disparate consecutive image pairs were brought into good alignment. However, composition of the corresponding transformation fields, necessary for tracking accumulated deformations over the course of a video sequence, was found to yield artefacts and unphysical deformation estimates in some cases. These were judged to result both from deficiencies in the methods themselves, and flaws in the experimental arrangements. Therefore, while the proposed registration approach appears to show promise, further work is needed to establish its validity conclusively. The thesis closes with a discussion of possible approaches to the latter.

## **Dedication**

I would like to acknowledge the support of all the individuals that have aided and supported me through the course of my PhD.

Firstly, I would like to thank Dr Zeike Taylor for his support and guidance throughout. He has helped me to both improve my academic skills, critical thinking and perception of research, but also supported my wider development through university teaching and part time employment. I would also like to thank my second supervisor Dr Matt Carre who has provided both additional academic support, and laboratory and experimental advice.

Secondly, I would like to thank my colleagues and fellow PhD students Nishant Ravikumar and Christopher Noble for sharing their knowledge and working together on projects and ideas.

I would like to acknowledge the excellent technical support available at the University of Sheffield with a particular mention to be made about Leslie Morton, Richard Kay and Jamie Booth who have enabled me to undertake the experiments and testing, often going above and beyond to help me achieve my goals.

Next, I would like to thank whole heartedly the entire CISTIB team. You made a wonderful environment that was inclusive and inspired people to share not just their knowledge but culture, beliefs and drive. I wish to give special thanks to the Project Management Office for letting me become part of their team and giving me the opportunity to work and learn a different aspect of university life.

Finally, I wish to thank my family and friends who held me up when things were difficult. I must particular thank my wife Iris Hacke and mother Lynne Cramphorn who gave up their time to proof read my thesis.

I dedicate this work in the memory of my father,

Colin Cramphorn

## **Table of Contents**

I.	Table of Figures .....	x
II.	Table of Tables .....	xvii
III.	Executive Summary .....	xix
	a. Research question .....	xix
	b. Rationale of research.....	xix
	c. Project scope .....	xx
Chapter 1.	Introduction and context .....	1
	1.1. Current conflicts and technology .....	1
	1.2. Wounding epidemiology of current conflicts .....	3
	1.3. Assessing penetrating impacts .....	4
	1.4. Blast experiments.....	5
	1.5. Image registration .....	6
	1.6. Thesis proposition.....	7
Chapter 2.	Explosive injury and fragments generated from explosive devices	10
	2.1. Introduction.....	10
	2.2. Military explosive ordnance and usage.....	14
	2.3. Injuries from explosive devices .....	16
	2.3.1. Primary (Blast) explosive injury .....	17
	2.3.2. Secondary (fragment) explosive injury .....	18
	2.3.3. Tertiary (blunt force) explosive injury .....	21
	2.3.4. Quaternary and Quinary explosive injuries.....	21
	2.4. Analytical study of the mechanical process of explosive detonation.....	21
	2.4.1. Selection of weapon and simplification .....	21
	2.4.2. Initial fragment velocity .....	23
	2.4.3. Peak over-pressure generated from blast .....	24
	2.4.4. Fragment flight.....	25
	2.5. Results of analytical assessment .....	30
	2.5.1. Peak over-pressure .....	30
	2.5.2. Shrapnel Concentration.....	31
	2.5.3. Initial velocity and fragment flight .....	32
	2.6. Impact on experimental conditions .....	34
Chapter 3.	Selection and characterisation of tissue surrogate .....	36
	3.1. Selection of surrogate.....	36
	3.1.1. Organically Derived Tissue Surrogates .....	36
	3.1.2. Synthetically derived tissue surrogates .....	38



3.1.3.	Animal and cadaveric tissue .....	40
3.1.4.	Selection of ballistic gelatine as surrogate material .....	40
3.2.	Characterisation mechanical testing.....	43
3.2.1.	Previous work .....	43
3.2.2.	Proposed method.....	46
3.2.3.	Sample preparation .....	47
3.2.4.	Methodology .....	48
3.2.5.	Testing results .....	56
3.2.6.	Selected constitutive model .....	66
3.2.7.	Optimisation of material parameters.....	69
3.2.8.	Optimised material parameters .....	70
3.2.9.	Final material parameters.....	76
3.3.	Discussion.....	77
Chapter 4.	Image registration as a means of quantifying displacement and strain	81
4.1.	Introduction.....	81
4.2.	Optical methods for quantifying deformation.....	82
4.2.1.	Digital image correlation (DIC) .....	82
4.2.2.	Photoelasticity.....	84
4.2.3.	Marker Tracking .....	86
4.3.	Theory of image registration.....	87
4.3.1.	Transformation.....	87
4.3.2.	Penalty Term.....	88
4.3.3.	Optimisation.....	88
4.4.	Project registration method .....	89
4.4.1.	B-spline formulation .....	90
4.4.2.	Similarity Metrics .....	91
4.5.	Calculating displacement and strain from image transformation.....	96
4.5.1.	Composition of displacements from consecutive registrations.....	96
4.5.2.	Calculating Strain.....	100
4.6.	Discussion .....	101
Chapter 5.	Assessment of registration-based measurements of displacement and strain	103
5.1.	Introduction.....	103
5.2.	Outline of image registration frame work.....	104
5.2.1.	Pre-processing of captured data .....	105
5.2.2.	Application of pair-wise registration .....	109

5.2.3.	Application of composition of the pair-wise transformation .....	110
5.3.	Synthetic image registration.....	111
5.3.1.	Basic synthetic images .....	112
5.3.2.	Synthetic gridded images .....	117
5.4.	Experimental validation of registration method.....	120
5.4.1.	Sample preparation .....	120
5.4.2.	Experimental procedure .....	121
5.4.3.	Captured data pre-processing.....	123
5.4.4.	Optimisation of the image registration parameters .....	123
5.4.5.	Further options for improving registration accuracy .....	128
5.4.6.	Application of optimised image registration method.....	129
5.4.7.	Experimental registration assessment method .....	129
5.4.8.	Results.....	130
5.4.9.	Comparison to Finite Element Model.....	139
5.5.	Discussion.....	145
Chapter 6.	Application of image registration to penetrating projectile impact tests	150
6.1.	Introduction.....	150
6.2.	Review of previous penetrating projectile impact experiments .....	150
6.3.	Explorative testing .....	153
6.4.	Experimental arrangement .....	155
6.4.1.	Air-cannon .....	155
6.4.2.	Image collection method.....	157
6.4.3.	Sample mount and mould .....	158
6.4.4.	Projectile .....	159
6.5.	Experimental method.....	160
6.5.1.	Sample preparation .....	160
6.5.2.	Sample mounting arrangement .....	161
6.5.3.	Data capture .....	162
6.5.4.	Data pre-processing.....	164
6.5.5.	Determining impact velocity.....	166
6.5.6.	Application of image registration .....	166
6.5.7.	Refinement of registration parameters .....	166
6.6.	Results.....	171
6.6.1.	Experimental results.....	171
6.6.2.	Registration Output.....	172

6.7.	Discussion.....	178
Chapter 7.	Thesis conclusion.....	182
7.1.	Meeting the aims of the project.....	182
7.1.1.	Define experimental conditions .....	182
7.1.2.	Confirm that image registration can be used as a method for quantifying displacement.....	183
7.1.3.	Characterise the tissue surrogate mechanical material properties.	184
7.1.4.	Apply image registration method to mechanical tests .....	185
7.1.5.	Apply image registration to penetration tests on the defined tissue surrogate.	187
7.2.	Conclusion .....	188
7.3.	Future work to address limitations identified.....	189
Chapter 8.	Bibliography .....	192
Chapter 9.	Appendix.....	215
9.1.	Registration Toolkit Parameters.....	215

## **I. Table of Figures**

Fig: III-1: A flowchart representation of the chapter headings and how they interconnect and inform the following chapters and their role in the thesis as a whole.....	xxii
Fig: 2-1: A range of examples of IEDs, which include modified hardware such as rockets and shells, and homemade devices such as pipe and shoe bombs. A range of examples can be seen in the figure above which includes several small devices that will be considered as the explosive device under investigation in this thesis. [93].	16
Fig: 2-2: Detonation of a hand grenade. The dust and gases can clearly be seen expanding from the point of detonation. The black arrows indicate where the initial shock wave that generates the rapid change in pressure has interacted and kicked up dust ahead of the main dust and smoke cloud from the explosion [94].	17
Fig: 2-3: The basic form of pressure generated from explosive detonation at a given distance from detonation, showing the transition from positive over-pressure to corresponding under-pressure before pressure returns to equilibrium after the pressure wave has dissipated [80].	18
Fig: 2-4: Graphic demonstrates the key stages of cavity formation during penetrating impact of a fragment, showing the temporary (labelled maximum penetration and maximum rebound) and the final, permanent cavity. ....	20
Fig: 2-5: Graphic demonstrates the assumed spherical shape used by this thesis. The yellow region highlights the volume of the charge (a sphere with diameter of 58 mm) and the grey outer region represents the 6 mm ball bearings spread evenly in a single layer over the surface of the explosive charge. ....	23
Fig: 2-6: Figure demonstrating the relationship between the individual variables from equation (9) and (10) for a sphere in flight [108].	27
Fig: 2-7: Peak over-pressure drops off sharply the further the distance from the point of detonation. This indicates that the lethal range of the blast pressure will be close to the point of detonation with lethal over-pressure considered to a value of $\approx 20$ kPa while above $\approx 6.5$ kPa will result in survivable injuries. ....	30
Fig: 2-8: The concentration of fragments can clearly be seen to decrease from the initial outer casing over the increasing distance from the device. The graph sets zero as the centre of the device so graph starts at the radius of the casing as this needs to be accounted for as if included it would not be a true representation of the change in fragment concentration. ....	31
Fig: 3-1: The image shows the concentric ring pattern on the mounting plates produced during the manufacturing process. Marks and patina can be seen from the corrosion of the plate material due to the interaction with the water content of the gelatine, emphasising the need for regular cleaning. ....	50
Fig: 3-2: Configuration (3) shown with a sample under preload before testing was undertaken, showing surface marks induced from the cutting of the sample. This can also be seen in the difference in the upper diameter to the lower diameter. This difference was minimal for the sample used and if found to be large, the sample was not used. ....	51

Fig: 3-3: Sample undergoing loading showing uneven barrelling that resulted from slippage at the interface which can be seen on the upper surface compared to the lower surface. This varied between samples which supports that slippage would introduce variation between different samples. ....	52
Fig: 3-4: Displays the loading profile for the load only uniaxial compression test, for the three separate compression speeds.....	53
Fig: 3-5: Displays the loading ramp curve showing the triangular wave-form for the three compression speeds.....	54
Fig: 3-6: Displays the loading curve for the three compression rates showing the 3 minute holding period. ....	55
Fig: 3-7: Plot of the uniaxial compression data including error bars that represent the standard deviation of the samples of a specific loading rate, displaying the difference between the different compression speeds. Also showing the effects of sample slippage during initial loading which can be seen as variation at the beginning of the loading curves. ....	56
Fig: 3-8: Shows the experimental results that were achieved by N.Ravikumar, and the similarity in the response of the loading curve can be seen, alongside the lower variance when compared to the results obtained [113]. ....	57
Fig: 3-9: All the samples' responses tested at compression speed of 2 mm/s, which clearly show that the initial impact of slippage is consistent among all the samples and that all curves show a similar response. ....	59
Fig: 3-10: All sample responses for loading speed of 0.2 mm/s, with the similarities between the responses. However, an increase of variance and impact of the slippage can be seen in the initial part of the loading curves across all the samples. ....	59
Fig: 3-11: As with the figures above, this shows the response of all the samples tested at 0.02 mm/s compression speed. The greater variance and anomalies in the curves can clearly be seen with outlier samples also visible when compared to the other compression speeds.....	60
Fig: 3-12: The plot demonstrates the hysteresis output showing the different compression speeds and expected time dependence. It also highlights how the mean data did not return to zero as expected but still demonstrated the expected time dependency, alongside the spike in loading for the fastest compression speed at the point of maximum loading due to the experimental rig limitations.....	61
Fig: 3-13: The inverse barrelling shape (dog bone) that was seen during the unloading process during the hysteresis tests. This was presents in all sample and varied in degree in relation to the loading speeds with 2 mm/s showing the greatest change in shape. The sample interfaces can be seen to be in full contact with the plate.....	62
Fig: 3-14: Plot of all hysteresis test conducted at 2 mm/s compression speed where the samples show similar responses apart from the two clear outlier samples. All responses show the spike in response at maximum loading were the testing rig was unable to rapidly change direction. ....	63

Fig: 3-15: The tests conducted at 0.2mm/s showed more consistent responses across all bar one of the samples which showed a different response, which would indicate from the uni-axial compressions tests a higher degree of slippage has occurred.... 63

Fig: 3-16: As with the previous uni-axial tests, it can be seen that the response is consistent across the samples, with the same anomalies seen on each of the curves that most likely are the result of the same slippage that was identified previously for the same compression speed in the uni-axial compression tests..... 64

Fig: 3-17: Experimental results of the stress relaxation experiments with the time normalised to the mean experimental total time to allow plotting on the same axis to allow for comparison. It can be seen that the response of the fastest compression speeds unloading curve is not as expected, as it was expected to show higher force and hence, follow the trend of showing greater load values than the previous compression speeds outputs with all the loading speeds not reaching equilibrium within the specified time period..... 65

Fig: 3-18: The unloaded and loaded configuration of the FE model with the loading plate and sample clearly visible alongside the symmetry used. The upper image represents the unloaded configuration and the lower image registration represents the loaded configuration. The scale represents the Von-Mesis strain..... 70

Fig: 3-19: Overlays of the fitted material to the mean experimental output, which shows that the anomalies that were induced in loading have influenced the fitting. However, even with the limitation, it can be seen that for the curve with the most variance, the slowest compression speed remains within the standard deviation of the sample response. .... 71

Fig: 3-20: Overlays of the fitted material to the mean experimental output. This shows that the optimisation was not successful with only the middle compression speed having been fitted effectively as the curve shows the same shape and has a large degree of overlap with the experimental curve, and if it does deviate, it is within the standard deviation. .... 73

Fig: 3-21: Overlaid fitting data for the hysteresis experiments again showing the optimisation was unable to fit the parameters to the fastest and middle compression speed. The model does produce an effective fit to the slowest compression speed. .... 74

Fig: 4-1: Example of a common speckle pattern applied to the surface of a sample for DIC the irregular nature of the pattern can be seen (note: the image was taken using a greyscale camera) [178]..... 83

Fig: 4-2: From P.Moy. Shows the application of DIC to crack tip propagation in a ballistic gelatine sample. The calculated strain field can be seen overlaid on the sample at key points in the loading curve, and the speckle pattern is clearly visible in the inlaid images [185]. .... 84

Fig: 4-3: An example of a common experimental polariscope setup, (1) light source, (2) quarter wave plate (2 plates), (3) polarizer, (4) sample, (5,6,7) sample and experimental mounts, (8) analyser and (9) camera [128]. .... 85

Fig: 4-4: shows an example of two different soft tissue surrogate materials birefringent patterns when under compression loading, (a) konjac gel (plant derived gelatine) and (b) ballistic gelatine (animal derived gelatine) [128]. ..... 86

Fig: 4-5: Graphical representation of the image registration process, created by the author showing a flowchart representation of how the registration algorithm generates the optimal transformation. Once the optimal value has been reached, it is then used to generate the registered image [101]...... 89

Fig: 4-6 Is an example of free-form deformation using B-splines showing how the grid of control points (black and red points) is distributed in the 3D space defined by  $(s, t, u)$ . The B-splines are the lines that connect the points. The motion between  $P(s, t, u)$  and  $P'(s, t, u)$  is smoothly interpolated to allow capture of the transformation while maintaining the splines and control point connections, the spline allowing the smooth curved deformation in the region between the defines points [45]. ..... 90

Fig: 4-7: Shows how each pair-wise registration defines its own independent initial coordinate system from the floating image. The resultant transformation is defined by the motion of the specific coordinate system as the transformation is optimised to give the new control point positions for that given pair-wise registration process. Consecutive registration will use independent coordinate systems to determine the optimal transformation. .... 97

Fig: 4-8 The composition of the pair-wise transformation over two consecutive registrations using a user defined initial coordinate system were the B-spline registered transformation from Registration 1,2 ( $T_{1,2}$ ) is applied producing the displacement  $X_{1,2}$ . Then the second registrations  $R_{2,3}$  B-spline transformation ( $T_{2,3}$ ) is applied producing  $X_{1,3}$ . .... 98

Fig: 5-1: Process layouts of the two methods that form the basis of the registration method, including the pair-wise registration and the composition of the pair-wise transformation to produce the cumulative deformation over the experimental data captured. .... 104

Fig: 5-2: Example of the image recorded on the Phantom V210 camera of the 3 cm diameter indenter and the gelatine sample with injected grid pattern before pre-processing of the image data. The image shown is the initial image from the data capture before loading occurred. .... 107

Fig: 5-3: The indentation data capture opened in the CineView software. The upper image shows the initial frame of the capture and the lower image shows the cropping which selects the ROI removing the unnecessary image data and the image manipulation interface of the CineView Software tool as shown on the left of the window to adjust the gain and intensity of the recorded images [233]. .... 107

Fig: 5-4: Depicts examples of barrel distortion on the left and pin cushion distortion on the right. This shows clearly how this distortion would impact any attempt to quantify deformation from images subjected to this distortion [234]–[236]. ..... 108

Fig: 5-5: Experimental image of the grid pattern used to investigate the possible impact of lens effects. Taken at one of the series distances from camera for the defined camera arrangement used for the penetrating impact tests (40 cm from camera to the grid pattern) and match focal lens and aperture. .... 109

Fig: 5-6: Left, the undeformed configuration of the image. Right is the deformed configuration 10 pixel extension. Both images have a Gaussian noise applied of mean 0.0 and a variance of 0.001 to account for noise that could occur in the experimental data. .... 114

Fig: 5-7: A shows the undeformed synthetic image and B shows the deformed synthetic image. C and D represent the results of the Nifti-reg toolkit registrations, with C being the result of the SSD metric and D being the result of the NMI metric. E and F results of the Matlab toolkit with E being SSD metric and F being the PI metric. .... 118

Fig: 5-8: The initial frame open in the CineView software ready to calibrate the sample with the indenter. The mounting plate can be clearly seen which is being viewed in the CineView software interface window. .... 122

Fig: 5-9: Images that formed the basis of the optimisation of the registration parameters, A: Moving Image, B: Static Image 1 pix Transform, C: Static Image 2 pix Transform and D: Static Image 4 pix Transform. Due to small amount of motion, images have been magnified. .... 124

Fig: 5-10: A is the 4 pix transformed image and B is the output of SSD metric registration with the initialisation applied to the non-rigid registration. Visually, the two images are very similar but differences can be seen around the indenter and upper surface of the gelatine which is surrounded by the red box. Difference are also highlighted around the edges of image B as a dark frame can be seen, this is highlighted in the image by the red arrows which shows that the whole image has been transformed. .... 125

Fig: 5-11: as with Fig: 5-10, A represents the static image and B represents the output from the NMI metric registration with the initialisation applied to the non-rigid registration. This registration shows less difference in between the two images particularly around the sample's upper surface (highlighted within the red rectangle) when compared to the SSD response in Fig: 5-10. The same black border can be seen around B (red arrows) which is evidence of the image transformation. .... 126

Fig: 5-12: Shows the ITK Snap working window with the indenter highlighted which will be used to define the mask for the given frame. The area that is highlighted in red is the area that is selected as the region defined as the mask, with the software control panel on the left of the image. .... 128

Fig: 5-13: Overlaid registered image and experimental image for frame 13 in MedInria showing the similarity between the images as they have aligned very well almost showing no difference between the two images. The red area highlighted by the yellow arrows shows the contraction of the registered image to capture the motion of the gelatine resulting from the repositioning of the control point grid due to the optimisation. While also highlighting were blur due to differences in the images can be identified. .... 131

Fig: 5-14: Overlaid registered image and raw image for frame 41 on MedInria showing the similarity between the images again as minimal difference can be seen. The red area shows the contraction of the registered image which indicates the general direction of motion captured by the registration as it is located at the indenter



in opposite direction of the captured motion. This and the regions where image blur due to differences in the image are highlighted by the yellow arrows..... 132

Fig: 5-15: Comparison of the different displacements showing that the outputs of the registration are comparable to the manually measured indenter motion. However, the difference between these and the experimental measurement (machine head motion) are clear, especially during the initial loading region and at the end of the loading believed to result from optical distortion due to changes in the surface geometry as seen in the captured experimental footage. .... 135

Fig: 5-16: Diagram of model showing the  $\frac{1}{4}$  symmetry that was applied along the central axis of the indenter and the rigid body that represents the indenter. The fixed condition can be seen on the lower edge of the main gel body..... 140

Fig: 5-17: In this figure, it can be seen that the FEA loading body maximum displacement has been chosen to ensure it is in a bracket to allow comparison between the different results. .... 141

Fig: 6-1: A schematic cross section of the sabot used showing the EVA core (in grey), magnet (in blue) and mounting plate (in light grey)...... 156

Fig: 6-2: The cannon in the lab the mounting plate can be seen suspended from the frame and the ballistic shield can be seen surrounding the barrel aperture, with the compressor tank seen below the cannon body. .... 157

Fig: 6-3: A top view schematic of the arrangement used to film the ballistic impact, showing the camera and connected laptop used to record the impact, with the lighting rig visible on the opposite side to the camera arranged to produce a diffuse back light and the sample mounted centrally in the air-cannon..... 157

Fig: 6-4: An image of the mould that was used which shows the transparent window to allow the visualisation of the sample, which allowed the casting 160 mm x 160 mm x 160 mm gelatine. Please also note the hole that the projectile will pass through to impact the sample. .... 159

Fig: 6-5: This shows the two mounting arrangement. On the left, the sample is confined on all faces bar the top and freely resting on a support block at the bottom. On the right, the unconfined sample rests on the support block to ensure it is at the correct height. Support blocks were manufactured from a single sheet of plywood with a hole that aligns with the sample mount hole. It should be noted the light blue represent the clear panels and the dark blue the mould/cartridge. .... 161

Fig: 6-6: The grid pattern is extracted from the frame and the same pre-processing is used to improve the contrast. These images were not back lit due to the opaque nature of the board the grid pattern was mounted on so to perform the calibration, the gain and intensity had to be altered to allow measurement (This uses the CineView software package). .... 162

Fig: 6-7: An example of the penetration data captured showing the point of the maximum penetration that occurs before the gel rebounds to form the permanent cavity. Picture here open in the CineView software before initial editing occurs. On the right of the image is the control panel and the frame position in the movie. .. 165

Fig: 6-8: The cropped region of the data and the CineView tool that was used to adjust the gain and brightness to maximum contrast to optimise the image for the

best possible registration. In some samples, variation in the material resulted in an asymmetric cavity growth and motion that results in the general tear drop shape that the maximum cavity forms before the rebound and collapse occurs to dissipate the energy of impact. .... 165

Fig: 6-9: This shows the response of the nifti\_reg toolkit, A: Moving Image, B: Static Image. The warping and inability to capture the projectile movement can be seen with C: NMI registration and D: SSD. The region is indicated by the blue rectangle is the region with the greatest difference with the variation in the projectile and cavity position. Also note the area that has been highlighted by the yellow arrows, as C and D both show distortion that is not present in the static image. .... 168

Fig: 6-10: Shows the response of the Matlab toolkit for penalty term of 0.0015. As before, A and B are the moving and static image. The results of the registration C: PI metric and D: SSD metric. In these images, it can be seen the cavity and grid pattern motion for these frames are captured including the kink in the cavity, which is the region that is contained in the blue rectangle. The differences in the projectile position indicate further refinement is possible to improve the result but will need to be performed using the experimental footage which is indicated by the red arrow. .... 169

Fig: 6-11: The mean penetration for all confined and unconfined tests normalised to the experimental launch speed, with the standard deviation between the curves shown using error bars with the initial incline representing the initial penetration with the rebound and settling that was witnessed during the filming of the penetration impact..... 171

Fig: 6-12: Shows the comparison of the measured penetration and the registered penetration, for the confined mounting arrangement. There is a clear difference in the two responses both in magnitude and curve shape. .... 174

Fig: 6-13: This figure shows the comparison off the registered and measured penetration for the unconfined impacts. Again there is a clear distinction between the two responses. The second set of registration is a result of anomaly at impact due to the failure of the sabot which resulted in the projectile impact and launch speed varying as seen by the difference in the curves. .... 174

Fig: 6-14: Demonstrates the experimental output for 22<sup>nd</sup> frame of an unconfined impact test. The blue box highlights the multi-planner motion with two grid lines clearly moving different directions or with the cavity passing in front or behind them. The registered image shows that the pair-wise registration again performs as expected tracking the cavity and the grid line motion. However, the failure of the composed transformations can be seen in the lower image, with the red rectangle highlighting the error caused by the continuous transformation assumption..... 177

Fig: 6-15: Shows the results for the registered output for the 42<sup>nd</sup> frame of the same experiment. Both boxes show the multi-planar motion of the grid pattern throughout the length of the cavity alongside the increasing error due to the assumption of continuous displacement as seen in Fig: 6-14..... 178

## II. Table of Tables

Table 2-1: Table shows the initial velocity and corresponding speed of sound and determined Mach number and the related drag coefficient that will be used as inputs for equations (9) and (10) to determine the forces acting on the fragment. ....	27
Table 2-2: Resulting velocity change of the fragmentation in relation to the initial angle of flight and the distance from the point of detonation, to the maximum radius where the first fragment no longer follows a flat trajectory. Excluding 0 ° for reason described above.....	33
Table 3-1: Table shows the average temperatures for the uni-axial compression tests, alongside the maximum and minimum and range between these values showing that all samples fell within the defined bracket for consistency. ....	57
Table 3-2: Indicates a summary of the recorded temperature information from the hysteresis testing showing the similarity to the uni-axial compression test.....	61
Table 3-3: The temperature data from the stress relaxation test which indicated that unlike previous tests the fastest compression speed showed the greatest variation and range.....	66
Table 3-4: The optimised material parameters for the uniaxial compression tests.	71
Table 3-5: Shows the parameter optimisation including the individual fits and the optimised parameters for the uniaxial compression test for comparison. ....	72
Table 3-6: The material parameters from fitting to the individual strain curves for the stress relaxation experiments, with the uniaxial compression fittings for comparison. ....	75
Table 3-7: the material parameters from the fittings that can be considered to be successful from all the optimisations for the different mechanical tests.....	77
Table 5-1: The table below represent the key registration parameters used for the Nifti-reg toolkit. The spacing of the B-spline grid and the penalty term used in the definition of the transformation alongside the specific similarity terms that are being investigated. ....	113
Table 5-2: The key registration parameters used for the Non-Rigid Version 3 toolkit are specified below. This, as in Table 5-1, shows the B-spline grid spacing, the specific penalty term that is used and the similarity metrics that have been used.	113
Table 5-3: The accuracy of the registrations that were performed using the nifti_reg toolkit for the synthetic images. Assessed using two methods the intensity difference and image similarity score using the similarity metric Sum of Squared Difference ....	115
Table 5-4: The accuracy of the registrations that were performed using the Matlab based toolkit for the synthetic images. As with the output of the Nifti-reg toolkit, it displays the intensity difference and similarity score. ....	116
Table 5-5: The results of the similarity score for the synthetic images. The similarity difference method was previously defined in section 5.3.1, and in this case, all use the SSD similarity metric to calculate the similarity score for the given registrations. ....	119

Table 5-6: The assessment of the registration outputs of the different displacements for the proposed similarity metric including the Mean Intensity Difference which shows higher accuracy the closer to zero the value is. The Similarity Score remains as used previously and the Maximum Displacement was registered at the tip of the indenter. ....	126
Table 5-7: This table represents the final registration parameters that were applied to the experimental testing for the Nifti-reg toolkit. ....	127
Table 5-8: Shows the parameters that were used form the reg_aladin toolkit for the purposes of generating the initial affine transformation used in non-rigid registration. ....	127
Table 5-9: Shows the registration and the corresponding images, pairs aligned with the mean intensity difference and the similarity score for the comparison of the registered to the reference image. ....	134
Table 5-10: Shows the series of frames and the corresponding X and Y displacement plots in m. As stated earlier, the origin is in the top left corner, with x positive in the up-right direction and y positive in the left-hand direction.....	136
Table 5-11: Shows the values of the material model parameters that will be used in the model.....	140
Table 5-12: Comparison between the output of the FEA model and the registered displacement field in the x axis. It should be noted that due to the registered images including the area above the surrogate, results in the differing sized plots. ....	142
Table 5-13: Shows the same table as in Table 5-12 for the Y axis displacement field. ....	144
Table 6-1: Shows the registration parameters used in the registrations of the images using the Nifti-reg toolkit.....	167
Table 6-2: The registration parameters used in the registrations of the images using the Non-Rigid Version 3 toolkit.....	167
Table 6-3: List of the registration parameters that will be used for the image registration of the data with the possibility to be further refined if needed. ....	170
Table 9-1: Shows all the options that can be used for the Matlab based toolkit. In the case of the toolkit only one option can be applied from each option class if defined, if not toolkit will use its default options [212].....	215
Table 9-2: Shows all the options that can be used for the nifti_reg toolkit. In the case of this toolkit in some case multiple options can be applied to achieve a combination effect, if not toolkit will use its default options .....	216

### **III. Executive Summary**

#### **a. Research question**

In this project, the author aims to ascertain the effectiveness of image registration as a method for the quantification of displacement in mechanical testing. Specifically, the application of such a method to the investigation of penetrating fragment impact tests on a tissue surrogate within a military context. The specific objectives are defined below as:

- i. Establish the context and analyse the mechanics of fragments encountered in a military setting, and define the experimental conditions needed to emulate the impact of such fragment on a tissue surrogate.
- ii. Review available tissue surrogates that have seen previous usage in the investigation of penetrating impact testing, and characterise the selected experimental tissue surrogate's mechanical material properties.
- iii. A comparison of image registration techniques and established mechanical testing arrangements currently used in the literature, with the aim to review the method's limitation and benefits when considering their usage with particular consideration to penetrating impact tests.
- iv. Validate the image registration method using a mechanical testing arrangement that has reduced complexity (a reduced loading speed and higher degree of control over experimental conditions) for the assessment of the methods output when compared to a finite element model of the experimental arrangement.
- v. Assess the effectiveness of image registration as means for the quantification of displacement for penetrating fragment impact experiment, using the defined experimental conditions previously defined.

#### **b. Rationale of research**

The investigation of penetrating projectile impact has presented challenges in dynamically quantifying penetration and the surrounding material response to loading. This is especially true when considering living tissue or tissue surrogates due to the complex material properties and the limited prediction of the wider material response resulting from the complex loading patterns and changing loading

rates. The established optical methods for the quantification of displacement currently in use, range from specialist automated techniques that require a large investment in materials and equipment, to manual methods that are time expensive but can be performed with minimal investment in equipment. The more specialist automated methods large experimental set ups are often impractical or carry a high risk of damage to equipment. Furthermore the equipment has to be placed at such a distance that the quality of the data gathered has limitations. However the data that these methods can collect, provide valuable insight to impacts and detonation. Image registration, however, is an automated method that can be used with minimal specialist preparation of samples and the methodology can be used with a large range of camera equipment and video capture formats both in 2D and 3D arrangements. This would allow for assessment with reduced experimental complexity experimental, as established high speed video technologies could be applied with minimal sample preparation and experimental specialisation, while the possibility of 3D assessment of the dynamic impact would greatly aid in the understanding of the mechanical impact allowing it to be used as a tool to validate computational models and the biological effects of such impacts.

### **c. Project scope**

This project will have several milestones to allow the investigation of the research question above. These are multifaceted to provide the foundation for the exploration of the application of image registration as a method for quantification of displacement during penetrating impact. Each milestone can be considered to represent the topic of a chapter of this thesis, and the connection between these chapters can be seen in Fig: III-1. It should be noted that the figure also includes the project introduction, conclusion and discussion. The milestone are listed below by chapter number:

- i. Establishing context for project work: a discussion in detail of the reason to undertake this work and defining how this thesis will achieve the project goals.
- ii. Review epidemiology of fragment injuries within a military setting and sources or ordinance that generate the potential fragments. This chapter establishes the conditions that will be applied to the penetrating impact tests.

- iii. Selection and characterisation of the tissue surrogate: a review of the different tissue surrogates that have applied to similar experiments in the literature will be presented. Additionally the characterisation of the chosen tissue surrogate allow a deep understanding of the material and allows the optimised material model to be used to validate the image registration output.
- iv. Discussion of existing optical-based methods for the quantification of deformation: explores how optical methods have been used in previous work. It also defines the image registration theory and the methodology that will be applied in this project, alongside presenting specific formula that form key parts of the registration algorithms.
- v. Assessment of registration-based measurement of displacement and strain: application of the image registration toolkits to both synthetic images and synthetically transformed experimentally captured images. That will assess the accuracy and effect of altering the image registration parameters. Followed by applying the optimised registration parameters to mechanical experimentation specifically a uniaxial indentation test, which will be validated using a computational model created using the material parameter output form the characterisation.
- vi. Application of image registration to penetrating impact tests: this focuses on the application and suitability of image registration methodology to penetrating impact tests. Using the experimental boundary conditions identified and building on the experimental method that was identified in the previous Chapter.
- vii. Thesis conclusion and proposal for future work: a discussion of the key findings of the project and the conclusion that the author has drawn from the work undertaken. Followed by a discussion possible avenues of future research to overcome the short comings identified in this thesis.

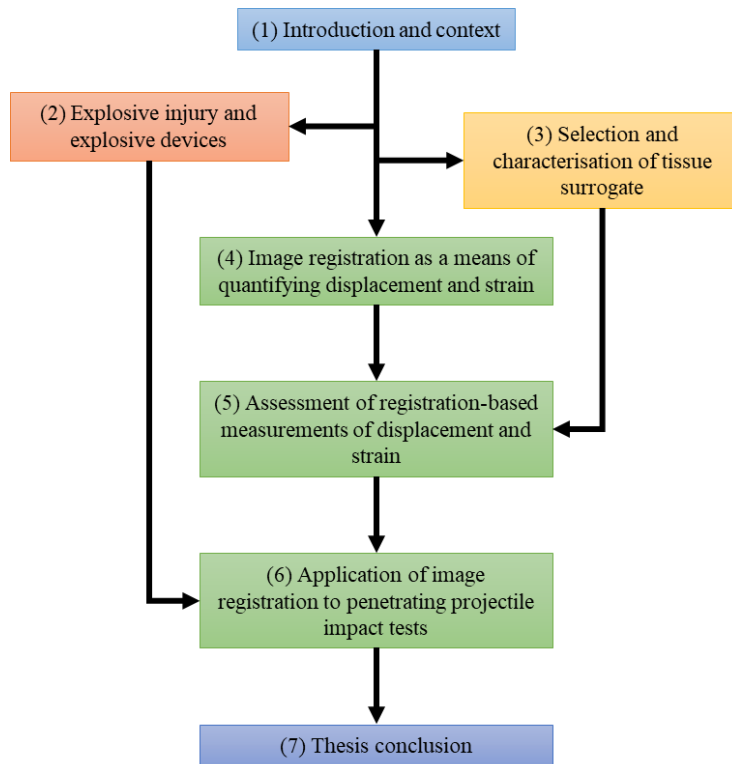


Fig: III-1: A flowchart representation of the chapter headings and how they interconnect and inform the following chapters and there role in the thesis as a whole.



## **Chapter 1. Introduction and context**

The purpose of this project is to explore the use of image registration as a method for quantifying displacement during penetrating impact on tissue surrogate-like material with specific focus on considering its application where traditional techniques would not be appropriate or difficult to implement. The application of a quantitative measuring technique for assessing the dynamic response of tissue surrogates has presented many challenges and resulted in a wide variety of responses due to the natural variation of biological or biological-like materials. This is complicated further when considering the complex and dynamic motion generated by penetrating impacts. Image registration could provide a way to minimise these limitations due to its ability to track the motion between image frames, recorded by a range of different image capture methods. This can be further enhanced with the ability of the image registration to capture and quantify deformation in 3-Dimensions or between different image modalities (recording devices). When considering these benefits, image registration could be a powerful tool in the quantification of deformation during penetrating impact for a range of situations and experimental arrangements.

This chapter presents a background literature review of both the current conflicts and how these changes have driven the use of new weapons and technologies which in turn have led to a change in epidemiology of currently identified injuries. This is followed by a review of the current methods used to experimentally assess or simulate such injuries. Finally, the chapter concludes with the proposed ideas that will be investigated throughout this thesis.

### **1.1. Current conflicts and technology**

Modern conflicts differ greatly from those of a hundred years ago; those fought in the past have mainly been classified as high intensity conflicts, referring to open warfare between two forces of comparable strength. Several other types of conflict that have been classified over the past hundred years were defined as medium and low intensity conflicts, which are informed by the intensity of the conflict in relation to time between engagements. Most modern conflicts are now classed as low intensity due to the large amount of time between contacts of opposing forces [1]–[4]. There has also been changes in the types of forces that are opposing each other: Until recently, conflicts have been fought by well organised and equipped forces

supported by a nation or group of nations. This meant that they were similarly equipped and trained, while employing similar tactics that could be considered comparable. However, a new type of warfare has emerged, seen during the “Troubles” in Northern Ireland and the continuing unrest in Israel and Palestine and, more recently, Iraq and Afghanistan. This is referred to as asymmetric warfare [1], [5], [6]. It describes that the forces opposing each other are different in size, organization and military technology used. These can be distinguished between modern armed forces while others are similar to a militia or paramilitary organisation. This has caused a large shift in both the tactics and technology encountered in battle field and civil conflicts around the world.

This change has meant that combat forces that now take to the field differ drastically in terms of equipment and tactics but can still be considered as effective fighting forces that present a real threat in a tactical and strategic sense. A modern army is considered to be a force that employs a combined arms approach, using advanced networking and communications allowing commanders and troops to manage large amounts of information while permitting rapid communication to deploy specialists and weapons in the most effective manner possible.

A force that is considered to have low technology may in fact have access to quite advanced equipment, normally acquired from countries’ surplus stock or acquired illegally through the black market or clandestine operations [1], [5], [7]. The main technology these forces lack is integrated communications as well as battle command and control structures meaning such forces have to rely on simple radios and mobile phones in some cases.

Consequentially, these changes have led to the use of what has been called terrorist and insurgent tactics, traced back to guerrilla and militia tactics used in the past. These have focused on smaller, fast moving forces or groups working independently to attack and disrupt larger forces as well as directly targeting infrastructure. The main tactics employed are ambushes and raids using bombs or groups of fighters. These are designed to inflict maximum damage on personnel and material in any given terrain. The greatest change in recent years is the indiscriminate targeting of civilian targets such as markets, schools or residential areas in non-conflict zones around the world, alongside the increasing use of scaled down versions of these tactics employed by criminal gangs and other organisations [1], [5], [6], [8], [9].

## **1.2. Wounding epidemiology of current conflicts**

The injuries which occur as a result of these conflicts discussed in 1.1 statistically differ between the epidemiology (classification and description of injury) when noncombatants such as civilians or bystanders are compared to combatants such as fighters or military personnel. Major factors for such injuries are the use of body armor, distance from the devices and the type of device used. The most likely devices that cause fragment related injuries are generated by explosive devices, as bullet and other purpose designed projectiles are considered to have a different and distinct wounding epidemiology. So for the purposes of this work we will consider injuries caused by explosive devices and their usage [1], [5], [10]–[12].

The primary reason for injury in these conflicts is hostile action resulting from direct conflict with the enemy forces [1], [2]. With such injuries, two basic classifications have been used. Firstly, injuries compatible with life (non-lethal injuries) which are focused on the extremities and core. Most commonly recorded are laceration, penetration and contusions of the extremities, of both the upper and lower body, with lacerations being deep cuts or tears in the skin, and contusions being an area of skin with ruptured blood vessels that form bruises of varying severity.

Secondarily, injuries that are incompatible with life or lethal are focused on the head, the upper torso where vital organs are present or areas where main arteries are located [6], [11], [13], [14]. Injuries inflicted will include many separate specific pathologies which stem from the primary injury mechanism, further compounded by the local environment and specific conditions that resulted in the injury. A common pathology presented is ischemia or inadequate blood flow and hemorrhaging which describes blood loss from wounds or injuries; this results from the rupture or occlusion (blockage) of the lymphatic or circulatory system [6], [11], [13], [14].

Examples of other injuries include traumatic amputation due to the pressure wave or shrapnel, fracture and rupture due to pressure differential and impact with the environment due to the propellant force of the blast. Other injuries include lacerations or air embolism that block blood vessels, resulting from the penetrating shrapnel or blunt impact with another object or the environment itself [14]–[16]. There are also unseen injuries that may not present in the acute period of time after the injury such as compartment syndrome, crushing or infection. Compartment syndrome is when the soft tissue swells so to decrease or block fluid flow, preventing oxygen reaching organs and tissue and if left this can result in those vessels rupturing. The pressure that this places on medics and forward medical centres has necessitated the refinement of triage techniques used in combat medical care and

now seen in civilian medical care. This is normally referred to as mass casualty incidents. In these cases, the prior training of the medical professionals, available equipment and types of injury impact the effectiveness of medical care that can be provided [1], [9], [11], [12], [17], [18].

This means the two areas that can be most affected by research are the training of medical professionals and the maximization of both the effectiveness and usage of medical supplies. This work will inherently focus on those injuries that directly pertain to penetrating impact.

### **1.3. Assessing penetrating impacts**

The main aim of this research project is to investigate if image registration can be used to quantify the physical response of soft tissue surrogates during penetrating impact by fragments in an experimental setting with the results of this project being applied to aid in furthering the understanding of such injuries.

There are a range of methods that have been previously applied to the investigation of penetrating projectile impacts which have included computationally modelling the impacts which is then validated with experimental testing. There are multiple different approaches in the literature; some examples are reviewed below.

After impact, a measurement of the depth of penetration using a ruler or measuring tool can be taken. This can give an accurate measure of the depth of the permanent cavity, but it does not allow the investigation of the dynamic or wider material impact beyond a qualitative assessment of the after impact damage [19]–[22]. A second example is a full hybrid assessment of the after impact surrogate material, which includes assessing the wider damage such as rupture or laceration from the impact, taken directly from the surrogate used or from detailed images of the surrogate recorded over the course of the penetrating impact. Visual assessment is not possible when using opaque tissue surrogates or cadaveric tissue as it is not possible to image through these surrogates without specialist equipment.

One of the most common methods to collect experimental data is to use video equipment to record the impact. The specific configuration varies in the literature and it is directly tied to the goal of the test. Examples include high speed video technology (often paired with backlighting), or arrangements that make use of multiple individual pieces of video equipment enhanced with finely controlled lighting arrangements to capture the impact between the different cameras. All these methods have relied on point-to-point tracking approaches for the region of interest

[19], [23]–[27]. Point-to-point based tracking methods are often based on the principle of motion capture, which means this is often used to track the projectile as it penetrates the material. The manual tracking employed is often used on specific frames, such as the maximum temporary cavity or a sequence of frames and is a time consuming process. Image registration with its capacity to be automated and ability to be tailored to a broad range of imaging methods, highlights its possibility to be a versatile tool for the assessment of penetrating impacts.

#### **1.4. Blast experiments**

While considering the methodology of penetrating impact due to explosive devices, it's important to also consider the methods applied to assessing blast injuries and mechanics. The reason for considering these methods is twofold: they have to record data in the same or greater dynamic range as the common velocities tested during penetrating impact experiments, and the well-established link between penetrating injuries and the detonation of military ordnance has to be observed [28]–[31]. These investigations have centred around three main areas: injuries due to detonation, the effectiveness of both personnel armour and vehicular defences, and the development of ordnance designed to eliminate structures or hardened targets such as bunkers or buildings [32]–[36]. These methodologies are often arranged around a combination of both video capture and embedded sensors positioned at key points or areas of interest. In this case, embedded sensors refer to sacrificial blast tubes, electronic pressure sensors and thermometers used to capture the change in physical variables due to the detonation. To allow for assessment of injury, these methods use human surrogates or tissue surrogates (such as ballistic gelatine) [28], [31], [37]–[39]. One of the significant limiting factors in these experiments is the massive forces and violence of the detonation. This limits the use of active and precise sensitive equipment as it can be damaged or produce erroneous results or fail due to damage. This means the use of video capture technology for both qualitative and quantitative measurement has become a standard method for the capture of penetrating impact and explosive detonation. However, this requires the careful placement of camera and recording equipment to avoid damage and maximise the quality of the recorded images, becoming a balance between the risks of damage and accuracy. Specific measurement of deformation or motion has been achieved using calibrated scales affixed to the target or the surrounding area to allow the defining of spatial resolution. Alongside considering the footage collected from multiple viewing angles, this can be an effective measurement of the response to such tests. From this,

it can be concluded that any effective method will likely need to be optically based and will need to be adaptable. Image registration can be used to compare multiple angles and track the motion from all the different frames of the captured experimental video, which further highlights that image registration could be an effective and useful tool for such experiments.

## **1.5. Image registration**

Image registration is an image-based assessment method that has been applied to several fields of study. These have included image processing, target tracking and object identification, with considerable use in the field of medical imaging [40]–[42]. Image registration is the process where two or more images are compared and the alignment or transformation between the two images is calculated; this can be performed in either 2D or 3D. Normally, the image taken at the target point is called the reference or target image and the image being transformed is referred to as the moving or floating image. The process aligns the moving image to the static image and defines the transformation in terms of pixels motion, which can then be calibrated to achieve displacement [43]–[46]. There are many different formulations and methods that can be used to define both the optimisation and transformation which have been tailored to achieve a specific goal or work on a particular platform. These methods commonly uses a B-spline function and control points grid to define how the image transforms and an interpolation function to define the new pixel positions producing a pixel wise transformation. Common algorithms that have been used to describe B-spline transformation are rigid, affine or non-rigid which have increasing complexity. Possible transformations for the rigid transform can be where only rotation, translation and reflection is considered, to non-rigid applications where the transformation image is freely transformed to define motion between the images. It is also possible, with the correctly selected toolkit or formulation, to compare images from multiple different imaging sources or imaging modality (recorded using different imaging methods such as X-ray or MRI) [47]–[52]. These are normally chosen based on the desired function or experiment that is being undertaken. Image registration has seen usage in motion capture and tracking targets for various other applications such as geophysics and satellite/aerial-based imaging or identification [43], [53], [54]. This work will focus on the image registration that is used in the medical field. The theory of image registration will be explored in full later in this thesis.

Image registration in medical engineering has been used for many applications, mainly in diagnostics and visualisation. It should be noted that some methods have been tailored to be used with a specific organ or pathology to account for any difficulty in the collection of images or the possible content of the collected images. However, this thesis will focus on the actual applications of image registration over the specific differences in theory. As with its wider use, these applications have included the alignment of images and the tracking of changes due to pathology or organ growth and motion [55]–[59]. Image segmentation and identification methods have been included in these particular formulations of image registration to aid in tracking objects or organs between different image modalities or different imaging planes [60], [61]. When considering medical image registration that have specifically been used to track motion over time, examples include the investigation of myocardial and cardiac objects [57], [58] and respiratory motion [59]. In these cases, image registration was used to track the motion between images that have been taken sequentially in time. The speeds considered here do not match the speeds that have been encountered with fragment impact; however, this shows that in principle, image registration can be applied consecutively to assess dynamic deformation. Further applications include active surgical tracking to aid in understanding how the organ and tissue moves during surgery, which highlight the flexibility of image registration and the possible toolkits that are available [62], [63].

## **1.6. Thesis proposition**

This thesis proposes an image registration method to allow quantification of the deformation over the course of the penetrating impact of the fragments encountered within a military setting; specifically, in an accessible laboratory setting using 2D image registration to quantify the deformation, with the possibility to further develop the method to allow 3D registration or explore more complex impacts. The information that this could provide would help inform the understanding of the mechanical processes that occur in penetrating impact and open up a new experimental arrangement that can be applied to a wide range of different tests that is highly flexible in terms of filming arrangement and compatibility with a range of camera technologies. The possibility of 3D image processing could greatly aid in the validation and creation of accurate computational models or the assessment of the biological impact of different penetration helping to further the medical understanding and treatment. With this thesis having the core focus on establishing

the suitability of image registration as an experimental technique to assess penetrating impacts.

To achieve, this the work undertaken will be presented as self-contained chapters that explore the key aspects of the project which each aim to achieve a specific goal or answer a specific research question.

Initially, background information and previous work will be reviewed to clearly establish the rationale of why this work is being undertaken investigating the impact of fragments in a military setting. As discussed, these normally result from the use of explosive devices. In modern military setting, there is a wide range of different devices that have been encountered which include both conventional and unconventional explosive devices. As testing the type of fragments that are produced by such devices would require blast experiments to be performed, which would incur a large experimental investment in both time and resources, a more simplified experimental approach will be used in this work alongside a review of available literature to determine the speeds, distribution and shape of the fragment that are generated, which will then be used to inform the boundary conditions for the impact tests.

This is followed by a chapter exploring the available tissue surrogates and the selection of the tissue surrogate that will be used in later testing. This will include a characterisation of the material properties, helping to establish how the material responds during testing, with the primary objective to produce a material model that can be used to generate a computational model to allow the validation of the image registration output for a simpler and lower speed mechanical test. Secondly identifying any experimental concerns that relate to the material that will need to be accounted for moving forward, while also identifying and refining the manufacturing process to ensure consistent sample across all the planned testing.

This following chapter provides a review of the optical methods for the experimental quantification of displacement that are currently in use and the current uses of image registration. Followed by a review of the theory of image registration, including a description of all key functions and algorithms in relation to the toolkits that will be used in this thesis.

To validate the application of the registration method, a series of indentation tests was performed at a lower velocity for ease of assessment, while also allowing the material model identified in the previous chapter to be used to validate the image registration output. Even though this is a large reduction in speed when compared to



common penetrating impacts, it allows a greater control of the experimental arrangement and reduces some of the complexities that arise from such penetration tests easing the assessment of the registration output. This also has the benefit of showing that the image registration could be applied to a range of different mechanical loading speeds and testing arrangements.

After establishing the optimal initial registration parameters, the final chapter will then apply this arrangement to the penetrating impact tests to determine the response of the tissue surrogate. This chapter will initially review available literature for the experimental assessment of penetrating impacts to allow the comparison of the proposed method to those that are already in use, while also informing the experimental arrangement supported by the work in the previous chapter.

This thesis will conclude with the final findings of the project in relation to the objectives and aims presented in the executive summary, alongside proposing future work that builds on the findings or addresses any issues that have come to light during this thesis.

## **Chapter 2. Explosive injury and explosive devices**

### **2.1. Introduction**

As discussed in Chapter 1, the main focus of this work is to assess the applicability of image registration as a method to quantify the displacement due to fragment impact and as identified in that chapter explosive ordnance is the most common source of fragments encountered. However there is a wide range of different explosive devices encountered which produce a range of different fragments. So to establish the boundary conditions for the later impact test and for the assessment of the impact the injuries that are encountered when considering explosive devices, it is important to understand how these devices differ.

When investigating military ordnance or any form of explosive devices, it is important to understand both the mechanics of the detonation and the intrinsic discontinuity due to the random nature of the material fracture/failure of the explosive device casing. The design of the specific devices, be it anti-personnel (humans) or anti-material (hardware, vehicles and aircraft), alongside the specific explosive compound that is used, will directly impact on how the device detonates and its mechanical interaction with the human body. It should also be noted that information on current military technology is often restricted in access; however, literature is available for older weapons as well as research into defensive and related technology. When supported by available literature on military wounding and previous literature in the civil and industrial fields can provide useful insights into the mechanism of detonation and mechanical interaction with the human body alongside considering the experimental arrangements that have previously been used in industrial and published military research. Combining these literature sources and an analytical study of an example device will enable a deeper understanding of the proposed experiment and define the experimental conditions that will need to be applied for the penetrating impact tests. This chapter focuses on establishing these parameters and assumptions, while reviewing the injuries that are associated with the detonation of military ordnance.

A large amount of work has been done regarding the chemical composition and physical detonation process of explosives with the goal of improving weapons technology and the wider application of explosives in heavy industry. This has been extended to the thermal energy release and the concussive force produced by the detonation.

Previous research into explosive chemical composition relates to the specific compounds used to produce the explosives material. By controlling these compounds, it is possible to achieve fine control over the rate of combustion, the magnitude and force of the blast [64]–[66]. The blast from explosive compounds is the rapid expansion of the gaseous by-products from the combustion process and the rapid release of exothermic energy. In the case of more specialist explosive compounds, the actual chemical reaction can be tailored to achieve a higher blast but reduce the amount of energy released as light energy and maximise the thermal energy released during detonation. Current examples include thermo-baric devices which maximise the pressure from the blast and heat produced as well as stun grenades (flash bangs) which are tailored to produce a large flash and noise but minimising the blast and thermal energy to ensure the device is non-lethal [67]. To allow ease of use and safety in storage and transport, there is a need to stabilise the explosive compounds. Industry focuses on stable compounds that produce the desired outcome.

A good example of tailoring an explosive is Compound 4 or C4, a plastic explosive (so called as it can be reshaped as needed and has a plastic feel) which has been specifically designed to be detonated only with a specific detonator. C4 can be lit and will burn at a similar rate to camping fuel but will not combust explosively. However, when the detonator is triggered, the compound will detonate explosively. A detonator contains a small amount of explosives which is ignited by an electrical pulse that generates very high but brief energy release triggering the C4 detonation. This allows a high degree of safety when handling C4 as it is highly resistant to shocks and impacts, with the added benefit that it can be moulded or shaped to achieve better results. This has made C4 one of the most common military explosives, with other related plastic explosives for use in industrial and civilian setting. It should be noted, as with any explosive compound, there are scenarios where it will react explosively without an electrical pulse [30], [39], [67], [68].

The mechanical interaction of the explosive device and surrounding objects, such as buildings or debris, form the second avenue of research which can be identified in the available literature. This includes the delivery system and structure of the

particular devices heavily investigated by industry [35], [69], [70]. During the detonation, the explosive compound rapidly combust producing a rapid expansion of the gaseous by-products produced by the combustion, and thermal energy due to the exo-thermic reaction. The pressure that is produced imparts kinetic energy to the surrounding material and casing, propelling this material outwards from the detonation as the material continues to travel outward until all the energy from the blast is dissipated. Of course, this transfer of kinetic energy can be imparted to surrounding objects [32]. This work will focus on the previous literature that relates to military explosives and the research that has been undertaken to understand the mechanical impact these explosives have on humans and the mechanics of the detonation of the device [70]–[74].

Explosive military ordnance used in current conflicts and modern advances have led to devices being tailored to achieve specific goals, or to give specific tactical advantage in a particular combat scenario or terrain. This has resulted from the evolution of both chemical and physical understanding of explosives. Several methods have been well established in the investigating of physical impact of explosives. However, there is limited access to the literature on the specific applications of modern devices. An equation that has seen considerable use in this field of research is the Gurney Equation developed in 1943 [75] shown in equation (1). This function is based on the principle of the ratio of mass of the explosive charge and mass of the device casing and is focused on calculating the velocity of the casing as it travels away from the point of detonation. In principal the Gurney equation is reliant on the Gurney velocity, which is derived from the density and detonation velocity of a particular explosive compound, alongside a constant that has been derived based on the shape of the explosive and casing. The limitation and corresponding values are discussed by P.W.Cooper [76].

$$V_G = \sqrt{2E} \left( \frac{M_C}{M_{EC}} + \frac{n}{n+2} \right)^{-\frac{1}{2}} \quad (1)$$

An example of the further refinement of the work that was started by Gurney is the equation developed by Fisher and Maserjin for over-pressure [33]. Over-pressure is the peak positive pressure that results from the detonation of explosives and rapid expansion of gaseous by-products expanding outward from the device. These in turn have undergone several derivations to tailor to a specific environment or use specific input variables. Other approaches combine these methods to allow more detailed

analysis of impulse or thermal expansion. It is important to note that two key limiting factors to these equations are the N.E.W (Net Explosive Weight) and the mass of explosive that is being considered. There are several options to calculate the equivalent mass of T.N.T. (Trinitrotoluene) which is the main principle of N.E.W. Depending on the method used to calculate the N.E.W., this can lead to variation in the R.E. (Relative Effectiveness), leading to small variation in the calculated over-pressure [67], [70], [77], [78]. Limitations directly relate to the level of accuracy the methods used to determine the R.E.F (Relative Explosive Factor) for a given explosive compound. If measured at close range, due to the very large pressures, the extremely rapid rate of change can have intrinsic errors. This area of uncertainty is directly correlated to the mass of the explosive used. As the mass of the charge increases, the maximum over-pressure increases as well as the distance that is needed for the over-pressure to reduce to a level where the various equations can be assumed to be capable of providing effective results. To define this area of uncertainty, comparisons to experimental data are used to validate the values calculated [35], [69], [79], [80].

An in depth review of these equations is beyond of the scope this work and so the chapter focuses on established equations. As such, the following work uses the Gurney equation for a sphere with an established approximation of loss of velocity due to fragmentation [71], [72], [81]. The over-pressure will be calculated using the Mills derivation of the Fisher and Maserjin equation (2) that allows calculation using the principle of equivalent mass of TNT. This simplifies the equation as the main source of variation will arise from the specific R.E. and will produce the over-pressure in KPa [35]. As in this work, the main focus is on penetrating impacts caused by fragments and have minimal interest in the area where over-pressure injuries occur. These injuries occur close to the device and most likely to be within the area of uncertainty for the equation for a given mass of explosive helping to reduce its impact on the results of the equation.

$$P_{So} = \frac{1772}{z^3} - \frac{114}{z^2} + \frac{108}{z} \quad (2)$$

The following chapter explores the types of military ordnance that are applicable, the injuries resulting and an analytical assessment of a surrogate explosive device, which will inform the key experimental assumptions that are needed for the penetration experiments that will be performed later.

## **2.2. Military explosive ordnance and usage**

The following work will consider the device being investigated to be an IED (Improvised Explosive Device) or equivalent type of device. These devices do not follow any specific design or uniform manufacturing process. However, it is common for them to be built to maximise the blast force and include material/objects that maximise the shrapnel or fragments produced, increasing the lethality of the device against the intended target. The term IED is a modern term for what used to be called ‘booby traps’ or homemade devices or bombs [68], [82], [83], and have origins in the conventional conflicts that have been considered the norm for most of the last century, alongside what has been referred to as civil conflict and rebel or guerrilla conflicts.

Guerrilla conflicts are those fought between factions in a defined region which can occur over several national borders, and have been related to ideology, race, religion or illegal drugs trade as reasons for the conflict [84], [85]. Modern terrorist forces can be considered comparable to guerrilla forces that make use of scavenged, homemade or acquired equipment from the black market relying on non-standard infrastructure for supply and support. The high degree of variation in the equipment means that it is difficult to establish a specific description of current IEDs other than general classes [4], [84]–[86]. For this reason, an approximate representative device must be used to assess the detonation of a homemade or unknown explosive device.

When reviewing the devices used in current conflicts, there is a growing trend for them to be deployed in areas that are close to civilians or where the terrain makes it very difficult to identify and render the devices safe, due to the close proximity and range of environmental factors [84], [85]. This means when devices are detonated, the reflection of concussive pressure waves and the increase in the number of fragments generated, due to material being propelled as well as the fragments from the casing, need to be considered when assessing an explosive device’s impact. This greatly increases the complexity of any study, so for the purposes of further work, the environment will be taken as open terrain with only the blast and fragments generated by the device being considered.

The main components of an IED as stated are often derived from scavenged or existing military grade ordnance (examples can be seen in Fig: 2-1), ranging in size from small ordnance, such as a grenade or demolition charge, to large munitions, such as artillery or tank shells, and improvised triggers mechanisms, which are often homemade or salvaged [4], [83], [87]. Sometimes the construction can be purely

homemade from a suitable material for the casing and a charge of improvised explosive. Examples include fertilizer derived compounds [83], [87]. In many cases, fuel and other flammable substance are added to increase the chances of burns and chemical based injuries. A consistent addition to devices is the inclusion of scrap and other items to increase the fragment produced and hence increase the likelihood of inflicting injury to those within the blast radius.

By cross referencing the available literature, an affective analogue for an IED can be identified for the project's experiments, specifically focusing on small devices targeted at personnel [2], [82], [88]. Large anti-personnel devices and anti-materiel devices shall not be considered as they increase the level of complexity due to the volume of fragments and the very high pressure that would be involved. These small devices have a similar function to a grenade or a pipe bomb that have seen previous usage in conflicts around the world.

How the device is deployed and the environment conditions that are present will directly affect the boundary conditions that will need to be accounted for. A common tactic is to hide such devices to inflict an injury on a patrol or passing civilian, highlighting that personnel are the primary target. This forces the unit into a defensive posture while the injured are treated. This can be followed by a second, much larger device or an ambush, if being used in an offensive manner. If used in a more defensive tactic, the device will be planted in a dispersed area to restrict or direct the target's movement, limiting the ability to move freely [4], [16], [68], [82], [83], [88]–[90].

When considering the specification of comparable devices to the IEDs that are being considered, a common source identified is the ordnance that had been used in large numbers during Desert Storm and the conflicts in Korea and Vietnam, which has included various types of grenades and munitions such as artillery shells, rockets etc. This is because large stockpiles of such devices were produced and supplied to multiple independent factions and now, after the conflict has officially ended, are available through the black market and old stockpiles. From the literature, the most appropriate device to investigate is a small device that has been designed to produce the largest number of fragments. These devices share a number of common features including purpose, size, and the expected blast radius, with military analogues being Claymore mines and other anti-personnel explosive devices [4], [14], [39], [67], [87], [88], [91], [92].

Please see overleaf for Fig: 2-1.



Fig: 2-1: A range of examples of IEDs, which include modified hardware such as rockets and shells, and homemade devices such as pipe and shoe bombs. A range of examples can be seen in the figure above which includes several small devices that will be considered as the explosive device under investigation in this thesis. [93].

### 2.3. Injuries from explosive devices

The injuries from explosive devices are directly linked to the mechanical detonation process. The explosive tiers are defined as Primary Blast Injury, Secondary Fragment Injury, Tertiary Injury, Blunt Injury and Quaternary Burns Injury. It is important to also note that in current analysis, there is also Quinary Chemical or Biological Injury which is specific to biological, chemical or radiological agents that have been included in the device to increase lethality [9], [14], [39]. An example of a detonation can be seen below with the shockwave visible at ground level where dust and other material as well as expansion of the dust, gases and fragments can be seen in Fig: 2-2.

Please see overleaf for Fig: 2-2.





Fig: 2-2: Detonation of a hand grenade. The dust and gases can clearly be seen expanding from the point of detonation. The black arrows indicate where the initial shock wave that generates the rapid change in pressure has interacted and kicked up dust ahead of the main dust and smoke cloud from the explosion [94].

### **2.3.1.Primary (Blast) explosive injury**

Primary Injury or Blast Injury is considered the injury inflicted due to the rapid transmission of the pressure shockwave and the resulting mechanical interaction that occurs in various gas and fluid-filled organs such as the lungs and blood vessels between the over-pressure produced from the detonation, and the concussive force applied to the body [9]. Fig: 2-3 shows the rapid change in pressure over time clearly showing the over-pressure (highest pressure) and under pressure (vacuum that occurs after the blast wave has passed) [9] which due to the pressure differential can cause organ to rupture or collapsing. These injuries will occur over a relatively short radius from the detonation due to the rapid dissipation of the pressure wave.

Please see overleaf for Fig: 2-3.

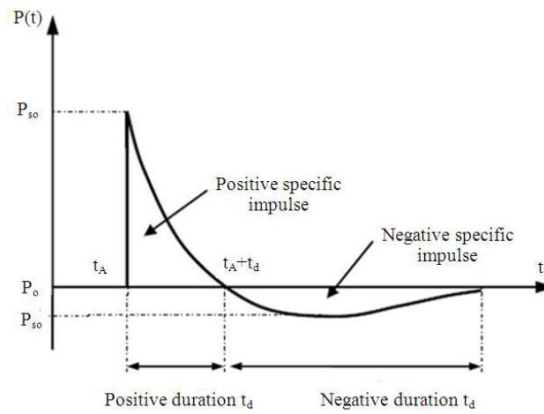


Fig: 2-3: The basic form of pressure generated from explosive detonation at a given distance from detonation, showing the transition from positive over-pressure to corresponding under-pressure before pressure returns to equilibrium after the pressure wave has dissipated [80].

In cases which result in an injury classified as incompatible with life (lethal injuries), the mechanical interaction of the blast wave leads to massive vital organ failure and exsanguination (massive blood loss) due to ruptured organs and vessels. Even with rapid treatment, these will result in death due to the size of the trauma or number of traumas.

In the case of serious and life threatening injuries, these include traumatic amputation from the pressure wave which, if the individual is close enough, will result in the loss of a full limb and the complications that arise from such an injury. Other injuries that can also be inflicted include compartment syndrome and severe tissue rupture. Compartment syndrome is where fluid builds up due to a collapse of the blood vessels or inability for fluid to drain due to trauma. [13], [16], [90]. Ischemia or blood loss is still highly possible but due to the reduced pressure this is more manageable when treated rapidly. If not this will still lead to exsanguination.

Survivable injuries can be considered to range from those that, if not treated rapidly, will result in serious complications or become incompatible with life, to minor injuries that may need minimal or no medical treatment [9], [14], [31], [95]. These include severe haematological trauma from ruptured vessels, burst eardrums and bruising. There is also the consideration of the injured suffering from shock which could further complicate treatment.

### 2.3.2.Secondary (fragment) explosive injury

Secondary Injuries or Penetrating Injury can be considered one of the main components of injury and death due to explosive devices alongside Blast Injuries,

and have the largest possible injury radius around the device. These fragments can be generated from the device itself or from the environment around the device and vary a great deal in geometry, mass and material composition [9]. For anti-personnel ordnance, maximising the number and speed of the fragments increases both the effective range and lethality of the device.

The injuries that are caused by fragments relate the mechanical interaction during the impact of the fragment and the resulting penetration or laceration. Since they act like projectiles, the types of injuries sustained have direct parallels with the injuries encountered from gun shots which can be broken into two main categories, penetrating and laceration injuries [10], [13], [14]. The specific mechanical interaction is the result of the angle of impact and the kinetic energy at the point of impact, further complicated by the geometry of the fragment. This combination can lead to a wide range of different interactions. The mechanical properties of clothing or armour and then the properties of the tissue further complicate the interaction and mechanical response.

Penetrating injuries occur when a projectile has enough force to rupture and penetrate the tissue which continues until its energy has been dissipated. This leads to a large range of different types of injuries, like haemorrhaging from the rupture of blood vessels and organ failure due to damage along the path of the projectile. This also leads to the loss of interstitial fluid from the organs and lymphatic system, leading to ischemia and dehydration of the tissue. Another injury identified is major organ failure due to tissue disruption which depends on depth or location of impact [7], [96]. The localised shock wave produced by the impact and the cavity expanding and contracting along the wound path is now believed to contribute to the long term effects of wound healing. Some work has shown that it effects the clotting and tissue viability in the area surrounding the wound and can lead to tissue necrosis within the body leading to long term complications [5], [9].

Laceration injuries are due to a fragment glancing across the tissue or travelling through the tissue below the surface and rupturing the epidermis or skin above the projectile path. The main concern with lacerating injuries is blood loss, which can result in exsanguination (severe blood loss), in injuries incompatible with life and ischemia survivable injuries. Though it should be noted that if there are any ligaments and other important tissue in the projectile path, these will be ruptured or severed, which can result in long-term and life effecting injuries if not treated effectively [5], [90], [97].

The mechanics of the penetration process are of great interest to this work so they warrant further discussion in the context of the injuries that have been described in the paragraphs earlier in this section. In simple terms, laceration and penetration initialise with the same mechanical process in which the force generated from the impact is enough to overcome the mechanical properties of the skin and muscle leading to a localised failure. Laceration differs after this initial stage as two possible mechanisms occur: the first is that the fragment impacts at such an angle that it glances the body only rupturing the upper layers of skin and muscle leading to an open wound. The second possible laceration mechanism occurs when the projectile penetrates and follows a path that is very close to the surface of the body and the projectile has enough force to rupture the skin and muscle above its path [9], [22], [98]. In the case of penetration after the initial tissue failure, the projectile continues to penetrate the tissue underneath. This will continue until all the projectile energy is spent. During this penetration process, a temporary cavity is formed and material along this cavity expands outwards in response to the force of the penetration's kinetic energy. This expansion then collapses and the surrounding material rebounds to disperse the absorbed energy. This process continues until the projectile energy drops below that required to rupture the tissue ahead of it. This energy is absorbed by the material compressing until all the energy is absorbed and the maximum depth of the penetration is reached. The projectile then rebounds down the cavity then continues to oscillate and dispersing the absorbed energy before coming to rest and forming the permanent cavity [9], [25], [99]. This permanent cavity is the primary region of damage. However the temporary cavity and the propagation of the motion outward, if significant will result in damage to the tissue surrounding the cavity and the possibility of the collapse of blood vessels. Fig: 2-4 shows these three basic steps of penetration.

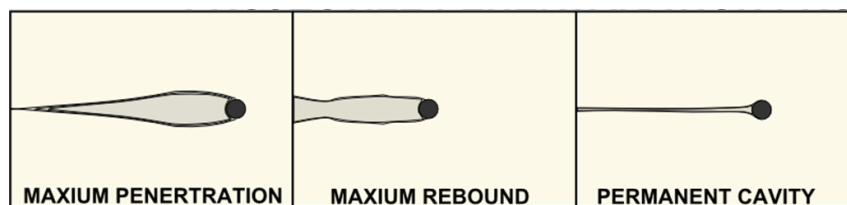


Fig: 2-4: Graphic demonstrates the key stages of cavity formation during penetrating impact of a fragment, showing the temporary (labelled maximum penetration and maximum rebound) and the final, permanent cavity.

### **2.3.3. Tertiary (blunt force) explosive injury**

Tertiary injuries are described as blunt force injuries. This occurs in two ways: either, large objects are propelled into the target, or the target is propelled into environmental objects. Blunt force injuries are the mechanical damage caused when an object impacts with the target but does not penetrate the skin such as glancing impact or the object having enough contact area to disperse its kinetic energy without penetrating. This is similar for small objects that do not have the energy to rupture the skin. This causes haematomas (local swelling due mass of blood) below the surface of the skin or in other tissue, leading to separation of the tissue layers which can lead to compartment syndrome and ischemia due to the pressure of the fluid that will pool where there is tissue disruption. With larger objects, traumatic amputation is a possibility [5], [9], [16].

### **2.3.4. Quaternary and Quinary explosive injuries**

Quaternary and Quinary injuries are the results of energy transfer, chemical or biological agents. This means that in a normal device, there is minimal need for them to be considered as they are normally inflicted within the kill zone of the weapon. This is not the case in weapons that have been specifically designed to deliver these agents. However, this is beyond the scope of this work so will be left for other work[5], [9].

## **2.4. Analytical study of the mechanical process of explosive detonation**

As this thesis is considering fragment impact, it is important to consider the range of possible velocities and if multiple fragment impact needs to be considered because it is more efficient if the experimental set has the flexibility to test the range of possible impacts. Such an analytical study will provide the necessary information to determine the experimental boundary condition.

### **2.4.1. Selection of weapon and simplification**

Identifying the specification of the weapon presented some difficulties. The investigation of IEDs presents challenges as by their nature, they do not conform to any particular construction specifications, making specific information on such devices difficult to acquire. In this case, after considering the available literature and accessible military weapons specifications, that were accessible a precedence was

found. A common analogue used in a wide range of papers is a ball bearing as this is a standard in many ballistic and penetrating impact tests [27], [100], [101]. This has also been used in many anti-personnel ordnances such as claymore mines which contain large numbers of ball bearings as its primary way of maximizing injury. This choice supported by research conducted on the epidemiology of the injuries caused by IEDs and similar devices in recent conflicts around the world [1], [18], [20], [39], [67], [83], [88], [102], [103]. The size of the ball bearing varies, literature includes examples ranging from 5mm and 9mm [27], [100]. So due to the reasoning above, in all future, work the fragment is assumed to be a steel ball bearing of 6 mm as it falls between minimum and maximum diameter in the literature. If the image registration method proves to be successful, the thesis will be expanded to investigate other sizes of ball bearings [28].

Reviewing the available literature, it was possible to identify that common IED types such as pipe bombs share a lot commonality in design with grenades and other small personnel ordnance such as grenades and claymore mines [4], [28], [91]. As the specification for a M67 Fragmentation Grenade and similar ordnance are available and they are designed to achieve the same effects as the IEDs discussed, it is a logical step to use the charge weight from such a device for the following analytical study which for an M67 Grenade is 180 g of Composition B (a mixture of TNT and RDX stabilised with paraffin wax) with a density of  $1650 \text{ kg/m}^3$  [67], [70], [102], [104]. Using the mass of explosive compound identified. This thesis assumes a spherical device with a core of explosives with a diameter of 58 mm as this is a simpler shape that will reduce the complexity of the analytical assessment while also allowing ease of modification if other fragment sizes or explosive compounds are considered later in the thesis. This allows the casing mass to then be calculated. For this arrangement, carbon steel with a density of  $7850 \text{ kg/m}^3$  assumed and the calculated volume of the casing or fragment layer resulting a thickness of 6 mm, meaning the overall casing mass of 7.10 g with the individual fragments having a mass of 0.89 g, meaning the casing is made up of 44 ball bearing spread evenly over the surface of the charge.

Please see overleaf Fig: 2-5.

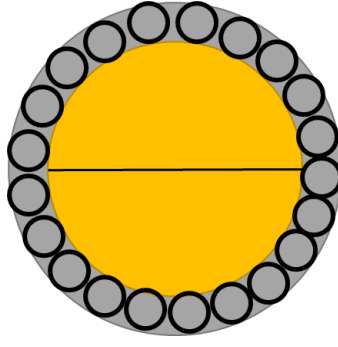


Fig: 2-5: Graphic demonstrates the assumed spherical shape used by this thesis. The yellow region highlights the volume of the charge (a sphere with diameter of 58 mm) and the grey outer region represents the 6 mm ball bearings spread evenly in a single layer over the surface of the explosive charge.

#### 2.4.2. Initial fragment velocity

The initial velocity of the fragments after detonation was calculated using the Gurney equation, which is based on the relationship between explosive charge mass  $M_{EC}$  and casing mass  $M_C$  and a dimensionless shape function. This is a simplification that removes the need for complex energy balances and gas production/expansion equations to calculate the velocity of fragment [75]. The equation can be seen below:

$$V_G = \sqrt{2E} \left( \frac{M_C}{M_{EC}} + \frac{n}{n+2} \right)^{-\frac{1}{2}} \quad (3)$$

$V_G$  is the Gurney Velocity/Initial Velocity.  $\sqrt{2E}$  represents the Gurney constant expressed as a velocity and with a different specific value corresponding to different explosive compounds. In the context for Composition B, the value of  $E$  is 2.70 mm/ $\mu$ s.  $M_C$  and  $M_{EC}$  represent the mass of the casing and charge respectively.  $n$  is the dimensionless shape constant for the shape of casing and explosive, which are as follow  $n=1$  sandwich,  $n=2$  cylinder,  $n=3$  sphere [75], [81].

The Gurney equation has seen usage for the investigation of fragmenting ordnance and explosive welding. The exact formulation and methodology varies depending on the experiment. Its use in explosive welding has focused on calculating the velocity of the propelled plate or body. This formulation as described in equation (7) with modification to account for various geometries or materials. B Gulenc used the Gurney equation to investigate explosive welding between aluminium and copper [105]. There have been many different formulations that have used different principles to account for the fragmenting casing. The exact approach has varied

depending on the goal of the investigation. This has included the application to devices with a complex geometry or varying casing thickness to identify how the fragments from the different regions differ in terms of the Gurney Velocity [74]. M Hutchison has undertaken extensive work in combining the Gurney equation with gas impulse and found that the equation provides a good estimation of the initial fragment velocity, but by combining the gas law, this can increase the accuracy [71], [72], [81]. The Gurney equation has also seen use in various investigatory reports that have been undertaken by international bodies and governments including general research on explosive blasts or more specific research into the effects of device detonating under vehicles [31], [70].

M Hutchinson proposed a generalised modified Gurney equation for use with fragmenting ordnance [71], [81]. It was proposed due to the difficulty in calculating a constant to account for casing fracture without specific data or functions. It was found that the velocity of generated fragments can be roughly approximated to a loss of 80% of the Gurney Velocity. This is a broad assumption, however, due to this being a simplified analytical model. This assumption resulted in the equation below was used to calculate the initial velocity given in equation (10).

$$V_G = 0.2 \left[ \sqrt{2E} \left( \frac{M_c}{M_{EC}} + \frac{3}{5} \right)^{-\frac{1}{2}} \right] \quad (4)$$

### 2.4.3. Peak over-pressure generated from blast

To determine the region where fragments are the primary means of wounding it is necessary to first determine the region where blast wounding is the primary wounding mechanism. As this can be discounted when determine the radius where fragments are the primary wounding mechanics. To calculate the peak over-pressure generated from the device, the Mills derivation of the Fisher equation was used [33], [35]. This equation has been specifically developed to produce the over-pressure in kilopascals. The purpose of this is to identify the radius within which the pressure can be considered lethal and where it can be seen as the major contributing factor for causing injury over those of fragment impact or thermal effects. This equation uses the casing to charge mass relation to avoid the inclusion of complex energy properties. In the assessment of over-pressure, it uses a universal normalized description given by scaling distance relative to  $(E_R/P_0)^{1/3}$  where  $P_0$  represents the ambient pressure (typically 100 KN/m<sup>2</sup>) and  $E_R$  is the energy released (KJ).



However, it is more common to express the explosive input as the equivalent mass of charge in equivalent mass of TNT which is input as a dimensional distance parameter or scaled distance  $Z$ , which uses the actual effective distance from the explosion input as  $R$ . In the Fisher equation (9), the units are balanced as in this case, the terms of this equation assume that the calculation is at a single instantaneous point in time:

$$P_{SO} = \frac{1772}{Z^3} - \frac{114}{Z^2} + \frac{108}{Z} \quad (5)$$

$$Z = \frac{R}{W^{\frac{1}{3}}} \quad (6)$$

Equation (9) represents the Fisher equation where  $P_{SO}$  represents the peak over-pressure in kPa.  $R$  represents the radial distance from the centre point of the explosion and  $W$  is the N.E.W. (Net Explosive Weight). A term used to convert the charge mass to an equivalent mass of TNT. This is an established method for effectively assessing different explosives given by:

$$W = Q \cdot M_{EC} \cdot R_{EF} \quad (7)$$

Here,  $Q$  represents the number of devices used (example blocks or grenades) and  $M_{EC}$  represents the weight of the charge used in each device. The  $R_{EF}$  (Relative Explosive Factor) for composition B is 1.35. This is a measure of how each individual explosive compound compares to an equivalent mass of TNT.

#### **2.4.4. Fragment flight**

To better understand how distance from the device effects fragment wounding, the flight path of the fragments was calculated as this will define impact angle and, more crucially, the impact velocity. This information allowed the concentration of fragments to be calculated for a selected bracket that represents the region of interest. The assumption is that the ground is level and that the target is 2 m high and 0.5 m wide which represents a possible casualty as these represent the 95<sup>th</sup> percentile of

male height rounded to the nearest metre and width and the nearest 10 cm [106], [107].

An aerodynamic modelling framework produced by M Carre to assess sports balls is used in this case to assess the flight of the fragments generated by the device. In this framework, the ball and hence the fragment is considered to be a uniform sphere [108]. The model is dynamic and takes into account the changing velocity and drag force dependent on the selected time step. Equation (12) uses drag due to friction and gravity with the lift that is induced due to the imparted spin of the ball while accounting for angle of travel throughout the time of flight. As with any object in flight, the path it takes and the time of flight are influenced by the drag experienced as a result of resistance and gravity and the lift forces aiding the flight. The equation below relate this to the time period.

$$\left(\frac{d^2y}{dt^2}\right)_{tn} = \left[\frac{1}{m}(-F_d \cdot \cos\theta - F_l \cdot \sin\theta)\right] \quad (8)$$

Where  $m$  is mass of object and  $F_d$  is drag force, this is calculated using equation (14).  $F_l$  expresses the lift force due to the Laplace effect.  $\theta$  Represents the current angle of flight and  $tn$  is the time step used with the second derivative given by  $d^2y/dt^2$  indicating the current point on the flight path.

To simplify the application of this method, there is no spin imparted on the fragment from the detonation as it is not possible to accurately estimate the fragment spin. Also, any force generated by the pressure wave that would act on the fragment is ignored. This is based on the work undertaken by M.D Hutchinson which showed that the impulse from the gas from combustion has little effect beyond the initial fragmentation and the resulting propellant force as after fracture the rapid expansion of gas through the crack reduces the pressure on the casing, which rapidly reduces the gas impulse acting on the casing after that point [71], [72], [81]. As such, the assumption is that all the impulse is supplied by equation (10) for the purposes of this analytical study.

$$\left(\frac{d^2y}{dt^2}\right)_{tn} = \left[\frac{1}{m}(-F_d \cdot \cos\theta)\right] \quad (9)$$

$$F_d = \frac{1}{2} \cdot C_d \cdot \rho \cdot A \cdot v^2 \quad (10)$$

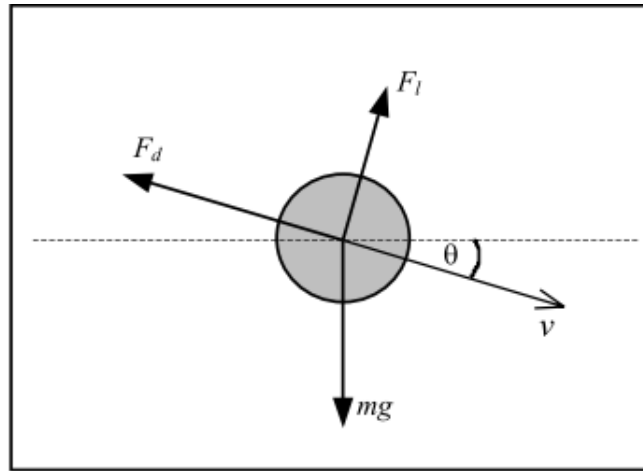


Fig: 2-6: Figure demonstrating the relationship between the individual variables from equation (9) and (10) for a sphere in flight [108].

Where  $C_d$  represents the drag coefficient of 0.9, this was found using the graph produced by A Bailey [109], [110]. This was determined by first calculating the Mach number from the initial velocity produced by the Gurney equation (8). The Mach number is calculated dividing the velocity by the speed of sound. The corresponding values can be found in Table 2-1. As the region of interest is within a small radius of the device, assuming a constant drag coefficient will have limited impact on the accuracy of the output.  $\rho$  represents the density of the fluid, in this case, atmospheric density.  $A$  is the frontal area of the object and  $v$  is the velocity relative to the fluid.

Table 2-1: Table shows the initial velocity and corresponding speed of sound and determined Mach number and the related drag coefficient that will be used as inputs for equations (9) and (10) to determine the forces acting on the fragment.

Initial Velocity	Speed of Sound	Mach Number	Drag Coefficient
463 m/s	340.29 m/s	1.3	0.9

The velocity in Table 2-1 is the maximum speed that could be tested. However, it is important to note that as mentioned earlier, the actual velocities will relate to the regions that fall outside the radius where blast wounding is the primary source of injury. To complete the process, the velocity and distance at each time step used a

summation method to allow dynamic assessment. This work used a time step integral to allow for the estimation of the flight across the progression through time assuming that the initial detonation is considered zero time. In this case, the initial velocity is taken from equation (8) and the equations (15-18) below use an integration process to determine the changing velocity over time for the specified time step  $t_n$ .

$$(V_y)_{t_{n+1}} = (V_y)_{t_n} + \delta t \left( \frac{d^2y}{dt^2} \right)_{t_n} \quad (11)$$

$$(V_x)_{t_{n+1}} = (V_x)_{t_n} + \delta t \left( \frac{d^2x}{dt^2} \right)_{t_n} \quad (12)$$

$$(x)_{t_{n+1}} = (x)_{t_n} + \delta t (V_x)_{t_n} \quad (13)$$

$$(y)_{t_{n+1}} = (y)_{t_n} + \delta t (V_y)_{t_n} \quad (14)$$

In this case,  $x$  references the vertical direction as during the testing, a vertical orientated air-cannon will likely be used due to its availability.

From the results of these equations, the angle of flight can be calculated by working out the resultant velocity and angle of initial launch velocity defined as an input variable in the initial time step, and by sequentially applying the previous velocity and flight angle to the current time step and the current velocity and angle of flight can be identified. From the results, it is possible to define area where fragments follow a flat trajectory for varying launch angles, up to the point where the fragment will begin to follow a curving trajectory.

In the region where all fragment trajectories follow a flat path, it is possible to estimate the fragment concentration for a given radius within this defined region. This will help to estimate the radius at which multiple or single fragment impacts are most probable and thereby infer the likelihood of injuries incompatible with life.

To calculate the concentration of fragments from the device, when assuming a flat trajectory, the relationship between the effective surface area of the expanding detonation wave of the device and effective fragments per metre needs to be defined. It should be noted that the fragment size has been chosen earlier to be 6 mm sphere.

For this estimation, it is assumed that the mass of the casing is concentrated in these spheres and that the casing is made up of these spheres each connected to each other where they are in contact, and during fragmentation, each sphere separates cleanly from its neighbours with no imparted spin or change in geometry. As stated previously, this assumption has its limitations due to the random nature of fragments generated from explosives devices but it can be considered a close approximation to certain anti-personnel devices such as claymores, which have individual ball bearing embedded in an explosive compound which when detonated, propels them in a predictable spread at the front of the device.

The number of fragments  $N_c$  was calculated using the surface area of the charge  $C_{Sa}$  which is defined as the area that is half the thickness of the casing which is the centre of the spheres that make up the casing. Any radius less than this ignored as this defines the explosive charge. The effective cross sectional area of the fragment  $F_{ca}$  the area calculated from the diameter of the 6 mm sphere:

$$N_c = C_{Sa}/F_{ca} \quad (15)$$

Once established, the effective cross sectional area of the fragment referred to as  $F_a$  was calculated in relation to the distance from the centre of detonation and to the expanding effective surface area of the blast referred to as  $S_a$ . The maximum area was defined by the point where the first fragment flight path begins to curve, which is defined as any point at which the angle of flight differs from the angle of launch, which was found to be at a radius of 25 m from the device.

$$F_a = S_a/N_c \quad (16)$$

The concentration of the effective fragments per metre was calculated, identified as  $C_F$ :-

$$C_F = 1/F_a \quad (17)$$

All equations were processed using Microsoft excel 2010 and plotted using Matlab version 7.2.

## 2.5. Results of analytical assessment

### 2.5.1. Peak over-pressure

The graph below shows the results from equation (9) which defines the peak over-pressure as the radius increases from the point of detonation.

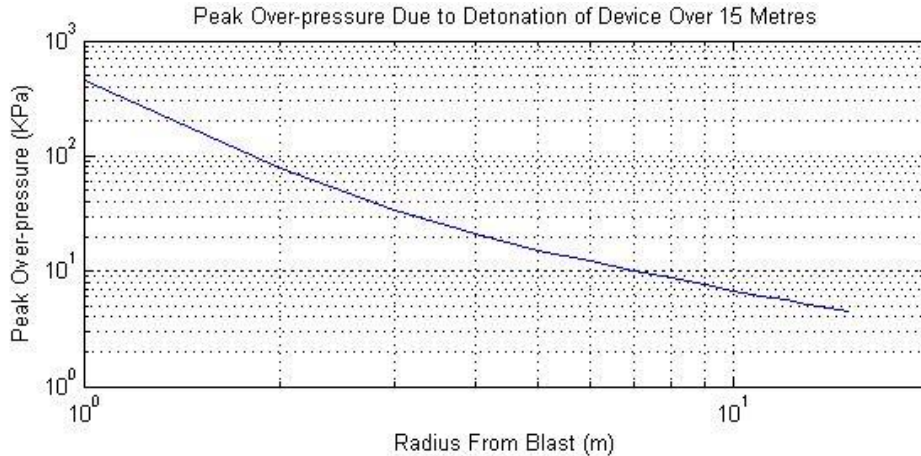


Fig: 2-7: Peak over-pressure drops off sharply the further the distance from the point of detonation. This indicates that the lethal range of the blast pressure will be close to the point of detonation with lethal over-pressure considered to a value of  $\approx 20$  kPa while above  $\approx 6.5$  kPa will result in survivable injuries.

The peak over-pressure was calculated up to a 25 m radius. The pressure magnitude is in line with previous literature that is available when considering the lethality of the over-pressure a value of  $\approx 20$  kPa which lead close to 100% fatalities by the over-pressure alone. If the value is above  $\approx 6.5$  kPa, this will result in severe survivable injuries with some fatalities if treatment is not delivered rapidly due to fragments and over-pressure. Below this value, the injuries are considered to be minor a survivable due to over-pressure alone, rapidly decreasing likelihood as the over-pressure drops further [9], [107]. As such, the wounding radius was identified to be approximately within the bracket of 4.5 m-7.6 m, and the region close to the device being considered to be the lethal radius [9]. The results show the rapid drop in pressure over the expanding radius and support the literature that states the blast lethality and wounding is the primary injury mode at close range.

### 2.5.2. Shrapnel Concentration

The graph below was calculated using equation (21). As stated previously, this allows to determine the likelihood of multi-fragment impact and therefore approximate lethal or wounding radius. As the greater the number of fragments that would occupy the volume of the target, the greater the likelihood of a single or multiple fragments impacting a critical organ or cause multiple injuries which increase the probability of death or severe wounding. As stated in 2.4.1, the maximum number of fragments is 44.

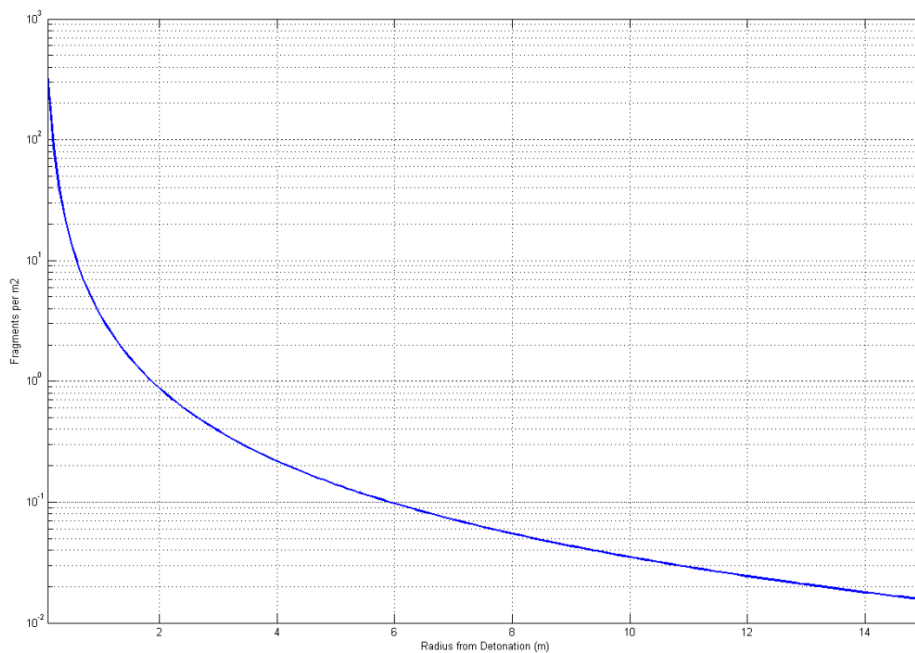


Fig: 2-8: The concentration of fragments can clearly be seen to decrease from the initial outer casing over the increasing distance from the device. The graph sets zero as the centre of the device so graph starts at the radius of the casing as this needs to be accounted for as if included it would not be a true representation of the change in fragment concentration.

As stated in section 2.4.4, the equation was performed over a radius 25 m, where the fragment flight followed a flat trajectory. Fig: 2-8 shows a rapid decrease in concentration of fragments as the volume of the blast expands. As the cross-sectional area of the target specified earlier (2 m high and 0.5 m wide), is 1 m<sup>2</sup>, this can be used to assess the equation output. From the figure, it can be seen that within the first 4.5 m, the concentration has already dropped below 1 m<sup>2</sup>. This also assumes that in the radius of 0 m to 4.5 m, there is high chance of fragment impact. After the radius of 4.5 m, there is an increasingly rapid decrease in the concentration until by a radius of 15 m. The concentration reaches approximately 0.01 fragments per m<sup>2</sup> which

means the effective likelihood of impact has dropped below 10%. After this point, the values decrease to such a degree that the concentration is effectively less than 1%, so the likelihood of injury is minimal. So with the region between 4.5 m to 15 m, the lethality or wounding is based on the velocity of the fragment and the likelihood of impact.

### **2.5.3. Initial velocity and fragment flight**

The initial velocity of the fragment after the detonation was found to be 463 m/s. This is a reasonable outcome as it is expected that the fragments are propelled by blast above the speed of sound but are typically below 600 m/s [28]. By comparing the flight path of the fragment and the defined target 2 m high and 0.5 m wide which was assumed to face the device perpendicular to the horizontal axis and in contact with the ground standing vertically any fragment that would not hit this target was discounted. Any fragments with launch angle of  $0^\circ$  were not considered as in reality, these fragments would impact the ground and either be stopped or deflected at a random, even assuming there were no environmental obstructions due to  $0^\circ$  being ground level. So to avoid complications, these will not be considered in this case.

Please see overleaf for Table 2-2.



Table 2-2: Resulting velocity change of the fragmentation in relation to the initial angle of flight and the distance from the point of detonation, to the maximum radius where the first fragment no longer follows a flat trajectory. Excluding 0 ° for reason described above.

Launch Angle	0 m	5 m	10 m	15 m	20 m	25 m
90 °	463 m/s	-	-	-	-	-
80 °	463 m/s	254 m/s	139 m/s	75 m/s	-	-
70 °	463 m/s	341 m/s	252 m/s	186 m/s	-	-
60 °	463 m/s	376 m/s	305 m/s	248 m/s	201 m/s	-
50 °	463 m/s	394 m/s	335 m/s	285 m/s	242 m/s	-
40 °	463 m/s	404 m/s	353 m/s	308 m/s	269 m/s	235 m/s
30 °	463 m/s	410 m/s	364 m/s	323 m/s	286 m/s	254 m/s
20 °	463 m/s	414 m/s	371 m/s	332 m/s	297 m/s	266 m/s
10 °	463 m/s	419 m/s	375 m/s	337 m/s	303 m/s	273 m/s

As expected, the higher the angle of flight, the less distance the fragment stayed in the target corridor, and the velocity decreased as the distance from the device increased. By comparing the information of resultant velocity with the results in sections 2.5.1 and 2.5.2, it is possible to identify that the combined lethal radius is 0m to 5m and the combined wounding radius is 5 m to 15 m, which is realistic for the size of ordnance and supported by available literature [9], [28], [72], [111], [112]. As the main focus of this work is to look at fragment wounding, the outer radius of this wounding radius is important. As identified, over-pressure continues to contribute to wounding in the range of 4.5 m to 7.6 m. So to mitigate having to include any effects due to over-pressure injuries, the velocities that should be considered are between 7.6 m to 15 m, which from Table 2-2 can be seen to range from 375 m/s to 75 m/s.

## **2.6. Impact on experimental conditions**

The results above show the high level of complexity that is present when considering the detonation of explosive ordnance as there are multiple components that have a direct impact on how a tissue surrogate or human body would react. From the results above, it can be seen that the wounding and lethal radius of the weapon is influenced by multiple components including the over-pressure from the device and the fragment impacts. This was evident even with the assumptions that have been applied to reduce the complexity of the analytical assessment. To fully simulate the interaction would require an extremely complex experimental arrangement or require the use of a bomb range and actual explosive. The facilities that were available for the work undertaken in this thesis meant that testing with real explosives devices was not possible. As such, the results above provide necessary information to identify the specific key conditions that need to be applied to the experimental investigation of fragment impact, and define a suitable analogue for fragments that is possible with the available facilities, which in this case are a vertical oriented air-cannon in an indoor laboratory. This limits the speed that can be safely investigated which meant that from the results above, choosing the velocity bracket at the outer most wounding radius was the most logical decision. This means that the velocities considered in this thesis will be 75 m/s to 337 m/s. As this thesis propose to use an interior testing rig used within a laboratory it is prudent to initially test at the lower velocity range of 75 m/s to 100 m/s and increase over the course of the testing if the registration is successful within this bracket, with the goal to increase to the maximum speed of 337 m/s. This also gives the scope to increase further depending on the capability of the experimental set and the camera arrangement, or if a different testing arrangement can be found. As this is an optical-based method, the quality of the registration is based on the quality of the images that are captured. The faster the projectile, an increased framerate and backlighting will be needed. Starting at the lower velocity is more accessible in terms of available equipment and to better test the core image registration theory as progressing directly to the higher velocity would retract from the primary goal of assessing if image registration can be used as assessment method for quantifying the deformation during penetrating fragment impact.

This project is focused on identifying if an optical method can be used to assess the deformation of penetrating impact. It is possible to reason that in this case, validating the results will not require inclusion of the pressure effects. In assessing any likely injuries, the velocity used will need to be compared to the velocity above and where they would then correspondingly be on the graph of pressure injury. When assessing

multiple impacts, the complexity resulting from the possible variable speeds and impact areas (when not considering the simplified approach above) is beyond the scope of this work. However, this is an area that could be investigated in future work which will be discussed at the end of this thesis. This means that for all following work, only single fragment impact will be considered. Using this assumption also allows the comparison to the various methods that have been used for the investigation of penetrating impact in the literature.

From this, the key experimental points that need to be taken forward are as follows: the fragment will be represented by a 6 mm ball bearing. For the experimental testing, only single fragment impact will be considered and the impact velocity bracket that will be tested is between 75 m/s to 100 m/s.

## **Chapter 3. Selection and characterisation of tissue surrogate**

*Please Note: This chapter has work published in the following [113]*

### **3.1. Selection of surrogate**

An understanding of the material that is being used as the tissue surrogate is a key aspect in allowing effective assessment of any experimental results. These include specific considerations that need to be taken into account for use of the particular tissue surrogate such as temperature effects or manufacturing method and the expected material response of the surrogate. Presented below is an overview of the major surrogates that are currently in use in ballistic penetration and blast impact experiments which aim to assess the response of a specific live tissue or as a general analogue for living tissue. The review will be broken down into subsections which explore the three main surrogate types: those derived from organic material, inorganic material and biological tissue with a final subsection that defines the surrogate that will be used for the validation and penetrating experiments.

#### **3.1.1. Organically Derived Tissue Surrogates**

Organically derived tissue surrogates are defined as surrogates whose constituent materials are derived from organic source materials but these have been processed to be distinctly different from the original material. Most organically derived tissue surrogates are either animal or plant derived with gel based organic surrogates having seen wide usage and being well established in the field of ballistic and blast investigation [114], [115].

Ballistic Gelatine is an umbrella term that encompasses a wide range of types and formulations that are produced by a range of manufacturers to achieve a specific response or structural aspects, such as transparency or material repeatability. The material properties have been identified in previous literature to be a close approximation to soft-tissue (muscle, organs and connective tissue) and have seen extensive usage in ballistic testing, with increasing usage as a tissue simulant for a variety of experiments including as a phantom for organ or tissue simulating/imaging [21], [23], [113], [114], [116]–[121]. All ballistic gelatine is derived from denatured animal collagen, normally porcine and is normally given a bloom value that relates to the strength of the gelatine, 90 being the weakest and 300 being the strongest. For this work consider a wide range of different materials and hence will focus on the characterised material properties as bloom is a specific to gelatine measure and not commonly used with other tissue surrogates. The raw material is then stabilised and

modified to extend its shelf-life, as well as to improve the experimental repeatability ensuring a constant material response. The final material is a soft translucent gel that can be cast into a range shapes at the desired concentrations. The two most common concentration that have been previously used are 10% and 20% [23], [120], [122]–[125]. The manufacturing process varies depending on the sample size or concentration and specific type of gelatine being used and commonly follows three basic steps: Firstly, the mixing of the gelatine and water adding any additives being used. Then, the dissolution of the gelatine to a uniform consistent liquid removing any impurities that form. The final step is the casting and moulding of the gelatine to the desired shape that is being tested. It should be noted that ballistic gelatine can come in several grades of clarity which stem from its well established use with high-speed video technology [101], [124]. The clarity is defined by how clear the gelatine is when in its final form and by the level of light transmission through the sample. It also accounts for how the gelatine clarity changes for given concentrations of gelatine. The specific labels vary but examples include scientific grade that has good clarity and extra stabilisation for consistency in manufacturing or photo-grade which is tailored for maximum clarity above all others. This is an important factor as the need to effectively capture high quality video of the impact is a crucial experimental consideration in this thesis. Thermal stability is defined as the degree at which the material maintains the same properties in relation to the material temperature and shelf-life or longevity in relation to decomposition due to its nature as an animal based product of the final product are areas that have been identified as restrictive to the material usage or that can directly impact the experimental response [113].

Another animal-based tissue surrogate is ballistic soap. This is created from organically derived oil or fats that undergo saponification in an alkali solution to produce a soap of varying clarity. Ballistic soap differs from other surrogates presented as it designed to have a high level of plasticity. This means that when the projectile impacts the soap, the material will be deformed and stay deformed at the point of maximum deformation. This makes it very effective to investigate the temporary cavity that is caused by the penetration, but limits its usage to investigate the cavity collapse and wider settling that occurs once the permanent cavity has formed. Since the goal of this project is to capture the deformation over the whole of the penetration purpose, this means that ballistic soap would be a unsuitable surrogate to use [23], [126], [127].

Plant based gelatines such as Arabic gum, Konjac and Agar-Agar have been proposed as a tissue surrogate. These gelatines are produced in a similar manner to the animal based gelatines extracted from plant compounds which are modified to

produce the end product. The material is again supplied as a dried powder which is then mixed to the desired concentration. Plant derived gelatines have been found to have interesting properties such as thermal stability and fibrous heterogeneous structure. However, unlike the animal derived gelatine, the material clarity is limited which is a limitation when trying to maximise the contrast of images recorded during experimentation and to identify the motion within the sample from the penetration. This makes these plant based gelatines unsuitable for this project as clarity is a crucial component for collection of data during penetration [128].

All organically derived tissue surrogates suffer from degradation over time. This is due to the material decomposing due to dehydration or digestion from bacteria or fungal growth which occurs [113]. They, however, are easy to produce in large quantities and have very little risk or ethical concerns associated with their usage making them suitable for producing large number of samples for multiple tests.

### **3.1.2. Synthetically derived tissue surrogates**

Synthetically derived surrogates are derived from chemical manufacturing or from inorganic materials that occur naturally. The range of material properties that are available is greater than that of organically derived materials as the chemical and physical makeup can be more effectively controlled.

Examples of inorganic gels that have seen usage as soft tissue surrogates are silicone and synthetic hydrogels alongside silicone rubbers and foams. These are produced by mixing multiple components to the desired concentration as with organically derived gelatine. These can include mineral oils and other liquid components with some gelatines. By controlling the ratio and the specific chemical components with specific additives, a wide range of material responses or consistencies can be achieved allowing the creation of specific organ or tissue phantoms, such as skin, liver or brain phantoms [22], [125], [129]–[132]. Silicone gels are stable and do not suffer from the decomposition and breakdown that can be encountered with organic surrogates. However, as with many polymers, it will suffer from UV and slow degradation due to wear. These will occur over a time period that will likely have little effect the material experimental response for a given investigation or testing set [27], [133]–[135].

Synthetic hydrogels are a second example and, as the name implies, the main constituent material is water mixed with synthetic gelling material. There are a range of materials that, when combined with water, form a matrix that creates a gel. This

can include mineral oils and polymers. They can be seen as a closer approximation to the organically derived gels. They are more stable due to the controlled chemical engineering but will suffer from dehydration and UV degradation over a longer time period than organically derived gelatines. While not suffering from the decomposition that occurs with organic materials [27], [136], [137], these materials have not seen much usage in penetration testing. However, they have seen use in high speed Hopkinson bar experiments which highlight their possible application for this project [138]–[140].

Common examples of synthetically produced hydrocarbon polymers are silicone rubbers and polymer sponges. Silicone rubbers have seen use as standalone surrogates for impact testing, as well being used as with other tissue surrogates to create composite tissue systems. These have been used for investigating high speed impact on body armour or in vehicle testing, as they can be embedded with sensors and stored for long periods. Currently, the material has also been used to produce medical imaging phantoms and in physical impact of shock testing as a skin and muscle surrogates [22], [114], [130], [134], [141], [142]. As with the inorganic gelatines, due to their synthetic composition, they allow for a high level of control over the material behaviour [143], [144]. A commercially available product from this family is PERMA-GEL. This is a thermoplastic material which can be melted and cast into a wide range of shapes using suitable equipment. It has been designed for a high level of clarity alongside showing similar properties to ballistic gelatine but at room temperature with none of the associated thermal degradation and organic decay, with the material also having the ability to be re-melted and reused for multiple test before needing to be replaced. It has seen usage in blunt and penetrating impact test with a particular focus on the investigation of the wound cavity. The main drawback is the cost of buying the samples or the cost of the equipment needed to mix and reuse the samples [24], [115], [133], [138].

In general, synthetically derived surrogates are more stable and suffer less from decomposition or degradation. However, they are often more expensive and can require a greater time to prepare or more complex manufacturing equipment and precautions for storing the constitutive materials. It is important to note that the clarity of the surrogates can vary greatly depending on additive or constitutive components.

### **3.1.3. Animal and cadaveric tissue**

Animal tissue or cadaveric specimens are the closest analogue to live tissue when harvested soon after death, and have specific characteristics that differ from all other surrogates so require specific attention when reviewing their usage.

Animal tissue, specifically porcine tissue, is well established as an effective surrogate for human tissue. The previous literature has focused on specific tissue types which have included arterial tissue and soft tissue such as muscles and organs. A large breadth of testing has been performed which includes characterisation of tissue and comparison with human analogues [145]–[148]. In the investigation of cancellous bone, the human and porcine bones were found to have very high degrees of similarity [149]. With particular relevance to ballistics tests, it has been used to calibrate ballistic gelatine and act as a surrogate for blunt and penetration impacts. Alongside porcine tissue, live pigs have been used to investigate immune response or wound healing [21], [120], [150]–[152].

Cadaveric human tissue is the closest surrogate to live human tissue that is possible. There is a large amount of ethical concerns to be addressed and the cost of acquiring such tissue is high. Both these surrogates do differ from the material properties of live tissue. This is due to a change in the hydration and other factors which are unique to live tissue such as the rigor mortis process and self-repair, which influence storage and preparation of the samples and testing environments. Most vitally, there are several difficulties concerning storage in order to prevent the decomposition which can occur rapidly if allowed to begin which is further compounded by the considerable ethical and safety considerations that have to be made [31], [91], [145], [153].

It is important to note in this work that cadaveric and animal tissue is opaque meaning that it is impossible to image the internal response to the impact using high-speed cameras. As it would require the use of medical imaging technology or specialist high-speed x-ray equipment, these factors make using these surrogates impractical for this thesis.

### **3.1.4. Selection of ballistic gelatine as surrogate material**

In this project, it was decided that the tissue surrogate that will be taken forward is porcine-derived ballistic gelatine. The decision for this is based on three points: the primary reason is that the material's mechanical properties have been proven to be similar to human tissue providing a strong base of work to build on. The second



reason is that there are very few ethical and safety concerns with the material meaning that its use in experimentation has very few restrictions which simplifies cost and experimental setup. The final reason is that the material has good transparency maximising the image quality that can be captured, which is a crucial factor in the proposed penetration experiments and assessment. An added benefit is this material highly flexible due to its ability to be cast in a wide range shapes which facilitates a wide range of loading arrangements. It is also a well-established material that, as mentioned in section 4.2.1, has seen comprehensive usage in ballistic impact and penetration experimentation [21], [114], [124], [154], [155].

Ballistic gelatine is produced using a common method across the different manufacturer's products. The initial step is mixing the water and powdered gelatine to the desired concentration and allowing time for the powder to absorb the water. The mixture is then heated to a specified temperature supplied by the manufacturer to ensure that the material is homogenous and has not suffered from thermal degradation if overheated. J Jussila conducted a comparison test where it was found that a dissolution temperature of approximately 60 °C for 10 % concentration produced consistent samples. However, if temperature is increased beyond this point, sample consistency was shown to suffer, increasing the variation the higher the temperature. This is mirrored in many of the papers and the manufacturer's instructions [113], [122], [123], [156]. During the dissolution, process any impurities are removed which take the form of a scum (white viscous foam) that rises to the surface of the gelatine. After the dissolution, the liquid gel is then poured into the desired mould and left to re-gel. Once set, the gel is removed from the mould for testing taking care not to damage or over-stress the final product. Depending on the specific gelatine before testing, a curing period may be included to achieve a specific response or represent a particular aging process. J Jussila explored both of these processes and found that for the re-gelling or cooling off period, the length of time correlated with a decreasing Mann-Whitney significance (0.163 for 48 h and 0.025 for 72 h) but the longer the cooling off time the greater the chance of degradation and contamination so finding the correct balance for the given experiment will need to be decided before testing occurs. Alongside this J Jussila also performed a comprehensive investigation of the curing at temperature of 4 °C in refrigerator which varied between 1.3 °C to 8.2 °C for a time period of 24 h. Finding that the internal temperature after curing ranged from 3.6 °C to 4.4 °C for the given temperature range and this was consistent within 20 minutes of the samples being removed. This again has a similar method seen in other papers [113], [122], [157].

When considering any specific requirements for the proposed experiment usage for the ballistic gelatine, two were identified from the specific manufacturer's information and literature. A high degree of repeatability, specifically that the gelatine could be produced to the same standard across a large number of samples, by ensuring that temperatures are kept constant throughout each step of the manufacturing and during the dissolution process removing the greatest amount of impurities as possible which further aids repeatability. This permits to achieve the same clarity, geometry and mechanical response with no significant difference, which can be accounted for with effective monitoring and assessment of the experimental data. The second requirement was that the material allowed for imaging of the internal material response to the penetrating impact with the highest clarity possible.

When considering these points, it was found that type 3 250 bloom scientific grade ballistic gelatine supplied by GELITA of Germany met the requirements [158]. This particular formulation is manufactured to have maximum repeatability and still have a good clarity for filming. The company supplies its recommended manufacturing process with the surrogate, which can be incorporated in the experimental method of the project. The gelatine is manufactured from denatured porcine collagen which undergoes treatment to prevent bacterial and fungal growth and stabilises the material for transport and storage. This includes sterilisation by anti-bacterial and anti-fungal chemicals of the original source material and radiation treatment of the final powder form. The exact method of treatment is confidential. In its raw form, it is a fine yellow powder and in its manufactured form, a yellow soft transparent gel. The material's near transparency simplifies identifying defects induced during sample preparation. Additionally, the gel's raw powdered form allows control over the concentration and volume of the samples that are produced. Thermal sensitivity and the effects of inter-batch variation during sample preparation were identified as areas where potential errors may be induced. This sensitivity is also affected by large temperature variation between tests or in transport and will lead to an increased variation in the mechanical response of a given test with the exact value depending on the specific concentration, test or temperature difference [122], [157]. As such, any method will have to account for this by either controlling or monitoring the temperature throughout testing [113], [157].

## **3.2. Characterisation mechanical testing**

The work that has been undertaken in Section 3.2 on the construction and running of the model and optimisation was undertaken by a colleague, Christopher Noble, with the proposed method, experimentation and explorative testing undertaken by the author.

### **3.2.1. Previous work**

There have been relatively few studies investigating ballistic gelatine's behaviour at slower, quasi-static strain rates, compared to the investigation at the high speed strain rates that are normally encountered during impact and ballistic penetration. In recent years, the use of tissue and organ phantoms for surgical training and pre-operative planning, driven by advances in 3D printing technology, enabled increased production of high quality *in vitro* models. Examples include the use of constructed phantoms to characterise and optimise a robotic needle guidance system for lung biopsy procedures. Similar computer-assisted needle guidance systems have focused on the extraction of biopsies or targeted drug delivery also employed tissue phantoms for performance evaluation in a variety of experiments and testing arrangements [128], [159], [160].

Characterising the mechanical response of soft tissues and tissue simulants presents several challenges which include the non-linearity of the material response, varying strain rates and complex loading/interface conditions. Previous studies have employed hyperelastic and quasi-linear viscoelastic constitutive models to allow characterisation of the non-linear behaviour. Hyperelastic models allow the non-linear behaviour that is observed in soft-tissue-like materials following large deformations under load. However, it has a limitation in capturing any strain rate-dependent characteristics of the material. Due to this, the rate-dependent behaviour is often modelled by fitting it to specific experimental data for a given strain rates which allows the hyperelastic model parameters to vary individually which then allows reporting after tabulation the optimal parameters for each loading regime[27], [121], [157], [161], [162]. Viscoelastic models have an inherent ability to emulate viscous processes which include rate-dependence, creep, stress relaxation and hysteresis which have been frequently identified in soft tissue-type materials. This enables the formulation of a simple constitutive model with material parameters to describe the response over multiple strain rates [23], [113], [116], [128], [140], [163].

Previous literature that has investigated tissue surrogates and tissue like material has focused on the static, quasi static and the dynamic regimes which have been selected

due to either the specific use of selected surrogate or the effects of an experimental arrangement. Previous experimental arrangement has included split Hopkinson bar at high speeds, plate and pendulum impacts used at intermediate speeds and, for quasi-static or at static speeds, compression hydraulic and mechanical loading rigs. These tests use loading conditions such as uniaxial compression or tension [113], [117], [123], [156], [157], [164]–[166]. Another type of material response that has been investigated is hydrodynamic behaviour where the solid material deforms at such a rate that it can be considered to act like a liquid. In this case, the material possess negligible strength and hence only weakly supports a shear wave component. In the previous literature, this has normally been considered for high strain rates at  $1000 \text{ s}^{-1}$  or more which are typically seen at explosive and ballistic impact speeds. This has meant that this has normally focused on testing rigs such the split Hopkinson bar or instrumented air cannons using a range of different projectiles or impactors [22], [23], [123], [167]–[169].

Previous literature which investigated the response of ballistic gelatine at ballistic or dynamic speeds has included several different arrangements normally focusing on a single impact and has not investigated the cavity rebound a surrounding gelatine motion. D.S Cronin investigated in the dynamic and high speed regime (strain rate of  $10^2 \text{ s}^{-1}$  to  $10^4 \text{ s}^{-1}$ ) and found that ballistic gelatine at 10% had similar material properties to human soft muscle tissue when using the Hopkinson bar [165]. G Subhash has investigated the response of ballistic gelatine at high shear rates (during testing, this equated to impact speeds of between 5 m/s to 20 m/s) using power-law based constitutive models validated by using observed shear thickening behaviour which identified rate-dependent response behaviour which is similar to soft tissue [166]. In the impact tests performed by C.J Shepherd at speeds of 75 m/s to 860 m/s, the material exhibited a response that was comparable to human soft-tissue, while also identifying that the gelatine exhibited hydrodynamic behaviour during shock loading [123]. Y Wen has also explored the hydrodynamic response of the ballistic gelatine under ballistic penetration at speeds of 728 m/s and 947 m/s using an elastic-plastic material model [23]. C.J Shepherd also identified that the strain rate of  $10^3 \text{ s}^{-1}$  and greater can be considered comparable to ballistic strain rates [27], [123], [170]. Using an experimental arrangement that included a split-Hopkinson bar, J Kwon investigated ballistic gelatine response to compressive strain rates of  $2000 \text{ s}^{-1}$  to  $3200 \text{ s}^{-1}$ . This paper noted that the material had distinct responses between loading regimes. This difference was identified by an increasing viscosity and compressive strength in relation to higher the strain rate. To achieve this, the paper used a multiple Maxwell-element viscoelastic model [156]. A similar test was performed by C.P

Salisbury which investigated strain rates from  $1000 \text{ s}^{-1}$  to  $4000 \text{ s}^{-1}$ , using a hyperelastic-viscoelastic material model which found that at these high strain rates. Ballistic gelatine still showed strain rate sensitivity [117]. The clear strain rate dependence is visible at these high strain rates and they support the conclusion that ballistic gelatine has a response similar to biological tissue.

Much of the previous literature has focused on the characterisation at the high strain-rate of penetrating impact and shock loading. However, the penetration process includes a range of different components which include the transmission of the kinetic energy due to the cavity collapse, settling and the dissipation of the kinetic energy from the rebound which both occur at much slower strain-rates than the initial penetration. The quasi-static loading regime effectively represent the responses of the tissue surrogate and long-term movement at the very end of the penetration as the whole body responds to the dissipation of the potential and kinetic energy from the penetration, which is one of the focuses of this work as the wider response of the surrogate is directly comparable to this long term injury response and healing. Previous literature investigated the strain rate response between  $0.001 \text{ s}^{-1}$  to  $10 \text{ s}^{-1}$  and has identified rate dependent behaviour. D.S Cronin used a hydraulic test frame in a temperature controlled environment to investigate the 10% ballistic gelatine's response at three strain rates ( $0.1 \text{ s}^{-1}$ ,  $1.0 \text{ s}^{-1}$ ,  $10.0 \text{ s}^{-1}$ ) which produced results that showed an increasing stiffness. Hence, the gelatine developed a time dependent behaviour that was captured using an Ogden hyperelastic model [164]. D.S Cronin also published work that looked at the effects of temperature, aging and strain rates of  $0.01 \text{ s}^{-1}$ ,  $0.1 \text{ s}^{-1}$  and  $1.0 \text{ s}^{-1}$  where they identified the specific relation between the sample temperature and the mechanical response identifying that the increase in temperature changes the material response. For these tests, they used a compression rig and lubricated the samples before testing using a water-based lubricant [157]. A similar arrangement was used by J Kwon for the nominal strain rates of  $0.0013 \text{ s}^{-1}$ ,  $0.0053 \text{ s}^{-1}$  and  $0.0107 \text{ s}^{-1}$ . However, they applied lubrication and the results produced were consistent for all strain rates with an initial modulus from the stress strain curve of  $10.9 \text{ KPa}$  and showed at these very slow strain rates a highly linear elastic response with only minimal rate dependence [156]. N Ravikumar used a uniaxial compression loading arrangement and a viscoelastic-hyperelastic Ogden model for three strain rates ( $0.1 \text{ s}^{-1}$ ,  $0.01 \text{ s}^{-1}$  and  $0.001 \text{ s}^{-1}$ ). These tests identified time dependent behaviour with increasing stiffness as strain rate increased and found the parameters to be similar to porcine live tissue with the specific optimised material parameters given by the following a shear modulus  $\mu_1$  of  $11,934 \text{ Pa}$ ,  $\sigma_1 \gamma_1$  of  $0.56$ , relaxation time constant  $\tau_1$  of  $5.85 \text{ s}$  and the dimensionless Prony constant  $\alpha_1$  of  $1.90$  [113]. The

applied strain varied for each method and included up to 50% but are commonly approximately 30-40% strain.

### **3.2.2. Proposed method**

This chapter is built on the constitutive model proposed by N Ravikumar to characterise the mechanical response of ballistic gelatine at quasi-static strain rates. They proposed a visco-hyperelastic model validated using uniaxial compression experiment, which captured the gelatine's time-dependent behaviour across multiple strain rates [113]. These strain rates allow a detailed investigation into the material model but are also at speeds which can be achieved with the experimental equipment available, alongside allowing the author to undertake a series of validation tests that can be undertaken at slower and more controlled speeds to aid in the analysis of the effectiveness of the image registration. This also allows the possible exploration in later test of rebound and wider sample motion that occurs after the penetration and away from the cavity which is still a crucial area as this identifies the forces that are now acting on the damaged regions around the permanent cavity and on the cavity itself. As these strain rates are low, this reinforces the use of the selected model as the material will still express hyperelastic and viscoelastic properties due to the biological nature of the surrogate. However, it is far below the strain rates investigated in relation to hydrodynamics which would indicate that the visco-hyperelastic approach is more suitable in this case.

The following work characterised the gel's response to uniaxial compression, hysteresis and stress relaxation and compares it to other material models of similar complexity. The loading requiems was selected as it specifically relates to later settling and movement that occurs during the rebound and dispersion of the potential energy that has been transferred to the surrounding tissue during penetration, as discussed in section 3.2.1. This focus combined with the multiple different loading tests to further explore the response of ballistic gelatine within this response bracket, while also furthering the understanding of ballistic gelatine at surgical strain rates. To optimise the material model, a finite element model was generated to allow fitting of the constitutive models to the recorded experimental response. This work applied a global optimisation-based curve-fitting framework. The optimal model and material parameters are identified by the accuracy of the curve fitting to the experimental data.

### 3.2.3. Sample preparation

All samples were produced at 10% w/v concentration (gelatine powder to water). For this work no additive was added for preservation, supported by previous work and allows the characterisation to focus the material without compensating or including the assessment of how the additive would affect the material response [113], [117], [164]. The temperature at the dissolution stage for the gelatine and the water bath was measured using a digital thermometer with a needle probe, which can be sterilised to avoid introduction of fungal and bacterial contaminants to the gelatine. If the gelatine temperature rose above  $52\pm 1$  °C, the material was not used. Manufacturer's advice and the previous literature specified  $60\pm 5$  °C as the maximum temperature gelatine could reach before detrimental effects occur. Limitations of the water bath built-in temperature control meant that the lower value of  $52\pm 1$  °C was chosen to ensure that the gelatine would be highly unlikely to reach the manufacturer's threshold, maintaining sample consistency and account for any variation in the water bath due to ambient temperature or due to accuracy of the water bath's temperature sensor. However, this meant that the dissolution process took longer. To identify if this would have a negative impact on the samples, a series of test samples were produced and it was possible to identify that the longer dissolution time period allowed more scum to form indicating a larger amount of impurities is released and can be removed improving the homogeneity of the final gelatine [113], [157], [158].

Previous work has identified that the temperature has a direct impact on the mechanical response. Temperature variation was monitored at key points in the manufacturing process allowing identification of samples that had an increased likelihood of variation [113], [157]. Monitoring was performed at three key points: (1) during dissolution process, when fully in its liquid state, (2) before testing and (3) after testing. These three points represent the three points where the gelatine is most susceptible to excessive temperature variation and have been identified from previous explorative work undertaken during pretesting and in the literature [113].

To prepare the samples, the correct weight of gel powder measured using a digital scale with a accuracy of  $\pm 1$  g was then mixed with the corresponding volume of cold water in a container (to ensure 10% w/v concentration), ensuring the gel powder was evenly mixed and left to hydrate for 24 h at room temperature. Once the mixture was fully hydrated, the dissolution was performed in a water bath heated to  $56\pm 1$  °C; this heated the gelatine to  $48\pm 1$  °C. When the dissolution of the gelatine was complete, the scum was removed to maximise the gel's homogeneity in the form of a viscous white foam. The liquid gel was then cast into sheets of  $14\pm 1.5$  mm thickness and left

to gel at room temperature for 24 h. After it solidified, it was placed in the fridge at  $8\pm 1$  °C and left to cure for 24 h. As mentioned earlier, explorative testing was performed to assess the effect of different and compared to information in the literature. Some selected lower temperature for a shorter time periods; for example, G Subhash cured for 2 hrs at 5 °C and D.S Cronin cured for 2 hrs at 4 °C [157], [166]. The higher temperature longer time period as used by P Moy included curing for 24 hrs at 10 °C and N Ravikumar that cured for 24 hrs at a similar temperature [113], [171]. Before testing, a series of samples were produced and cured in line with the literature and it was found that a longer time at a higher temperature method was more successful at achieving a uniform temperature throughout the produced sample.  $8\pm 1$  °C was found to be the best temperature for consistent curing across multiple samples. Once fully cured, cylindrical samples of  $42\pm 1$  mm diameter were cut using a metal ring cutter. This produced a sample with a thickness to diameter ratio of 1:3. This ratio has seen previous usage and was used in the paper produced by N Ravikumar and others [113], [117], [157], [164]. The samples were cut as close to the centre of the sheet as possible to minimise any effect that would result from the curved edge of the casting tray and any edge effects. Samples exhibiting defects or damage resulting from the cutting process were discarded. This includes fracture or inclusions of bubbles or textural differences that would represent poor homogeneity. Some surface marks were introduced due to the compliance of the material during the cutting process which resulted in samples not being perfectly cylindrical. The experimental impact of this was minimised by the applied preload and can be considered to be negligible. It should be noted that all samples used in one testing arrangement were produced from the same mixing batch of material and cast across three different casting to ensure no bias from casting process.

### **3.2.4. Methodology**

#### *3.2.4.1. Sample interface*

In this work, the sample interface determines the constraints imposed on the numerical/analytical model employed to characterise the material response. To identify the optimal sample-grip interface, a series of proof of concept tests were performed exploring three possible interface conditions: (1) Fixing the sample at the interface (infinite friction). This was achieved by either gluing or using very low grit sandpaper to fix the sample. (2) Lubricating the interface (negligible friction) using a hydrophilic mineral oil. (3) Untreated sample interface (sample in contact with flat



metal plate). The plates were cleaned and dried to ensure plate to sample contact was free of dirt and residue. Testing these interface conditions allowed the identification the most effective interface to use in the characterisation experiments. Multiple compression speeds were tested for each interface. These were filmed to identify the material's response and any slippage that occurred. Filming was undertaken using a digital camera, specifically a Nikon COOLPIX 10 megapixels camera, and dedicated lighting source (desk lamp) to illuminate the sample. To ensure the footage clarity, a uniform white background was applied behind the sample in the form of a plain sheet of white paper attached to the experimental rig. The recording was manually triggered before the loading was initiated and manually stopped after loading was completed. This was performed for each test and the footage extracted after testing.

From the tests performed, it was found severe frictional effects were induced by configuration (1) resulting in significant degradation and failure of the sample at the interface when using the sandpaper ranging from 40 grit to 200 grit values. In this case, the application of the glue was considered and multiple different glue types were used which included Cyanoacrylate glue (Super Glue), Nitrile Rubber/Resin glue, Polyvinyl Alcohol, and double sided tape. However, there was no adhesion between the samples with any of the glues that were tested. This is believed to be due to the high water content of the gelatine. (2) resulted in a large amount of slipping induced by the lubrication which resulted in erroneous load-displacement data, which could be identified by two main points of variation: Firstly, even after preload, the sample did not begin loading from the same compression which results from the sample moving and shifting during the initial loading. Secondly, the sample did not reach full loading or showed very large standard variation due to the sample moving under loading or shifting free from the mounting plates. As a sufficient contact interaction could not be established for the mechanical testing rig, this meant it was not possible to extract meaningful data from the tests. It should be noted that these failures occurred despite careful sample handling and the cleaning metal loading plates after each test to minimise any build-up of sample residue or lubricant.

The manufacturing method used to produce the plate resulted in a circular ridged pattern (having been lathe-turned) which can act on the sample is assumed to have produced a frictional effect on the interface. The specifics of this problem are beyond the scope of this work. This conclusion was reached by considering previous literature for both characterisation and penetrating impact, such as the work undertaken by N Ravikumar who previously achieved effective results using a similar configuration arrangement to that proposed for condition (3) [113]. Penetrating impact papers have used configuration (3) or similar indicating that this

is a suitable arrangement for the characterisation as this is in line with furthering the understanding of the gelatine behaviour for a latter component of penetrating impacts as discussed earlier [21], [23], [155], [172]. This was complimented with some exploratory work that was undertaken in conjunction with a tribology lab, where a series of gelatine samples were produced ranging in size and concentration under advisement from the laboratory experience. These samples were used to investigate the friction using a drag testing apparatus. For the explorative samples, it was not possible to achieve consistent results and in discussion, it was identified that this would require a large degree of testing. This work would have presented limited benefits to the later penetrating impact experiments and characterisation; previous work had already identified that condition (3) provides good results, as discussed above.



Fig: 3-1: The image shows the concentric ring pattern on the mounting plates produced during the manufacturing process. Marks and patina can be seen from the corrosion of the plate material due to the interaction with the water content of the gelatine, emphasising the need for regular cleaning.

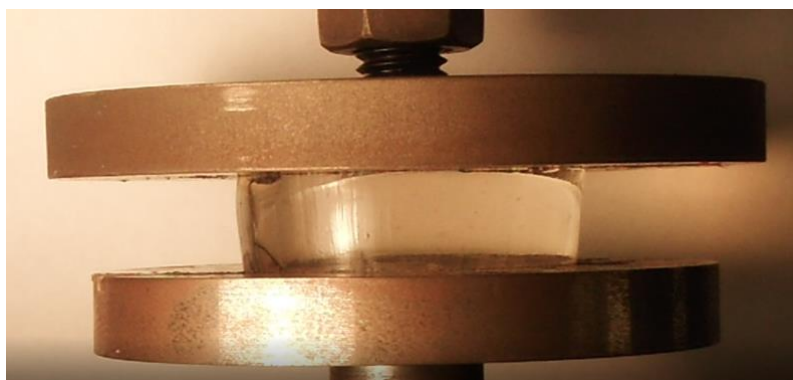


Fig: 3-2: Configuration (3) shown with a sample under preload before testing was undertaken, showing surface marks induced from the cutting of the sample. This can also be seen in the difference in the upper diameter to the lower diameter. This difference was minimal for the sample used and if found to be large, the sample was not used.

Configuration (3) was identified to be most suitable. The metal loading plates can be seen in Fig: 3-1 with the machined surface visible as concentric rings. An image of the sample on the plates under preload can be seen Fig: 3-2 with the surface marks induced by the cutting visible around the edges of the sample (visible as striated marks on the vertical surfaces). However, this arrangement produced consistent results during explorative testing with some slippage visible at the interface. An example of the slippage can be seen in Fig: 3-3 with variation between the upper and lower surfaces visible. This appears large when compared; however, when comparing to the sample under preload in Fig: 3-2, it can be seen that the difference in amount of slippage between the upper and lower surfaces is smaller than it appears and this was true for all samples tested when the footage was compared. It was found that the surface of the plate imparted a high degree of friction at the sample interface which lends weight approximation to a fixed boundary interface. This is similar to previous work which assumed a fixed boundary condition for a similar arrangement of ballistic gelatine to untreated metal plate interface and achieved consistent results across the testing done [113] supporting the validity of the assumption. However, as slippage was identified, there is a need to consider that this could mean the model and optimisation parameters may require manual adjustment of the upper and lower bounds, or in the case of the model, the coefficient of friction to account for variation induced. Ensuring this is accounted for in the assessment of the results when identifying errors or anomalies in the model outputs.

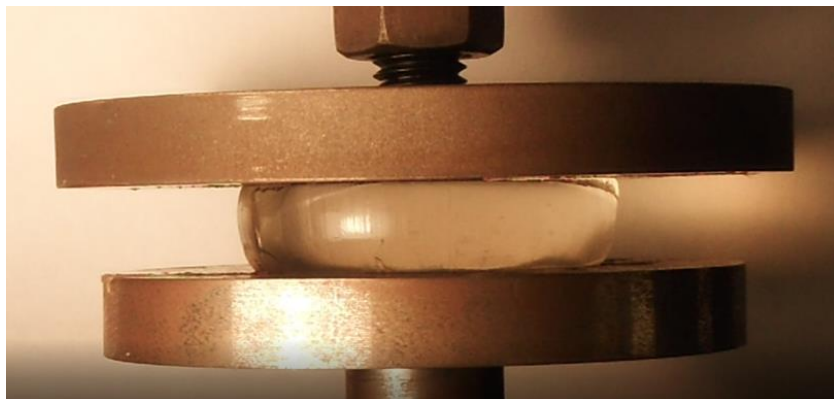


Fig: 3-3: Sample undergoing loading showing uneven barrelling that resulted from slippage at the interface which can be seen on the upper surface compared to the lower surface. This varied between samples which supports that slippage would introduce variation between different samples.

#### 3.2.4.2. *Experimental method*

To characterise the material rate dependence response to compression, a range of mechanical uniaxial compression tests were employed, including (1) uniaxial compression loading, (2) single-cycle hysteresis, and (3) stress relaxation. By performing (1), it was possible to effectively compare the fitted material model with previous literature that has primarily investigated the quasi-static uniaxial compression of ballistic gelatine. While experimental arrangement (2) and (3) allow for further investigation of the time dependent behaviour during compressive loading. As with the tests in section 3.2.4.1, all test were filmed using the same arrangement and process used in the investigation of the sample interface.

Three compression speeds were employed in all tests: 2 mm/s, 0.2 mm/s and 0.02 mm/s to explore the rate dependence in the quasi-static regime. All samples were measured using Vernier callipers to record the individual sample thicknesses and the pre-test and post-test temperatures were recorded using a digital thermometer with a probe attachment and an accuracy of  $\pm 0.01$  °C. The temperature of the storage container was measured and the internal temperature of the sample was taken after testing of each sample. The author identified a variation from the average sample temperature of  $\pm 1.5$  °C to be considered detrimental to the results and samples outside this range were discarded [113].

All tests were performed on a Tinius Olsen 25 kN machine with a 5 kN load cell mounted to the machine arm with a screw drive system. The sample plate was attached to the load cell, with the lower plate attached directly to the base of the machine. All programming and measuring was performed using a connected PC and machine sensors. Using the Tinius Olson's Horizon software, all data was extracted from the tests and processed using Matlab v8. It is important to note that until testing, all samples were kept in a cool box and spent minimal time out of the fridge to minimise temperature effects ensuring all samples started testing at the same approximate temperature between  $10 \pm 1$  °C to  $12 \pm 1$  °C depending on the ambient temperature in the laboratory.

Please see overleaf for section 3.2.4.3.

### 3.2.4.3. Uni-axial Compression Tests

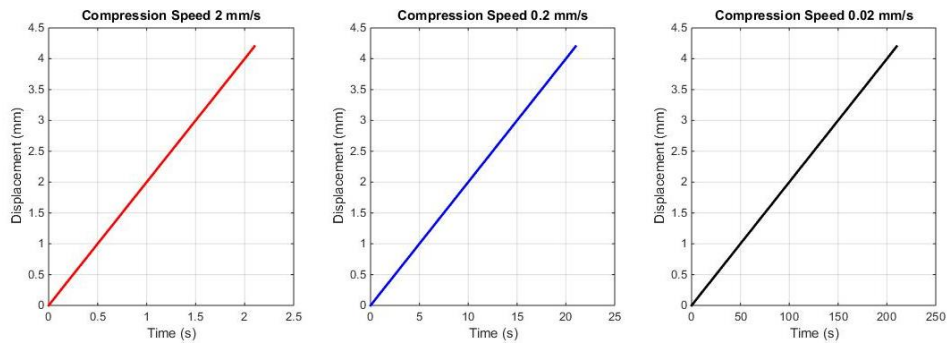


Fig: 3-4: Displays the loading profile for the load only uniaxial compression test, for the three separate compression speeds.

All samples were loaded to 30 % nominal strain, which is equivalent to  $4.2 \pm 1$  mm displacement. The loading ramps can be seen in Fig: 3-4. Ten samples for each compression speed were tested to ensure sufficient statistical significance and account for sample variation. The load, displacement (actual distance machine head travelled), time and machine head speed were recorded for each sample from the machine sensors and load cell.

Each experimental sample was removed from the cool box and the thickness was measured. The sample was then placed centrally on the lower sample plate and the machine head lowered and the preload of 1 N was applied. The experimental rig was then zeroed and the test conducted. The sample was then removed from the machine and the temperature measured by inserting the probe into the core of the sample. At this point, any signs of failure or damage induced during loading were noted for future reference. All test were followed the same procedure differing only in the loading process.

Please see overleaf for section 3.2.4.4.

### 3.2.4.4. Uni-axial Compression Hysteresis Test

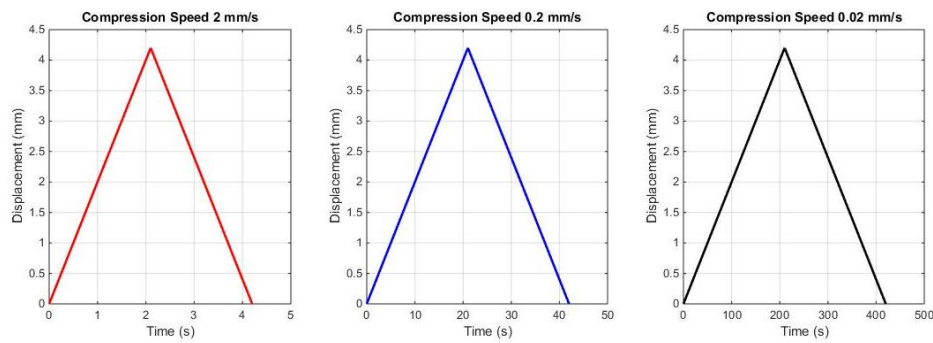


Fig: 3-5: Displays the loading ramp curve showing the triangular wave-form for the three compression speeds.

Single cycle hysteresis tests were conducted using the same experimental arrangement for the previous compression tests. These tests had a particular focus on investigating the loading and unloading response. During a normal hysteresis cycle, the unloading curve will return to zero. Any discrepancy in this could highlight that the experimental arrangement has limitations or slippage at the sample interface. As the material model assumes a homogenous isotropic material, this test will also allow the identification of the accuracy of this assumption.

A triangular loading profile was specified (instead of a ramp) as depicted in Fig: 3-5 with a maximum compression of 36 % nominal strain equating to 5.0 mm before returning to the zeroed position. The reason for the increased strain is to explore the response and to see if with increased strain, there would be any further noticeable increase in stress stiffening and the impact on the response to rebound which has previously been identified as an area of interest for the penetrating impact assessment. This was repeated for all three different compression rates. As above, four experimental variables were recorded for analysis of the response.

Please see overleaf for section 3.2.4.5.

### 3.2.4.5. Uniaxial Compression Stress Relaxation Tests

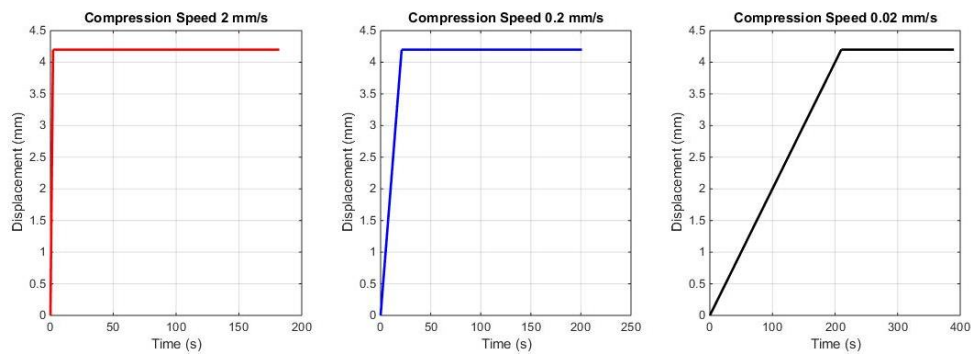


Fig: 3-6: Displays the loading curve for the three compression rates showing the 3 minute holding period.

When performing the stress relaxation tests, the sample was loaded to 36 % nominal strain or 5.0 mm compression and held for three minutes at maximum strain (Fig: 3-6). All tests had a pre-load of 1 N applied before loading was undertaken. The time period was chosen to minimise possible temperature effects while still allowing relaxation to occur over a sufficient time period to enable analysis of the curve. The use of a uniform relaxation period simplified the comparison of the observed mechanical responses across different loading rates, with a particular focus on enabling the comparison of the relaxation process allowing investigation of the time dependent response of the material during relaxation. By using this fixed time period, it was possible to assume that in this case (if temperature variance did occur), it will be constant as all samples are subjected to a constant load time for a given compression speed. [113], [157].

Please see overleaf for section 3.2.5.

### 3.2.5. Testing results

#### 3.2.5.1. Uniaxial compression test results

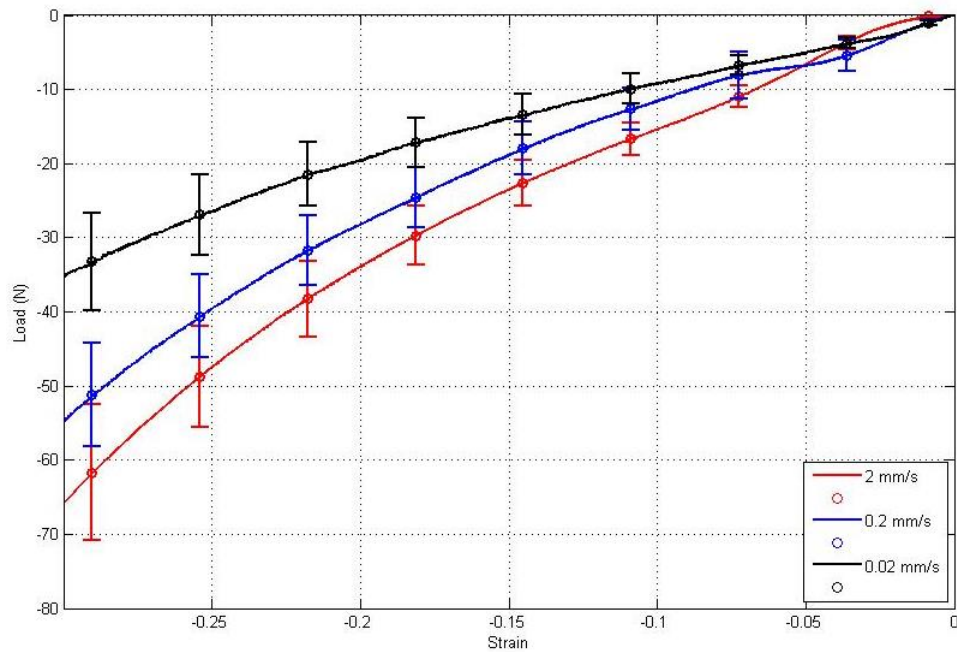


Fig: 3-7: Plot of the uniaxial compression data including error bars that represent the standard deviation of the samples of a specific loading rate, displaying the difference between the different compression speeds. Also showing the effects of sample slippage during initial loading which can be seen as variation at the beginning of the loading curves.

When assessing the results of the uniaxial compression tests, the mean force-strain curves as shown in Fig: 3-7. In this work, strain was defined to be the compression displacement divided by the sample thickness. The response is indicative of the strong rate-dependent nature of the gel which shows good correlation with the previous study performed N Ravikumar and supports the choice of visco-hyperelastic models to characterise the material as there is clear strain-rate dependencies on the response of the samples and the characteristic stiffening that is seen as the strain increases [113]. However, compared to previous work, the sample variance is seen to be larger than expected which is believed to be the result of the use of a cool box and the slippage at the sample interface. The primary factor of difference between the two testing arrangement related to the size of the sample being 30mm diameter by 10mm having the same aspect ratio as the samples in this test, and the use of a refrigerator to store the sample before testing unlike the coolbox that was used in these tests [113]. The reason for the increased variance are discussed below.



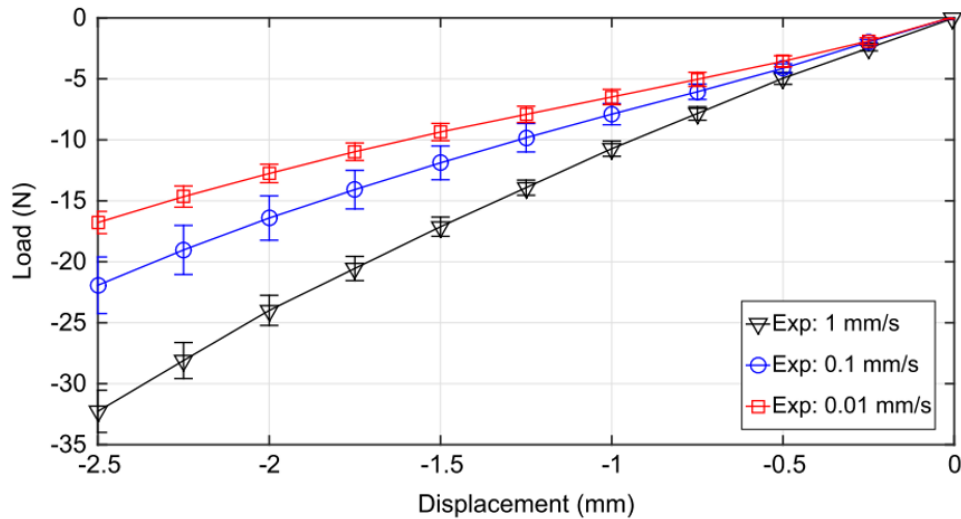


Fig: 3-8: Shows the experimental results that were achieved by N.Ravikumar, and the similarity in the response of the loading curve can be seen, alongside the lower variance when compared to the results obtained [113].

Table 3-1: Table shows the average temperatures for the uni-axial compression tests, alongside the maximum and minimum and range between these values showing that all samples fell within the defined bracket for consistency.

Compression Speed	Average Temperature	Maximum Temperature	Minimum Temperature	Temperature Range
2 mm/s	13.25 °C	14.00 °C	12.10 °C	1.9 °C
0.2 mm/s	14.59 °C	15.10 °C	14.00 °C	1.1 °C
0.02 mm/s	19.81 °C	20.70 °C	18.30 °C	2.4 °C

All samples for a given test were taken from the same batch of material, which produced multiple castings, with samples being selected from across the different castings, which could lead to variance due to the different casting. This then implied that even with careful controls over temperature at dissolution, curing and temperature difference there was still sample variation between both batches and casting. However, as the manufacturing method was based of the work by N Ravikumar, temperature monitoring and sample checks were increased as described in 3.2.3. This, combined with the consistency of the temperature variation as seen in Table 3-1, would indicate that this variance is minimal.

Another possible contributing factor to the sample variance could relate to the use of a cool box as it is not a maintained temperature but a dynamic environment that

increases in temperature over time, all be it slowly, with the increase in temperature directly proportional to the length of time the cool box is in use. As shown in Table 3-1, it can be seen that all samples were in the defined temperature range, showing that the cool box was able to effectively maintain all samples at the same temperature during testing. It was expected that the slower the compression speed, the greater the end temperature as the sample was exposed longer to achieve the same nominal strain. This indicates that inter-sample temperature differences had a minimal impact on the variance seen in the results.

The difference in curve shape that can be seen at the beginning of the loading as seen in Fig: 3-7 between 0 to -0.05 strain (which can be seen for each compression speed) is believed to be caused by a degree of initial slippage at the sample interface during the initial loading which is corroborated by the interface condition tests that were performed. Once this initial slippage has occurred, from the results, it can be seen that the sample's response does not show the variation seen in the initial stages of loading which would indicate that the load force overcomes the majority of slippage effects with increasing load. However, it is possible that small amounts of slippage occur but they are not significant enough to greatly affect the loading curve. This can be seen in Fig: 3-7 from -0.05 strain onward. However, the influence of the variance induced by the sample slippage can be seen in the increased standard deviation between the samples. This can be seen in the Fig: 3-7. The higher the loading speed the less variation which indicates that the loading speed, overcomes the effects of slippage at the interface, as shown in Fig: 3-9 and Fig: 3-10. However at the slowest compression speed, the effects of slippage can be seen throughout the loading in the anomalies in the curve shape and indicates that slippage occurs throughout the loading and has the biggest impact on the results. This form the greatest sources of variance in the experimental results.

Please see overleaf for Fig: 3-9.

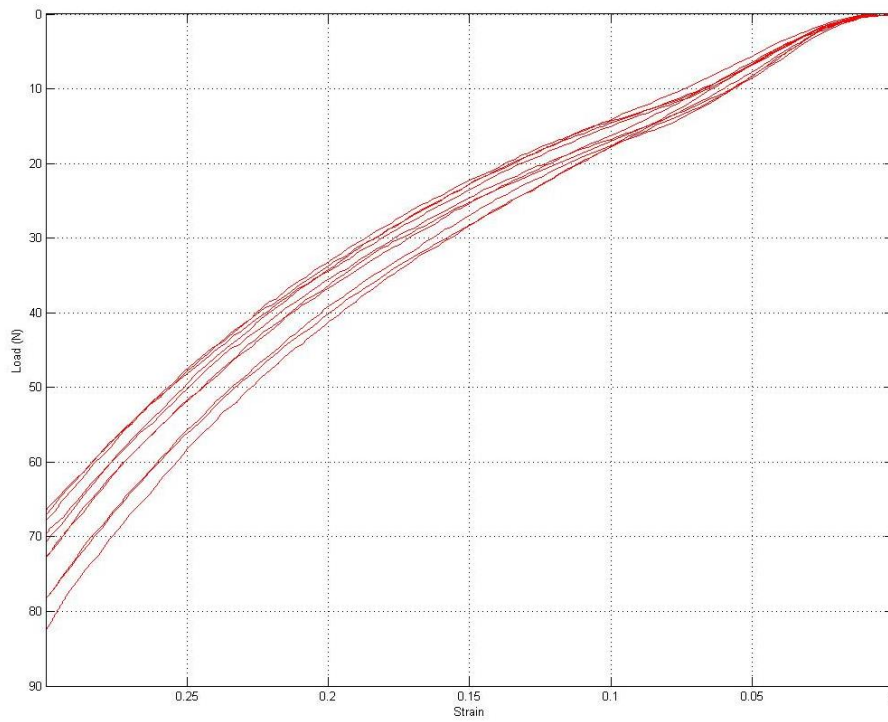


Fig: 3-9: All the samples' responses tested at compression speed of 2 mm/s, which clearly show that the initial impact of slippage is consistent among all the samples and that all curves show a similar response.

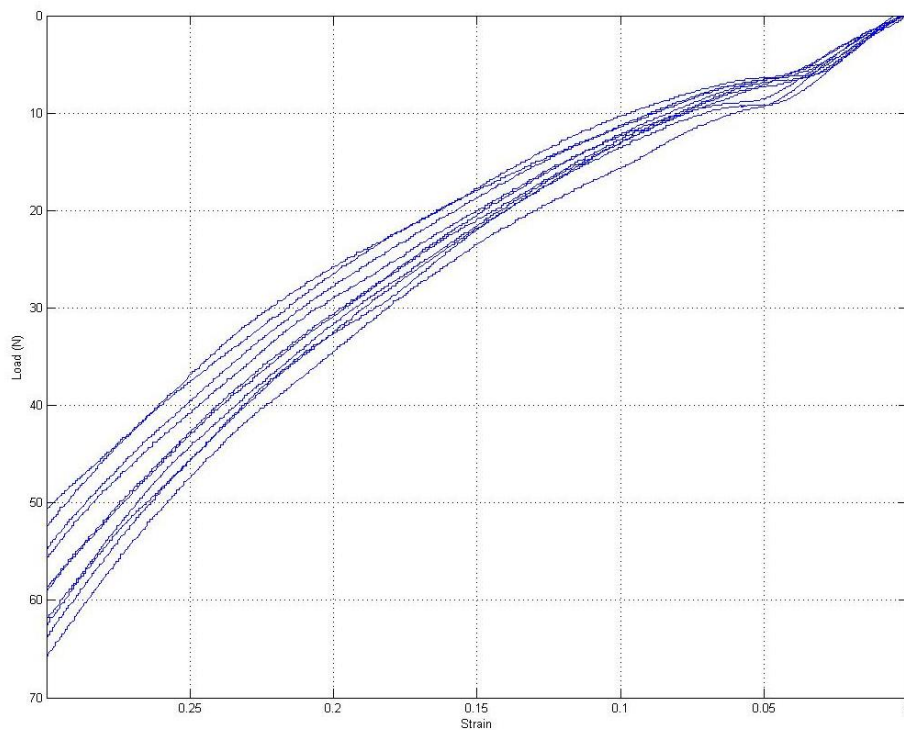


Fig: 3-10: All sample responses for loading speed of 0.2 mm/s, with the similarities between the responses. However, an increase of variance and impact of the slippage can be seen in the initial part of the loading curves across all the samples.

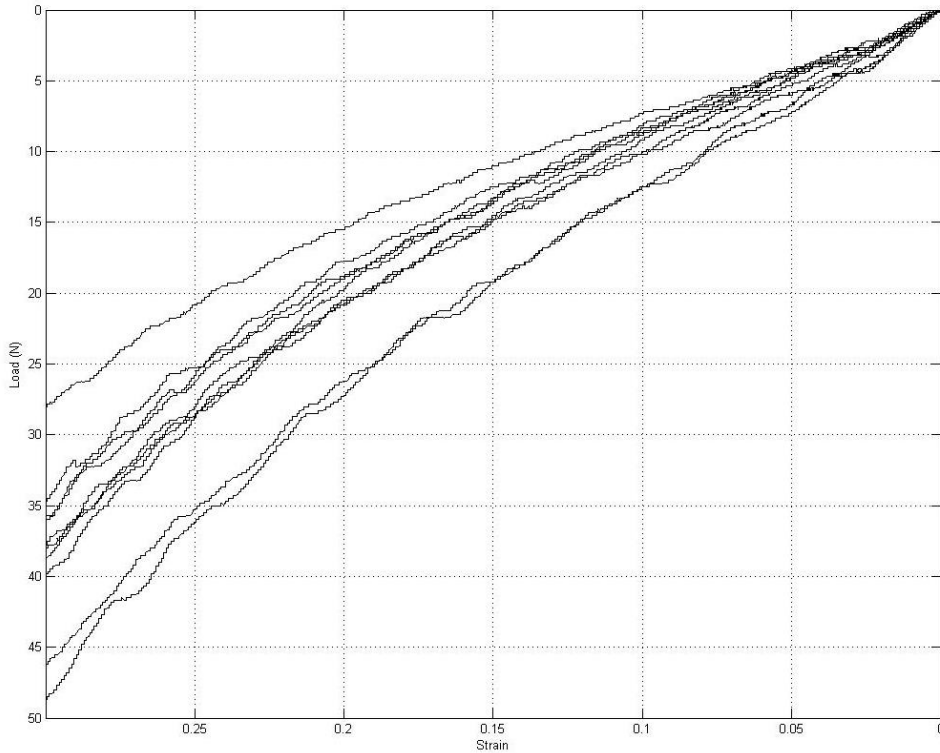


Fig: 3-11: As with the figures above, this shows the response of all the samples tested at 0.02 mm/s compression speed. The greater variance and anomalies in the curves can clearly be seen with outlier samples also visible when compared to the other compression speeds.

The overall behaviour that is shown in Fig: 3-7 is in line with the expected results indicated by previous literature [113]. With the consideration of the possible sources of variance identified, it was most probable that in this case, the different amount of slippage of each sample at the contact interface will have the most significant impact on consistency as discussed in 3.2.4.1, where it was clearly found that inconsistency at the interface will result in a greater variation in sample results at the slower compression speed. It is possible that a manufacturing difference that resulted from variance was induced due to the difference between individual castings and cutting, impacted on the amount of slippage by influencing the sample interface with the plate in the initial sample placement and preload. The sample testing, however, showed consistent and repeatable results which indicates that the method used can be taken forward with extra care taken in the sample mounting to minimise slippage and to minimise the impact of surface or sample surface marks from cutting. Special attention must be taken when testing at the slowest compression speeds.

### 3.2.5.2. Uniaxial hysteresis test results

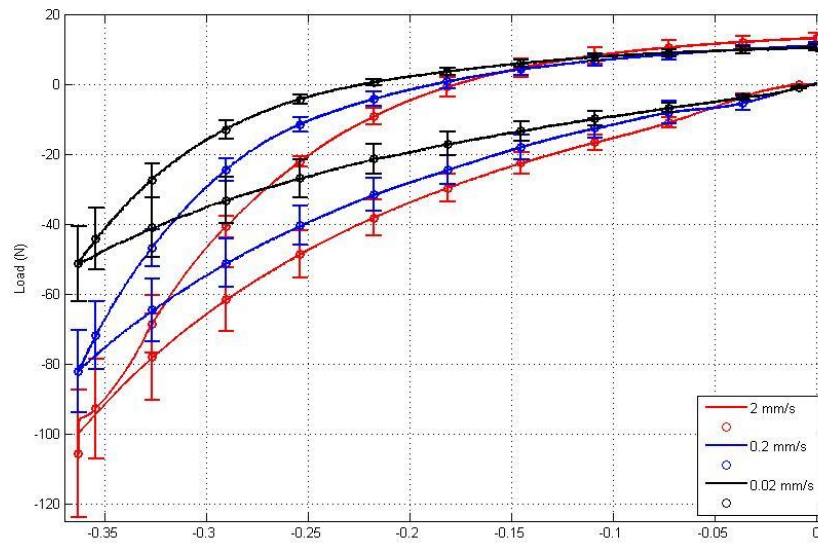


Fig: 3-12: The plot demonstrates the hysteresis output showing the different compression speeds and expected time dependence. It also highlights how the mean data did not return to zero as expected but still demonstrated the expected time dependency, alongside the spike in loading for the fastest compression speed at the point of maximum loading due to the experimental rig limitations.

Table 3-2: Indicates a summary of the recorded temperature information from the hysteresis testing showing the similarity to the uni-axial compression test.

Compression Speed	Average Temperature	Maximum Temperature	Minimum Temperature	Temperature Range
2 mm/s	15.05 °C	15.40 °C	13.60 °C	1.8 °C
0.2 mm/s	17.26 °C	19.10 °C	16.30 °C	2.8 °C
0.02 mm/s	22.58 °C	24.00 °C	21.40 °C	2.6 °C

The plots shown in Fig: 3-12 show a similar rate dependence as seen in Fig: 3-7, and evidence of viscous dissipation in response as the unloading curve does not have the same shape as the loading curve which indicates that the viscoelastic properties of the gelatine are dampening the elastic relaxation. If the material was fully elastic, the J shaped curve would not be present during loading and would overlay during unloading, as long as the sample strain remained in the elastic region and did not begin to show plastic responses. This same rate dependence can also be seen in the unloading curves. In Fig: 3-12, the unloading curves of all three strain rates do not return to zero loading. The results identified that the samples did exhibit a pull on

the plates during unloading due to the positive loading results. When reviewing the filmed footage, it was found that during unloading, there appeared to be adhesion between the sample surface and the mounting plate which can be seen in Fig: 3-13. It was not possible to specifically identify the reason for this adhesion. There is a possibility that surface marks leads to higher friction during unloading, or hydraulic adhesion occurred due to the water content of the sample being displaced during loading. Slippage that was seen during the loading process would indicate the contact area would increase during loading increasing the surface area in contact with the loading plates increasing the impact of friction during unloading. This would in turn result in the resistance encountered during unloading. Any adhesion or fictional affects would likely increase proportionally to the increase in the area in contact with the plate.

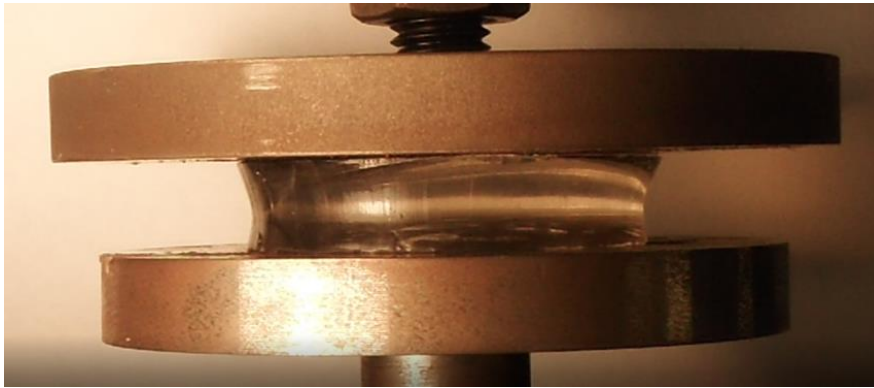


Fig: 3-13: The inverse barrelling shape (dog bone) that was seen during the unloading process during the hysteresis tests. This was presents in all sample and varied in degree in relation to the loading speeds with 2 mm/s showing the greatest change in shape. The sample interfaces can be seen to be in full contact with the plate.

Please see overleaf for all sample loading figures.

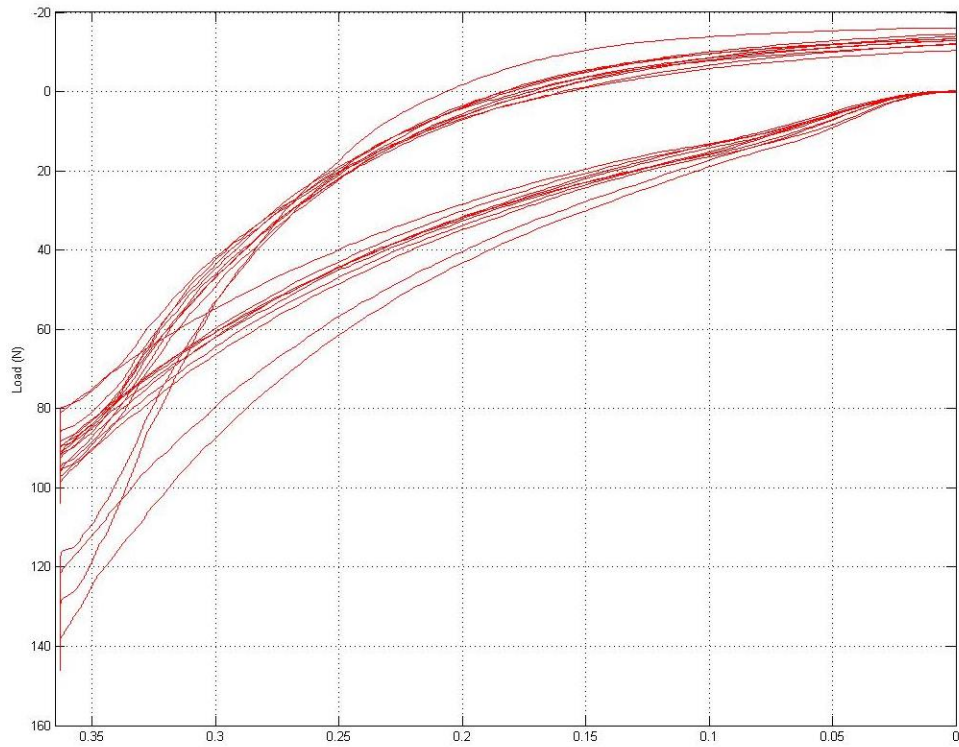


Fig: 3-14: Plot of all hysteresis test conducted at 2 mm/s compression speed where the samples show similar responses apart from the two clear outlier samples. All responses show the spike in response at maximum loading were the testing rig was unable to rapidly change direction.

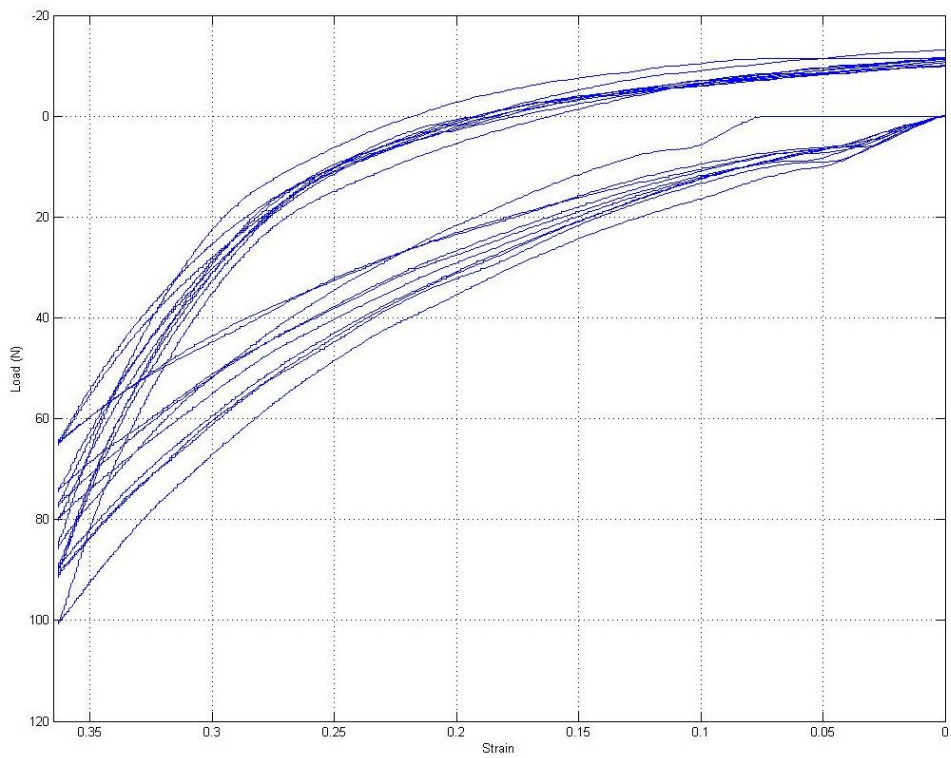


Fig: 3-15: The tests conducted at 0.2mm/s showed more consistent responses across all bar one of the samples which showed a different response, which would indicate from the uni-axial compressions tests a higher degree of slippage has occurred.

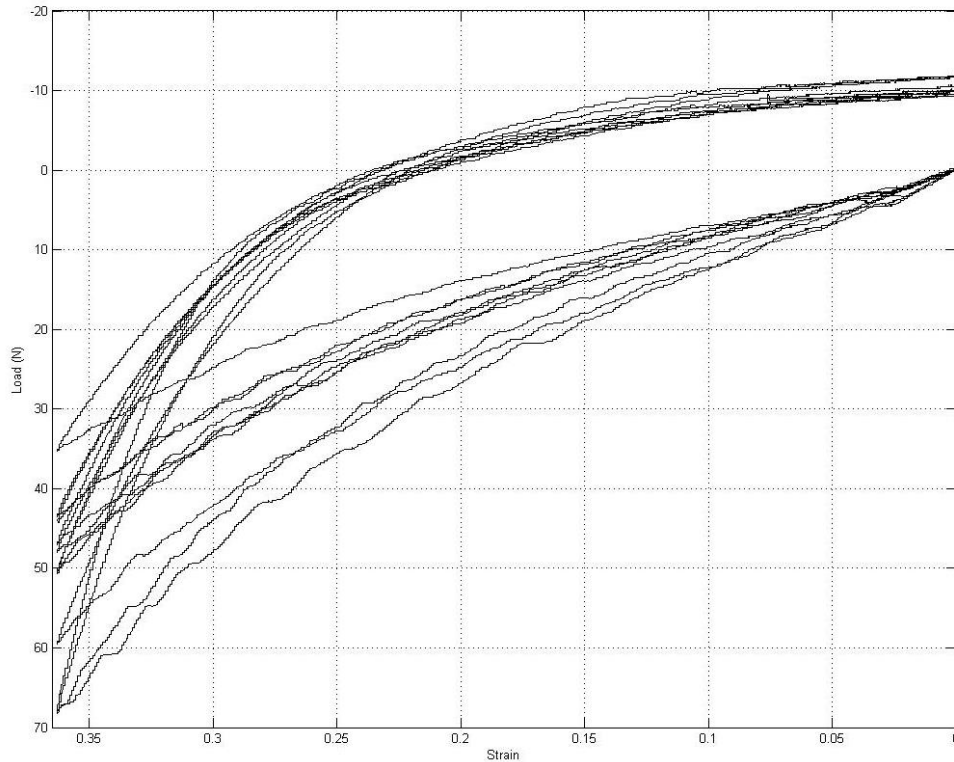


Fig: 3-16: As with the previous uni-axial tests, it can be seen that the response is consistent across the samples, with the same anomalies seen on each of the curves that most likely are the result of the same slippage that was identified previously for the same compression speed in the uni-axial compression tests.

The curve variation between the unloading curves, which is comparable to the loading curve shape, reinforces the material's time-dependent response between the differing compression speeds. The fastest loading rate (shown in red in Fig: 3-12) demonstrates an erratic loading response which is distinctly different from the other curves. This is believed to result from the machine's head employing a motorised screw drive system. This arrangement has mechanical limitations when the loading speeds (strain rates) employed are high and results in a period of the arm being stationary as the machine overcomes inertia to then reverse the direction of loading. However, this was not identified before testing and would indicate the experimental rig is actually not suitable for this specific loading arrangement at speeds above approximately 0.2 mm/s.

If considering the responses of the experimental data, the anomalous spike at the peak of the fastest compression speed and the sample variation seen will have a large significance on the optimisation of the material parameters as these fall outside the



expected responses and will most likely be difficult for the optimisation and material model to account for.

### 3.2.5.3. Uniaxial relaxation test results

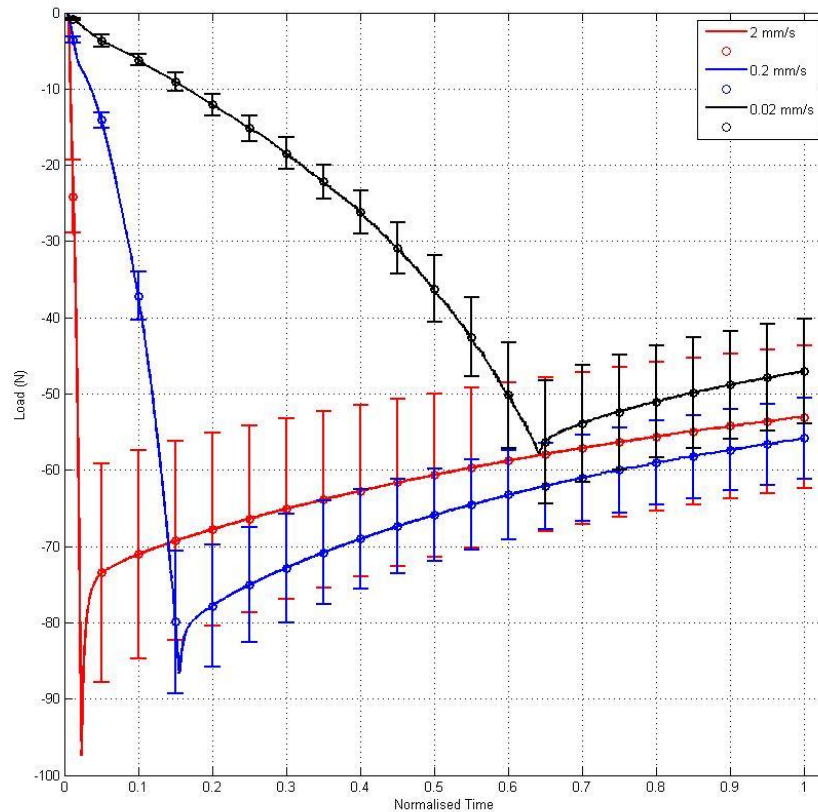


Fig: 3-17: Experimental results of the stress relaxation experiments with the time normalised to the mean experimental total time to allow plotting on the same axis to allow for comparison. It can be seen that the response of the fastest compression speeds unloading curve is not as expected, as it was expected to show higher force and hence, follow the trend of showing greater load values than the previous compression speeds outputs with all the loading speeds not reaching equilibrium within the specified time period.

Please see overleaf for Table 3-3.

Table 3-3: The temperature data from the stress relaxation test which indicated that unlike previous tests the fastest compression speed showed the greatest variation and range.

<b>Compression Speed</b>	<b>Average Temperature</b>	<b>Maximum Temperature</b>	<b>Minimum Temperature</b>	<b>Temperature Range</b>
<b>2 mm/s</b>	18.93 °C	17.40 °C	20.60 °C	3.0 °C
<b>0.2 mm/s</b>	19.69 °C	20.00 °C	19.00 °C	1.0 °C
<b>0.02 mm/s</b>	21.11 °C	21.90 °C	20.10 °C	1.8 °C

As with the previous experiment, the loading curves show the same variation due to the rate-dependence in the loading phase of the curves. The loading and relaxation of the curves highlight the material's time-dependent nature. The fastest compression rate shows behaviour that differs from the expected result. This could result from an error that is induced due to the experimental arrangement, either due to an anomaly during loading or at the sample interface during the relaxation process. From recorded footage, it was not possible to identify the reason for the difference in the relaxation curve for the fastest strain rate. It is, however, clear that this will have a direct impact on the optimisation of the material parameters as this is a considerable difference from the expected behaviour. The variation between samples for this tests can be seen in line with the previous tests, which highlights that this increased sample variation has a direct correlation to the combined effects of the slippage at the sample interface and the intrinsic variation between samples. However, the temperature variation was within the limits specified by the author and was in line with the previous tests, showing that the use of the cool box provided the consistent temperature control.

### **3.2.6. Selected constitutive model**

The non-linearities observed in the mechanical response of ballistic gelatine arise from finite strains and the rate-dependent characteristics of the material. In order to characterise the complex behaviour of the material across multiple loading rates and types of mechanical tests with a single material model, this work adopted a hyper-viscoelastic constitutive formulation. This class of models comprise a hyperelastic, instantaneous and viscous, time-dependent component, making it suitable for capturing the observed mechanical responses of ballistic gelatine. Hyperelastic theory, originally formulated to characterise the finite strain-induced non-linearities of rubber-like materials, has been widely employed previously to capture the elastic, instantaneous response of various soft tissues and soft tissue surrogates. Among the

class of hyperelastic material models, the Ogden model is of particular interest, due to the general form of its underlying mathematical formulation, which provides it with a high degree of flexibility that allows the model to capture a diverse range of mechanical responses. Subsequent sections discuss basic kinematic relations used to formulate the class of hyper-viscoelastic constitutive models and the particular form of the material model chosen (from this class) to characterise ballistic gelatine at these loading rates.

Kinematics, the study of the motion of continuum bodies, can be discussed from a Lagrangian or Eulerian point of view. The former, describing the deformation of a body with respect to its initial/reference configuration, is adopted throughout this study. A Lagrangian description of deformation is expressed as  $\mathbf{x} = \boldsymbol{\chi} \mathbf{X}$ , where  $\boldsymbol{\chi}$  represents the deformation field mapping the body in its reference configuration  $\mathbf{X}$ , to its current configuration  $\mathbf{x}$ . Following such a representation, the deformation gradient tensor defined as  $\mathbf{F} = \partial\mathbf{x}/\partial\mathbf{X}$  completely describes the deformation at a point within the body and is used to derive various strain measures such as the right Cauchy-Green and Green-Lagrange tensors [113]. Due to the high water content of soft tissues in general and soft tissue simulants such as the gelatine used in this study, materials of this nature are often assumed to exhibit near-incompressible behaviour. In the context of the kinematics of such near-incompressible materials, the volume changing component of the material's response is assumed to contribute negligibly towards the overall material response, with the primary contribution arising from the isochoric (volume preserving) component. This leads to a useful mathematical representation of the deformation gradient tensor ( $\mathbf{F}$ ), as an isochoric-volumetric split expressed as  $\mathbf{F} = J^{1/3}\mathbf{F}_{iso}$ , and subsequently, the derivation of corresponding modified strain measures (such as the modified right Cauchy-Green deformation tensor [113]). These kinematic quantities are subsequently employed to formulate various types of constitutive material models.

Hyper-viscoelastic models are often formulated as convolution type models using a Prony series representation to describe the evolution of the shear and bulk moduli with time. As soft tissue type materials such as ballistic gelatine are assumed to be nearly incompressible, the discussion of the time-dependent characteristics of the material's response limits to the isochoric component. The strain energy function for such models is formulated as a convolution of the instantaneous (elastic) and time-dependent (viscous) isochoric components expressed as (an over bar represents the modified gradient):

$$W(\overline{\lambda}_1, \overline{\lambda}_2, \overline{\lambda}_3, J, t) = W_{iso}(\overline{\lambda}_1, \overline{\lambda}_2, \overline{\lambda}_3, t) + W_{vol}(J) \quad (18)$$

where  $W$  represents the Helmholtz free energy equation with  $W_{iso}$  and  $W_{vol}$  representing the isochoric and volumetric component consecutively.  $t$  is time and  $J = \det \mathbf{F}$  is the Jacobean determinant with the modified principle stretch given by the term  $\overline{\lambda}_a$  which corresponds to the modified right Cauchy-green tensor.

$$W_{iso}^E(\overline{\lambda}_1, \overline{\lambda}_2, \overline{\lambda}_3) = \sum_{i=1}^{N^H} \frac{\mu_i}{\alpha_i^2} (\overline{\lambda}_1^{\alpha_i} + \overline{\lambda}_2^{\alpha_i} + \overline{\lambda}_3^{\alpha_i} - 3) \quad (19)$$

The shear moduli are defined by  $\mu_i$  and a dimensionless constant is given by  $\alpha_i (i = 1, \dots, N^H)$  with the number of terms in the series being defined by  $N^H$ . As previously described, the shear modulus and dimensionless constant are related to the initial shear modulus given by  $2\mu_0 = \sum_{i=1}^{N^H} \alpha_i \mu_i$ . This formulation was found to be most effective with the optimisation script that was used which was achieved with minimal change to the formulation.

$$W_{vol}(J) = \frac{K_0}{2} (J - 1)^2 \quad (20)$$

The volumetric component is defined by the bulk modulus which in this case was estimated as  $K_0 = 2\mu_0 (1 + \nu)/3(1 - 2\nu)$  where it is assumed that the Poisson's ration is given as nearly incompressible as stated above ( $\nu = 0.49$ ). The commercial software package Abaqus which employs the following form of the relaxation function was used where  $\tau_1$  gives the relaxation time constant and  $\gamma_1 = \varphi_1/\mu_0$  and  $\gamma_\infty = \varphi_\infty/\mu_0$ .

$$\varphi(t) = \mu_0 (\gamma_\infty + \gamma_1 e^{-t/\tau_1}) \quad (21)$$

During the creation of the of the constitutive model using the experimental result from the mechanical tests, the effect of increasing the number of Prony terms was investigated ranging from 1 up to 4. However, over the tests, it was found that the

increase in Prony terms did not lead to an increase in the fit's accuracy but did increase the computational cost of running the optimisation. So from this work, it was decided that the use of a single Prony term would be sufficient for the fitting and reduce the computational cost associated with the optimisation of the characterisation.

Strain energy functions of this form capture the stored elastic energy in the material following large deformations and load-history dependent dissipative effects such as creep, stress relaxation and loading rate-dependence.

### **3.2.7. Optimisation of material parameters**

An FE model of the sample under load and a multi-start least square non-linear optimisation algorithm were used to fit the material parameters to the experimental results. The 4 parameters being optimised are the shear moduli  $\mu_i$ , relaxation time constant  $\tau_1$ , Prony series dimensionless constant  $a_1$  and  $\gamma_1$ .

The FE model was constructed using axisymmetric principles and the mounting plates were represented by rigid bodies, which have been used previously for material parameter fitting for uniaxial compression test data for ballistic gelatine giving confidence to the model [113].

The model elements were 4-node quadrilateral elements (Abaqus 6.13 element CAX4R) used with a fully non-linear large deformation analysis. A mesh independence study was undertaken for the model with the final mesh containing 2100 elements.

As previously stated in section 3.2.4.1, a fixed boundary condition was assumed using tie restraints applied to the model enforcing a non-slip boundary condition.

This work used the same formulation that has been used previously in [113]. This made use of the 'trust region algorithm' present in Matlab's 'lsqnonlin' function script, which was performed over multiple evaluations of the FEA model output for the given parameter optimisation. To aid the accuracy of the optimisation, multiple different upper and lower bounds were specified alongside the optimisations initial point for each of the parameters that are being optimised. This was done in an iterative process based on the previous results.

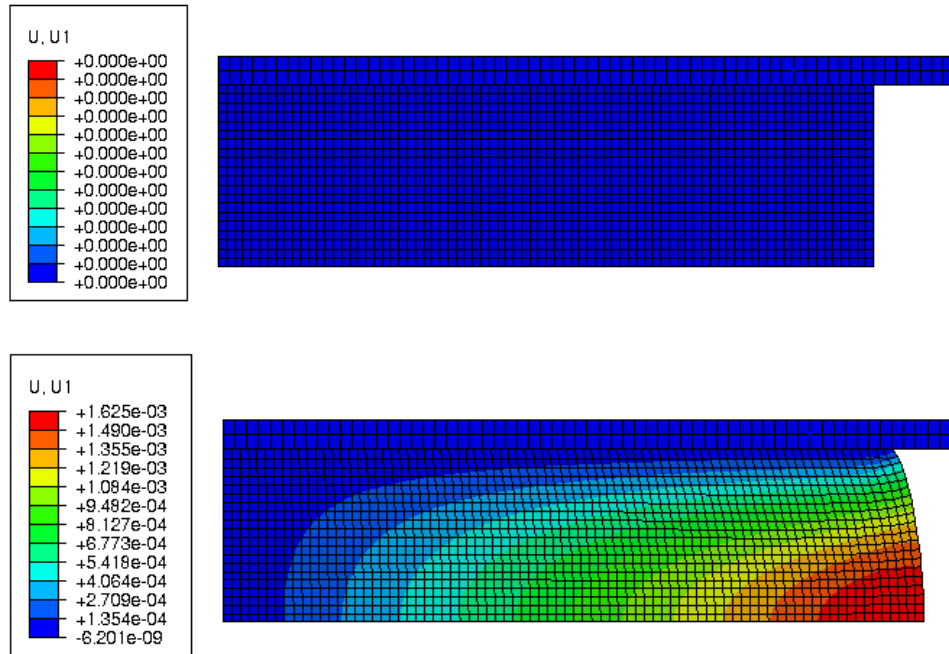


Fig: 3-18: The unloaded and loaded configuration of the FE model with the loading plate and sample clearly visible alongside the symmetry used. The upper image represents the unloaded configuration and the lower image registration represents the loaded configuration. The scale represents the Von-Mesis strain.

Initially, the optimisation was performed over the averaged sample response for each compression speed individual. Then, the optimisation was performed over all the response curves simultaneously to produce parameters that account for all the tested compression speeds. If the multi-curve fit was unsuccessful, the reason was analysed and the averaged sample curves were used individually and compared to identify if the fitting had been consisted. Another approach would be to average the resulting parameters which was not undertaken due to the error and inaccuracy that this would have introduced. For details, please see the optimisation section for a detailed description [113].

### 3.2.8. Optimised material parameters

The section below is a discussion of the parameters that were produced from the fitting process that was performed for the specific experimental tests.

### 3.2.8.1. Optimised uniaxial compression parameters

Table 3-4: The optimised material parameters for the uniaxial compression tests.

Parameter	$\mu_1$	$\alpha_1$	$\gamma_1$	$\tau_1$
Estimated Parameter (Multi-fit)	22,110 Pa	3.64	0.53	6.66 s

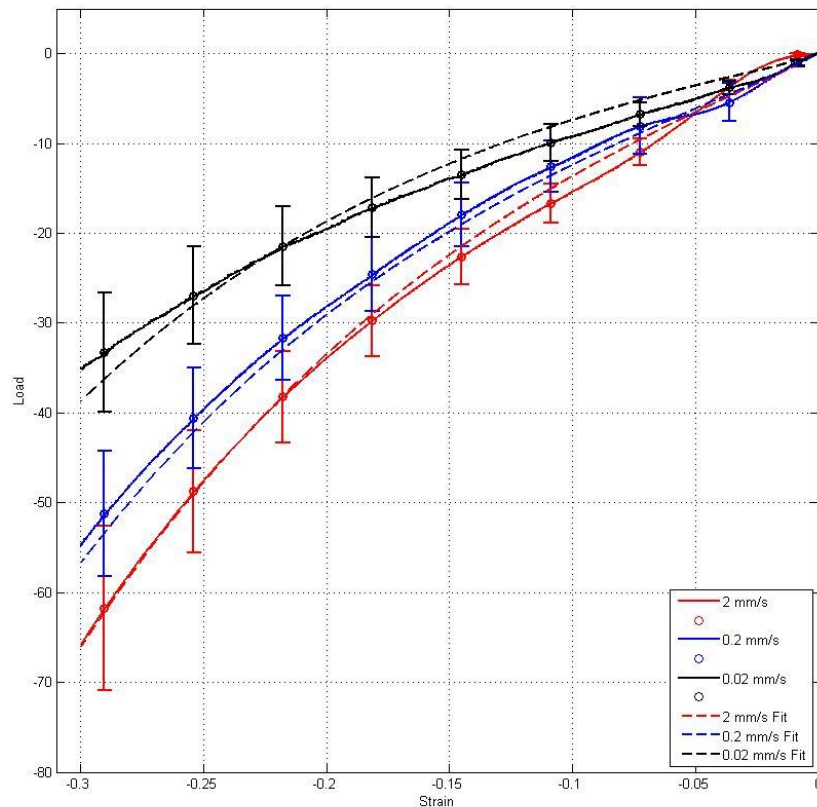


Fig: 3-19: Overlays of the fitted material to the mean experimental output, which shows that the anomalies that were induced in loading have influenced the fitting. However, even with the limitation, it can be seen that for the curve with the most variance, the slowest compression speed remains within the standard deviation of the sample response.

The fitting process was able to be performed over the three compression speeds simultaneously, which was expected. The results are shown in Fig: 3-19. It can be seen that the material model is able to capture the material response. However, there is clear influence from the anomalies that were identified from the mechanical tests. The fastest and middle compression speeds showed the most effective fits with the optimised curve sitting close to the experimental data and with minimal difference

in the shape. In the case of the slowest compression speeds, it appears that the fit is dominated by the curve shape of the other two compression speeds which can be seen to have a similar shape to the higher compression speeds highlighting a possible dominance in the fitting process. This is most probably due to the influence of the slippage previously identified. This highlights the impact that the slippage has on the experiment and optimisation. This would indicate that the assumption of infinite friction for the experimental arrangement, which is what defined the model parameters, is not wholly accurate.

### 3.2.8.2. Optimised uniaxial hysteresis parameters

When fitting the FE model to the hysteresis data, it became apparent that the method was unable to fit to all three loading rates simultaneously with sufficient accuracy. Consequently, the model was fit to each curve independently and a set of optimal parameters for each loading rate are shown in Table 3-5.

Table 3-5: Shows the parameter optimisation including the individual fits and the optimised parameters for the uniaxial compression test for comparison.

Parameter	$\mu_1$	$\alpha_1$	$\gamma_1$	$\tau_1$
<b>Estimated Parameter Uniaxial Load Fittings</b>	22,110 Pa	3.64	0.53	6.66 s
<b>Hysteresis Fit 2 mms</b>	35,723 Pa	2.11	0.59	0.43 s
<b>Hysteresis Fit 0.2 mms</b>	19,984 Pa	3.82	0.62	2.43 s
<b>Hysteresis Fit 0.02 mms</b>	23,656 Pa	1.47	0.67	22.12 s

The sensitivity of the optimisations was found to be comparable with the previous work undertaken, with the uni-axial optimisation. However, before looking at the sensitivity of the individual parameters, the effects of the interface will have a greater impact on the individual fitted parameters. As for the slowest compression speed, the slippage and adhesion has the greatest impact on the fitting. For the fastest compression speed, the impact of the machine limitation has the most significant impact on the optimised parameters. It was identified that in the fitting of the middle strain compression, the sensitivity of the parameters was found to be the same as the



uni-axial fitting which is to be expected as the optimisation method and model parameters are the same, apart from the specific loading regime.

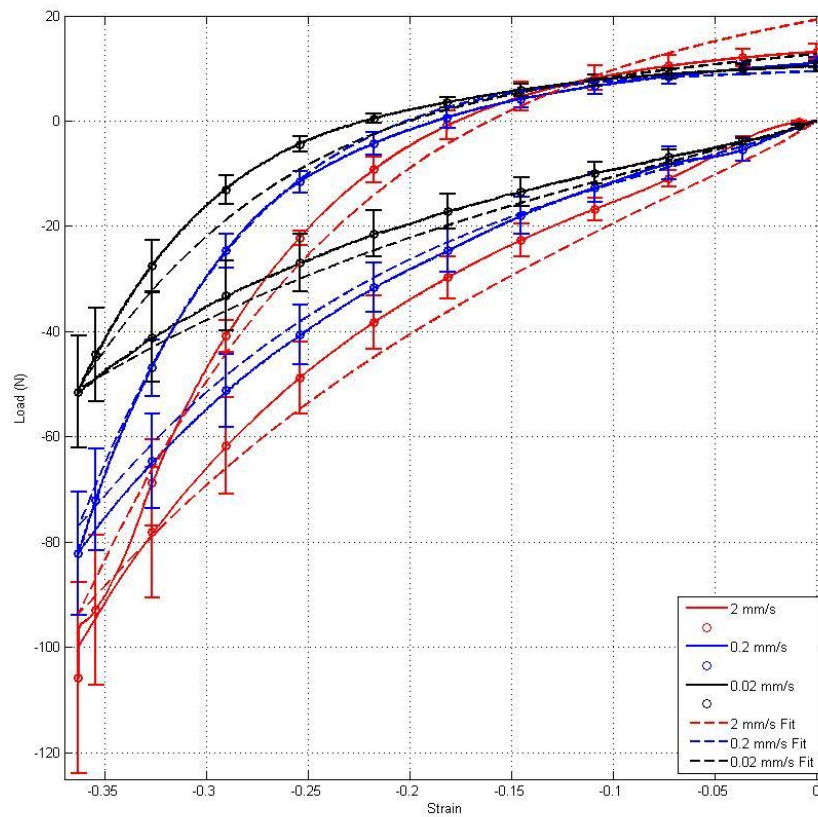


Fig: 3-20: Overlays of the fitted material to the mean experimental output. This shows that the optimisation was not successful with only the middle compression speed having been fitted effectively as the curve shows the same shape and has a large degree of overlap with the experimental curve, and if it does deviate, it is within the standard deviation.

In this case, the most effective fit can be seen to be the middle compression speed, seen in Fig: 3-20. The other fits, especially in the case of the fastest compression speed, show an unsatisfactory fit to both the loading and unloading curve. The slowest strain showed a good fit for the loading curve; however, the unloading curve can be seen to fall outside the sample variance. The poor fit in the case of the fastest compression speed was not unexpected due to the unusual curve behaviour that was previously identified in the discussion of the experimental results. With it being constant throughout all the samples tested, it highlights that this experimental rig is suitable for uni-axial compression tests but not hysteresis test at the compression speed of 2 mm/s which was not known before testing took place. This factor combined with the clear inverse barrelling response and resistance to unloading can be seen to

complicate the fitting process, which is further complicated by the material constitutive model lacking the flexibility to optimise the parameters for the other the experimental results, which is not due to the model used but rather the identified mechanical anomalies: at the slowest compression speed, the slippage that occurs and the error at the peak loading of the curve.

### 3.2.8.3. Optimisation of uniaxial relaxation parameters

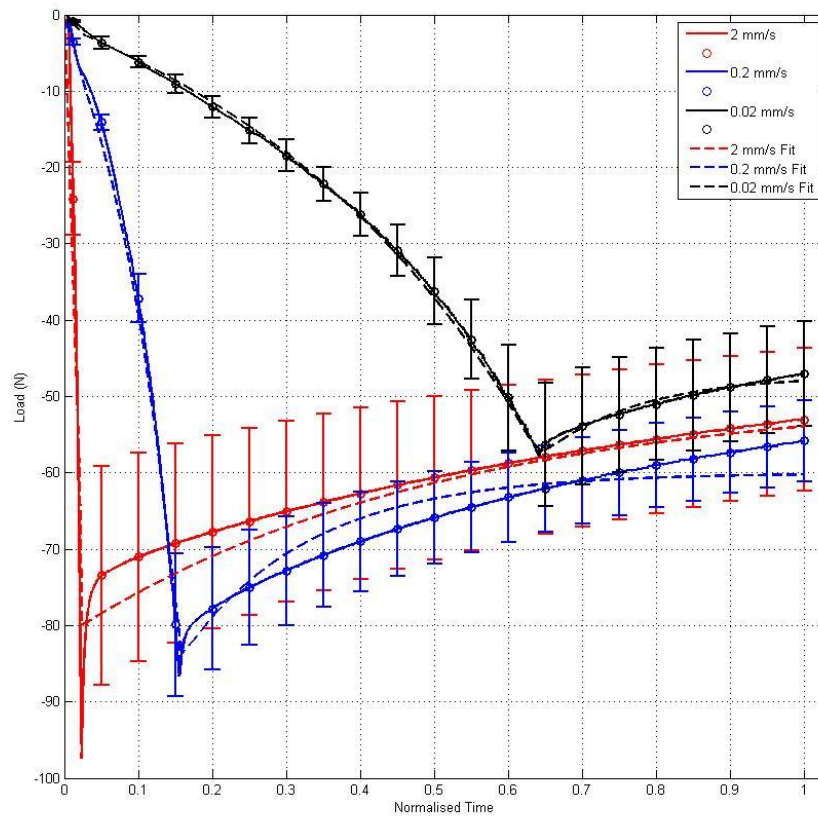


Fig: 3-21: Overlaid fitting data for the hysteresis experiments again showing the optimisation was unable to fit the parameters to the fastest and middle compression speed. The model does produce an effective fit to the slowest compression speed.

Table 3-6: The material parameters from fitting to the individual strain curves for the stress relaxation experiments, with the uniaxial compression fittings for comparison.

Parameter	$\mu_1$	$\alpha_1$	$\gamma_1$	$\tau_1$
<b>Estimated Parameter Uniaxial Load Fittings</b>	22,110 Pa	3.64	0.53	6.66 s
<b>Relaxation Fit 2 mms</b>	22,598 Pa	3.47	0.41	57.57 s
<b>Relaxation Fit 0.2 mms</b>	29,108 Pa	3.24	0.38	21.48 s
<b>Relaxation Fit 0.02 mms</b>	27,654 Pa	2.60	0.43	37.97 s

The experimental stress relaxation data for each strain rate was fit individually to the experimental curves and the resulting curve fits are depicted in Fig: 3-21. The same inability to accurately fit the material model simultaneously as with the optimisation of the hysteresis experimental results was present. This again seems to be a combination of the errors that were identified for fastest compression speed and the already identified lack of flexibility in the current material model to allow fitting across multiple experimental data sets. In this specific case, the only effectively fitted curve is for the slowest compression speed with the middle compression speed fitting not capturing the relaxation curve effectively, and the fastest compression speed having poor fit for the complete response. It should be noted that in this work, the time step used in the optimisation was defined as the loading time for each data point of the averaged data which varied with the compression speed but has 42000 data points for the given time series.

A longer relaxation time, if applied, would allow the material to reach equilibrium. However, this was not achieved in this work and its inclusion would greatly benefit the fitting process. It was considered in order to attempt to control the temperature of the experimental arrangement but it was decided against this as controlling the temperature of the air-cannon is not viable and as this characterisation is being undertaken to better understand how the gelatine responds and the experimental considerations that are needed for the later air-cannon tests, the test without environmental temperature controls provided more benefit for the end goal of this thesis.

### **3.2.9. Final material parameters**

The method produced a series of material parameters from the optimisation of the material model over the three independent experimental arrangements. The values for the successful fittings can be seen in Table 3-7 for the hysteresis and relaxation test compared to the uni-axial optimisation parameters. By comparing the different responses, it can be seen that even though it fitted to the experimental data sets, the differences in the variables make it clear that the experimental arrangement and model parameters do not allow the flexibility to fit to all data sets. However, as the uni-axial compression tests have been found to be comparable to the parameters found by [113] which the author took part in publishing, the model is capable of fitting to this experimental arrangement, including the impact of variation induced by the experimental anomalies. However, the current arrangement cannot be used to simultaneously fit or individually fit all the loading curves for the hysteresis and stress relaxation tests. This can be related to two key factors: experimental anomalies that were incurred due to the slippage across all compression speeds that have been identified and the specific errors that were identified for the fastest compression speed in both the hysteresis and relaxation tests.

As stated earlier, the material model was able to fit to one curve in each of the later tests and the results can be seen to vary for each of the fits as seen in Table 3-7. This brings the material model into question. The process was able to fit the uniaxial compression loading experiments and was unable to effectively capture the material response over the other experimental arrangement. This would point to the material model being too specific to have the flexibility to optimise the response of the hysteresis and stress relaxation tests with the current experimental assumption that have been. It would be prudent in any future work to revisit the experimental assumption and conditions in future tests to remove the variable and better explore the material model response, with a suggested focus on the interface between the sample and the plate. The material model needs to also be expanded to account for the identified interface condition. Alongside expanding the fitting process to include a comparison with other material models. Such as the Ogden Hyperelastic model proposed by D.S Cronin [164] which has been tested at similar speeds.

Table 3-7: the material parameters from the fittings that can be considered to be successful from all the optimisations for the different mechanical tests.

Parameter	$\mu_1$	$\alpha_1$	$\gamma_1$	$\tau_1$
<b>Estimated Parameter Load Fittings</b>	22,110 Pa	3.64	0.53	6.66 s
<b>Hysteresis Fit 0.2 mms</b>	19,984 Pa	3.82	0.62	2.43 s
<b>Relaxation Fit 0.02 mms</b>	27,654 Pa	2.60	0.43	37.97 s

In conclusion, the material model and process are able to capture and provide meaningful material parameters for uniaxial for quasi-static compression speeds 2 mm/s, 0.2 mm/s and 0.02 mm/s. The fitting values were in line with previously published work, but in this case increased variation was incurred due to experimental slippage during loading. Also, due to experimental anomalies resulting from the experimental rig and material slippage, it had limited success fitting material parameters individually for the stress relaxation and hysteresis tests. The testing was undertaken in environmental conditions that will be similar to those used in the later proposed air cannon impact tests.

### 3.3. Discussion

From the work that has been undertaken in this chapter, the key details that will impact future experiments is the limitation of the constitutive material model applied and the difficulties that have been encountered during experimental testing. Conclusively, it is not possible to say that the temperature did not have an effect. However, from the data obtained for the temperature monitoring and then comparing this across the mechanical tests, the effect that temperature variation had on the samples was minimal as consistency was maintained in the recorded experimental data. This also highlights that the same approach can be applied to the air cannon tests to minimise temperature variation in the proposed experiments and should be applied as the base for future sample creation and storage. To address the issue of possible variation due to casting, careful monitoring of the temperature and careful documentation of any difficulties or possible anomalies that could occur during the manufacturing processes will aid in maximizing the sample consistency achieved.

The use of the cool box to store samples helped to maintain consistency in the final temperature that was measured. However, if possible, a constant temperature storage

device would have been more effective. Therefore, it is important that in future work, an arrangement is found to support this. This could be achieved with either a similar cool box that can maintain its temperature for extended periods or by leaving samples in the fridge until testing. This will rely on the specific arrangement and location of manufacturing and testing site.

During the pre-work, as outlined, multiple loading condition interfaces were explored. It was found that fixing the gelatine was not a trivial process. Several glues were tested including cyanoacrylate and gel-based glues, which were unable to effectively form a bond with the gelatine surface. Water based glues were also tried and also were unable to bond the gelatine. It was theorized that this was due to the gelatine's high water content [139], [173]. This prevented the glue from bonding to the gelatine molecules which rendered the glue incapable of adhering and fixing the samples. Double sided adhesive tape was also attempted but was unsuccessful as it is believed the same mechanism prevented bonding with the gelatine. A detailed investigation was beyond the scope of this work as it would not have been beneficial as the air-cannon experimental rig will not permit gluing the sample in place.

When considering previous literature, another method which has been applied to fixing samples is sand-paper as a way to approximate infinite friction. The tests that were conducted showed unpredictable surface failure that occurred as the material was compressed. Due to this, no repeatable results could be extracted from the tests. It is believed the failure results from the high shear failure at the interface. The curve shape remained constant but the loading value varied by a great deal as the failure occurred at different points during loading. This would highlight that sample variation has an impact on the response compounding the difficulty in extracting meaningful data for this arrangement.

From literature, the use of oil was found to have precedence as a method for achieving a friction-less interface [133], [173]. Both organic and inorganic oils have been used. Mineral oil (specifically a gun oil, chosen for availability) were tested as possible lubricants. The result was highly inconsistent as the samples were not confined so during loading, the samples consistently shifted and did not remain central to the loading plates. This meant that it was not possible to acquire meaningful results as it was not possible to complete a loading cycle. This clearly showed that the use of a lubricated interface in an unconfined experimental arrangement as used in this work was incompatible with extracting meaningful results. This resulted in the use of an interface where the samples were directly placed onto the mounting plate with no preparation. Some slippage was identified

during testing, but in the compression tests, this proved to have minimal effects on the results. Altering the sample size was considered; however, this would have required the manufacturing of new loading plates, which would have been limited by the available space on the loading rig, as the aim was to ensure the aspect ratio of the sample was maintained to allow the comparison to previous work that has been undertaken. So in future work, it would be prudent to consider an equivalent interface. This presents several benefits for the later work in this project as this simplifies the experimental mounting arrangement. It is clear that the loading speeds that have been undertaken in these experiments are different from the ballistic loading speeds that will be used in the later chapters. However, the work undertaken does provide an effective assessment of a likely interface which will provide an initial arrangement that can be assessed and modified as required.

As discussed earlier in the chapter, the interface condition highlighted that slip can occur so during the air-cannon test. It would be prudent to explore interface conditions if any anomalies or experimental difficulties are encountered.

The specific material parameters that were achieved with the optimisation process highlight that the selection of the material model was partially effective at capturing the material response beyond the uniaxial compression tests which themselves showed accurate fitting of the material model. In the case of future work, this means that proposed validation test should be conducted at a comparable compression speed and in the uni-axial compression loading regime. This should not be too limiting as the main goal of validation tests focuses on the method of data capture and the accuracy of the proposed image registration method. These results also provide an interesting avenue for the discussion of the material response in future work beyond this thesis.

To conclude, the key findings of this chapter are the following: that the current material model and fitting process lack the flexibility to characterise all the loading arrangement due to the experimental anomalies present in the results and the assumption used in the construction of the computational model. However, it is able to specifically characterise the uni-axial compression experiments over all the compression speeds tested. The uni-axial compression material parameters identified for GELITA type 3 scientific ballistic gelatine will allow the construction of a computational model to validate the image registration method as long as the loading speed and arrangement can be considered comparable. The second key finding is that the sample interface could lead to complications in testing. In the following

chapters, the interface conditions used in the work above should be applied as an initial starting point as this gave the most consistent results.



## **Chapter 4. Image registration as a means of quantifying displacement and strain**

*Please Note: Portions of this work have been published in [101]*

### **4.1. Introduction**

Image registration has been used in medical engineering imaging and has several features that would be beneficial for the assessment of deformation and strain in mechanical testing. One of the most interesting features is the capability for image registration to be performed in 3D or across images captured from a multitude of different distance and angles with relatively accessible experimental equipment as image registration can be performed on images captured using a wide range of different cameras including grey scale, colour, high speed cameras and the medical imaging equipment that it has seen extensive usage with such as MRI, X-ray CT and Ultrasound. This also highlights another beneficial capability that is presented by the use of image registration in its ability to compare images taken with different types of camera using its multi-model approach. This would, when using suitable cameras and experimental arrangement, allow the assessment of the penetration and cavity expansion of fragment impact in 3D and could be further expanded to compare and assess data captured using ultraviolet or thermal cameras. The aim of the thesis is to establish if image registration is suitable for the quantification of deformation strain that result from penetrating impact of fragments from explosive ordnance. A 2D assessment will be undertaken as this allows the focus to be on the accuracy of the image registration approach rather than the camera arrangement.

This chapter presents the image registration framework that this thesis proposes to be used for optical strain/displacement quantification for both pair-wise images and sequentially composed pair-wise transformations, over a video containing multiple frames that have been recorded sequentially in time. In this case, pair-wise defines images that are sequential in time and which the registration is performed between. Thus, this method allowed an assessment of the dynamic change in deformation over the recorded video time period and individual pair-wise images, enabling a multi-layered approach which allows the assessment of the whole captured video and if desired, a more detailed specific assessment of sections of the captured video of the impact. The proposed method has two levels: One level performs the pair-wise registration, which is between movie frames that are consecutive in time. The second level performs the composition of the pair-wise transformation between the movie frames to produce the dynamic displacement over the course of the captured footage. Alongside this, a method for assessing the resulting strain field is also presented

which has been designed to assess the outputs from the registration and composition processes. Before exploring the method, a review of the current optical-based experimental assessment methods that are used to measure mechanical tests used in previous literature will be discussed.

## **4.2. Optical methods for quantifying deformation**

Optical methods have seen extensive employment in the field of deformation measurement which have allowed the assessment where the application of traditional methods, such as manual measurement and mounted sensors, would be impractical or detrimental to the assessment being undertaken.

### **4.2.1. Digital image correlation (DIC)**

This method shares the greatest similarity with image registration, both in its application and the supporting mathematical framework. The theory is based on being able to assess the correlation of image patterns between two frames specified by a monochrome speckle pattern that has been applied to the mechanical sample and assessed by a framework that defines the image as a series of subsets, which, when tracked using a transformation algorithm, defines the deformation. The subset size is defined by two factors: how fine the applied speckle pattern is and imaging quality of the camera. However, this does mean that there is a minimal size of subset that can be used, as if the size is below a critical value specific for the speckle pattern applied, it is not possible to identify specific patterns. This relies on the volumetric change and the corresponding change of the surface geometry, for example as tension is applied to a material which deforms the sample and warps the monochrome pattern that has been applied to the surface. An example is shown in Fig: 4-1 where the random nature of the speckle pattern can be clearly seen [27], [174]–[177]. DIC identifies this warping and uses this to construct a displacement map between the two frames. It is important to note that this monochrome speckle pattern has to be random to ensure the distinction between images and to avoid misidentification, so it is applied by hand and the size of the speckle can have a direct impact on the accuracy and computational cost of the method. In the case of sensitive or very small samples, this applied pattern needs to be thin as possible and not impact the material response to loading [174], [178], [179].

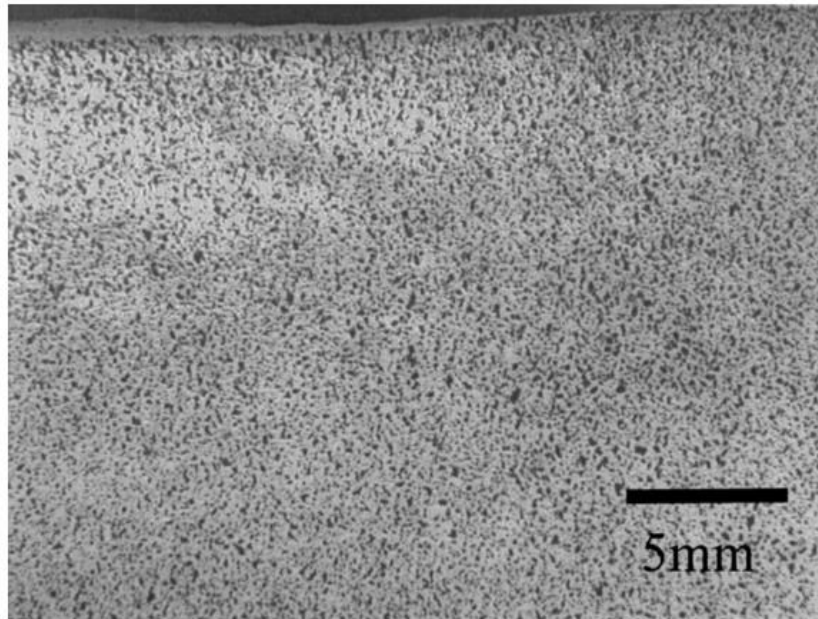


Fig: 4-1: Example of a common speckle pattern applied to the surface of a sample for DIC the irregular nature of the pattern can be seen (note: the image was taken using a greyscale camera) [178].

DIC constructed around the optimisation of the correlation of the pattern motion is used to generate an image transformation. To optimise the transform, the image is broken down into subsets, where size is defined by a particular method, experimental arrangement or applied speckle pattern as stated earlier [174], [179]–[181]. The centre of the subset is used to define the transformation point. A B-spline transform is used to define the pixel-wise deformation for the transformed image using the subset centre points as the control points. The optimiser uses an assessment metric to control the accuracy of the correlation between the image pairs [180]–[182]. DIC has seen established use in the fields of material classification and fracture toughness, alongside having been used for shock and impact experimentation [177], [183], [184]. There has been an increasing use of DIC to investigate tissue surrogates such as ballistic gelatine. An example can be seen in Fig: 4-2 where the strain generated over the crack propagation in a DIC experiment investigates the behaviour of a soft-tissue like material [178], [185].

Please see overleaf for Fig: 4-2.

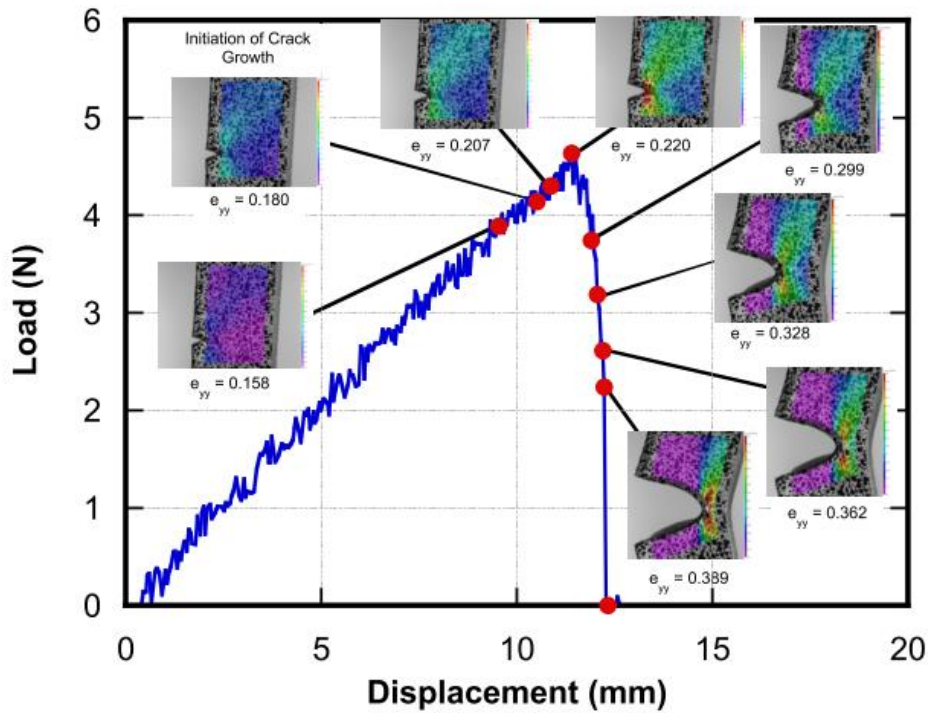


Fig: 4-2: From P.Moy. Shows the application of DIC to crack tip propagation in a ballistic gelatine sample. The calculated strain field can be seen overlaid on the sample at key points in the loading curve, and the speckle pattern is clearly visible in the inlaid images [185].

#### 4.2.2. Photoelasticity

Photoelasticity is an established technique for optical strain/displacement measurement. This method has several components with the core principal being the use of birefringent material properties to assess the strains and displacement of the samples being tested. A material which is described as being birefringent is a material that has two different refractive indexes which can be seen when light moves through the material. This also occurs when light is reflected back off one of the material surface and passes back through the material normally seen as a rainbow-like effect of distinct bands of colour. Good examples of the materials commonly used are plastics, resins and glass [100], [186]–[188]. In photoelasticity, the different refractive indexes of materials are exploited and the resulting phase difference being identified of the displacement as the two material surfaces (front face and rear face are perpendicular to the direction of light) move relative to each other, which results in a change in the material geometry and the induced phase difference. The specific detection method is dependent on the aim of the experiment or limits imposed by the geometry being tested. Common methods, as mentioned above, are transmission photoelasticity and reflection photoelasticity. Both methods

use a polariscope arrangement to identify the fringes that result from the changes in the phase difference during loading as seen in Fig: 4-3.

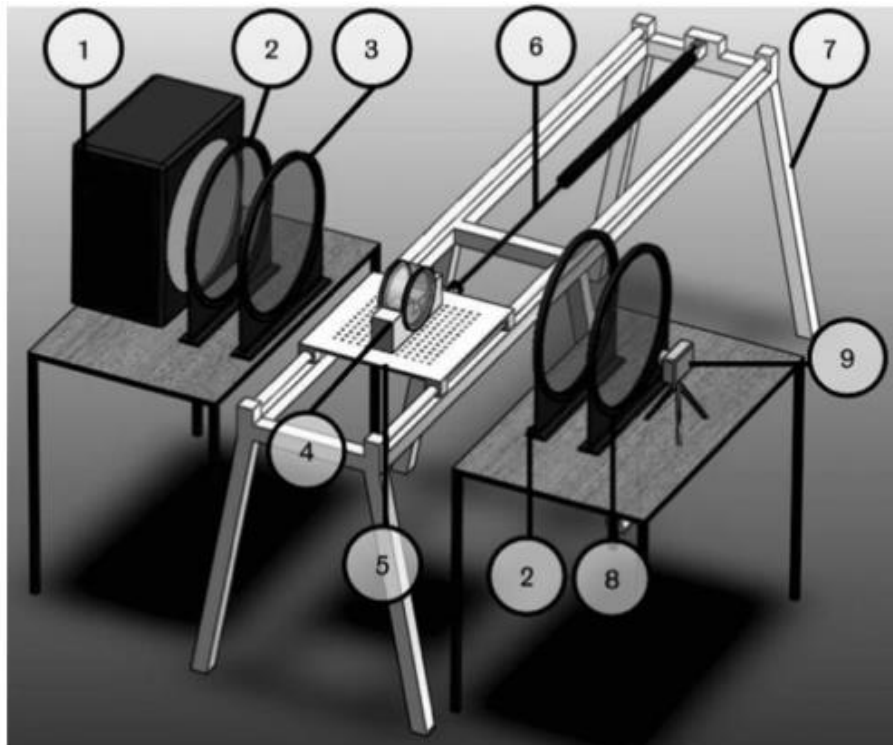


Fig: 4-3: An example of a common experimental polariscope setup, (1) light source, (2) quarter wave plate (2 plates), (3) polarizer, (4) sample, (5,6,7) sample and experimental mounts, (8) analyser and (9) camera [128].

A polariscope consists of a series polarising plates in various arrangements and by adjusting the angle of the phase plate, it changes the fringe pattern being measured [186], [189]. In the case of reflection photoelasticity, a birefringent material is applied to the outer surface with a light layer of reflective paint applied below the birefringent material to increase the amount of light reflected from the sample surface. As the sample deforms, this then deforms the birefringent material producing a representative fringe pattern. In the assessment of the fringes that are generated, there are two classes: Isochromatic and Isoclinic. For Isochromatic, the loci represent the difference in the first and second order principal stresses. The Isoclinic loci point along the principal stresses when they are aligned in the same direction [186], [189]. An example of these fringe patterns for soft tissue substitutes can be seen in Fig: 4-4.

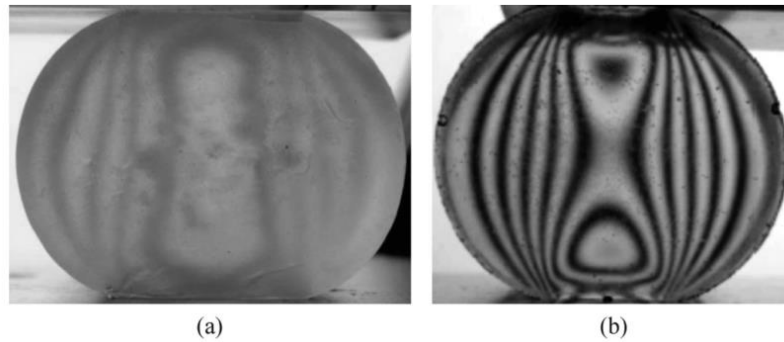


Fig: 4-4: shows an example of two different soft tissue surrogate materials birefringent patterns when under compression loading, (a) konjac gel (plant derived gelatine) and (b) ballistic gelatine (animal derived gelatine) [128].

There are several approaches, including 2D and 3D that either require multiple reflection polariscopes or a transmission polariscope. Stress fixing, which is used to investigate specific loading conditions of 3D samples involves producing a resin representation, loaded with a scaled load and fixed using a thermal setting process which allows the fringe pattern to be assessed without the need to load the sample. By taking a planar slice in the desired cross section, the change in loading throughout the sample can be visualized. Photoelasticity has also seen increased usage in the assessment of soft tissue-like materials such as gelatines for such applications as the study of needle insertion [128]. Photoelasticity has also been used to investigate dynamic crack growth and plate impact. This has been performed at comparable velocities to ballistic impact. The largest restriction to the use of such methods is the inability to work with opaque materials [100], [190], [191].

#### **4.2.3. Marker Tracking**

Markers or point tracking has also been applied for motion tracking often associated with high speed video equipment. The main difference in these tracking approaches relates to the use of an automatic algorithm or manually tracking the points of interest [192]–[197]. In the case of automatic methods, often referred to as motion capture, the body of interest has a series of fiducial markers placed on key points. Fiducial markers are specific objects such as white spheres or coloured dots that are placed at key points to serve as reference markers improving the ability to track motion. This can also include such things as a applied grid pattern that covers an object or body. The experiment is then filmed in the desired manner and the software automatically

identifies the markers and tracks their motion frame to frame. A drawback in this method is the number of cameras and fiducial markers have a direct impact on the quality of the acquired data. Automatic tracking has a reduced cost in time over manually processing, but requires a more complex experimental arrangement and the need to employ specialist algorithms which may need specific software to operate [23], [24], [118], [198]. In the case of the manual method, it involves the researcher manually tracking either by reference of an imposed coordinate system or assisting software to identify the points of interest over the video. This is a very time intensive method, however and often used for validation of many optical measuring techniques.

### **4.3. Theory of image registration**

Image registration is the process of aligning one image to another. These are normally sequential in time, and of the same structure or AOI (Area of Interest). It is a central enabling technology in medical imaging and much effort has been devoted to its development. However, its fundamentals can be applied to mechanical engineering problems and experimentation. Image registration is based on warping an initial image (moving image) so that the corresponding structures are correctly aligned with a second non-moving image (static image) using a transformation function. Transformations include affine, rigid, non-rigid or a combination of approaches which will be discussed in section 4.3.1 [42], [199], [200]. The process optimises the transformation between the images smoothed by a penalty term discussed in sub-sections 4.3.1 to 4.3.3.

#### **4.3.1. Transformation**

The transformation defines the spatial transformation that results from the registration process. As mentioned, there are several different transformation methods which each have a broad range of specific applications and algorithms for the implementation. Rigid transformations focus on matching the images by rotating and translating the moving image [201], [202]. Affine transformation expands on this by adding the capability of scaling the image and applying shear [41], [202], [203]. This work focuses on non-rigid transformation methods, which expands on the rigid methods to allow for stretching and a free-form transformation. This allows the capture of complex differences in the static and moving images. Some examples include spline based and ‘demons’ algorithm [42], [200], [204]. In the case of all

transformation processes, there are two components: firstly, the generation of the registered image transformation, and secondly resampling the image to define the new pixels intensities and positions. This resampling is normally performed using an interpolation function which defines the transformed pixels positions and intensities from the resulted control point transformation, which is then used to generate the resulting registered image.

#### **4.3.2. Penalty Term**

The role of the penalty term is to limit the maximum deformations of the B-spline knots and control points, thereby smoothing the transformation process to remove erratic motion, which will be discussed in section 4.4.1. This is needed as pixels or structures with similar intensity can be misaligned by the transformation or artefacts caused by erratic points of motion between images or which would lead to errors in the registration. Penalty terms are formulated as equations that have a given weight which is specified by the user, and are used to define the level of control the penalty term has on the transformation. Different equations have different weighting terms tailored to best control the formulation, but all serve the same function as above. Examples include Bending Energy Term or the Thin Sheet Elastic Bending Equation [200], [205]–[207].

#### **4.3.3. Optimisation**

The transformation is optimised to achieve the most accurate fit, which is defined by the score that the associated with the similarity measure. The main goal is to achieve the minima or maxima depending on which metric is used, that is possible or in line with user defined values. Many mathematical algorithms have been employed; two such algorithms are Least Trimmed Square (LTS) Regression Method and Quasi Newton Brogden Fletcher Goldfaab Shannon (BFGS) approaches. LTS is an optimisation approach that minimises the effects of outliers of the data set by minimising the sum of squared values within a defined region to minimise the influence of outliers and determine optimal value for each region, making it a highly robust optimisation algorithm. BFGS is a quasi-Newtonian method which is a hill-climbing optimisation that seeks a stationary point defined function, where the optimal has a gradient of zero. It is limited due to the lack of guaranteed convergence if the function itself has a Taylor expansion near its optimum. However, it has proven to have good optimisation performance even over data sets that are not smooth. The specific approach differs from toolkit and application but performs a similar function



[55], [56], [203]. This can be controlled by adjusting the number of iterations that the optimiser performs. It should be noted that in this work it was found that a large number of the toolkits employ a pyramidal approach of the LTS method, where each level applies a progressively finer grid pattern or control point arrangement at each optimisation step. At each step the previous transformation is used to initialise the next step so the previous transform is applied to the grid which is then further transformed to achieve the optimal transformation possible. This helps to produce a more optimal transformation.

#### 4.4. Project registration method

For this work, free-form deformation (FFD) was used in which a B-spline grid is specified by control points arranged in a grid over the image. The transformation is defined by the optimised parameters of the positions of the B-spline control points, and between the control points, the knots define the specific shape of the B-spline curve between two points [200], [208]. This is a general-purpose algorithm as it makes no assumptions about the physical structures in the images and may impose few constraints on the deformation. It also assumes that all transformations that occur in the registration are continuous deformation over time. In the case of chaotic materials or materials that have the possibility for delayed response, the selection of the time step is important to minimise error. So for penetrating impact, the smallest time-step between the images will maximise the registrations ability to identify small motions across all images and allow the identification and tracking of chaotic behaviour [200], [206], [209]. General-purpose algorithms provide flexible transformation models that allow reproduction of complex deformation fields, which can identify very fine structures in the images [42], [52], [210], [211].

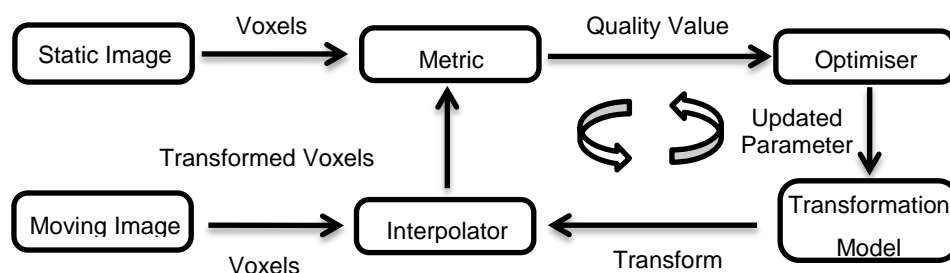


Fig: 4-5: Graphical representation of the image registration process, created by the author showing a flowchart representation of how the registration algorithm generates the optimal transformation. Once the optimal value has been reached, it is then used to generate the registered image [101].

#### 4.4.1. B-spline formulation

The initial B-spline control point coordinates  $\mathbf{c}_i$ , and the transformed control point position after the optimisation has been performed are used to define the position of the B-splines knots positioned between connected control points as seen in Fig: 4-6 [200]. The general formulation is given by equation (22).

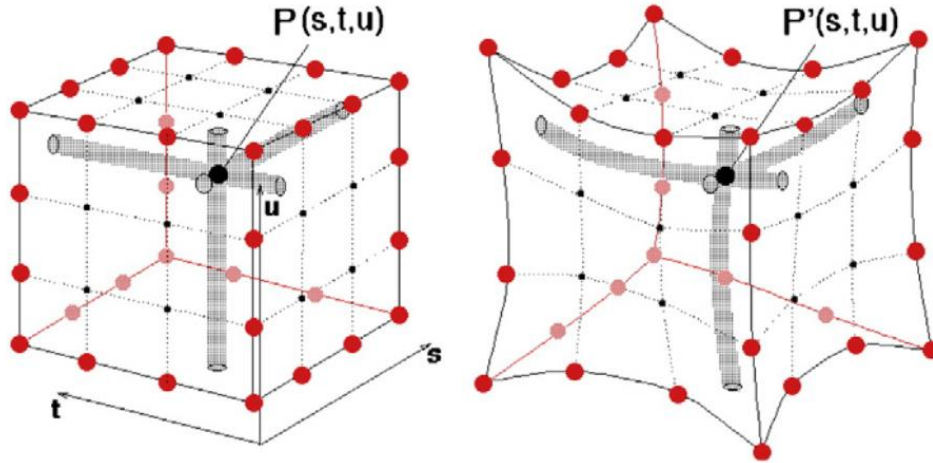


Fig: 4-6 Is an example of free-form deformation using B-splines showing how the grid of control points (black and red points) is distributed in the 3D space defined by  $(s, t, u)$ . The B-splines are the lines that connect the points. The motion between  $P(s, t, u)$  and  $P'(s, t, u)$  is smoothly interpolated to allow capture of the transformation while maintaining the splines and control point connections, the spline allowing the smooth curved deformation in the region between the defines points [45].

$$\mathbf{T}(X) = \sum_{i=1}^n B_{i,d}(t) \mathbf{c}_i \quad (22)$$

$\mathbf{T}(X)$  is the curve deformation,  $B_{i,d}$  the basis spline function and  $\mathbf{c}_i$ , as mentioned, represents the explicit control point coordinates. This means the parameter  $(t)$  is a special coordinate and is shown in the simplified piecewise B-spline basis functions to be assumed to be  $[0,1]$ . The basis functions are shown below in equations (23) to (26):

$$B_3^0 = \frac{(-t^3+3t^2-3t+1)}{6} \quad (23)$$

$$B_3^1 = \frac{(3t^3+6t^2+4)}{6} \quad (24)$$

$$B_3^2 = \frac{(-3t^3+3t^2+3t+1)}{6} \quad (25)$$

$$B_3^3 = \frac{t^3}{6} \quad (26)$$

Equations (23-26) are the cubic B-spline basis functions for a single axis transformation. The transformation in two axis is given by equation (27) [200]. The use of B-spline adds the advantage that changing control point spacing will only affect the local neighbourhood of B-spline knots, which will result in greater accuracy as the number of control points for a given area to define the transformation is larger.

$$\mathbf{T}(X) = \sum_{l=0}^2 \sum_{m=0}^2 B_l(u)B_m(v)\mathbf{c}_{i+l,j+m} \quad (27)$$

In this equation the two axis are defined by the subscripts  $l$  and  $m$ , with each of the axis using the cubic formulation of the B-spline basis function described above to determine the transformation in two axis. 3D transformations add a third set of basis functions for the third axis.

#### 4.4.2. Similarity Metrics

The similarity metric assesses the degree of similarity of the transformed image and static image until it reaches the optimal value as calculated by the similarity metric. This optimised transformation is used to produce the registered image. A range of similarity metrics that have been used in various applications was considered for this thesis.

##### 4.4.2.1. Pattern Intensity

$$P_{r,\sigma}(s) = \sum_{i,j} \sum_{d^2 \leq r^2} \frac{\sigma^2}{\sigma^2 + (I_{dif}(i,j) - I_{dif}(v,w))^2}, \quad (28)$$

PI (Pattern Intensity) is a regional pixel method that identifies patterns defined by the weight function in a defined region around each pixel in the image, as seen in equation (28).  $r$  defines region size,  $\sigma$  is constant variance function and defines if

the grey value is a structure, which is a range of pixels grouped together with intensity with the value specified by  $\sigma$ .  $I_{dif}$  is difference image,  $d = (i - v)^2 - (j - w)^2$  is the radius from voxel;  $i, j$  coordinates of current voxel and  $v, w$  coordinate of voxel being compared to current the voxel at radius  $d$  [41], [212]. This metric has a good robustness in the detection of large motion between images which are expected in this work [27], [213], [214]. The metric is also robust when dealing with large intensity difference between the pixels where the value of the difference is based on the intensities of the captured value. An example in a greyscale image would be pixels with values near 1.0 (white), which are close to pixels with a value near 0.0 (black), normally, a similarity would be dominated by the higher value pixels. However, PI defines the two different values as different objects and hence tracks both with the same accuracy.

#### 4.4.2.2. Sum of Squared Difference

The SSD (Sum of Squared Difference) metric has been used for multiple applications that include large and small deformation. It is a general measure so it can be applied to a wide range of images [42], [212], [215]. The specific formulation used in this work is given as:

$$SSD = \sum_i I_{dif}(x_i, y_i), \quad (29)$$

$$I_{dif} = (I_t(i, j) - I_s(x + i, y + j))^2, \quad (30)$$

$I_{dif}$  is the difference between the current transformed image  $I_t$  and the static or reference image defined by  $I_s$ . Where  $i$  and  $j$  as,  $i = x_m + x_t$  and  $j = y_m + y_t$ .  $x_t$  and  $y_t$  is the transformation at each pixel and  $x_m$  and  $y_m$  is the pixels in the moving image.  $I_s$  represents the static image where  $x$  and  $y$  are the pixel coordinates for that given image. The terms  $x_i$  and  $y_i$  are the position of the pixel over both images. This metric aims to reduce the difference between the images by making the transformed image as similar as possible to the static image [55], [210], [212], [216].

#### 4.4.2.3. Gradient Difference

GD (Gradient Difference) calculates the differences in the image gradients. Calculated by first considering the separate image specific gradient, it compares between the current transformed image and the static image [216]–[219]. The metric is given in equation (31) to (35):

$$GD_{(s)} = \sum_{i,j} \frac{A_v}{A_v + (I_x(i,j))^2} + \sum_{i,j} \frac{A_h}{A_h + (I_y(i,j))^2} \quad (31)$$

$$I_x(i,j) = \frac{dI_{static}}{di} - S \frac{dI_{moving}}{di} \quad (32)$$

$$I_y(i,j) = \frac{dI_{static}}{dj} - S \frac{dI_{moving}}{dj} \quad (33)$$

In the equations above,  $A_v$  and  $A_h$  are normalization constants and the variance of represented by  $I_x$  and  $I_y$  respectively. In this case, considering the variable  $S$  is the mean of static image divided by the moving image. From this, the metric can relate the gradient of the image and the magnitude of the intensity [41], [212], [216], [220]. From literature, it has been shown to have limitations where large intensity differences are present in the images as these dominate the mean calculated [41], [216], [220].

#### 4.4.2.4. Normalised Cross Correlation

NCC (Normalised Cross Correlation) is another similarity metric which is based on the intensity of the images when comparing the static and moving images. It uses the following formation (please note that in this case, a bar over a variable represents the mean of that variable) [141], [160], [221]:

$$NCC = \frac{\sum_{i,j} (I_{static}(i,j) - \bar{I}_{static})(I_{moving}(i,j) - \bar{I}_{moving})}{\sqrt{\sum_{i,j} (I_{static}(i,j) - \bar{I}_{static})^2} \cdot \sqrt{\sum_{i,j} (I_{moving}(i,j) - \bar{I}_{moving})^2}} \quad (34)$$

$\bar{I}_{moving}$  and  $\bar{I}_{static}$  are the mean of the images which are reliant on the intensity of the images. This means the metric is highly susceptible to high pixel intensities values in greyscale images with a value close to 1.0. These areas that are dominated by a high value of intensity and will dominate the response which can lead to the loss of information in the areas surrounding high intensity regions, which can cause errors in the registration or loss of detail in the transform [41], [212].

#### 4.4.2.5. Gradient Correlation

A second gradient based method is GC (Gradient Correlation). Initially, the vertical and horizontal sobel template are used to inform the gradient of the images components given by  $dI_{static}/di$ ,  $dI_{static}/dj$ ,  $dI_{moving}/di$  and  $dI_{moving}/dj$ . A sobel is a specified matrix that is used to enhance image edges or distinct boundaries. These equations use a 2D formulation with two 3x3 matrixes, for 3D formulation there would be three 3x3 matrixes. Specific formulations of the algorithms can vary the size of the matrix by adding or removing information. For this function, the sobel matrices are given below by equation (35) and (36) [212], [222].

$$Sobel_x = \begin{bmatrix} 1 & 0 & -1 \\ 2 & 0 & -2 \\ 1 & 0 & -1 \end{bmatrix} \quad (35)$$

$$Sobel_y = \begin{bmatrix} 1 & 2 & 1 \\ 0 & 0 & 0 \\ -1 & -2 & -1 \end{bmatrix} \quad (36)$$

$dI_{static}/di$ ,  $dI_{static}/dj$ ,  $dI_{moving}/di$  and  $dI_{moving}/dj$  represent the intensity gradient in the two orthogonal axes in the images that are being registered. Using the gradients above, the following equations are used. The bar above the variable represents the mean of the variable [218]–[220], [223]:

$$GC = \left( \frac{R1+R2}{2} \right) \quad (37)$$

$$R1 = \frac{\sum_{i,j} \left( \frac{dI_{static}(i,j)}{di} - \bar{\frac{dI_{static}}{di}} \right) \left( \frac{dI_{moving}(i,j)}{di} - \bar{\frac{dI_{moving}}{di}} \right)}{\sqrt{\sum_{(i,j)} \left( \frac{dI_{static}(i,j)}{di} - \bar{\frac{dI_{static}}{di}} \right)^2} \cdot \sqrt{\sum_{(i,j)} \left( \frac{dI_{moving}(i,j)}{di} - \bar{\frac{dI_{moving}}{di}} \right)^2}} \quad (38)$$

$$R2 = \frac{\sum_{i,j} \left( \frac{dI_{static}(i,j)}{dj} - \bar{\frac{dI_{static}}{dj}} \right) \left( \frac{dI_{moving}(i,j)}{dj} - \bar{\frac{dI_{moving}}{dj}} \right)}{\sqrt{\sum_{(i,j)} \left( \frac{dI_{static}(i,j)}{dj} - \bar{\frac{dI_{static}}{dj}} \right)^2} \cdot \sqrt{\sum_{(i,j)} \left( \frac{dI_{moving}(i,j)}{dj} - \bar{\frac{dI_{moving}}{dj}} \right)^2}} \quad (39)$$

This method draws heavily from NCC. This means that it shares the inherent weakness in terms of its reliance on image intensity that is affected by large variations in image intensity as with the previous method [41], [212], [218], [219].

#### 4.4.2.6. Normalised Mutual Information

NMI (Normalised Mutual Information) is a multimodal approach, which means it can be applied to image pairs that have been captured using different methods for example an ultrasound image and an X-ray image. This metric uses the concept of joint entropy between the two images and this can be described by the formulation given in equations (40) to (42).

$$H(A) = -\sum_a p_A(a) \log p_A(a) \quad (40)$$

$$H(B) = -\sum_b p_B(b) \log p_B(b) \quad (41)$$

$$H(A, B) = -\sum_{a,b} p_{AB}(a, b) \log p_{AB}(a, b) \quad (42)$$

The marginal and joint probability distributions of the image intensity values are defined by  $p_A(a)$  and  $p_{AB}(a, b)$ . Both distributions are calculated by the normalization of the 2D joint histogram  $h(A, B)$  which contains intensity and identity of all pixels in the image and identify those that are the same in each image [41], [212], [224]. This is used to in the formulation of the NMI similarity metric given in equation (43).

$$NMI = \frac{H(A)+H(B)}{H(A,B)} \quad (43)$$

$H(A)$  is the entropy of  $I_{transform}$  and  $H(B)$  is the entropy of  $I_{moving}$  and the joint entropy of the two images is represented by  $H(A, B)$ . It should be noted that if the image is coloured, the metric consider both the hue and intensity. The metric uses the approach that assumes there is not a linear relationship between the pixel intensity and position between the two images. It uses the probability mentioned before to assume there is co-occurrences of the most probable value and this is maximised by the registration process [41], [207], [212], [225].

## **4.5. Calculating displacement and strain from image transformation**

As the aim of this work is to identify the suitability of image registration as a method for the quantification of displacement over a given time period, there was a need to consider a method that can be applied over multiple consecutive images to construct a dynamic deformation over time. In this work, this is consecutive frames that will be recorded during the proposed experiments. The following work expands on the pair-wise method that has been discussed in 4.3, by describing a method that allows for the composition of multiple pair-wise transformations that are sequential in time producing a dynamic displacement over the course of the experiment alongside a methodology for the assessment of the strain which results from the displacement generated by the experiment.

### **4.5.1. Composition of displacements from consecutive registrations**

Calculating the cumulative displacement is not a straight forward process as directly summing the individual registered transformations does not produce the equivalent to the overall transformation for a given set of images. This stems from how the registration is calculated. In the first instances, as described earlier, the position of the control point grid is defined based on a coordinate system for that specific registration. For example, the bottom left corner of a 2D image will be the origin and the control points each having a defined x,y coordinate. As the transformation is optimised, the algorithm calculates how the control points move, tracking the motion in the image as discussed in 4.3 and 4.4. Fig: 4-7 shows this with the example of tracking showing how a square is deformed over two registrations consecutive in time. Even though in the image the object has deformed and the deformation registered, the next pair-wise registration will not use the previous registration as the coordinate system. In the next registration, when the algorithm defines the control point position, it will again define the origin in the bottom left corner and assume there has been no deformation or transformation occurring before. This means even though the motion in the each image pair is consecutive, each registered displacement is calculated as an independent pair of images not consecutively over image pairs. This means if they are summed, the origin point of each of the registered displacement is defined differently, which means the value for each pixel displacement is not comparable as they are defined by the different origins.



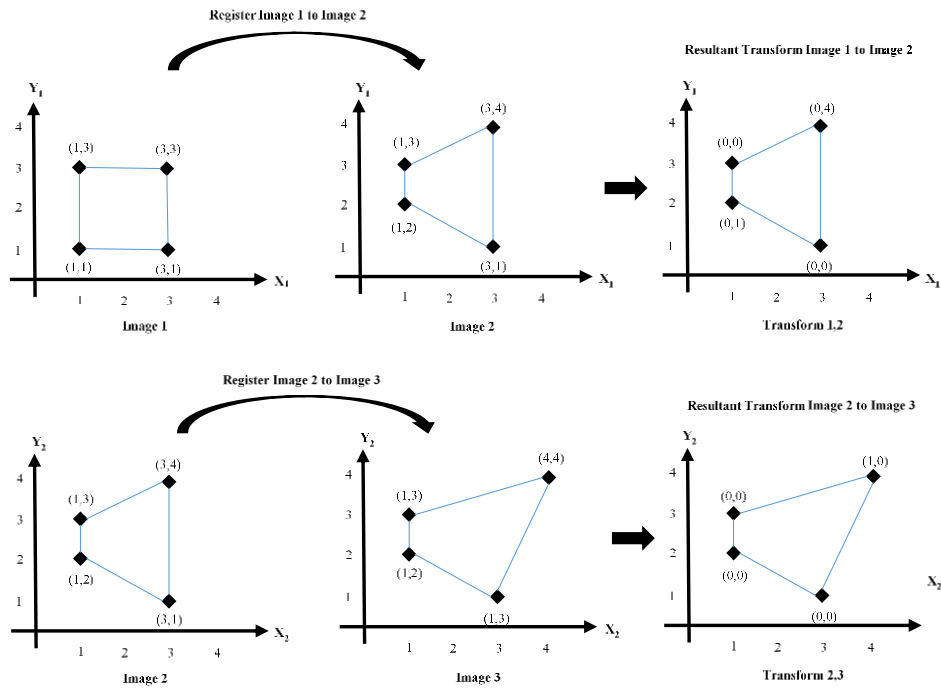


Fig: 4-7: Shows how each pair-wise registration defines its own independent initial coordinate system from the floating image. The resultant transformation is defined by the motion of the specific coordinate system as the transformation is optimised to give the new control point positions for that given pair-wise registration process. Consecutive registration will use independent coordinate systems to determine the optimal transformation.

A common method which is used to determine the cumulative displacement is to compose the B-spline transformations. This involves consecutively applying the pair-wise registered transformation in relation to a known control point grid. This methodology has some limitations as it requires a pixel-wise local transformation at the current point in time to be calculated from the B-spline transformation for the pair-wise registration, which, if any error is present (due to registration artefacts or poor overall registration), will directly impact the composition of the pair-wise transformations. This can limit the output as there is an induced error which limits the possible accuracy as the composition method itself includes an interpolation step which will lead to a rounding or constraint on the movement of the composed transformation [226]–[228].

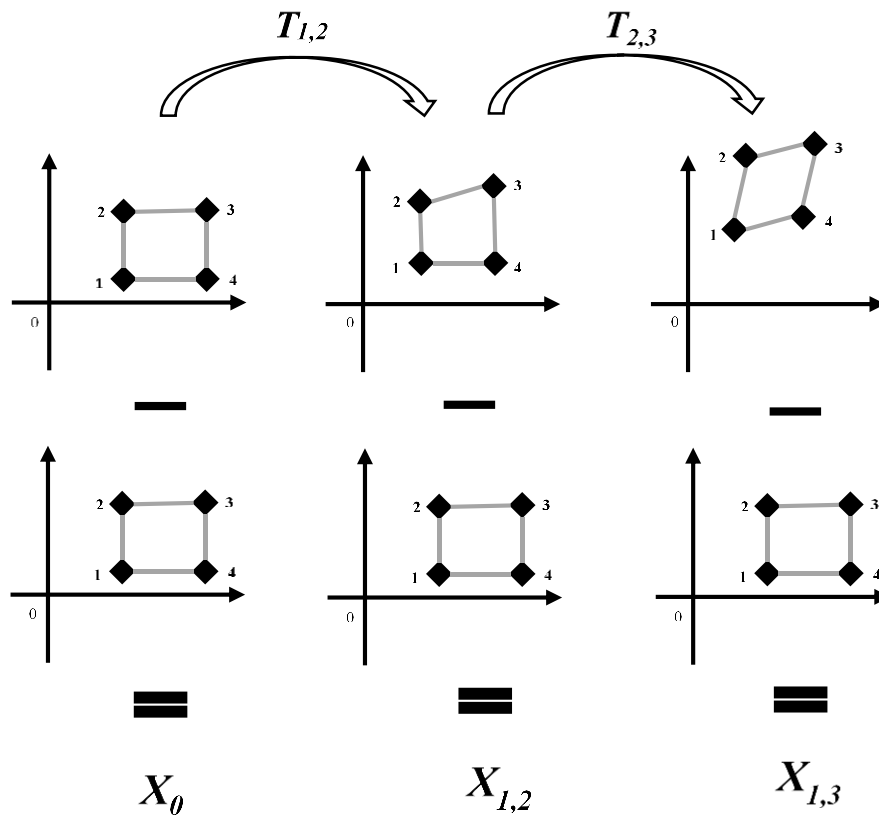


Fig: 4-8 The composition of the pair-wise transformation over two consecutive registrations using a user defined initial coordinate system were the B-spline registered transformation from Registration 1,2 ( $T_{1,2}$ ) is applied producing the displacement  $X_{1,2}$ . Then the second registrations R2,3 B-spline transformation ( $T_{2,3}$ ) is applied producing  $X_{1,3}$ .

In this work, a three step process was used which addresses the issues encountered above. The initial step is to extract the pixel-wise local transformation from each registration, then to generate an initial coordinates system represented by an  $n \times m \times 2$  matrix representing the x coordinate and y coordinate at the initial point in time. The pixel wise transformation is then applied consecutively to the initial coordinate system. This produces the changing coordinates for any given pixel in relation to the initial coordinate system. The displacement is then extracted by subtracting the initial coordinate from the current coordinates. This process can be seen in Fig: 4-8 and is described in the equations below.

$$X_{(1,2)} = T_{(1,2)}(X_{(0)}) \quad (44)$$

$$\mathbf{X}_{(1,3)} = T_{(2,3)}(\mathbf{X}_{(1,2)}) = T_{(1,3)}(\mathbf{X}_{(0)}) = T_{2,3}(T_{(1,2)}(\mathbf{X}_{(0)})) \quad (45)$$

In a general formulation, it can be written as follows:

$$\mathbf{X}_{(1,m)} = T_{(n,m)}(\mathbf{X}_{(n-1,m-1)}) \quad (46)$$

There are two inherent sources of error that will have an effect on the accuracy of the method which have been discussed above. These are based on the individual pair-wise registrations as any error that is present in the pair-wise registration will be applied to the composed transformation, which will result in a compounding effect on accuracy of the composition. This error in accuracy will come from the registration method itself which will include the overall accuracy of the registration and the impact of any artefacts or misalignments which are present in the pair-wise transformation which can be further compounded by minor errors in the interpolation process for defining new pixel positions and intensities. The limitation of the transformation algorithm is inherent and can be minimised by again maximising the image registration accuracy and defining the optimum interpolation parameters. The composition itself has two key aspects that can induce error: the first is, as with the pair-wise transformation, the composed transformation which uses an interpolation process to define the new pixel positions so the same method for minimising errors discussed above. Furthermore, any error that is already in place in the pair-wise registration will be compounded over the subsequent composition.

Mitigating these errors can be achieved by maximising image resolution in the collection of the experimental data, and ensuring that the optimal registration parameters are used to minimise the registration error. The induced error due to the interpolation is more difficult to account for. However, this should be minimal as the more accurate the transformation and the finer the control point that was used in the generation of the transform, the finer the B-spline and the reduced need for the interpolator to account for artefacts in the transformation. These steps will be used to achieve the best possible accuracy when applied to the experiments that will be undertaken.

#### 4.5.2. Calculating Strain

The Eulerian strain tensor (44) [229] was used to define the strain and the formulation can be found below:

$$\mathbf{F} = \nabla \mathbf{u} + \mathbf{I} \quad (47)$$

$$\boldsymbol{\varepsilon}(\mathbf{X}, t) = \frac{1}{2} \left[ \mathbf{I} - (\mathbf{F}^{-1}(\mathbf{X}, t))^T \cdot \mathbf{F}^{-1}(\mathbf{X}, t) \right] \quad (48)$$

For equation (43),  $\mathbf{F}$  represents the deformation gradient,  $\nabla \mathbf{u}$  material deformation gradient tensor and  $\mathbf{I}$  is the identity tensor.  $\boldsymbol{\varepsilon}$  is the strain tensor where  $\mathbf{X}$  represents the current coordinates and  $t$  is the current point in time.

$\mathbf{I}$  is the spatial velocity tensor, formed using the deformation gradient tensor. This allows an Eulerian term to be calculated from the Lagrangian variable using equation (45) where  $\dot{\mathbf{F}} = D\mathbf{F}/Dt$  defines the value of *change of the deformation* gradient tensor. The dot representing the derivative of the term:

$$\mathbf{I} = \dot{\mathbf{F}} \cdot \mathbf{F}^{-1} \quad (49)$$

Using this formulation, the velocity can be decomposed in to two components: the symmetric and anti-symmetric, expressed in equation (46).

$$\mathbf{I} = \frac{1}{2}(\mathbf{d}) + \frac{1}{2}(\mathbf{w}) \quad (50)$$

The 1<sup>st</sup> component is called the Rate of Deformation Tensor which can be called the Rate of Strain Tensor. The formulation, in terms of the spatial velocity vector, is given in equation (47) and is given in its differential formulation in (48).

$$\mathbf{d} = \frac{1}{2}(\mathbf{I} + \mathbf{I}^T) \quad (51)$$

$$\mathbf{d} = \begin{bmatrix} \frac{\partial v_x}{\partial x} & \frac{1}{2} \left( \frac{\partial v_x}{\partial y} + \frac{\partial v_y}{\partial x} \right) & \frac{1}{2} \left( \frac{\partial v_x}{\partial z} + \frac{\partial v_z}{\partial x} \right) \\ \frac{1}{2} \left( \frac{\partial v_y}{\partial x} + \frac{\partial v_x}{\partial y} \right) & \frac{\partial v_y}{\partial y} & \frac{1}{2} \left( \frac{\partial v_y}{\partial z} + \frac{\partial v_z}{\partial y} \right) \\ \frac{1}{2} \left( \frac{\partial v_z}{\partial x} + \frac{\partial v_x}{\partial z} \right) & \frac{1}{2} \left( \frac{\partial v_z}{\partial y} + \frac{\partial v_y}{\partial z} \right) & \frac{\partial v_z}{\partial z} \end{bmatrix} \quad (52)$$

The second component is the anti-symmetric component and is called the Spin Tensor  $\mathbf{w}$  given by (49).

$$\mathbf{w} = \frac{1}{2}(\mathbf{I} - \mathbf{I}^T) \quad (53)$$

#### 4.6. Discussion

From the review of other optical methods, it can be seen that image registration shares similarities with currently used optical-based mechanical measuring techniques. This helps to support this thesis's proposition that this method can be used for the quantification of the deformation of mechanical experimentation. This chapter focused on establishing the core theory of image registration which will be applied to the work undertaken in this thesis. The chapter was able to highlight the flexibility presented by the wide range of algorithms that are available. This flexibility derives from the wide range of transformation, optimisation and penalty terms that are available and allows the tailoring of the method to the specific experiment or video capture method.

The greatest experimental benefit that has been identified is that image registration images do not require specialist equipment or preparation for the recording of experimental when compared to the other methods. When considering all of these aspects, this clearly demonstrates that image registration is a comparable method to DIC and Photoelasticity for the quantification of displacement for mechanical testing, considering the method discussed above in section 4.2.

In terms of the impact on the proposed work, this chapter has proposed a method for the application of image registration to be performed over sequential images and with the transformation composition method describes how a transformation across the images in time can be achieved with the need to maximise the accuracy of the generated transformation from the initial registration and hence improve the composition of the consecutive transformation. Depending on the software or toolkit

that is selected to undertake the registration, it may not have all the necessary functionality. This was addressed when identified during later chapters and if required, all equations or scripts that were generated will be discussed.

## **Chapter 5. Assessment of registration-based measurements of displacement and strain**

*Please Note: This chapter has work published in the following [101]*

### **5.1. Introduction**

This chapter aims to identify an optimal set of image registration parameters for the toolkits discussed in Chapter 4. Using them as an initial starting point will allow further refinement to be applied for use with the experimental test footage that was collected. This will identify any particular aspects that need to be considered in the assessment of the final experimental registrations, or that should be accounted for in the experimental arrangement, including maximising the clarity and quality of the images collected and the optimised software parameters. To assess the output, a combination of both qualitative and quantitative approaches will provide the most effective method to assess if the pair-wise image registration was successful alongside comparing the displacement field generated from the composition of the pair-wise transformations to a computational model of the experiments using the material characterisation parameters described in Chapter 3 to validate the output.

To ensure the effectiveness of the method when applied to the quantification of mechanical displacement during penetrating impact, this chapter presents the result of applying the registration framework to uniaxial indentation tests using ballistic gelatine as the specified tissue surrogate. This simpler arrangement allows a much more in depth analysis of the registration output and the use of the computational model to validate the output. This is supported by testing of the specific toolkit's accuracy and registration response, using user-generated images that represent the approximate cavity motion of the penetrating process. This forms a usable starting point to investigate the toolkit's response, as using experimental data would greatly increase the difficulty and not allow accurate analysis as the deformation between experimental images would not be known. Furthermore, to allow an in depth analysis of the image registration output, it is logical to first investigate if the image registration is applicable for a slower simpler experimental arrangement. Uni-axial compression was selected as it shares several similarities to the types of motion that occur during the initial indentation before penetration but at a greatly reduced speed. By testing this arrangement at a quasi-static loading regime, it simplifies the experimental arrangement and allows the results of the registration to be validated using the uni-axial material parameters that have been identified in Chapter 3, increasing the confidence in the results acquired, while enabling the specific investigation of the most effective camera arrangement that can be applied to the

penetrating impact test including lighting, frame size and camera position. This slower strain rate would seem to be disjointed considering the aim is to use image registration for penetrating impacts, but the quasi-static speeds investigated are actually comparable to the later settling and relaxation response that occur after penetration and rebound. This will then also further enhance the outcome of the project as it allows the method to be used to identify this longer term response of the gelatine after impact which was discussed in Chapter 2 and Chapter 3.

## 5.2. Outline of image registration frame work

As discussed in [101], this thesis outlines a framework for the application of image registration to the quantification of displacement in penetrating impact on ballistic gelatine tissue surrogate. This follows a two stage process: first, defining the pair-wise registration and secondly, the composition of the transformation over the course of the extracted pair-wise transformations for the given number of frames. The process is highlighted in the figure below Fig: 5-1. This builds on the theory that has been described in Chapter 4.

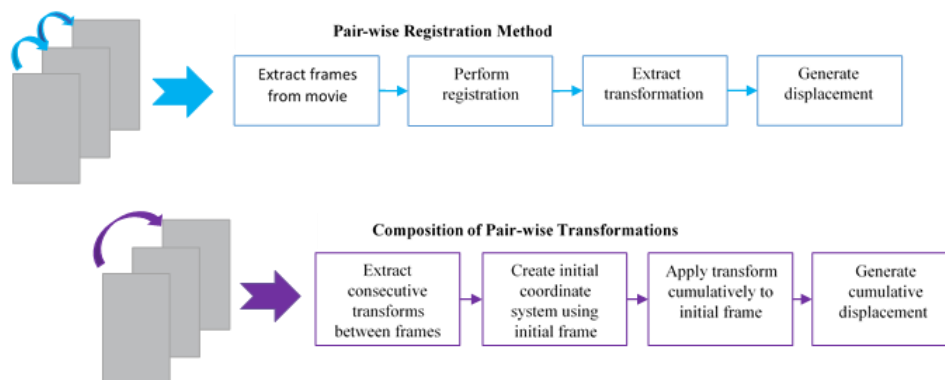


Fig: 5-1: Process layouts of the two methods that form the basis of the registration method, including the pair-wise registration and the composition of the pair-wise transformation to produce the cumulative deformation over the experimental data captured.

This chapter applied the method shown Fig: 5-1 to a series of indentation tests that will be conducted at speeds of 10 mm/s using the same Tinius Olsen machine used in Chapter 3, but without any rapid changes in the direction that was identified to induce output errors in experimental data. For the specific method used, please see section 5.4.2 where it is explained in detail. There are a large number different registration toolkits available, including the software packages available in GIMIAS



and the inbuilt registration function in Matlab [230], [231]. These vary in software platform application, specific function and options available for the optimisation of the registration process. As the user may have access to or be familiar with a specific toolkit, the methodology described below can be applied with compatible registration toolkits that have a similar structure to those described in Chapter 4.

Two toolkits were considered in this project. They were selected due to ease of use and accessibility of the toolkit and required software to operate the toolkit. Firstly, this work consider a Matlab based toolkit called ‘Non-Rigid Version23; B-spline Grid, Image and Point based Registration’, which has a large degree of flexibility with a range of similarity metrics along with the capability to adjust B-spline options and to apply masks and other image modification tools [212].

The second toolkit considered is a C++ based toolkit called `nifti_reg`, which has a wide range of parameters to optimise the registration centring on various possible penalty terms and image-based manipulation. This includes the use of initialisation of the transformation allowing the use of a pre-existing transformation to define the start of the registration process. The range of the similarity metrics is smaller in comparison to the Matlab based toolkit but has finer control over the smoothing and penalty weighting [203], [232]. This toolkit also provides several contained functions that can be used to generate displacement or a specific affine registration. A list of the available options for each toolkit can be seen in the appendix in section 9.1.

In the application of the image registration methodology, a three step process was employed. This corresponds to the major steps that need to be undertaken to extract the results desired. The initial pre-processing of the captured raw data was followed by the pair-wise registration of consecutive images in time from the captured data. It finished with the composition of the resulting pair-wise local transformations. The pair-wise and composition steps have previously been outlined in Fig: 5-1.

### **5.2.1.Pre-processing of captured data**

The pre-processing is dependent on the exact method of image capturing, as specific cameras or experimental method/arrangement will define the specific needs or challenges accounted for during the pre-processing. This is also informed by the software package used to extract the images from the recording device, as this will often define the image format or file type necessary as input for the registration method. The main goal of the pre-processing stage is to identify the ROI (Region of Interest). The ROI is the region in the image that contains the information that is

being investigated; in this case, the indentation that is being assessed and the wider motion of the gelatine. Removing the pixels not in the ROI can reduce computational cost for the registration.

This work uses the CineView software as it has all the necessary tools and is also the software produced by the manufacturers of the camera equipment that has been proposed to be used. Initially, the ROI was extracted out of the captured experimental footage. The simplest method to achieve this was to use the last frame in the movie sequence to define this ROI as this represents the maximum deformation. This area was then extracted from each frame using an inbuilt tool in the software. Most software will have a function to apply the same cropping to all frames allowing this method to be used with other camera technology. Once this was generated, further post-processing was applied to enhance the contrast and gain to maximize clarity of the information in the images. This adjustment was the same for each experiment within a testing session. However, it did differ by small margins depending on the ambient light conditions across different testing sessions. This does not impact the image positions while still enhancing the image definition between objects and textures. Images from the films were then converted to the .tiff format needed for the registration using a custom script to convert from the CineView software format to the input format needed for the registration. The footage was recorded on a Phantom V210 digital high-speed camera recording grey-scale images where the intensity value of white is equal to 1 and black equal to 0. The gelatine block produced was a 6.2 cm cube and the grid pattern injected into the gelatine. For specific information, please see section 5.4.2.

Please see overleaf for Fig: 5-2 and Fig: 5-3.

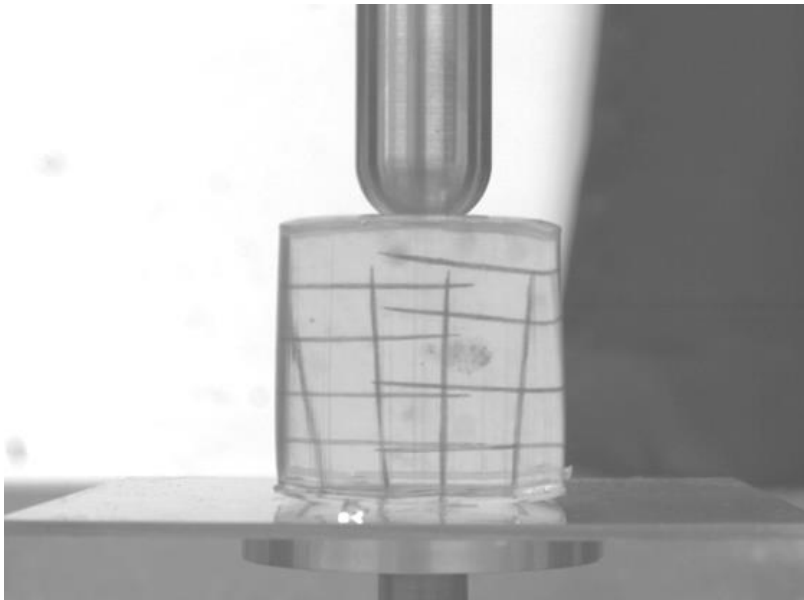


Fig: 5-2: Example of the image recorded on the Phantom V210 camera of the 3 cm diameter indenter and the gelatine sample with injected grid pattern before pre-processing of the image data. The image shown is the initial image from the data capture before loading occurred.

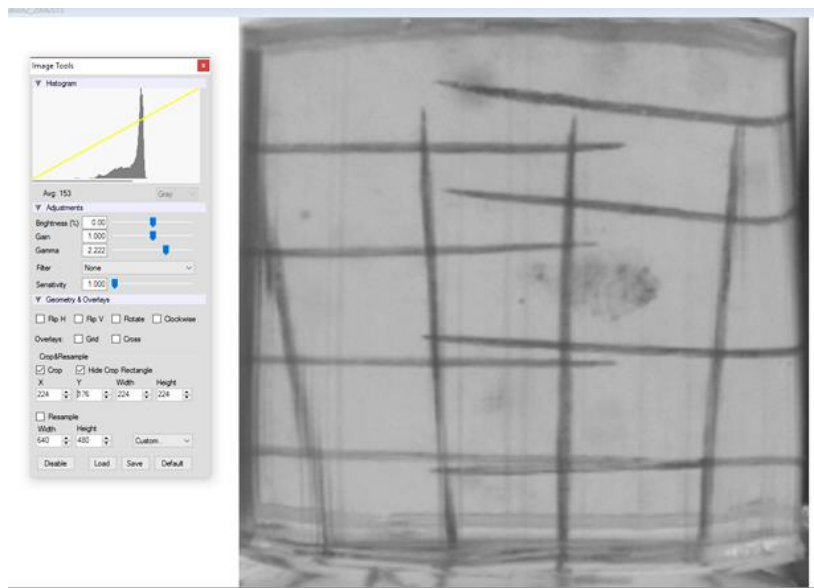


Fig: 5-3: The indentation data capture opened in the CineView software. The upper image shows the initial frame of the capture and the lower image shows the cropping which selects the ROI removing the unnecessary image data and the image manipulation interface of the CineView Software tool as shown on the left of the window to adjust the gain and intensity of the recorded images [233].

In this pre-processing phase, the vast majority of lens effects can be removed if the ROI is approximately central in the image. Lens effects are present in all images that are recorded using camera equipment. In the case of digital filming equipment, this is restricted to two core reasons: The first and most noticeable is distortion that is

induced by the shape or clarity of the lens including marks or dirt that will result in image blur or anomalies such as black dots or streaks. In the case of marks or dirt, regular cleaning and careful handling of the lens will minimise or even negate this. The second is the distortion due to the shape of the lens and focal length which is difficult to avoid. This is divided into two types of distortion that are commonly defined as barrel or pin cushion effect which can be seen in Fig: 5-4 [234]–[236].

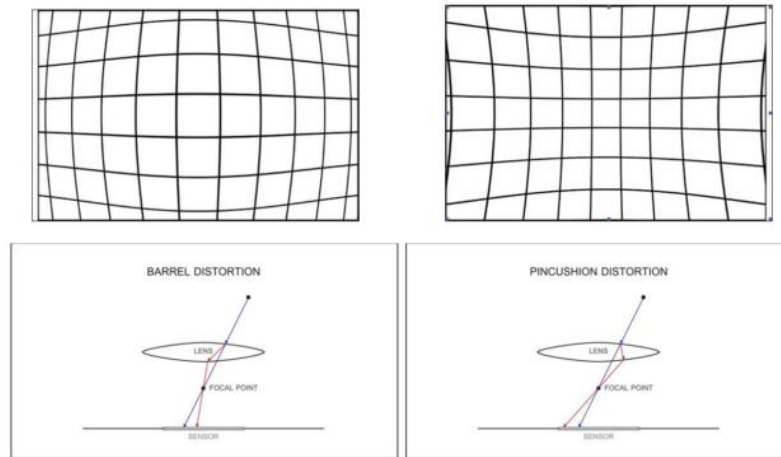


Fig: 5-4: Depicts examples of barrel distortion on the left and pin cushion distortion on the right. This shows clearly how this distortion would impact any attempt to quantify deformation from images subjected to this distortion [234]–[236].

Lens effects can result in progressively greater distortion the greater the distance from the centre of the image captured when using the lens. In the case of barrel effects, lines will appear to bend closer to the edge in the image. This is normally more associated with wide angle lens and focal lengths. In the case of the pin cushion effects, the image appears to be compressed at the centre, normally associated with telephoto focal lengths [234], [235], [237]. Several methods have been proposed to identify the magnitude of lens effects for a given lens and recording arrangement. In this work, it was prudent to investigate lens effects for each experimental arrangement used. The method used replicated the focal length and the distance from the lens to the sample and imaged a grid of known size. A black and white checkerboard pattern with 19 mm x 19 mm squares was used. By investigating any change in size of the imaged grid pattern and the position of the grid in the image, it is possible to identify if lens effects were present, and if present the level of severity could be investigated. This was selected as it allowed a maximum number of squares in the image but still allowed accurate measurement.

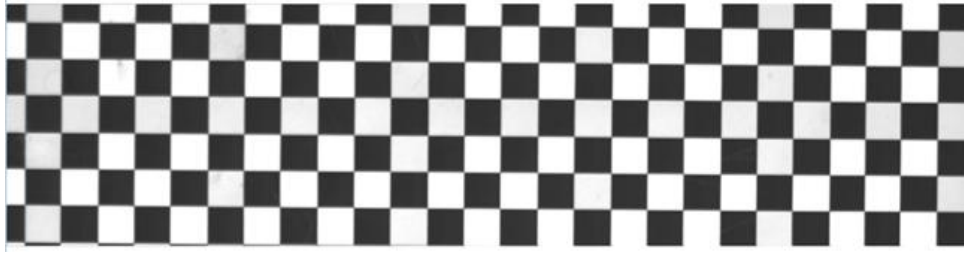


Fig: 5-5: Experimental image of the grid pattern used to investigate the possible impact of lens effects. Taken at one of the series distances from camera for the defined camera arrangement used for the penetrating impact tests (40 cm from camera to the grid pattern) and match focal lens and aperture.

As mentioned earlier, cropping can assist in minimising the likely impact of lens effect both barrelling and pin cushion. If the ROI is central to the image, removing the outer area of the image improves the result as this is the area where lens effects will be present. By ensuring that the ROI is in the centre of the image and with the camera positioned to allow this, minimal focus adjustment will reduce any possible lens effects. In this work, the filming equipment used was a Phantom V210 Digital High-speed Camera with a SLR Nikon Nikkor 24-85 mm Focus 2.8-4 mm DIFAF lens. Using the Phantom Cine software allows control of the specific image resolution of the digital photo-sensor contained in the camera. For every new camera arrangement, an image test was performed to identify possible errors or distortions.

Throughout all the testing in this thesis, it was found that by using this method, lens effects had a minimal impact on the ROI. Over each of the camera arrangements tested, it was found that in all axis of the image, the grid pattern showed no distortion in the large majority with only the outer most grids showing a slight variation that could be seen. It was found that it was of high importance to ensure the lens was cleaned regularly between tests, ensuring the camera arrangement was positioned to avoid large amounts of focussing and centrally position the detector in relation to the sample as each of these increased the measurable distortion at the borders of the filmed image.

### **5.2.2. Application of pair-wise registration**

The second step is the specific frame to frame pair-wise image registration. Generally, this involves the steps that can be seen in Fig: 5-1. Initial registration options need to be defined, which include the settings and parameters to define how the registration is performed. These can include initialisation, specific similarity metric and other options that are available in a specific toolkit.

As the assessment is undertaken over the course of consecutive frames of the experimental data capture, there is a need to identify the specific frame time step. This was identified as the time difference between pair-wise images. The CineView software was used to provide the information of the exposure time and the frame separation time. These differed as the exposure must occur within the frame separation time and allow the camera to process and save the image. The frame time step is defined as the actual time difference between the frames as defined by the recording software frame separation time not the exposure time.

In this work, it was found that if possible, the application of masks to both images aided in maximising the accuracy of the registration, which will be discussed later in section 5.4.5. Once the registration was performed, the local transformation was extracted from the registration output. This was the transformation for each pixel between image pairs, which was determined using the specific transformation options defined. It should be noted that this may not be the same as the transformation output by the registration process, which is more commonly the transformation of the B-spline control point grid pattern used during the registration. This will be different from the size of the images being registered. Often, registration toolkits will include a function to generate a pixel-wise transformation from the B-spline transformation. When the registrations are performed, they create a bank of consecutive pair-wise transformations over the time period of the data capture, which can then be composed into a continuous displacement over the captured time period.

### **5.2.3. Application of composition of the pair-wise transformation**

The next stage is the composition of the pair-wise transformations to generate the dynamic transformation over the course of the data capture as described in Fig: 5-1. The specific theory can be seen in Chapter 4. In brief, an initial coordinate system is generated from the first image of the data capture which assumes the initial transformation at each pixel is zero. The Matlab function 'ndgrid' was used to define the origin point of this coordinate system, which specified it as the top left corner of the images [230]. Modifying this involves simply flipping the generated axis to align with the desired arrangement for the specific experimental arrangement. However, this feature was not used in this case as the experimental arrangement in this chapter, as altering the origin point would have minimal benefits to the data processing.

The Matlab function 'bspline\_trans\_points\_nd' was produced by R Hua [228]. This uses the same B-spline formulation that has been described in Chapter 4. The registered pixel transform for each set paired images from the captured experimental

footage was extracted. These transforms are then applied to the coordinate system sequentially with the initial coordinates subtracted from the current coordinate for each pixel producing the transformation at the given frame of the data capture with corresponding time point in respect to the defined pixel origins. The steps can be seen in Fig: 5-1.

A separate code was written which utilised a B-spline transformation code and an interpolator to calculate the new pixel positions. The B-spline transformation approach has been described in Chapter 4. As its basis, the transformation code was built into the ‘Non-Rigid Version23; B-spline Grid, Image and Point based Registration’ toolkit [212], specifically the ‘bspline\_transform’. As described, the consecutive transformations was generated using the ‘bspline\_trans\_points\_nd’ [228]. The code firstly extracted the specific consecutive transformation for a given time frame applying to the user specified origin image. Once transformed, the B-spline transformation was applied to produce the new image for that particular transformation point. This could be run for individual transformations or all of them consecutively producing an image bank that could then be used to produce a video of the registered consecutive transformations.

Calibration measurement was performed using a grid pattern mounted on a board with squares of 19 mm x 19 mm. This was placed in the plane of expected loading, and an image was captured before any experiment testing was undertaken. This was performed to ensure there was minimal error induced due to the assumption of the same spatial resolution across multiple tests. Even using the same experimental arrangement, there will be a slight degree of variation due to the small difference in the position of the camera or sample position which would induce errors in the composition transformation if not accounted for as described above. Using this calibration, it was possible to convert the pixel wise transformation to the actual displacement. With the known time period of the individual captured frames and the number of frames in the capture, it is also possible to calculate the velocity over the captured images. This means the displacement and velocity for the given experiment could be extracted using the method above.

### **5.3. Synthetic image registration**

To investigate the registration toolkits capabilities, this work made use of author-generated synthetically produced images of the expected shape and of the penetration cavity. These images were then transformed using an author-defined synthetic transformation field, which was applied using the transformation function

‘bspline\_transform’ produced by D.J.Kroon [212]. The transformation was defined by assessing previous literature and available footage of penetrating impacts. From this research, three key points were identified: the forward motion of the projectile, the outward motion of the cavity behind the projectile, and finally, the complexity of the motion as the penetration process and cavity expansion occur at the same time but at different rates. This information was then used to create an approximated transformation of the expected motion. Initially, the image was constructed to have a central column representing the cavity with a point representing the projectile. For more in-depth description, see 5.3.1. This allowed the exploration of the various registration options with the capability to perform both a qualitative assessment and a quantitative assessment of accuracy.

To perform the assessment, this approach used a comparison of the transformation applied and the registered transformation providing the quantitative assessment, supported by the use of a scoring method using the similarity between the reference and registered images assessed using the SSD similarity metric as described in 4.4.2.2. This is a well established metric and common to the two toolkits proposed for the registration. The qualitative assessment was performed using the mean image difference and visual inspection of the registered images.

This section explores several levels of complexity to fully understand the registration outputs increasing in complexity the closer in similarity to the expected penetration test data they become. This culminates in an image that is considered to be the closest approximation to the expected data. In all cases, the transformation is known, allowing quantitative assessment of the resultant registrations. All registrations were performed in line with the defined pair-wise registration method described in Chapter 4.

### **5.3.1. Basic synthetic images**

The goal of these registrations was to establish an understanding of how the similarity metrics respond to changing image complexity and to identify any weaknesses or artefacts that need to be accounted for during the assessment of experimentally collected data. Assessing the output, as described in 5.3, used the mean image intensity (54) as a qualitative measure of accuracy.

$$I_{MD} = \overline{(I_S - I_R)} \quad (54)$$



In this case,  $I_S$  and  $I_R$  represent the reference image and the registered image which are then subtracted and the mean is taken of the resulting image. This results in the mean image difference represented by  $I_{MD}$ . The closer this term is to zero, the closer the images are in similarity and the assumed higher accuracy of the registration output.

For the registration, the default toolkit options were used and only the similarity metric was varied as this allows a comparison of the impact this has on the optimisation of the registration. The registration options for the specific toolkits are in the tables below:

Table 5-1: The table below represent the key registration parameters used for the Nifti-reg toolkit. The spacing of the B-spline grid and the penalty term used in the definition of the transformation alongside the specific similarity terms that are being investigated.

<b>Registration Options Nifti-reg</b>	<b>Condition 1</b>	<b>Condition 2</b>
<b>Spline Grid Spacing [x y z]</b>	[5 5 1]	[5 5 1]
<b>Bending Energy Penalty Term [weight (%)]</b>	[0.005]	[0.005]
<b>Similarity Metric</b>	NMI	SSD

Table 5-2: The key registration parameters used for the Non-Rigid Version 3 toolkit are specified below. This, as in Table 5-1, shows the B-spline grid spacing, the specific penalty term that is used and the similarity metrics that have been used.

<b>Registration Options Non-Rigid Version 3</b>	<b>Condition 1</b>	<b>Condition 2</b>
<b>Spline Grid Spacing [x y z]</b>	[10 10 1]	[10 10 1]
<b>Thin Sheet Bending Energy Penalty Term [weight (%)]</b>	[0.001]	[0.001]
<b>Similarity Metric</b>	PI	SSD

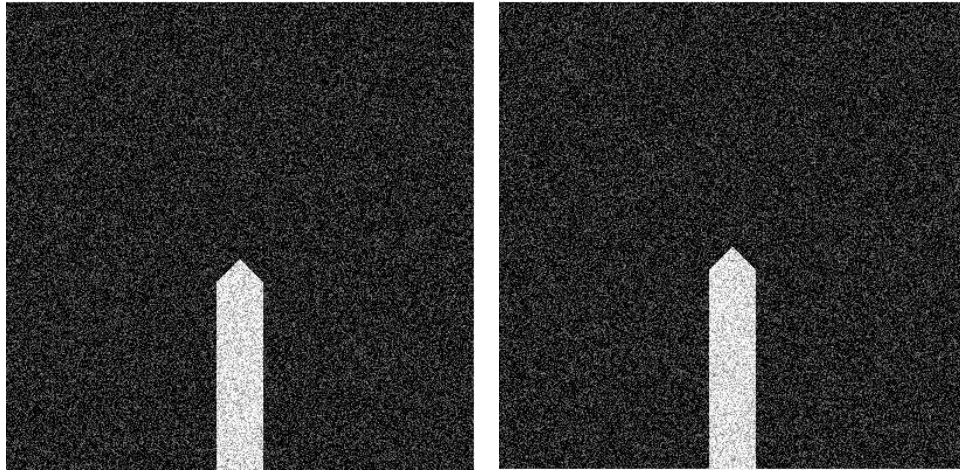


Fig: 5-6: Left, the undeformed configuration of the image. Right is the deformed configuration 10 pixel extension. Both images have a Gaussian noise applied of mean 0.0 and a variance of 0.001 to account for noise that could occur in the experimental data.

The basic images consisted of a 400 by 400 pixel dimensions with a white column on a black background. This image was then transformed by extending the column by 1, 5 and 10 pixels. An example can be seen above in Fig: 5-6. This represented the simplest case with maximum contrast between the image and the background. As noise is expected in the real filming and to allow for a greater understanding of how the toolkits respond to noise, two noise conditions were applied using Matlab function “imnoise” available in all versions, which used a Gaussian noise with a mean of 0 and two variance 0.01 and 0.05 respectively.

Please see overleaf for Table 5-3.

Table 5-3: The accuracy of the registrations that were performed using the nifti\_reg toolkit for the synthetic images. Assessed using two methods the intensity difference and image similarity score using the similarity metric Sum of Squared Difference

<b>Description Details</b>		<b>Intensity Difference</b>	<b>Similarity Score</b>
<b>Images</b>	<b>Metric</b>	<b>Mean (Ref-Reg)</b>	<b>SSD (Reg vs. Ref)</b>
<b>1 Pixel</b>	SSD	0.0001	0.00033
<b>No Noise</b>	NMI	0.0011	0.0018
<b>1 Pixel</b>	SSD	0.0011	0.0037
<b>M0 V0.01</b>	NMI	0.0002	0.0064
<b>1 Pixel</b>	SSD	0.0016	0.017
<b>M0 V0.05</b>	NMI	0.0010	0.022
<b>5 Pixel</b>	SSD	0.0003	0.00031
<b>No Noise</b>	NMI	0.0000	0.0028
<b>5 Pixel</b>	SSD	0.0010	0.0036
<b>M0 V0.01</b>	NMI	0.0002	0.0065
<b>5 Pixel</b>	SSD	0.0017	0.017
<b>M0 V0.05</b>	NMI	0.0010	0.022
<b>10 Pixel</b>	SSD	0.0003	0.00030
<b>No Noise</b>	NMI	0.0032	0.0030
<b>10 Pixel</b>	SSD	0.0010	0.0040
<b>M0 V0.01</b>	NMI	0.0013	0.0077
<b>10 Pixel</b>	SSD	0.0016	0.017
<b>M0 V0.05</b>	NMI	0.0022	0.045

Table 5-3 shows the mean image difference calculated by subtracting the registered image from the reference image and averaging the resultant matrix. The closer to zero, the more accurate the registration has been. The second column gives the result of the similarity score between the registered and reference image using the SSD similarity matrix as described in 4.4.2.2 where the closer the output to zero, the more similar the images. In relation to the table, it can be seen that the smaller the motion, the more accurate the registration. It should be noted that in this case, the image difference shows a much greater variation in the outputs of the images with noise. These images also show the most variation between the similarity metrics. This would indicate that noise effects the registration which is logical as noise adds randomized elements that occur differently in each image.

Table 5-4: The accuracy of the registrations that were performed using the Matlab based toolkit for the synthetic images. As with the output of the Nifti-reg toolkit, it displays the intensity difference and similarity score.

<b>Description Details</b>		<b>Intensity Difference</b>	<b>Similarity Score</b>
<b>Images</b>	<b>Metric</b>	<b>Mean (Ref-Reg)</b>	<b>SSD (Reg vs. Ref)</b>
<b>1 Pixel</b>	SSD	0.0000	3.0e-8
<b>No Noise</b>	NMI	0.0000	8.7e-7
<b>1 Pixel</b>	SSD	0.0001	0.0049
<b>M0 V0.01</b>	NMI	0.0003	0.0062
<b>1 Pixel</b>	SSD	0.0003	0.024
<b>M0 V0.05</b>	NMI	0.0002	0.028
<b>5 Pixel</b>	SSD	0.0000	2.0e-5
<b>No Noise</b>	NMI	0.0002	1.7e-5
<b>5 Pixel</b>	SSD	0.0000	0.0050
<b>M0 V0.01</b>	NMI	0.0010	0.0073
<b>5 Pixel</b>	SSD	0.0003	0.024
<b>M0 V0.05</b>	NMI	0.0007	0.032
<b>10 Pixel</b>	SSD	0.0000	1.7e-7
<b>No Noise</b>	NMI	0.0000	2.4e-7
<b>10 Pixel</b>	SSD	0.0005	0.0050
<b>M0 V0.01</b>	NMI	0.0026	0.0080
<b>10 Pixel</b>	SSD	0.0003	0.024
<b>M0 V0.05</b>	NMI	0.0017	0.032

Table 5-4 shows that when there is negligible noise in the image, the toolkit is highly accurate in terms of both the similarity score and image difference. Alongside this, it can be seen that the greater the transformation in pixels, the greater the image difference score and a similar trend can be observed when considering the increase in noise. It should be noted that this Matlab toolkit shows the greatest variation in the result obtained with warping at the border between the cavity and in some cases not effectively registering the change in the image underestimating the difference between the simulated cavities.

In this initial stage, the qualitative assessment proved to be the main source of assessment. This identified that nifti\_reg and the Matlab toolkit, both using the SSD metric, performed the most accurately. Both NMI and PI showing reasonable levels

of accuracy but artefacts were visible in the results. Artefacts in this case were defined as variations in the images such as large amounts of warping or misalignment when compared to the images being registered please see example in Fig: 5-7 which included warping in the proposed cavity or blurring and failure to register the motion. In this case, the artefacts identified were mainly blurring or warping in small amounts in around the cavity which can be seen to directly result in the variation in results output. From these results, it is logical to continue investigating all four metrics to develop an understanding of how changes in the image content will affect the response of the registration as the images may lead to a specific metric giving a better result.

### **5.3.2. Synthetic gridded images**

For these images, the background was adjusted to an intensity that can be expected from the ballistic gelatine, alongside including a grid pattern and the projectile being set for maximum contrast as it will be opaque steel ball bearings in the actual test. In this case, a distinct angular projectile was chosen to have as prominent shape as possible, to simplify the complexity and ease the generation of the image. The main goal of this set of images is to investigate how the registration accuracy would be affected by the approximated cavity motion; as such, the actual shape of the representation of the projectile has limited impact on this investigation. The grid pattern represents the proposed fiducial markers that will be added to the experimental samples to enhance and aid the registration identifying the motion of the wider sample area around the cavity.

The applied transformation approximated the expected ballistic gelatine response. The transformation was applied using the same approach as in section 5.3.1. It was assumed that the motion was symmetric with the axis of symmetry running through the centre of the representative cavity. The motion extends the cavity upwards and expands the lower half outwards approximating the dynamic motion seen in the literature. It is interesting to note that when considering the literature, it can be seen that the cavity would have a very high intensity. This will be caused by the back-lighting in the actual impact tests due to the light being refracted and reflected off the internal surface of cavity, which was included in the images. Image registration can be affected by regions of high intensity so it is prudent to investigate the impact this could have to be able to account for it in later tests [23], [24], [26]. Therefore, the cavity was given the maximum intensity to increase the similarity of the

approximated image to actual data. As stated above, to aid in understanding, Gaussian noise was applied with a mean of 0 and variance of 0.001.

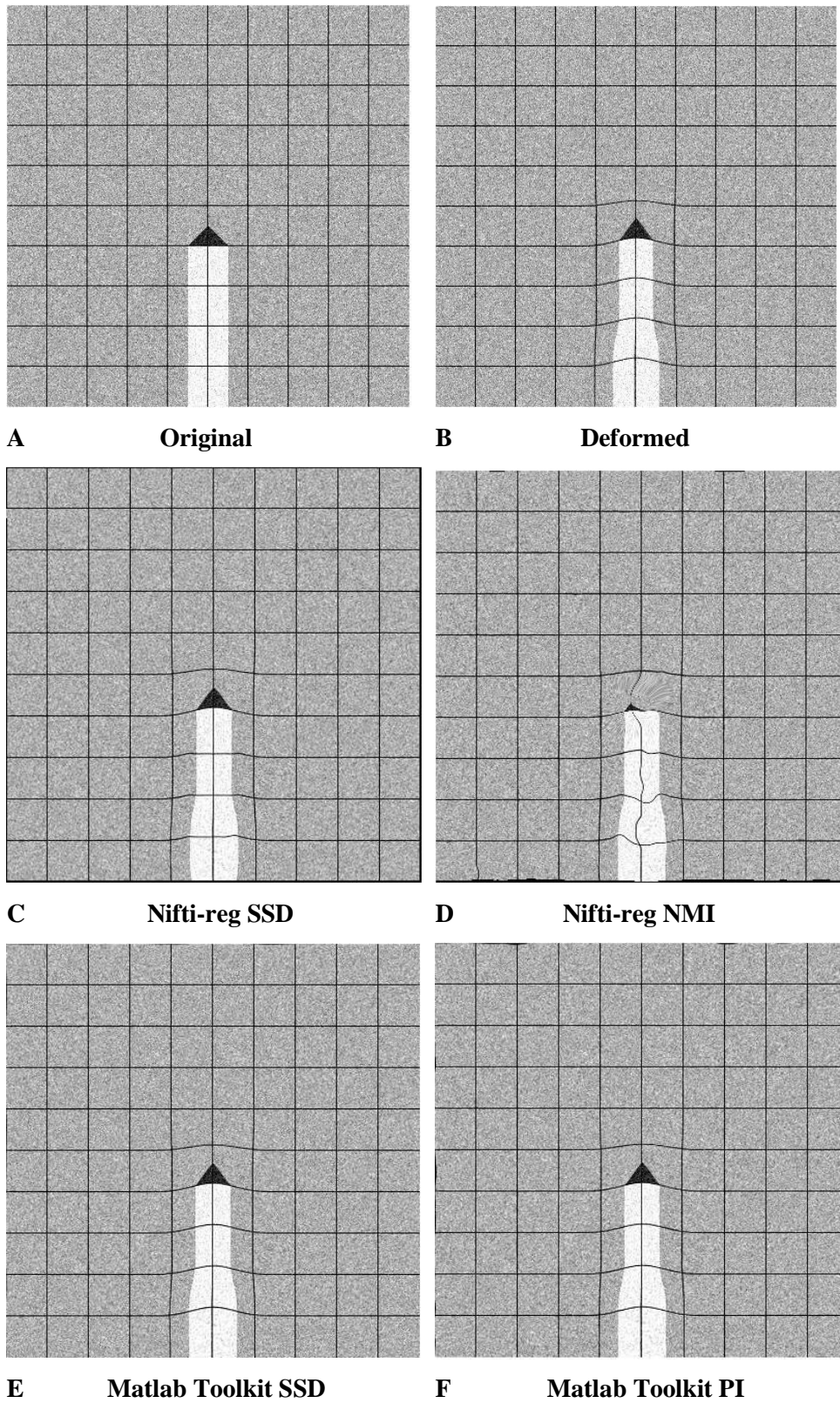


Fig: 5-7: A shows the undeformed synthetic image and B shows the deformed synthetic image. C and D represent the results of the Nifti-reg toolkit registrations, with C being the result of the SSD metric

and D being the result of the NMI metric. E and F results of the Matlab toolkit with E being SSD metric and F being the PI metric.

Table 5-5: The results of the similarity score for the synthetic images. The similarity difference method was previously defined in section 5.3.1, and in this case, all use the SSD similarity metric to calculate the similarity score for the given registrations.

<b>Tool Kit</b>	<b>Nifti-Reg</b>		<b>Non-Rigid Version23</b>	
<b>Metric</b>	SSD	NMI	SSD	PI
<b>Synthetic Truth</b>	0.022	0.024	0.015	0.014

From Table 5-5, it can be seen that the Matlab toolkit gave the most accurate response. This is supported when compared to the registered images produced from the registration outputs in Fig: 5-7. The response for the Matlab toolkit was very effective and this agrees with the values of the similarity score. For the nifti-reg toolkit, it can be seen that the response of the SSD metric is successful with some over-smoothing at the base. The NMI metric shows considerable warping in the pseudo cavity and indenter. The similar values of the similarity score would suggest that using this as a method of quantitative assessment is limited. As there is only a difference of 0.002 between the two similarity scores, it indicates a similar response; however, this is not the case. This will be directly related to the content of the image as most of the image remains the same before and after the transformation. In this case, the small difference would directly be related to how the cavity changes, which indicates that the methods can be used to assess the accuracy specifically to aid in determining how the registration method determines the optimisation. So for the purpose of assessing the result of the similarity metrics will be effective at identifying limitations of the registration when compared to the actual registered image and the deformed or static image. It should be noted that the result seen for Matlab achieved similar scores and showed very close similarity in the output images. Future methods will continue to use this assessment method to aid in understanding how the registration performs; however, the results will be treated carefully and closely compared to the transformations or quantitative assessment.

From the results above, it would indicate that both toolkits would be appropriate to be taken forward as it can be seen that SSD metric was able to accurately register the transformation. As minimal effort is required to run the registration with the two metrics and to aid in understanding of how the image registration response changes when applied to experimental data, both toolkits will be taken forward.

## **5.4. Experimental validation of registration method**

Before applying the registration approach that has been previously outlined to the penetrating impact tests, it was prudent to validate the method on a simpler experimental arrangement. In this case, a uniaxial indentation test was used. By using a simpler experimental arrangement, it is possible to validate the image registration output with experimental data collected by the testing rig's inbuilt instrumentation. However, it should be noted that the data collected through this instrumentation will only measure the motion of the indenter, not the motion of the whole sample which necessitates the use of a computational model to validate the wider motion of the sample.

The test involved a round head indenter being pressed into a ballistic gel surrogate, which was embedded with a disperse grid pattern acting as fiducial markers. For specific description of the insertion of the grid pattern see section 5.4.1. In this experiment, as the indenter moves downwards, the material is compressed at the tip and pushed away from the indenter's pathway over the rest of the indenter surface. Testing does not extend enough to rupture of the surrogate. To maximise the motion of the tissue surrogate, the indenter's size was large, increasing the ease of which the registration should approximate the motion.

The methodology has several components including the sample preparation and experimental capture of raw data, followed by the pre-processing (for each test) and optimisation of the registration parameters performed before the registration was undertaken. To confirm the results of the registration, an FEA model was used to allow comparison of the produced displacement field.

### **5.4.1. Sample preparation**

The tissue surrogate was produced in line with the manufacturing method that was used in chapter 4. However, as per the discussion, the temperature was monitored and any marks or failure that occurred during casting were identified. These included tears or surface marks that originated from casting. Non-homogenous samples which contained visible inclusion of scum or changes in the material colour or texture within the sample, if deemed detrimental to the testing, were not used. This was defined as being when handling of the sample resulted in damage or was in line with failure that had previously been identified in Chapter 3. It is also important to note in this case, a single mould represents 1 sample. The gelatine was cast into cubic moulds of dimensions  $61.5 \pm 1$  mm x  $61.5 \pm 1$  mm x  $61.5 \pm 1$  mm and left at room



temperature for 24 hrs to gel (solidify), before being placed in the fridge at  $8\pm 1$  °C and left to cure for 24 hrs. Once cured, the gelatine was removed from the mould carefully, to avoid tearing of the sample. A grid pattern is added to the sample by injecting black dye manually using a needle. The dye used was a gel based food grade dye at a very high concentration. This was selected for its non-toxic a non-corrosive qualities that make it readily accessible (produced by a wide range of companies and commercial available in a range of colours and quantities) and compatible with the ballistic gelatine, while also have a very intense colour even when diluted to be injected into the sample. The gridlines were injected using a 60 mm spinal hypodermic needle which was carefully inserted to minimise bending of the needle. Once to the correct depth, the needle was slowly removed and the black dye was slowly injected along the needle path. It was found that black gel food dye at very high concentrations did not show bleed into the surrogate maintaining the greatest contrast possible. The pattern was not uniform and arranged in a dispersed grid throughout the samples to provide the registration with distinct objects to track to avoid misalignment of the grid pattern during the registration process.

#### **5.4.2. Experimental procedure**

The majority of the experimental arrangement had a large amount of similarity to the experimental method that has been described in Chapter 4. The tests were performed using a Tinius Olsen 25K testing machine with a 5 KN load cell in a uniaxial arrangement with the contact body being a 15 mm radius round head steel indenter. All samples had a 1 N preload to ensure the tip of the indenter was in contact with the surface of the tissue surrogate but with minimal actual indentation. For all tests, a displacement of 30 mm was applied with a machine head speed of 10.0 mm/s and the response measured. The material was mounted on a Perspex sheet fixed to a metal base plate to ensure there was sufficient contact area to account for sample expansion if it occurred. No surface treatment was applied as the same assumption of high friction at the interface informed by the work undertaken in Chapter 3. It has been previously identified that using this interface meant that there was the possibility for slippage to occur. However, in this case, the likelihood of slippage occurring at the lower interface will likely be minimal due to the loading arrangement and the smaller strains that are expected. Identifying the level of slippage or sample movement at the interface, if it occurred, was done using the same high speed camera arrangement that is used to film the indentation experiments. This means it can be assessed throughout the loading. From assessing the footage that was recorded, if any slippage

was identified, it was found to be minimal. From this footage, it would add weight to the use of this interface condition for the penetrating impact testing.

The video capture arrangement used a Phantom V210 digital high-speed video camera supported by CineView software and the same Nikon Lens used in the lens effect study. The camera was placed at the same distance from the sample for each tests, and a resolution of 640 x 480 pixels was set. As the largest resolution achievable with the arrangement was 2400 x 2400 pixels and as the resolution is modified with centre point remaining constant, the smaller resolution effectively crops a large portion of the possible lens effects expected. This still leaves the possibility of the out of plane motion impacting on the recording. This has to be minimised by the accurate placement of the sample during testing and a consistent camera arrangement. The recording speed was specified as 100 fps, giving an exposure time of 9.9 ms, with an actual time step of 0.01 s. It was found that during testing, the ambient light was sufficient to capture images with significant contrast that no extra lighting was required. The focal length was set to achieve the maximum clarity for each test. There was no need to adjust the aperture or use backlighting as there was sufficient light to achieve good contrast. A white background was placed behind the sample to minimise the likely impact of artefacts caused from background objects impacting the registration. In this work, the indenter is a known size enabling calibration for each test.

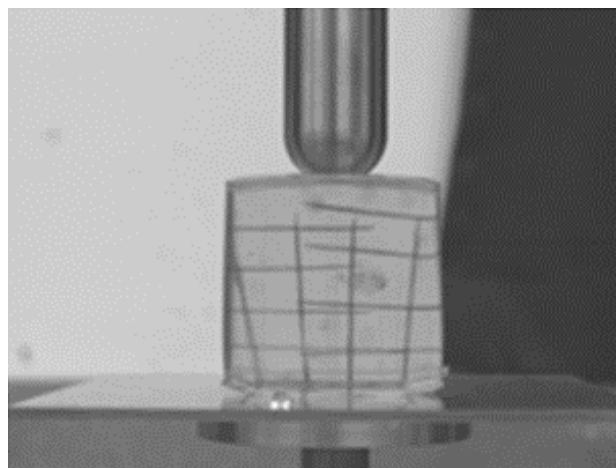


Fig: 5-8: The initial frame open in the CineView software ready to calibrate the sample with the indenter. The mounting plate can be clearly seen which is being viewed in the CineView software interface window.

### **5.4.3. Captured data pre-processing**

As described in previous work (5.2.1), a level of pre-processing was undertaken for all tests. This involved cropping the image to remove all of the image background that did not contain the sample (sample being the ROI) at the initial frame of the data capture using the CineView software. This was applied to all frames. In this case, there was minimal need to apply modification to the gain or contrast of the image due to sufficient ambient lighting and little need to adjust the focus. As discussed earlier, a lens effect study was undertaken and these effects were found to present minimal impact.

### **5.4.4. Optimisation of the image registration parameters**

To optimise the parameter of the image registration, an approximation of the transformation between the captured pair-wise images was generated by initially selecting a base image from the captured data set which has been pre-processed. Then, an approximated transformation is applied which has been estimated from the experimental data. This was determined by manually measuring the indenter motion over several consecutive image pairs. As the machine assumes that compression produces a negative displacement to reduce the processing time for comparing the data, it is important to align the registration coordinate system with this arrangement. In this case, as the image registration assumes for transformation, the origins of the grid points are in the top left hand corner with y-axis being positive in the down direction and the x-axis being positive in the right hand direction. To align with the machines measuring system, the axis are rotated by 90 degrees, meaning that the x-axis being positive in the upright direction and the y-axis being positive in the left-hand direction. This also assumed to be in line with the centre plane of the sample which is the plane in which the gel grid pattern was injected.

The indenter motion was found to be 2 pixels in the direction of indentation, and 1 pixel away from the centreline of the indenter in the opposite direction to simulate the material being pushed out of the path of the indenter. This is a very small motion, which increases the difficulty in assessing the accuracy of the registration. However, in this assessment, the indenter motion is the main area of assessment. If the registration is unable to identify its motion this brings its use into question. So to explore the effect of the varying impact of deformation, three indentation distances of 1, 2, and 4 pixels were generated shown in Fig: 5-9. The transformation was applied using the method specified in 5.3 with the transformation shown in both x and y for each pixel in the image.

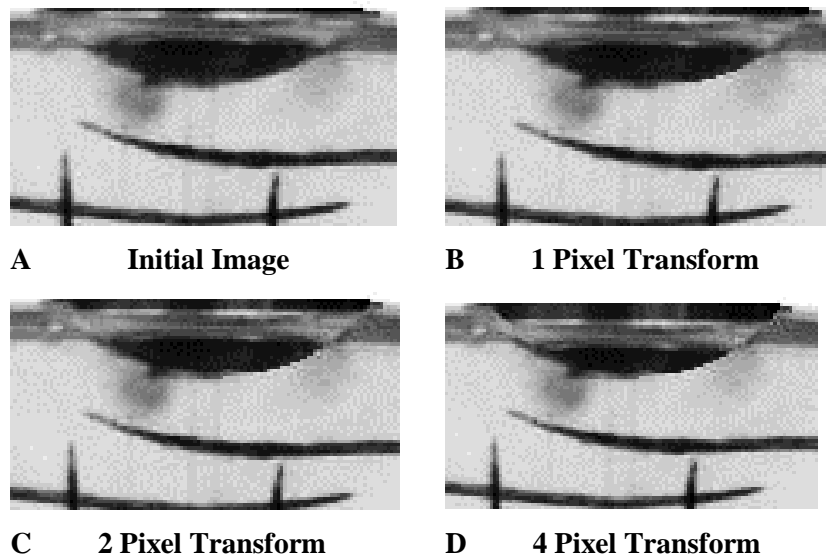


Fig: 5-9: Images that formed the basis of the optimisation of the registration parameters, A: Moving Image, B: Static Image 1 pix Transform, C: Static Image 2 pix Transform and D: Static Image 4 pix Transform. Due to small amount of motion, images have been magnified.

The optimisation of the image registration parameters was approached in a systematic manner, initially starting with the registration parameters derived from section 5.3. This was shown to give limited accuracy resulting in an overall poor registration. To improve the output, several different options were considered.

The refinement then diverged between the two toolkits. In the case of the Matlab toolkit, it was found that adjusting the penalty weight term provided the greatest impact on the results. It was found that the PI metric produced the best registrations, but still resulted in variations in the grid pattern of the image, particularly surrounding the loading region. Altering the spacing of the B-spline grid points affected the registration outcome. However, this was minimal and the variation was still present in the result. From this point on, work focused on the use of the `nifti_reg` toolkit.

The `nifti_reg` toolkit showed that the NMI metric gave the best response. It was found that altering the weighting of the penalty measure proved to have little effect on the registration output. When consulting the previous literature, it was recommended that the registration be initialised with an affine transformation. This can reduce both the work required for the non-rigid algorithm and the accuracy of the final registration. This works by first transforming the image with an affine transformations output to the moving image, which is then used in the non-rigid registration determined by an independent pair-wise affine registration of the images. Performing this initialisation means that the larger and clearly defined

motion is already accounted for before the non-rigid registration. This reduces the workload and allows for the optimisation to be focused on the specific non-rigid component of the transformation. In this thesis, it was generated using a tool in the Nifti-reg toolkit called ‘reg\_aladin’ which is an inbuilt function which follows the same registration process and optimisation; however, it is built around the affine transformation method.

Initialisation is a specific formulation where a previously registered or defined transformation is applied to the floating images before the current registration is undertaken. In this case, a prior registration was performed using a different transformation algorithm providing the initialisation. It showed the greatest impact on the output of the registration. The results of which can be seen in Fig: 5-10 and Fig: 5-11, with the results of the quantitative analysis shown in Table 5-6.

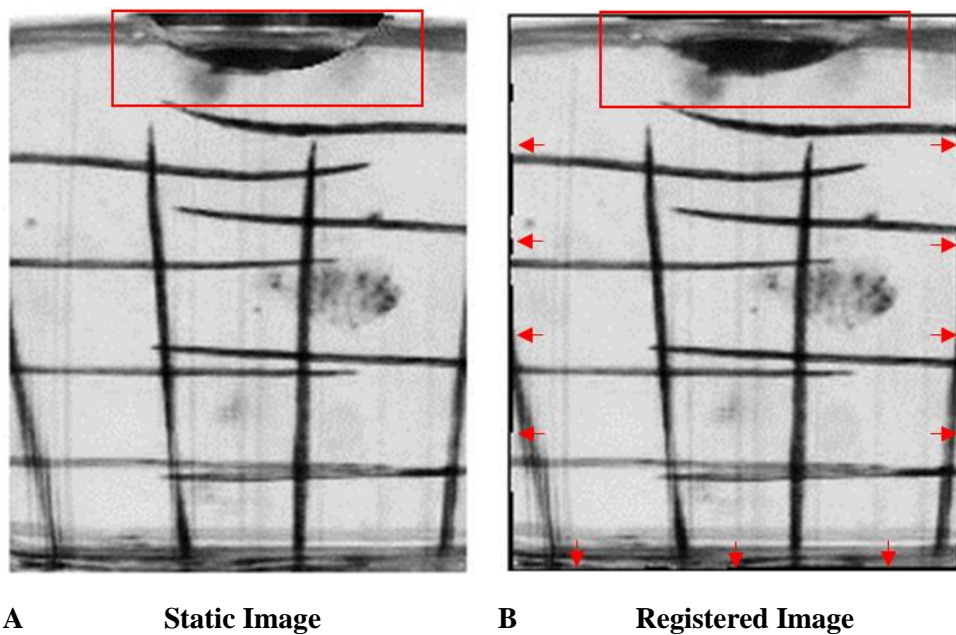


Fig: 5-10: A is the 4 pix transformed image and B is the output of SSD metric registration with the initialisation applied to the non-rigid registration. Visually, the two images are very similar but differences can be seen around the indenter and upper surface of the gelatine which is surrounded by the red box. Differences are also highlighted around the edges of image B as a dark frame can be seen, this is highlighted in the image by the red arrows which shows that the whole image has been transformed.

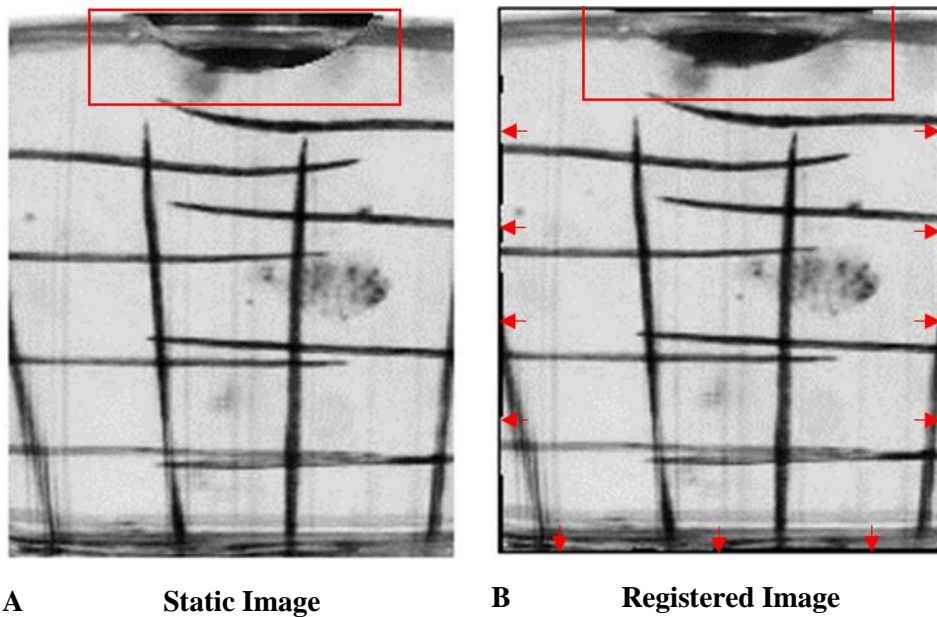


Fig: 5-11: as with Fig: 5-10, A represents the static image and B represents the output from the NMI metric registration with the initialisation applied to the non-rigid registration. This registration shows less difference in between the two images particularly around the sample's upper surface (highlighted within the red rectangle) when compared to the SSD response in Fig: 5-10. The same black border can be seen around B (red arrows) which is evidence of the image transformation.

Table 5-6: The assessment of the registration outputs of the different displacements for the proposed similarity metric including the Mean Intensity Difference which shows higher accuracy the closer to zero the value is. The Similarity Score remains as used previously and the Maximum Displacement was registered at the tip of the indenter.

<b>Indenter Motion</b>	<b>Tip</b>	<b>Similarity Matrix</b>	<b>Mean Intensity Difference</b>	<b>Similarity Score (SSD)</b>	<b>Maximum Displacement In X</b>
-1		SSD	0.016	0.011	-1.15
-2		SSD	0.016	0.011	-2.17
-4		SSD	0.018	0.012	-4.70
-1		NMI	0.017	0.010	-1.08
-2		NMI	0.017	0.010	-3.05
-4		NMI	0.016	0.011	-0.20

From the data above, the most effective metric was SSD. NMI showed a reduced accuracy for the largest transformation. As before, the similarity score and mean difference showed minimal differences between the registrations, highlighting its limitations as a method of assessing the accuracy of the registration. However, it does show that it has an impact in determining the motion within the optimisation.

The final optimised parameters that will be used to assess the captured data can be seen in Table 5-7. For the purposes of this chapter, both toolkits will be taken (even though the accuracy level varied between metric) to further understand why the difference occurs in relation to the application to the indentation tests and optimisation of the registration.

Table 5-7: This table represents the final registration parameters that were applied to the experimental testing for the Nifti-reg toolkit.

<b>Registration Options Nifti-reg</b>	<b>Specific Details</b>
<b>Spline Grid Spacing [x y z]</b>	[5 5 1]
<b>Bending Energy Penalty Term [weight (%)]</b>	[0.005]
<b>Similarity Metric</b>	NMI/SSD
<b>Reference Mask</b>	Applied (Indenter)
<b>Floating Mask</b>	Applied (Indenter)
<b>Affine Initialisation</b>	Applied (Pair wise)
<b>Pyramidal Levels</b>	3
<b>Level Iterations</b>	300

It is important to state the options that were selected for the reg\_aladin toolkit were to ensure that consistency was maintained throughout the following registration. The options are shown in Table 5-8. The toolkit does has further options available which were not considered in this work as they are specifically tailored towards medical imaging.

Table 5-8: Shows the parameters that were used form the reg\_aladin toolkit for the purposes of generating the initial affine transformation used in non-rigid registration.

<b>Option Class</b>	<b>Option</b>	<b>Description</b>
<b>Outputs</b>	'aff'	Contains the output affine transformation
	'res'	The registered image output file
<b>Registration</b>	'affDirect'	Rigid transformation initially then affine (Default)
<b>Verbose</b>	'-voff'	Toggle verbose on and off
<b>Optimisation</b>	'-maxit'	Maximum number of iterations [5]
	'-ln'	Number of levels to perform [3]
	'-lp'	Only perform the first level [ln]

#### 5.4.5. Further options for improving registration accuracy

Alongside the application of the initialisation, it was suggested in literature that the application of a ‘mask’ would aid in further improving the accuracy of the image registration as overlapping objects will create artefacts in the output. By applying a mask, this effectively removes the image data in front and behind the indenter minimising the multi-planar motion. A mask is a binary image that defines the region that will be registered and the regions that will be ignored during the registration process. The region that will be registered is defined by a pixel value of 1 and the pixels that will be ignored being defined by 0. The masks were generated using the manual segmentation tool that is built into software ITK-SNAP [238], which is a pre-existing software that has been developed as a medical imaging tool. An example of this process is demonstrated in Fig: 5-12, where the masked area is manually selected and covers all the indenter that can be seen in the image which is in line with the central pane of the indenter which is the same plane as the inserted grid pattern. The software was readily available and exported images that were compatible with the registration toolkit. It was characterised by ease of use allowing the generation and extraction of masks in a format which was compatible with the registration toolkit.

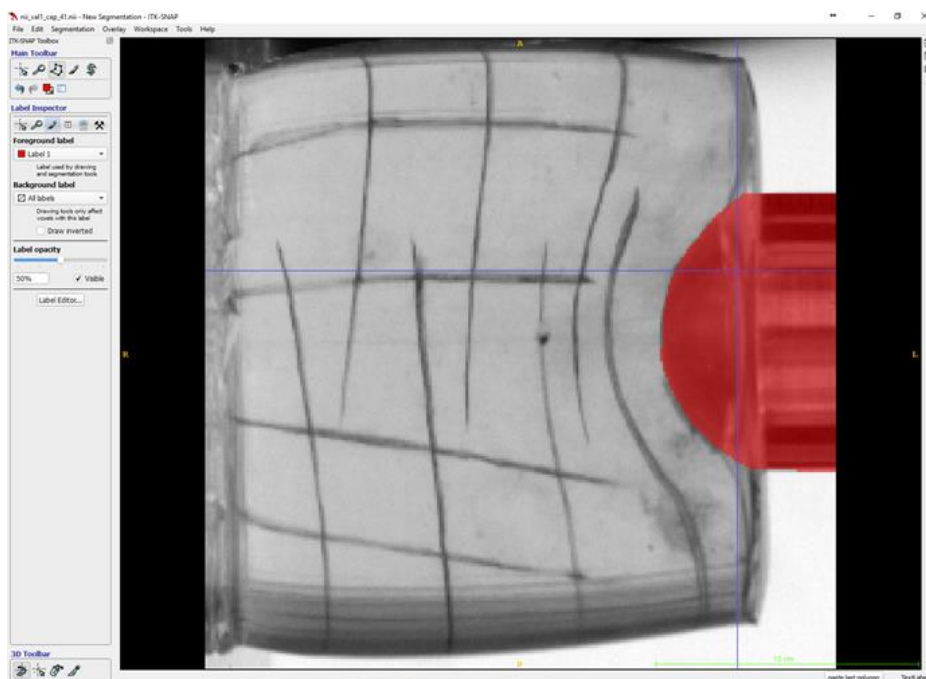


Fig: 5-12: Shows the ITK Snap working window with the indenter highlighted which will be used to define the mask for the given frame. The area that is highlighted in red is the area that is selected as the region defined as the mask, with the software control panel on the left of the image.



#### **5.4.6. Application of optimised image registration method**

The registration framework that has been specified early in this chapter (5.2.2) was then applied to the experimental results using the optimised registration parameters identified in 5.4.4. In this work, directly consecutive frames were not registered, as it was found that the indenter head motion between the frames was very small and it was felt that this may not be computationally effective and could lead to registration inaccuracies. So, every second frame from a data capture was extracted and then formed into a new modified data set. The composition of the transformation method does not change as the individual transformations can still be composed. The pair-wise transformation effectively represents the registration of the actual indenter motion at a different time step. During the registration, it was identified that anomalies or distortions present in the captured images had an impact on the accuracy of the registration. These resulted from marks on the outer surface of the sample that occurred during sample preparation or due to environmental factors, which did include marks on the experimental rigs. It was found that all the samples bore some form of anomaly, with some having clear large marks or small smears and flecks from handling the sample. In some cases, it was possible to clean the samples removing the marks; however, in some cases, it was not possible to remove all of them. To minimise the impact that this has, it was decided to assume symmetry along the centre axis of the indenter. This both reduced the computational cost (as it reduced the image size by 50 %) while also allowing the selection of the region with the least number of or no marks from the experimental data. This assumption will need to be taken forward to the computational model that has been proposed to validate the wider sample motion.

#### **5.4.7. Experimental registration assessment method**

The assessment method will follow the dual qualitative and quantitative assessment based on the method used earlier in the chapter expanded to include an assessment of the compositions of the transformations for the whole data captured. In the case of the pair-wise registration, the qualitative assessment was undertaken using the software MedInria, using the visualization tool to overlay the static/reference and the registered images. The quantitative assessment of the pair-wise registration has several components which include a manual measure of the indenter tip motion and a comparison of the similarity score which is performed to identify if the trend of variation in results of the similarity metric output is consistent across the experimental data.

The composition of the transformation was qualitatively assessed by applying the transformation to the initial images consecutively over the modified data capture. This is a quick and effective way to perform an initial assessment of the accuracy of the composition. To quantitatively assess the output, the method was compared for the manually tracked position of the indenter tip (the ground truth) and the output of the experimental rig data to the registered deformation at the data tip. This allows for confirmation that the method has been able to capture the indenter motion over the modified data set.

#### **5.4.8. Results**

When assessing the overlaid images using MedInria to qualitatively assess the pair-wise registrations, good alignment of the key objects (indenter and grid pattern) was seen in all pair-wise images. On visual inspection, the registrations would appear to have been effective in capturing the motion. This was supported by the assessment of the similarity scores, with the NMI metric showing a more effective response than the SSD metric. This was by a sufficient enough margin that this metric was selected as the primary metric for all future registration in this chapter. From this, it was possible to associate the use of a mask and initialised registration increases the accuracy of the NMI metric.

Please see overleaf for Fig: 5-13.

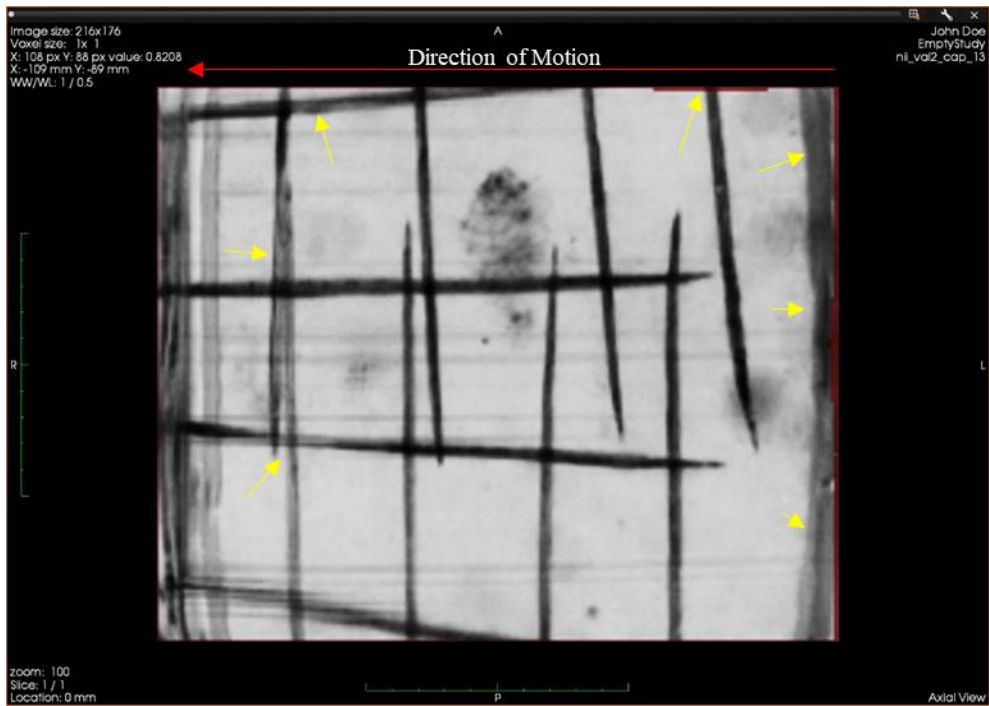


Fig: 5-13: Overlaid registered image and experimental image for frame 13 in MedInria showing the similarity between the images as they have aligned very well almost showing no difference between the two images. The red area highlighted by the yellow arrows shows the contraction of the registered image to capture the motion of the gelatine resulting from the repositioning of the control point grid due to the optimisation. While also highlighting were blur due to differences in the images can be identified.

Please see over leaf for Fig: 5-14.

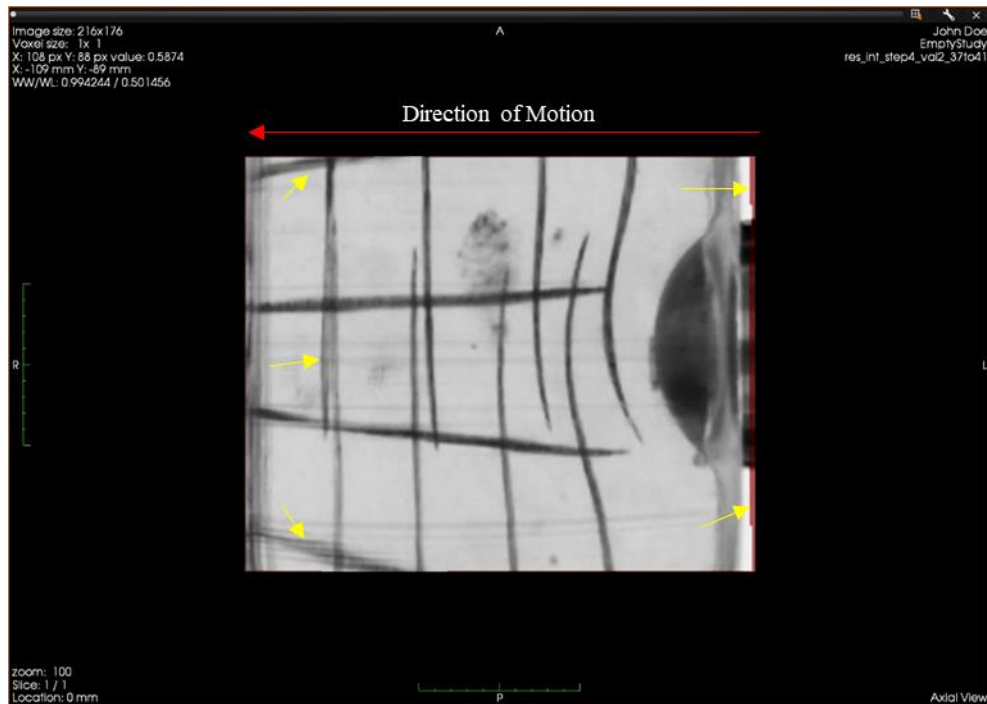


Fig: 5-14: Overlaid registered image and raw image for frame 41 on MedInria showing the similarity between the images again as minimal difference can be seen. The red area shows the contraction of the registered image which indicates the general direction of motion captured by the registration as it is located at the indenter in opposite direction of the captured motion. This and the regions where image blur due to differences in the image are highlighted by the yellow arrows.

The benefit of using the MedInria method is that it allows the direct comparison of the captured image to the registered images for the pair-wise registration. This can be seen for two different images at two different points during the initial loading (Fig: 5-13) and the mid-point of the indentation (Fig: 5-14). The movie frame is overlaid with the registered image set at 50% transparency, which allowed the comparison of the two images. The red demonstrates the outer edges of the images where the transformation has resulted in a change to the outer shape of the image. It can be seen that the two images overlay well. The images that are used here are from the tests optimisation using the fully captured images and provide a good example of the impact that marks had on the registration. When comparing the images, it is possible to identify that the mark does not move the grid pattern and hence would induce an artefact in the registration that would not.

The Table 5-9 shows the similarity score for the NMI metric that agrees with the MedInria assessment. The results would suggest that this registration process for each pair-wise registration is performed with the same degree of accuracy. However, a true measure of the effectiveness of the method proposed a comparison of the

composed transformation and the experimental measure of the indentation motion is necessary.

Please see overleaf for Table 5-9.

Table 5-9: Shows the registration and the corresponding images, pairs aligned with the mean intensity difference and the similarity score for the comparison of the registered to the reference image.

<b>Registration Number</b>	<b>Frames (Floating/Reference)</b>	<b>Mean Intensity Difference</b>	<b>Similarity Score (SSD)</b>
1	1/3	0.025	0.014
2	3/5	0.019	0.013
3	5/7	0.017	0.014
4	7/9	0.015	0.014
5	9/11	0.022	0.014
6	11/13	0.015	0.014
7	13/15	0.016	0.014
8	15/17	0.019	0.013
9	17/19	0.014	0.014
10	19/21	0.020	0.014
11	21/23	0.014	0.015
12	23/25	0.019	0.016
13	25/27	0.015	0.015
14	27/29	0.020	0.016
15	29/31	0.016	0.013
16	31/33	0.014	0.012
17	33/35	0.015	0.015
18	35/37	0.016	0.014
19	37/39	0.014	0.012
20	39/41	0.021	0.015
21	41/43	0.020	0.013
22	43/45	0.016	0.013
23	45/47	0.016	0.012
24	47/49	0.014	0.014
25	49/51	0.014	0.012
26	51/53	0.009	0.013

When the maximum indentation value is measured and the registered images composed and transformations are compared to the experimental machine data, it can be seen that the method has not been effective. During the application of the composition of the transformation to the initial image as part of the qualitative assessment, it was identified that the response had a large number of artefacts that

clouded the results. This seemed to confirm the concerns over the suitability of the similarity metric method as a method for assessing accuracy, as the results above did not represent the actual accuracy of the registration process were proven true. An attempt to improve the results was made by applying smoothing to the resulting composed transformation. To achieve this, a circular filter in MatLab's image processing tools called 'disk' was used. This applied a Gaussian smoothing to the area around each pixel for the specified radius defined by the number of pixels outwards from the centre pixel (in this case a radius of 14 was used). The outputs of the maximum indentation can be seen below in Fig: 5-15. The difference that can be seen in the initial loading is an anomaly that results from filming a single plane trough a sample. As the indenter makes contact and deforms the upper surface, this introduces a refraction affect into the sample as the high water content and change in shape result in a refraction of the light entering and leaving the sample which results in distortion in the filmed image. This was a source of error throughout the loading to varying degrees depending on the amount of change in the surface shape of the sample.

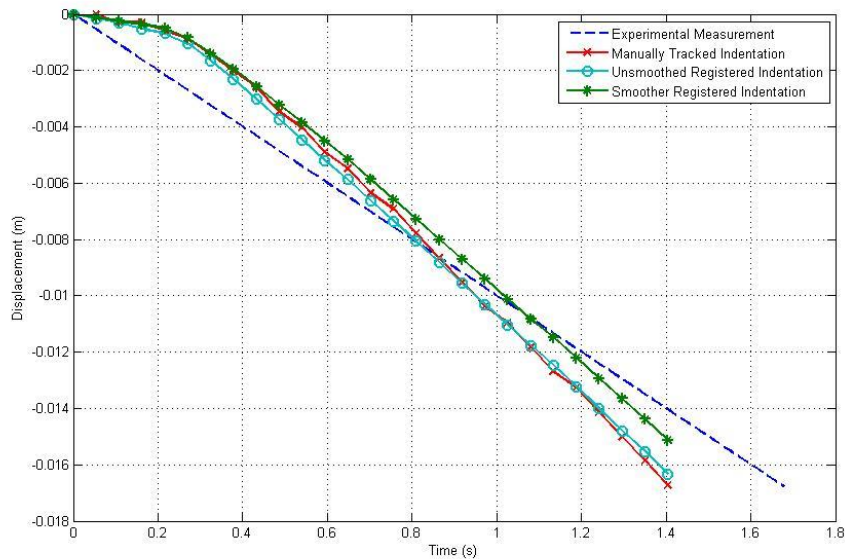


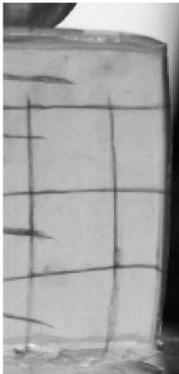
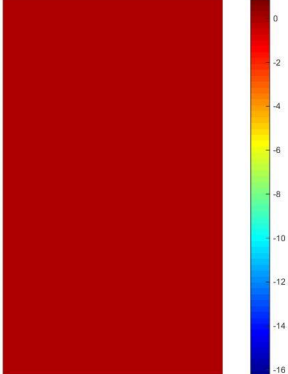
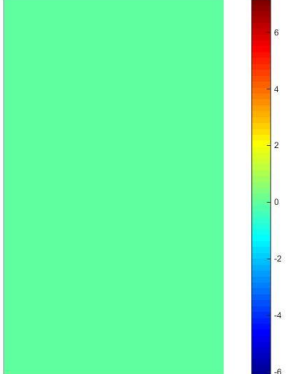
Fig: 5-15: Comparison of the different displacements showing that the outputs of the registration are comparable to the manually measured indenter motion. However, the difference between these and the experimental measurement (machine head motion) are clear, especially during the initial loading region and at the end of the loading believed to result from optical distortion due to changes in the surface geometry as seen in the captured experimental footage.

From the comparison above, two conclusions can be drawn: The first is the manually measured results taken from the experimental images and shown in Fig: 5-15 as the

red line showed a distinct difference from the machine output. It also showed that the composition of the transformation was unable to capture the indentation motion and was comparable to the measurement taken directly from the captured footage. The smoothing of the registered transformation impacted minimally on the accuracy of the registered indentation. This appears to relate to two components: the first is the effects of refraction of the light that is caused by the changing geometry of the sample during the indentation, presenting a varying source of error throughout the loading dependent on the specific changes in the geometry. Secondly, the composition of the registered pair-wise transformation has not been successful. Table 5-10 shows the composed transformation surf plots of the displacement field. From this, the transformation shows numerous artefacts, which can clearly be seen as the impact the grid pattern on the registration when compared to the wider sample motion when comparing the X and Y displacement to the captured frame in Table 5-10. The smoothing was unable to increase the accuracy of the registration.

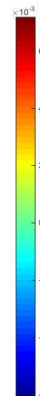
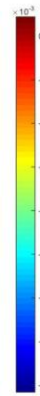
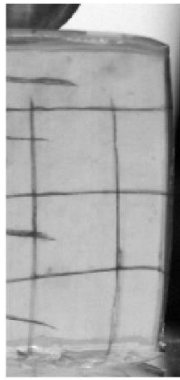
The following table Table 5-10 shows the comparison for composed transformation in the x and y displacement to the captured video of the experiment. This arrangement allows the comparison of the output and actual video footage. It should be noted that the image size represents the same images which include the small area at the top of the image and indenter are still represented in the shown gradient plots.

Table 5-10: Shows the series of frames and the corresponding X and Y displacement plots in m. As stated earlier, the origin is in the top left corner, with x positive in the up-right direction and y positive in the left-hand direction.

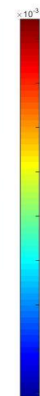
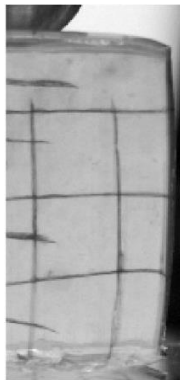
Frame	Captured Frame	X Displacement (m)	Y Displacement (m)
1			



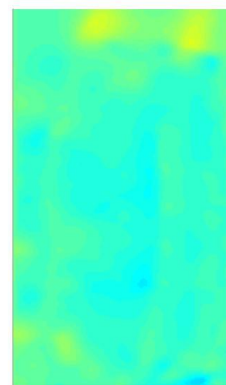
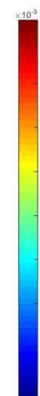
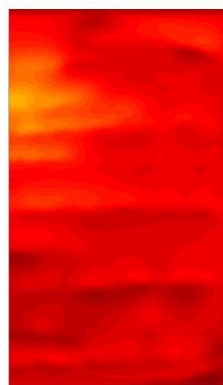
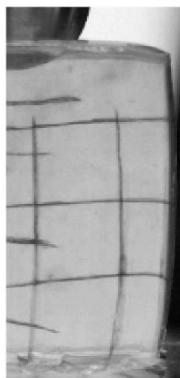
7



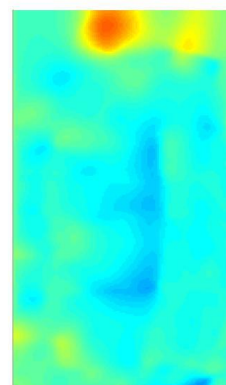
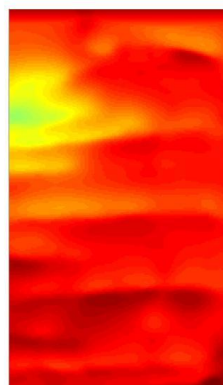
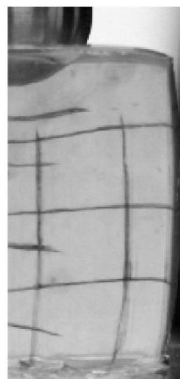
13



21

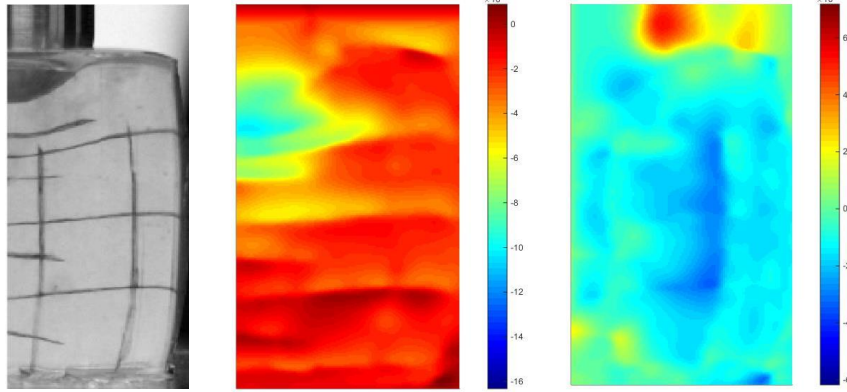


29



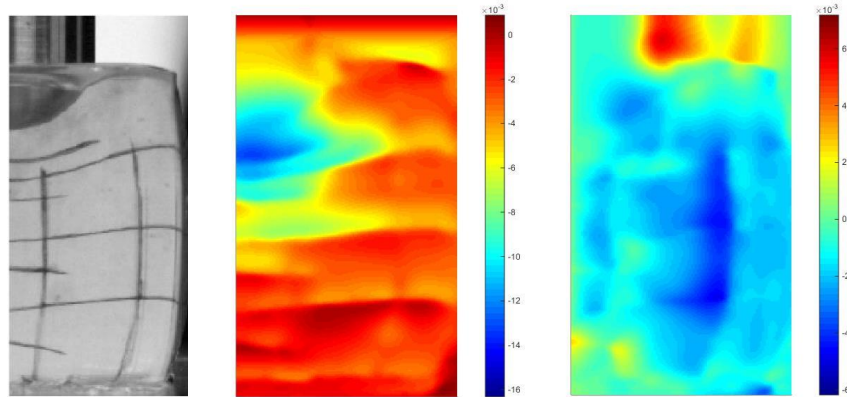
---

37



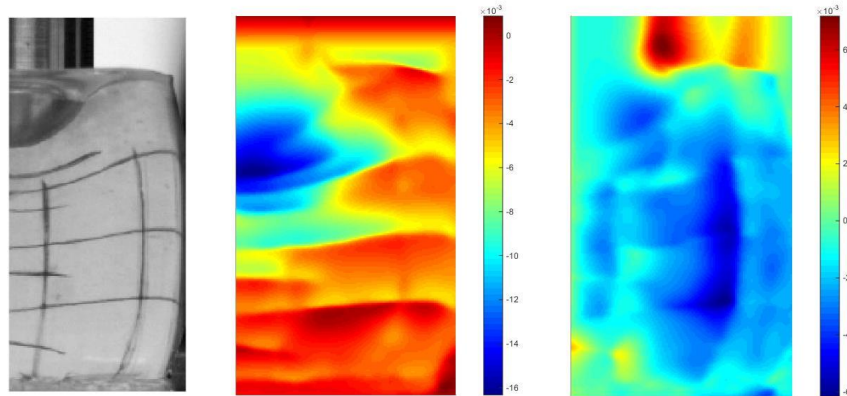
---

45



---

53



From the experimental output, it can be seen that the registration response clearly differs where there are fiducial markers in the sample and where there are not. If markers are present, the registration is more in line with what is expected but is still clearly ineffective. It should be noted that for each sample, the grid pattern was different. In this case, it would suggest the reason for the pair-wise apparent accuracy is due to the registration accurately capturing the motion of the objects in the image, but in the region which makes up the majority of the image, the registration is unable to capture the motion. As all components of the pair-wise transformation are

necessary to ensure accuracy of the whole composition, this would indicate that in this case, the lack of information or texture in the images limits the accuracy of the registration at the pair-wise level which inherently leads to an incorrect estimation of the transformation. This intrinsically means that it is not possible to compose the transformation across the consecutive registrations. This could be overcome by improving the accuracy of the registration so to account the region of similarities or of low data. It may be possible to improve and address the issue by increasing number of frames and a denser distribution of grid patterns within the sample or employing a 3D registration approach. However the accuracy of the registration method and ability to account for the areas of low data are limited as shown by comparing the model outputs to the peaks in the registered displacement.

#### **5.4.9. Comparison to Finite Element Model**

As identified, the registration has been unable to capture the displacement. This analysis will help validate the proposed reasoning for the error. Optical distortion and lack of markers resulted in the error in the pair-wise registration. To facilitate this a Finite Element Model was produced and loaded over the same time period as the indentation tests. From the model result, the displacement field was extracted.

The construction and running of the model was undertaken by a colleague, Christopher Noble, with the author providing all model inputs, boundary conditions, plan and data, alongside processing the model outputs.

To summarise, the model was constructed and run in the software Abaqus 6.13. To simplify the model, a formulation using the principle of  $\frac{1}{4}$  symmetry along the central axis of the indenter as the axis of symmetry was employed. The model uses the same fixed boundary condition and element arrangement used in Chapter 3, specifically 4-node quadrilateral elements (Abaqus 6.13 element CAX4R). A mesh independence study was performed for all individual indentation tests and the element number varied by a small margin for each. For the loading body, a rigid body was constructed using the measurement of the indenter and a loading speed of 10 mm/s which was applied in the downward vertical direction. The loading time period was the same as that extracted from the registration footage, using the CineView software package.

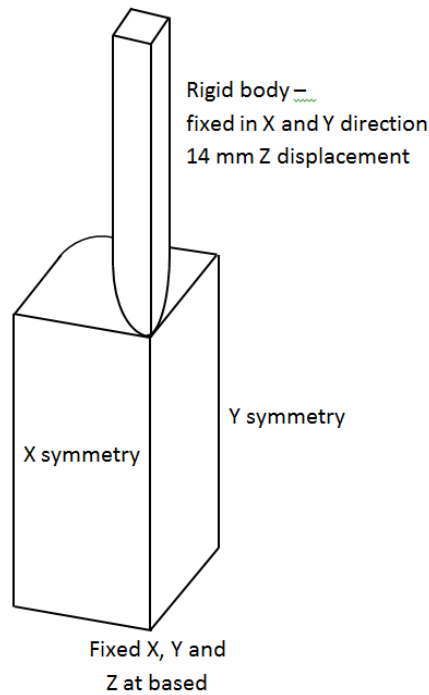


Fig: 5-16: Diagram of model showing the 1/4 symmetry that was applied along the central axis of the indenter and the rigid body that represents the indenter. The fixed condition can be seen on the lower edge of the main gel body.

For this model, the material model defined in Chapter 3 was used, specifically, the uniaxial compression test model. This hyper-viscoelastic model has been shown in the previous work to effectively capture the material response of ballistic gelatine at comparable loading rates to the indentation test being investigated. The material model parameters used can be seen in the Table 5-11.

Table 5-11: Shows the values of the material model parameters that will be used in the model.

Material Parameter	Value
$\mu_1$	22,110 Pa
$\alpha_1$	3.65
$\gamma_1$	0.528
$\tau_1$	6.66 s

The simulation was run over the same slightly reduced time period due to model limitations. This was still extracted from the testing footage and has been registered over to allow for a quantitative analysis. As with the registered deformation, the maximum indenter motion of the model output was extracted (from the displacement of the mesh which represents the maximum loading displacement) and plotted in black with the results that were extracted from the Tinius Olsen experimental

arrangement and registered data to allow visualisations as seen in Fig: 5-17. Where the Finite Element Model Input (black hashed line in Fig: 5-17), however due to the limitations occurred during the modelling you can see the maximum depth of indentation is not the same.

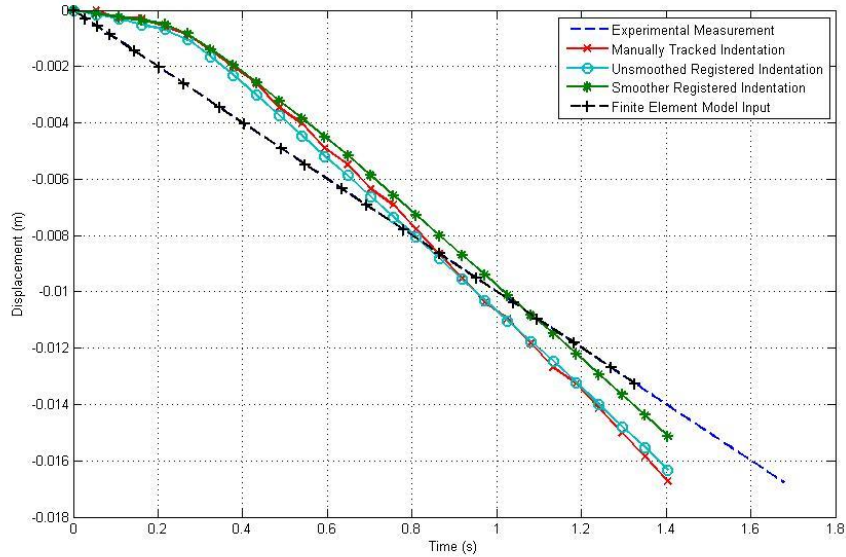
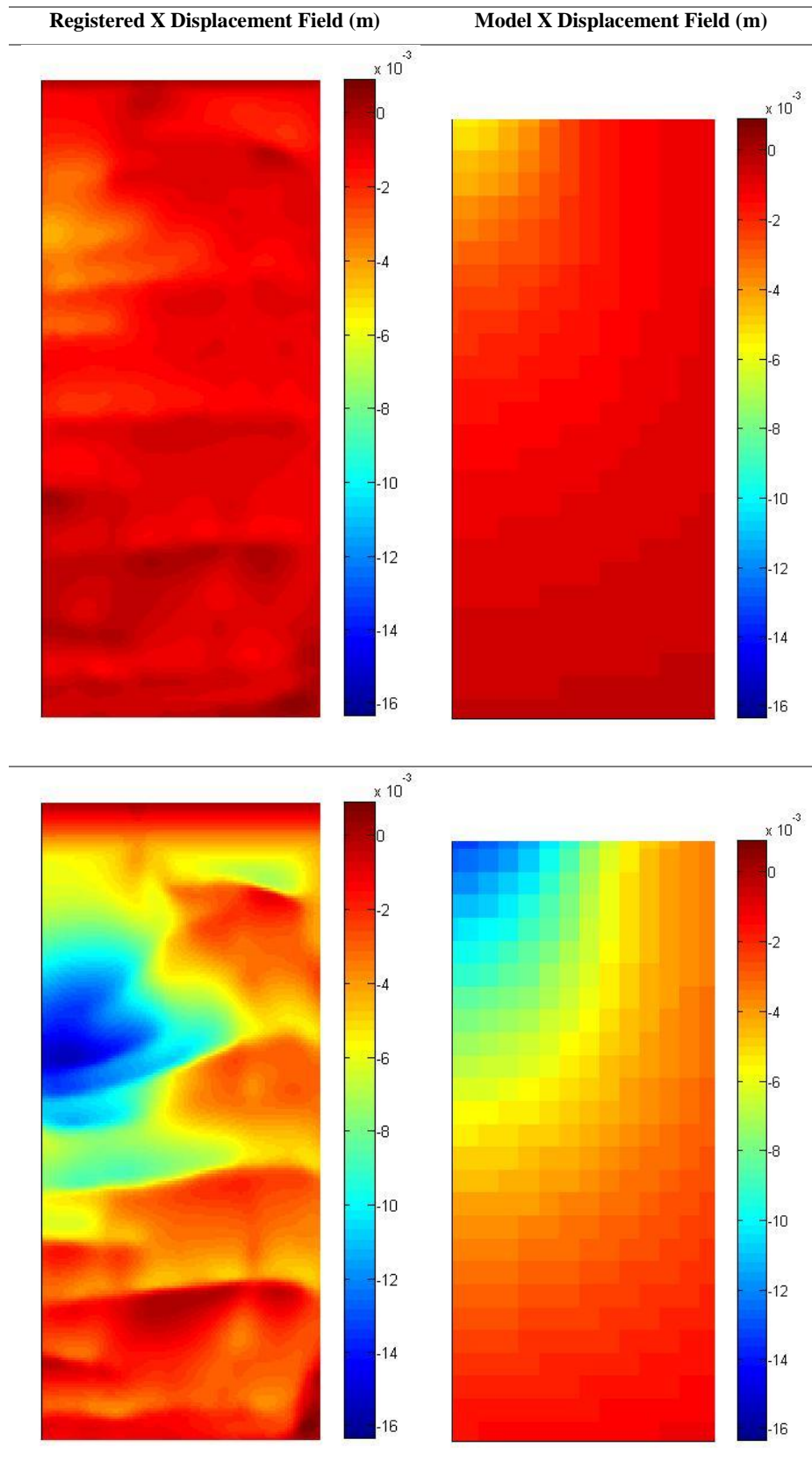


Fig: 5-17: In this figure, it can be seen that the FEA loading body maximum displacement has been chosen to ensure it is in a bracket to allow comparison between the different results.

The main model results can be seen in Table 5-12 overleaf. It should be noted that the size of the plots differ due to the composed transformation including a region that is above the surrogate. To allow comparison, the images were scaled accordingly to align with the surrogate.

Please see overleaf for Table 5-12.

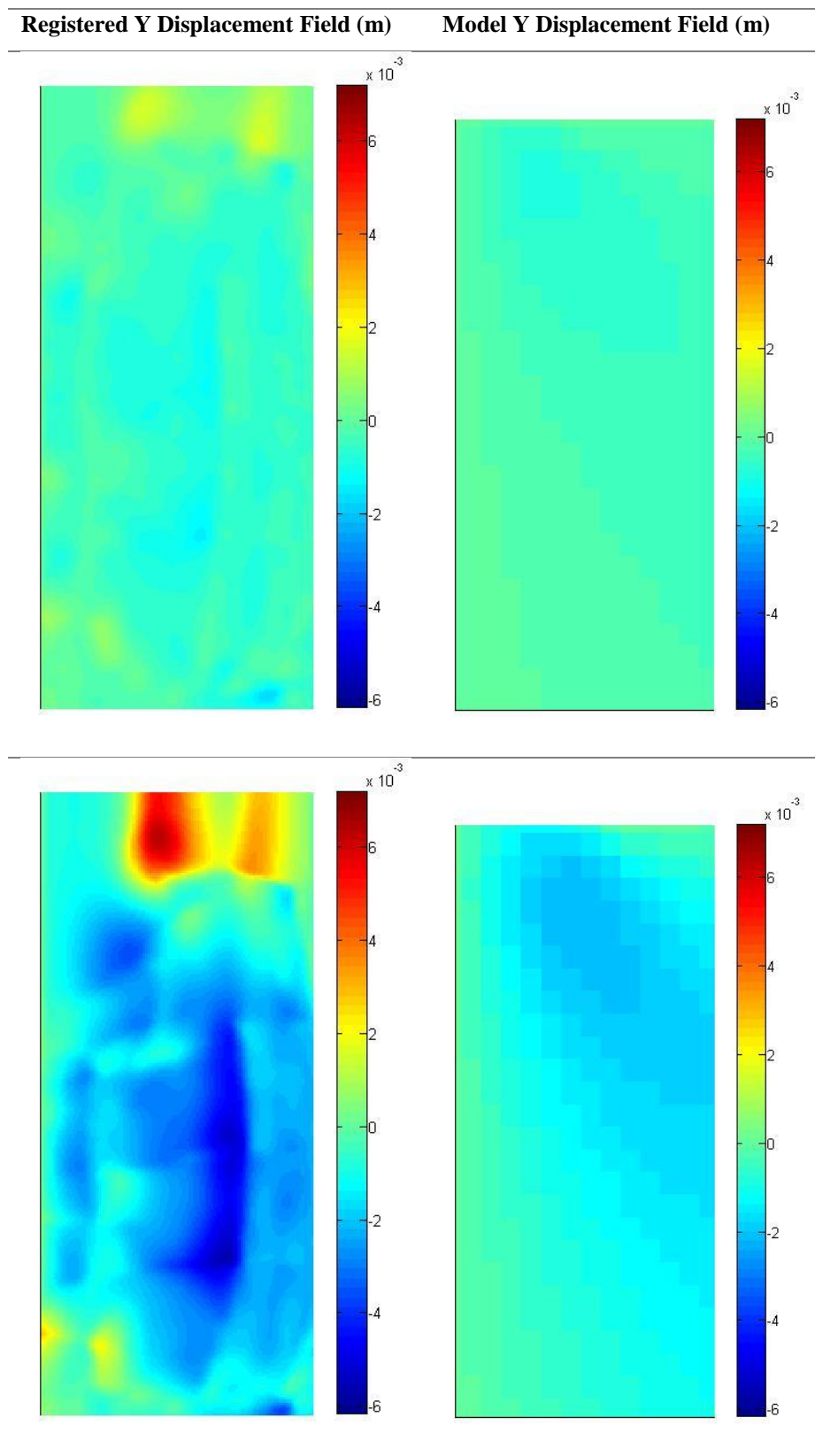
Table 5-12: Comparison between the output of the FEA model and the registered displacement field in the x axis. It should be noted that due to the registered images including the area above the surrogate, results in the differing sized plots.



The inaccuracy can clearly be seen in the images with a clear influence of the grid pattern in the composed transformation. Similarly, the FEA model shows a smooth displacement field. Table 5-12 shows the comparison of the displacement in x direction. The intensities can be seen to be of different magnitudes over the whole image. In regions where the grid pattern is present in the captured image, the result is more comparable between the composed transform and the computational model output. In the images above this is the clearly defined peaks in the composed transform. In the case of the y displacement shown in Table 5-13, this shows a high degree of difference between the composed transformation and FEA model. It is still possible to identify the influence on the grid pattern and of the upper area of the sample. The motion of the region above the surrogate surface can be seen when comparing the upper regions of the registered and model output. In the registered displacement, a mostly uniform downwards deformation can be seen across the upper surface but the model output shows a more uniform displacement radiating outward from the indenter. This is significant as this motion directly related to the upper surface of the sample being compressed by the indenter a multi-planar motion occurring. This is further complicated by a region above the sample having an opposing motion to the rest of the deformation which indicates it is moving away from the sample surface in registration. Please see Table 5-13 for a comparison of the y displacements, where the opposing motion is more significant and can be seen at the upper surface of the registered displacement. Also, a larger and more erratic output when compared to the model output can be observed. This implies that the motion of the surface and the region above the sample have significant impact on the quality of the image. This highlights that care must be taken to ensure that any non-related motion or image data is removed to avoid impacting the registration.

Please see overleaf for Table 5-13.

Table 5-13: Shows the same table as in Table 5-12 for the Y axis displacement field.



From these results, it can be seen that in this case, the application of the image registration to quantify of deformation was not successful. The accuracy of the pair-



wise registration was not able to capture the motion of the surrogate frame to frame, and hence, the composed transformation showed a great deal of artefacts from the individual registration rendering the results inaccurate. However, the qualitative assessment of the registration highlights that when objects are present in the image, the algorithm and method are able to capture the motion of these object frame to frame. In the majority of the images which have no texture and similar intensity values, the transformation is not able to effectively estimate the motion. During this assessment, it was also identified that the video capture method has had a direct impact on the maximum accuracy that could be achieved, as seen in the optical distortions in the captured experimental image discussed earlier in the Chapter. As only one camera was available for this testing, it would be prudent to investigate if other cameras would be available to be to try different arrangements which could improve the images captured.

## **5.5. Discussion**

When considering the work above, several points need to be discussed, which include the impact of the specific toolkit on the registration and the suitability of the method as a technique for the quantification of deformation for dynamic indentation tests.

As discussed in Chapter 4 and in 5.2, previous work investigated the use of different toolkits and the different options that were available. This included how the optimisation of the registration parameters and pre-processing of the images impacted the output of the pair-wise registration and composition of the transformations. When looking at the results of the experimental images, the need for pre-processing was clear as the nature of high speed video meant that the higher the frame rate, the shorter the exposure time. This can result in a need to backlight the sample if possible or an adjustment of the gain in pre-processing to maximise the contrast. In this work, there was limited space around the experimental rig, which meant that the camera arrangement was reliant on the ambient light which was sufficient due to the frame rate used. This resulted in minimal need to adjust the gain to improve the contrast as the exposure was sufficient to acquire images of the quality needed. However, as described in 5.2.1, it can be seen why cropping was necessary. As the image captured contained a lot of information that was not needed, and by removing these it increased the possible accuracy of the registration, while secondly reducing the computational cost and time taken to process the data. Registration computational cost were partially based on the number of pixels and the complexity of the images. This was further compounded by the multiple images

being registered sequentially over the data capture. There are other contributing factors such as the method, similarity metric and the specific algorithms (transformation/optimisation) that are used in the toolkit which can add to the computational cost. Pre-processing can be seen to have a large impact on the running of the registration but it was mainly focused on reducing computational cost and removing identifiable marks or distortions in the images that would negatively impact the registration method. For future work, the method used in this chapter was effective at this removal. However, as identified, the impact of using ambient light and the optical error that was identified need to be addressed using back lighting and adjusting the size of the sample to minimize the sample surface shape change.

The optimisation of the parameters for the specific experiment data set was important as it enabled an understanding of how of the algorithm will respond to a specific data capture. In the case of the toolkits suggested in this chapter, the application of optimised parameters can be seen to improve the response and has proven beneficial when considering the registration of synthetically transformed pair-wise images. This shows that the toolkits can be optimised for new experimental arrangements by tailoring registration parameters in line with the method used above. If the optimisation follows the method, it should be noted from the results that a quantitative measure should focus on the comparison of the transformation and direct measurement of the changes in the image not the similarity score. It was found that this was unreliable as a measured quantitative assessment. In future work, there will be a need to be cautious in the use of any metric as a method of quantitative analysis.

From the results that have been achieved, it is felt that this demonstrates that the registration method was unable to accurately capture the deformation that occurs over the course of the indentation tests. Three identifiable areas contributed to the inaccuracy: the errors induced in the experimental image capture method, the effectiveness of the pair-wise registration and composition of the consecutive pair-wise transformations.

From the results, obtained the impact of imaging a single plane in a 3D body has on the registration process has been highlighted. When looking at the images and the results plotted in Fig: 5-15, the consistent error has a high probability that it results from the optical errors induced the sample motion during loading. This is supported when the manually measured loading is compared to the machine loading and composed transformation, as the areas believed to have highest impact on the results are during the initial loading and the point of maximum deformation of the loading curve. This can be seen in the captured experimental footage as distortion of the

indenter and reflection on the sample surface. Since the camera arrangement in this case used ambient light, this meant a large portion of the light is reflected into the camera after impacting the sample which increased the likelihood of this effect as the light passes through the material in two directions. A possible solution would be to backlight the sample to minimise the reflection identified.

During testing, it was found that these objects are both out of plane with the motion of the indenter and grid pattern. The registration process could not differentiate the different planes. This would lead to inaccurate results as the algorithm attempts to register multiple planes of motion at the same time. In future work, there will be a distinct need to ensure that these objects or marks are removed or avoided during testing.

As identified, the registration was unable to capture the deformation over the course of the image. However, the qualitative assessment showed good correlation, which would indicate the registration was able to track the defined objects in the images. It, however, was not able to estimate the motion of the mainly plain background which formed the majority of the images. There were several options that were considered: These included a dispersed pattern to be applied to the loading plane of the sample. However, this would present many challenges as there would be a large possibility that any submerged or implanted speckle pattern would have to be added in the casting stage or during the gelling process. This would increase the likelihood of the markers moving out of the central plane and hence misinterpreting the results from the registration.

During testing the insertion method for the grid pattern, it was found that any dye of similar material would easily bleed or deform if inserted when the material gels. Alongside this, the final material showed defects and failure that were considered detrimental to the sample. Other methods that were considered to improve the registration included projection system and physically marking the samples which have seen some usage in the literature. However due to the aim of using this method to register penetrating impact inducing a failure or pre-damaging, the sample should be avoided which limits the use of the method in this case. In terms of the projection system, the resources were not available to use the method and as the tests undertaken have raised suspicion of the transmission of light being source of error, as the outer sample surface deforms during loading the lasers or projected light will also be affected and hence, this would lead to false registration as the projection moves independently of the sample.

In line with the theory discussed in Chapter 4, the registration algorithm identifies the difference in the images and aligns the reference and the floating images to produce the transformation. In most cases, the algorithms perform accurately when there are objects present in the image such as the grid lines or indenter. As these are distinct, the metric used can more easily identify differences in the grid points in the regions where objects are present. However, in regions where there are little to no objects, the algorithm cannot estimate the motion as these regions will have similar intensities and could be mis-registered or mis-aligned during the transformation. This would result in the image under qualitative analysis appearing to be accurate, as assessment focuses on the objects in the image pair and as shown in Fig: 5-13 and Fig: 5-14, but then cannot identify the wider sample motion as there is no object in those regions to qualitatively assess those areas of motion.

This is also supported by the similarity scores as these would be dominated by the alignment of the objects in the image. As the pair-wise registrations was flawed, this inherently meant the composed transformation would be inaccurate. This is detrimental to the application of the method and clearly shows that the sample creation method (specifically the way markers are included) needs to be revised to maximise both the accuracy of placement and maximising position within the sample while also defining a more robust way of assessing the pair-wise accuracy to allow identification of similar error in future applications. It does show that image registration as a base method can be applied to the images from experimental data, with further work required to enable it to be used for the quantification of deformation over consecutive images. The registration method failure in this case was not in relation to the core principals as the registration was able to track the objects in the recorded image. This, combined with various further segmentation and processing, allows image registration to function well in medical imaging. When considering the pair-wise registration output, the overlay accuracy showed good correlation and accuracy when the grid patterns are compared. This means that in future work, the registration of this area of the sample must be further assessed in greater detail to avoid the same errors.

Moving forward, there are several points that will need to be addressed; the two most crucial is a way to minimise the optical distortions that were imparted due to the camera arrangement, while also addressing the limitation occurred in the registration of the images and to improve the distribution of markers throughout the sample and the registration of the area between the markers. It is important to note that any future use of image registration in this case needs to assume the likelihood of this variation

impacting on the results and robustly assess the accuracy by expanding the assessment method proposed in this chapter to have a greater quantitative accuracy.

## **Chapter 6. Application of image registration to penetrating projectile impact tests**

### **6.1. Introduction**

This chapter will explore the application of the image registration framework discussed in Chapter 5. This was modified to address the difficulties and issues that were identified with the specific goal to present image registration as a method to quantify the displacement in penetrating impact tests that simulate the fragments, impact from military explosive ordnance. As discussed in Chapter 2, the device is assumed to be an IED that generates fragments represented by a 6mm ball bearing. To simplify the experimental procedure, only the impact of a single fragment will be considered as this allows the Chapter to focus the effectiveness of the applied image registration method. This Chapter will include a discussion on the previous penetrating impact testing arrangements that has seen use in the previous literature, including the method applied for image recording. This will be followed by a description of the registration process and the results produced, concluding with the findings of this chapter and the implications this presents.

### **6.2. Review of previous penetrating projectile impact experiments**

The investigation of penetrating impacts in laboratory-based experiments have followed a general common arrangement. This is a launching mechanism that provides the propellant force for the projectile and a tissue surrogate or target material, as well as a method for measuring both the impact and the velocity of the projectile. The tissue surrogates have seen previous discussion in Chapter 3, so this section will focus on the launching mechanism and the measuring system.

The specific launching method is dependent on the velocity being tested and the projectile that is being investigated. In the case of bullets or other military projectiles, it is common to use an equivalent firearm or weapon. This is prerequisite if the ammunition is specific to a weapon or the weapon itself is being investigated. In these cases, it is not uncommon to use a fixed mount with a remote trigger as this provides a high degree of repeatability and reliability compared to an individual firing the weapon where there is a limit to the consistency that can be achieved even by a well-trained marksman [20], [21], [23], [28], [172], [239], [240]. Another common method of propelling the projectile is the use of air-cannons or other pneumatic cannons. In some cases, inert gases or specialist propellants are used

depending on the cannon arrangement. These systems provide several advantages over the use of firearms: It is easier to have a finer degree of control over the velocity of the cannon, alongside a high degree of flexibility meaning they can (with minimal modification) be used to fire different projectiles. This control is achieved by altering the pressure of the cannon. Further refinement can be achieved by adjusting the sabot or launch length. It should also be noted that firearms are limited to the specific ammunition or calibre they have been designed to be used with. A very important benefit is that (depending on institute or country in which testing occurs) there is often a large number of legal and ethical restrictions surrounding the use of firearms. Air-cannons are less restricted and do not require the same space as is needed for firearm tests reducing the experimental costs and restrictions [98], [101], [111].

The tissue surrogate or target material that has been used in previous penetrating impact or ballistic tests has been previously described in detail in Chapter 3. In the literature, it was noted that the exact shape or concentration of the material has varied dependent on the specific investigation. Three main configurations were identified from the literature: the first is a simple block or cylinder of the chosen surrogate. The second is an anatomical shaped surrogate and the third is a combination of different surrogates used in tandem to create a composite sample [20], [23], [124], [125]. The other materials have included inorganic surrogates such as rubber or polymer foam used to represent human skin, or the use of gelatine alongside animal tissue and other biological surrogates previously discussed in Chapter 3 [21], [22], [154]. In this work, only a block-like geometry of the ballistic gelatine surrogate will be used as this simplifies the manufacturing and mounting arrangement, as well as removing any impact other composite surrogates would have on assessing the effectiveness of the image registration method.

In previous literature, two main measuring methods have been identified. These are optical-based methods and those based on physical measuring devices which was discussed in Chapter 4 and Chapter 5. The benefit of an optical-based approach for the measuring the dynamic response to the penetration of tissue surrogates was identified; These have focused on the application of high speed video technology or multiple single capture cameras triggered in series by other sensors. In general, this relates to the specific experiment as to which approach applied. The main challenge for all methods is to capture the footage at such a high speeds, which included limited exposure time for the detector to capture the data with sufficient quality. This requires the use of separate lighting, either a continuous light source or strobing light source synchronised to the frame rate of the recording device. This is to ensure there is enough light available to capture the images with the best possible contrast. The

exact positioning of the lights has normally related to the specific tissue surrogate and experimental arrangement that is being used. If using a transparent or a translucent material, then the light source is mounted behind the sample to allow visualization of the internal response of the surrogate. In the other cases, the light sources can be positioned behind the camera or above depending on the particular approach. The higher the frames per second the camera is operating at, the greater the intensity of the light needed to achieve good quality images with the desired contrast for assessment or post-processing. When using high intensity lighting, the thermal effect from such high intensity lights needs to be considered [23], [100], [101], [195], [241]–[243]. This is especially important to consider since in Chapter 3, it was identified that ballistic gelatine’s mechanical response can directly be influenced by the materials current temperature. This has not seen a large amount of investigation in response to how the temperature of the gelatine alters over the course of penetrating impact test in relation to how lighting or ambient temperature can affect the gelatine response in respect to time. However, with many methods, the lights are only turned on during testing which assists in minimising the thermal impact on samples during mounting or moving.

The assessment of the output has been described in the previous chapter but this did not explore the specific approach for analysis of the recorded video footage of penetrating impact tests. A common process that featured in all the methods that have been identified in the literature is a qualitative assessment of the sample. This can identify the permanent damage that has been inflicted at the macro-scale and any anomalies that would suggest that the data would include variation. Two main assessment methods have been applied: Manually outlining or measuring the cavity and the use of automatic or semiautomatic methods which extract the speed or position of the penetrating projectile. [21], [114], [124], [154], [170], [244]. In this work, a combination of a manual measuring of the fragment path and velocity, combined with the use of image registration was used which can be classed as a semi-autonomous approach using a modified version of the assessment method applied in Chapter 5.

As it is very complex to measure penetrating impact and be able to validate the motion of the surrounding surrogate material, Finite Element Analysis and other computer models have been used to calculate the resulting displacement of the wider surrogate motion, which can also be expanded to include the flight of the projectile before and after impact. These models either take the cavity information from the experiments or as a standalone model with the same assumption applied in their creation to generate the output. This has led to promising results but is limited by the



capabilities of a particular software, modelling method and material parameters used [23], [121], [167], [172], resulting in the continued use of manual measuring, specifically of the after impact damage and depth of penetration, alongside the manual tracking of the projectile path over the captured video data. Often, the manual measuring or segmenting of the cavity and projectile path have been used as a form of validation for the model outputs. This is the method that will be used in the following work to validate the response of the registration as the focus is establishing the applicability of image registration to quantify displacement and to address the limitations that have been identified in Chapter 5.

### **6.3. Explorative testing**

Before the main experiments were undertaken, a number of explorative tests were performed to investigate the gelatine mounting arrangement, specific launch velocity and the achievable repeatability.

Several different mounting arrangements were explored which included both confined and unconfined arrangements. The gelatine itself was produced using the method described in Chapter 5; however, in this case, no grid pattern was added as this would have provided limited benefit in explorative testing. A range of different moulds were explored, which included the same moulds used previously in Chapter 5, alongside an 80 mm x 80 mm x 110mm cuboid food container. A range of other mould shapes were investigated. These were either found to be impractical in casting or during testing; this included cylinders and various cuboid moulds.

Two stages of testing were undertaken: the physical testing of the air-cannon including its effective use and the depth of penetration being one stage. The second being the camera equipment and lighting arrangement. All will take the approaches used in Chapter 5 as a starting point

To assess the impact and power of the air-cannon a physical measurement of the depth of penetration using a ruler was used to identifying the consistency while also investigating the ability to repeatedly and consistently load the sabot to the same position.

A range of loading depths were tested as it was believed that this would have an impact on the final velocity and accuracy. It was found that launch depth of less than 50 mm produced inconsistent impact both in terms of depth and angle. A launch depth greater than 250 mm lead to difficulties in ensuring the ball bearing was loaded correctly due to the ball bearing slipping out of the sabot. From these tests, it was

decided that the launch depth for all future testing would be 200 mm as it was repeatable and within the range identified supported by the explorative test that were performed.

Next, the effects of the launch pressure and cannon recharge were investigated for repeatability and consistency. A range of pressures were investigated from 1 bar to 6 bar. The depth of penetration was found to vary at different launch pressures but the angle of launch was near vertical for each. For launch velocities below 2 bar and above 4 bar, the cannon did not consistently recharge after each firing. An investigation in to why this occurred could not be easily defined as inspection of the cannon showed that all the seals and mechanisms were working as expected but the cannon drew its pressurized air supply supplied by the building compressor. This indicated that this was the limitation induced by the building systems.

This then led onto the investigation launch velocity between 2 bar to 4 bar while camera arrangement needed to capture these velocities. During pressure testing, it was found to be impractical to mount a light gate or other methods of recording the launch velocity with the cannon arrangement. The need to synchronise the cannon launch with the light gate was not yet possible with the specific camera equipment and cannon arrangement that was available. So it was decided that the most practical method would be to use the camera arrangement to also record the impact velocity with the added benefit that this allows the flightpath before impact to be investigated aiding in identifying why any miss-fire and outlier penetration pathways occurred.

Camera equipment is the same as that already been used in Chapter 5; However, as the exact arrangement required investigation, since filming high-speed penetrating impacts presented different challenges. This includes defining the resolution of the image, the position of the camera and the lighting required. The camera was initially set up to image through the sample in the same arrangement used in the Chapter 5. However, as the possible velocities involved are much faster, a higher FPS is required which then necessitated the use of backlighting as the ambient light in the lab did not provide sufficient illumination. Several different lighting methods were experimented with. LED lighting was initially tried as this would cause little to no heating of the sample. This was not found to be viable as the FPS that was required to capture the penetration was greater than the frequency of the LEDs. This meant the footage was not viable as the recorded material alternated between illuminated and not with the LED frequency. The arrangement found to be most suitable was a high wattage halogen spot light system. This provided the needed light intensity, but introduced a new issue in that in the region near the centre of the light source, the

intensity was so great that it impacted the clarity of the images collected. Producing a region of such high intensities meant that the grid pattern and projectile were not visible in the image. To address this, a twin halogen spot light arrangement with two lights positioned off-centre and angled inward by a small amount was found to produce a diffuse light that allowed clear imaging of the penetration without the high intensity regions caused by the single spot light, maximising the clarity of the recorded images.

Once this was identified, the next step was to determine the position of the camera. This focused on ensuring that the camera clearly images the region of interest where the penetration will occur as well as recording the flight path before impact. When adjusting the resolution, it was found the default was to adjust in the horizontal direction in-line with the camera's central axis. The software did not allow this to be adjusted so the camera was tilted to 90 ° on the camera's stand, so the image frame could now be adjusted in the vertical direction allowing the capture of the projectile's flightpath and penetration. This long rectangle could be adjusted as needed for the specific sample and projectile, maximizing the FPS achievable and the ROI that could be investigated, which for the 4 bar and 6 mm ball bearing was found to be a resolution of 1024 x 256 pixels, with the top edge of the image aligned with the top edge of the sample mount.

With this, all the main experimental arrangements and equipment settings were identified which allowed the work to proceed, while also helping in understanding the limits of the experimental equipment which will help with the analysis of the results that will be captured.

## **6.4. Experimental arrangement**

For these experiments, the following arrangement was used. The core components of the experimental rig can be divided into three parts: the launcher, the camera arrangement and the sample mounts/moulds.

### **6.4.1. Air-cannon**

The propellant force was provided by a vertically oriented air-cannon shown in Fig: 6-2. The reason for the use of a vertically oriented air-cannon is the availability of a suitable air-cannon and this also means that projectile flight path does not have to be taken into account to the same degree as when using a horizontally aligned air-cannon. The cannon is supplied by an external compressor system that was mounted

in a secure frame with a ballistic resistant shield for user protection with a sample mounting system positioned approximately 10 cm above the barrel aperture suspended from the cannon frame. A sabot with a magnetised projectile holder and metal launching plate was used to propel the projectile and ensure repeatability. The sabot was constructed from a stiff EVA foam core that was the same diameter as that the internal air-cannon providing an airtight seal. This then in the centre had the magnet embedded in it with the metal reinforcement plate mounted on top of the foam with a registration hole drilled in the top to align the projectile. A schematic is shown Fig: 6-1.

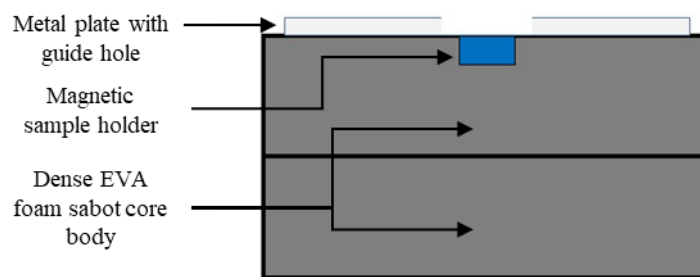


Fig: 6-1: A schematic cross section of the sabot used showing the EVA core (in grey), magnet (in blue) and mounting plate (in light grey).

Please see overleaf for Fig: 6-2.



Fig: 6-2: The cannon in the lab the mounting plate can be seed suspended from the frame and the ballistic shield can be seen surrounding the barrel aperture, with the compressor tank seen below the cannon body.

#### 6.4.2. Image collection method

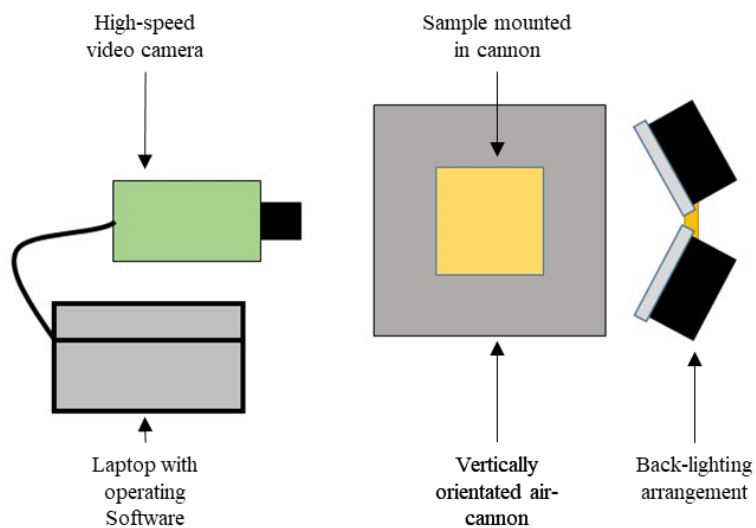


Fig: 6-3: A top view schematic of the arrangement used to film the ballistic impact, showing the camera and connected laptop used to record the impact, with the lighting rig visible on the opposite side to the camera arranged to produce a diffuse back light and the sample mounted centrally in the air-cannon.

The image capture method identified in Section 6.3 was used to capture the penetration, consisting of two main components: the camera itself and the back lighting arrangement. A Phantom V210 digital high speed video camera was used and was supported by the Phantom Cine software package which controlled the camera setting with a recording speed of 8501 fps with a resolution of 1024 x 256 pixels. This gave an exposure time of 116.89  $\mu$ s and a frame time of 117.63  $\mu$ s. As with the previous arrangement, a SLR Nikon Nikkor 24-85 mm Focus 2.8-4 mm DIFAF lens was used. The entire camera arrangement was mounted on a tripod to maximise ease of repositioning. All tests were backlit with an 800 W spotlight arrangement that consisted of a pair of 400 W spotlights arranged on multi axis mounts, positioned to produce a diffuse light to avoid intensity peaks. By back lighting the sample, it was found this minimised the optical effects that were seen in the previous chapter. It should be noted as before that the focus and aperture of the lens were modified and adjusted for each test to ensure the best image possible. With each modification of the focus and aperture, a calibration image is taken and reference to that arrangement to ensure spatial accuracy was maintained. For each of these different arrangements, a lens effect study was undertaken with the lens effects being found to be negligible.

The use of the powerful spot lights to back-light the sample led to sample heating. This was minimised by ensuring the lights were only used when necessary. This meant the cannon was set and prepped for firing, the sample was t but in place and the camera initiated; the light was turned on and the camera view checked; the cannon was fired and the light then immediately turned off. This short exposure time combined with the ballistic screen and the air gap meat that the main heating source is the ambient temperature within the cannon arrangement.

#### **6.4.3. Sample mount and mould**

The final components of the experimental arrangement are the sample manufacturing moulds. These were specifically produced to serve dual purpose as both a mould and cartridge for loading the samples into the air-cannon. It should be noted that the sample mount and the moulds both featured transparent sides to allow through imaging and transmission of light through the sample seen in Fig: 6-4. All the moulds were cleaned after usage to remove any marks that would reduce the quality of the recorded data. The same cleaning process was also applied to the window mount.

Imaging through two ballistic screens was not an ideal situation but due to the lab conditions, this was a necessary arrangement for health and safety reasons. This meant that artefacts that were on the screen such as dust or dirt could affect the images that were recorded, which necessitated regular cleaning to minimise this. As the surfaces were partially reflective, it could impact the imaging. This was overcome by reducing the ambient light during firing, to maximize impact of the back lighting. The ideal would be to image with no ballistic shielding; however, as mentioned this was not possible.

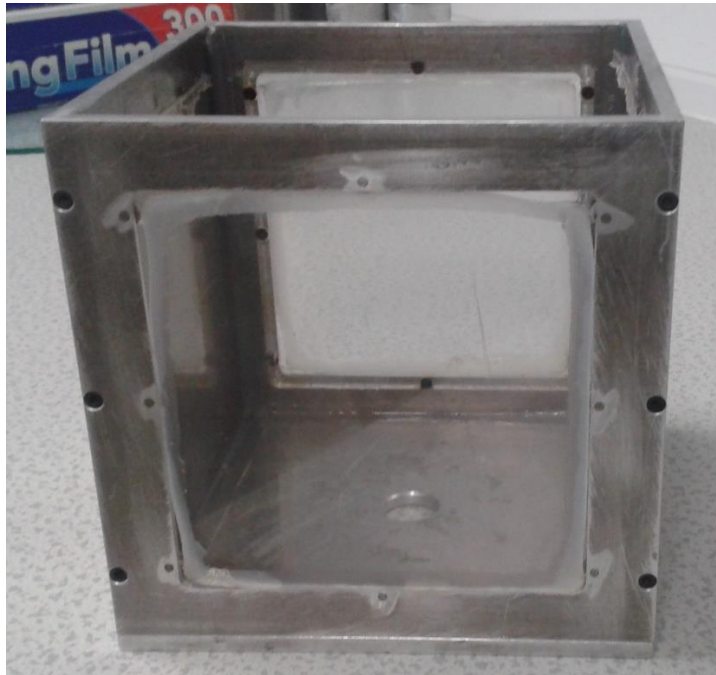


Fig: 6-4: An image of the mould that was used which shows the transparent window to allow the visualisation of the sample, which allowed the casting 160 mm x 160 mm x 160 mm gelatine. Please also note the hole that the projectile will pass through to impact the sample.

#### **6.4.4. Projectile**

As defined in Chapter 2, the fragment that will be used is a 6mm steel ball bearing. As previously discussed, this chapter will only consider single fragment impact during these tests. For full reasoning, please see the previous work in Chapter 2, but in summary, this work is focused on the validation of the method and multiple impacts would complicate the assessment. The technical specification of the ball bearing are as follows: 6 mm mild steel ball bearing weighing 0.89 g.

## **6.5. Experimental method**

Two different sample mounting conditions were investigated in this work: the first was a confined and the second an unconfined mount. The experimental method has three steps: manufacture of a consistent sample, the acquisition of the penetrating impact data from the experimental arrangement and the application of the image registration framework for the assessment of the penetrating impact videos.

### **6.5.1. Sample preparation**

For the experiment, the same manufacturing method that was applied in Chapter 5 was used. However, it was expanded to include the monitoring for material distortion and temperature during the casting process. There were several considerations that were taken into account due to the larger volumes of gelatine needed. The method differed in the casting as each mould required a single batch of material. In this work, the gelatine was cast into cubic moulds/cartridges of dimensions  $160\pm 1$  mm x  $160\pm 1$  mm x  $160\pm 1$  mm each representing an individual sample. The samples were cured in line with the previous method. After curing and removing from the mould, they were injected with the grid pattern both in the horizontal and vertical alignment using the same method applied in Chapter 5. The grid was injected using a 150 mm spinal needle which was marked every 10 mm. This was used to ensure that the dye was injected to the same depth each time. Initially, the vertical grid lines were injected to a depth of 140 mm taking care to minimize the needle bend that could occur, then, the horizontal grid lines were injected alternating the dye left to right until the full grid pattern was complete. Due to the errors induced in that method, it was modified to attempt to maximise the distribution of the markers across the sample while also maximising the accuracy of the placement in the expected plane of impact.

There are two considerations that should be noted that were particular to the experiments performed: The first is that in the case of the confined experimental arrangement, the samples were placed back into the mould/cartridge before testing. The second consideration is, as was highlighted in experimental work of the previous chapters, the effect of temperature on the material. To account for this and minimise the possible impact this will have, only three samples were produced and tested at any one time and the samples remained stored in the fridge until testing was undertaken resulting in minimal exposure to change in temperature before testing. By also using larger samples, the time taken for any thermal effects to occur is reduced as the thermal energy from the back-lighting and ambient atmosphere



increasing the time that the samples can be outside of the fridge, which in turn reduces the pressure when conducting experiments.

The sample produced was to represent a uniform composition of muscle and other soft tissue of an extremity as this was highlighted as the most likely site of impact for these types of injuries in Chapter 2. This also allows this analogue to be applied to a wide range of body regions alongside being in line with the material parameters identified in Chapter 4.

### 6.5.2. Sample mounting arrangement

As previously stated, two different sample arrangements were explored. These included a confined arrangement and an unconfined arrangement. In the case of the confined arrangement, the samples were fixed on all sides and free to move on the upper and lower sample face (see Fig: 6-5). This arrangement was used to allow investigation of the surrogate in situations where the body is constricted by either clothing or body armour as this will affect how the surrogate will respond to the penetration. Unconfined impact was also investigated as the comparison to the confined arrangement seen in Fig: 6-5. The unconfined arrangement allows the surrogate to respond freely for the given geometry which represents the impact of exposed body parts such as extremities which are not constrained during impact.

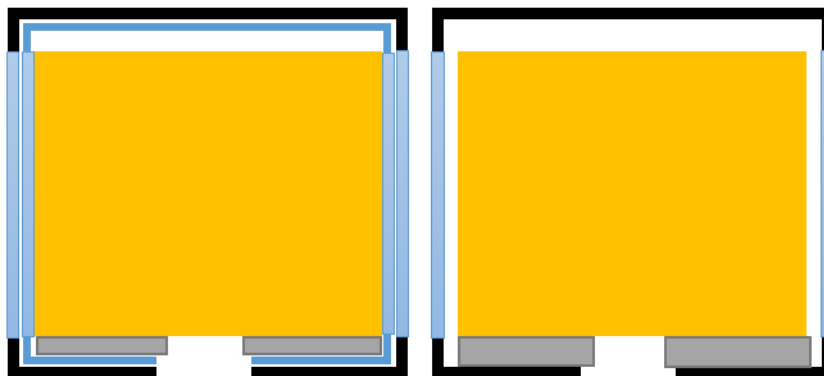


Fig: 6-5: This shows the two mounting arrangement. On the left, the sample is confined on all faces bar the top and freely resting on a support block at the bottom. On the right, the unconfined sample rests on the support block to ensure it is at the correct height. Support blocks were manufactured from a single sheet of plywood with a hole that aligns with the sample mount hole. It should be noted the light blue represent the clear panels and the dark blue the mould/cartridge.

### 6.5.3.Data capture

Using the experimental arrangement that has been described in 6.4, all tests were performed following the method described in this section. The method was the same for both sample mounting arrangements. Six impact experiments for each loading arrangement were conducted with each experiment being made up of three tests.

Initially, the experimental arrangement was set up and the cannon systems checked for defects or safety concerns. Once identified as safe to use, the experiment continued. The sample mount was put in place and the camera positioned and connected to the control and recording system. The camera was then focused and aligned to the expected impact plane, using a calibration board which had a checkerboard pattern applied with each square having the same dimensions of 19 mm x 19 mm. Due to the board being solid, it was not possible to back light this resulting in dark image. However, by post-processing using the gain modification tool in the CineView software, it was possible produce the images that had the needed definition to be able to measure the grid pattern. This was performed for each separating experiment session or if the camera was moved, this ensured that spatial accuracy was maintained for all tests in line with how the indenter was used in the experiment in Chapter 5.

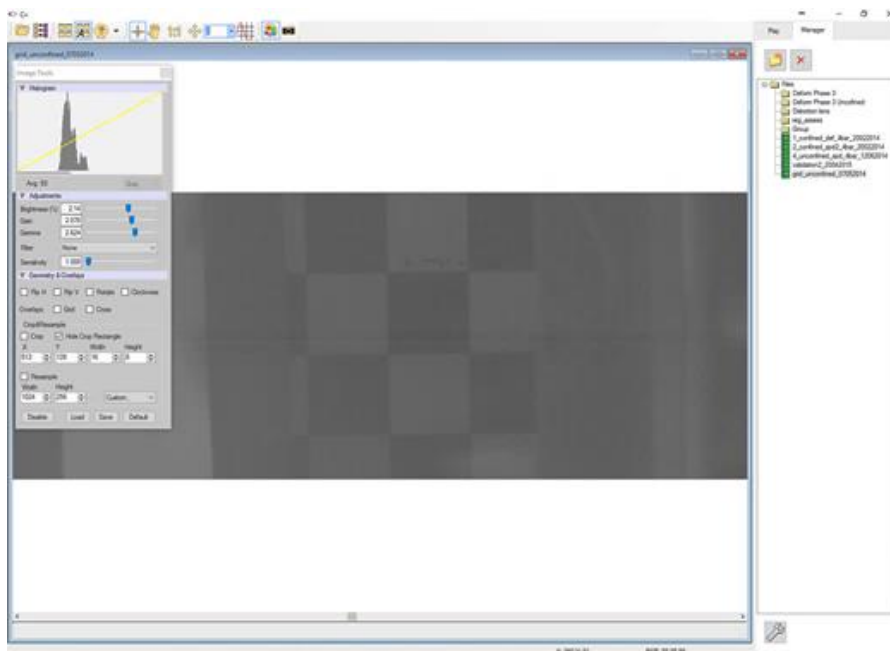


Fig: 6-6: The grid pattern is extracted from the frame and the same pre-processing is used to improve the contrast. These images were not back lit due to the opaque nature of the board the grid pattern was mounted on so to perform the calibration, the gain and intensity had to altered to allow measurement (This uses the CineView software package).

The ballistic gelatine samples were then removed from the fridge and transported to the cannon. In the case of the confined experiments, samples were in the moulds/cartridge designed to be mounted directly on to the experimental arrangement. In the case of the unconfined tests, samples were loaded directly into the sample mounts resting on supports to align the sample with the mount windows. In all cases, care was taken not to damage the sample and to ensure that the grid pattern was positioned centrally above the barrel and perpendicular to the camera in the expected plane of impact.

The 6 mm ball bearing was loaded into the sabot and pushed down the barrel to a set level which was the same for each test to a depth of 200 mm from the top surface of the cannon barrel using a custom tool to ensure that the cannon was consistently loaded. The cannon was charged to a pressure of 4 bar, measured on the pressure gauge mounted on the cannon rig. The space between the sample mounting plate and the barrel was 120 mm which required the loading of the cannon before the sample was put into place. This means that care must be taken to avoid accidentally firing. It should be noted that the cannon had an automatic re-pressure system to ensure consistency of cannon charge over multiple firings. The pressure was checked after each re-pressurisation to ensure that consistency was maintained. As the cannon was not equipped with a velocity sensor, the camera arrangement captured the barrel launch velocity for each test, being measured from the captured data footage.

Once these checks had been performed, the cannon was fired. During the firing, the sabot is propelled up the barrel until it impacts the barrel stop and the sabot is retained in the barrel and the projectile continues on impacting the sample. After the impact, the cannon was made safe and the desired movie frames were extracted and saved for analysis. It was not possible to perform multiple penetration test on the same sample due to damage changing the surrogate's material response. Once the penetration test was performed, two more firings were undertaken using the same sample. These are dedicated to identify the consistency of firing in terms of speed and plane of impact, while also looking for a similar depth of penetration for each impact. There were small variations due to the prior impacts but it provided a rapid means of assessing the consistency. This information aided in identifying variation or possible sources of error as it has been identified that out-of-plane motion can have negative impact on the results of the registration. This process was repeated for each sample in the given experimental session. All captured data was saved before passing on to the data processing stage.

#### **6.5.4.Data pre-processing**

As with the previous chapter, pre-processing involved the cropping of the data to remove undesired image information that will not be used in the registration. This was decided by assessing the raw data and identifying the maximum cavity and the maximum penetration while also assessing the transmission of the shock wave to define the ROI. When defining the ROI, it needed to account for the rebound of the projectile as this is beyond the point of where the projectile comes to rest. Assessing the shock was viable over the longer image as a whole as it possible to track the propagation through the motion of the grid pattern. This propagation was at a much slower velocity to the penetration but is still a component of the penetration process. Once this has been performed, the gain and gamma of the image is modified to allow the maximum contrast. This was modified uniformly across all the samples that were collected from the same experimental testing session as the lighting and camera arrangement was the same. However, it was found that across the different testing, the adjustment needed was comparable. This does not affect the motion in the image and this assumption has been proved to be effective in Chapter 5. This was performed for all tests to the extracted ROI of the penetrating impact (Fig: 6-7 and Fig: 6-8) and the projectile flight before the impact for the assessment of the initial impact velocity.

Please see overleaf for Fig: 6-7 and Fig: 6-8.

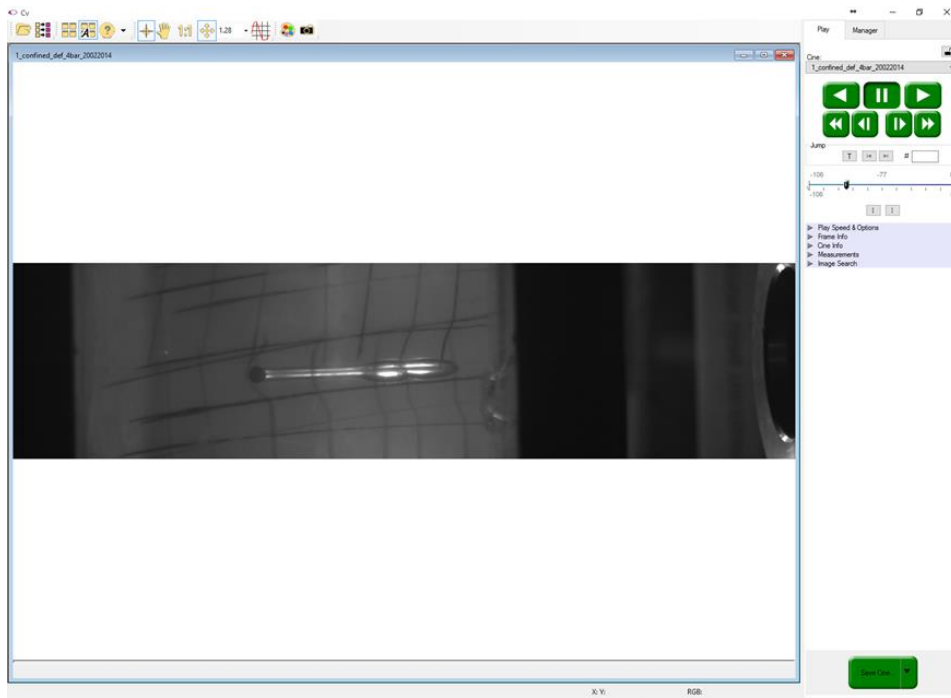


Fig: 6-7: An example of the penetration data captured showing the point of the maximum penetration that occurs before the gel rebounds to form the permanent cavity. Picture here open in the CineView software before initial editing occurs. On the right of the image is the control panel and the frame position in the movie.

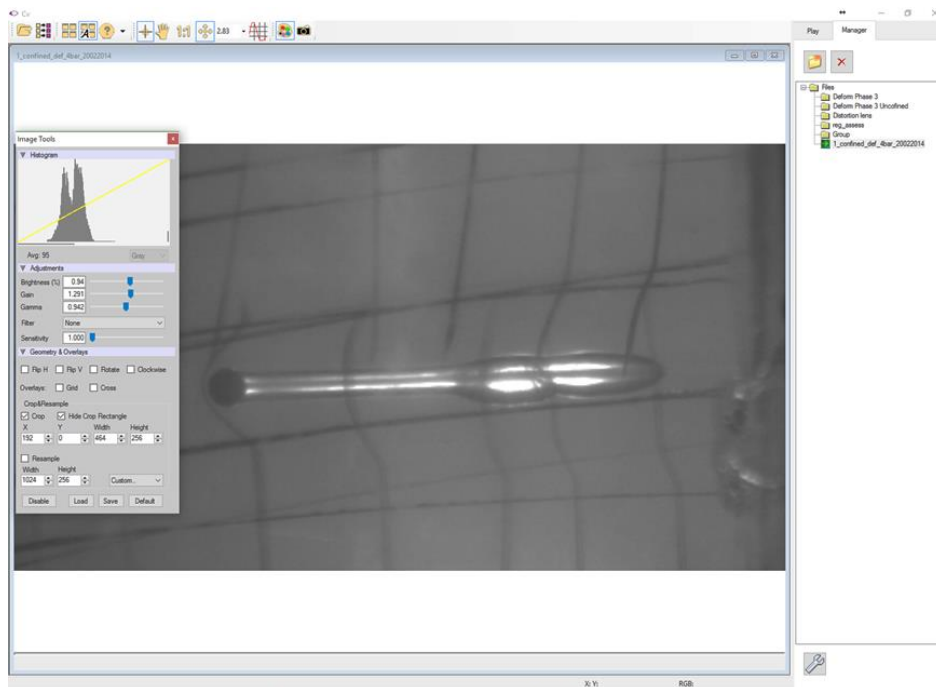


Fig: 6-8: The cropped region of the data and the CineView tool that was used to adjust the gain and brightness to maximum contrast to optimise the image for the best possible registration. In some samples, variation in the material resulted in an asymmetric cavity growth and motion that results in the general tear drop shape that the maximum cavity forms before the rebound and collapse occurs to dissipate the energy of impact.

### **6.5.5.Determining impact velocity**

To determine the impact velocity, the section of the data capture that showed the projectile travel was extracted as discussed previously in section 6.5.4. The velocity was measured by tracking the forward most tip of the projectile over the frames of the corresponding data. This spatial data was then calibrated to produce actual travel of the projectile. Then using the known frame-time, it was possible to generate the velocity which showed some minor variation between the tests the velocity achieved are discussed in 6.6.1.

### **6.5.6.Application of image registration**

The registration framework that was used in the previous chapter was applied to the experimental data with considerations made to address specific challenges that were presented by the penetrating impact and the limitations that were identified in Chapter 5. This included the effect of material failure and response of the surrogate surrounding the cavity throughout the different stages of penetration, specifically around the rebound and transmission of the shockwave as this is the location of the main dissipation of the absorbed potential energy that results from the gel absorbing and dispersing the kinetic energy of the projectile. It also identified if the grid patterns were effectively distributed to be captured by the high speed video camera. A crucial component of comparing the experimental data capture and the registration was to identify if there were any errors that resulted from marks on the sample or optical distortion that were discussed in Chapter 5. As before, the pair-wise transformations will be composed in-line with the previous chapter to allow for the assessment of the ability of the method to quantify displacement.

### **6.5.7.Refinement of registration parameters**

As with the previous chapter, an optimisation of the registration parameters was undertaken to maximise accuracy that could be achieved. This followed the same process as Chapter 5 with selecting an image from the data capture and applying an approximation of the observed image transformation. The image was transformed using the same function that was applied in Chapter 5. As with that Chapter, transformation was defined in terms of  $x$  and  $y$  for each pixel. The transformation follows the similar arrangement used in the synthetic images in Chapter 5 with a more complex expansion and extension of the cavity. The optimisation was started with the

same parameters that were used for the initial registrations undertaken in Chapter 5 shown in Table 6-1 and Table 6-2.

Table 6-1: Shows the registration parameters used in the registrations of the images using the Nifti-reg toolkit.

<b>Registration Options Nifti-reg</b>	<b>Condition 1</b>	<b>Condition 2</b>
<b>Spline Grid Spacing [x y z]</b>	[5 5 1]	[5 5 1]
<b>Bending Energy Penalty Term [weight (%)]</b>	[0.005]	[0.005]
<b>Similarity Metric</b>	NMI	SSD

Table 6-2: The registration parameters used in the registrations of the images using the Non-Rigid Version 3 toolkit

<b>Registration Options Non-Rigid Version 3</b>	<b>Condition 1</b>	<b>Condition 2</b>
<b>Registration Method</b>	NonRigid	NonRigid
<b>Spline Grid Spacing [x y z]</b>	[10 10 1]	[10 10 1]
<b>Thin Sheet Bending Energy Penalty Term [weight (%)]</b>	[0.001]	[0.001]
<b>Similarity Metric</b>	PI	SSD

It was found during these tests that the response of the Nifti\_reg toolkit resulted in warping and inclusion artefacts that resulted in a poor registration output. Including the application of an affine initialisation still resulted in poor registration accuracy. The warping and the inability of the toolkit to capture the cavity extension lead to the Nifti\_reg toolkit being no longer used for these data sets. Examples of the artefacts can be seen in Fig: 6-9 , with C and D showing clear difference in both the extension and expansion of the cavity (please see labels on figure) specifically noticeable along the edge of the cavity showing a step in the cavity. Grid distortion in the cavity that can also be seen in the deformed image and is not present in the registered images (C and D in Fig: 6-9) centred in the cavity. However, the wider grid pattern shows good correlation (B in Fig: 6-9). This has shown that even though the registration was ineffective in this case at capturing motion of the cavity, the wider motion for the grid pattern is captured.

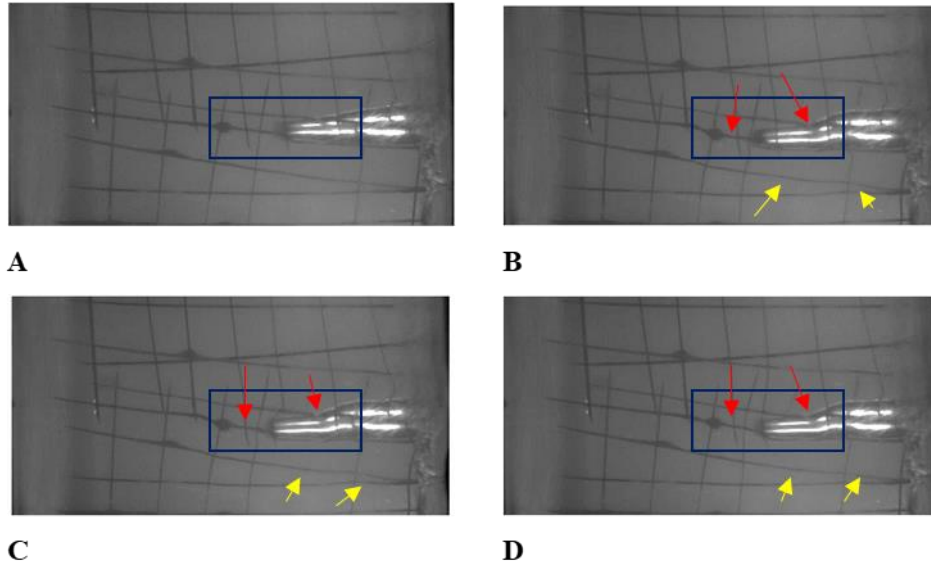


Fig: 6-9: This shows the response of the nifti\_reg toolkit, A: Moving Image, B: Static Image. The warping and inability to capture the projectile movement can be seen with C: NMI registration and D: SSD. The region is indicated by the blue rectangle is the region with the greatest difference with the variation in the projectile and cavity position. Also note the area that has been highlighted by the yellow arrows, as C and D both show distortion that is not present in the static image.

The Matlab-based toolkit was applied initially using the basic parameters already defined and this showed noticeably better response. However, artefacts were still present in the output, see Table 6-3. Further optimisation included the modification of the value of the penalty term and the B-spline grid size. The grid pattern was set to the finest possible setting and this caused a small increase in the smoothness of the transformation which was as expected. With the penalty term having the most distinct impact on the response, the output can be seen in

Please see overleaf for Fig: 6-10.



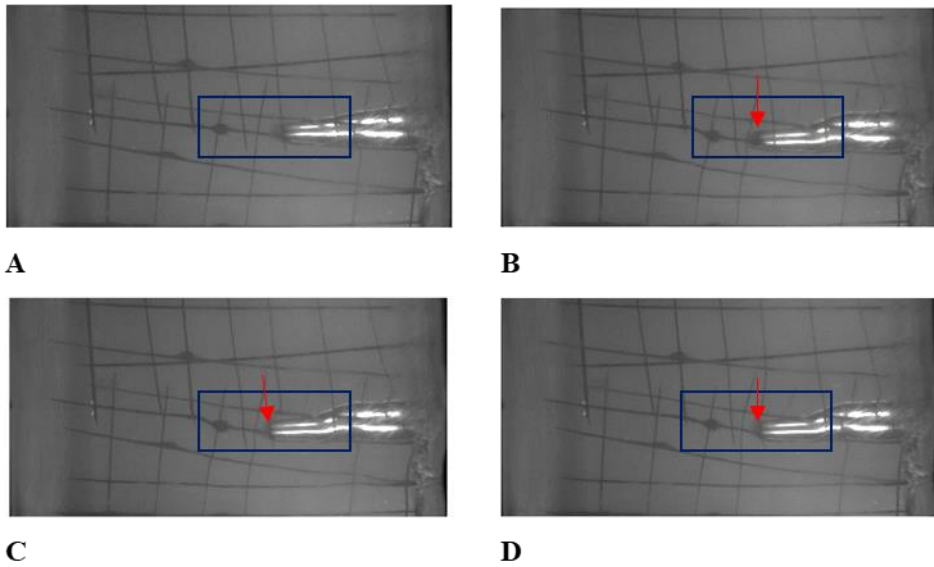


Fig: 6-10: Shows the response of the Matlab toolkit for penalty term of 0.0015. As before, A and B are the moving and static image. The results of the registration C: PI metric and D: SSD metric. In these images, it can be seen the cavity and grid pattern motion for these frames are captured including the kink in the cavity, which is the region that is contained in the blue rectangle. The differences in the projectile position indicate further refinement is possible to improve the result but will need to be performed using the experimental footage which is indicated by the red arrow.

It should be noted that the cavity accuracy can be seen to be an effective approximation with some difference in the actual projectile position which caused some concern. This is visible when comparing the static image (B Fig: 6-10) to the registered images (C and D) in

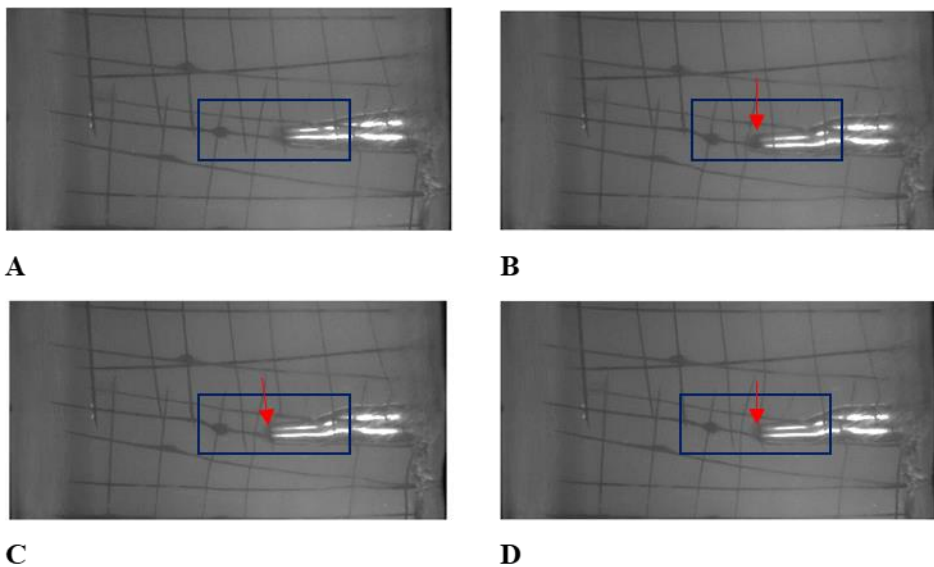


Fig: 6-10). But on inspection of the transformation produced by the registrations, it was found the PI metric was the closest match with some differences in the projectile.

However, the cavity is a good match with the SSD registration showing a more pronounced difference in the position of the projectile and tip of the cavity. The unusual kink in the penetration was an experimental anomaly that was caused during testing. The registration is able to account for its presence, meaning it is able to capture complex and unexpected motion which lends weight to using this toolkit. After further optimisation of both similarity metrics, any differences were reduced to a minimal difference when over-layed with Medrinna as with the registrations in Chapter 5. A minimal difference is defined as only showing very small variations such a difference of several pixel or slight blurring.

Table 6-3: List of the registration parameters that will be used for the image registration of the data with the possibility to be further refined if needed.

<b>Registration Options Non-Rigid Version 3</b>	<b>Condition 1</b>	<b>Condition 2</b>
<b>Registration Method</b>	NonRigid	NonRigid
<b>Spline Grid Spacing [x y z]</b>	[2 2 1]	[2 2 1]
<b>Thin Sheet Bending Energy Penalty Term [weight (%)]</b>	[0.0015]	[0.0015]
<b>Similarity Metric</b>	PI	SSD

The selection of the image registration parameters, specifically the choice of the penalty term, was made as during the investigation of the parameters. It was found that the computational cost of the higher penalty term greatly impacted the time the registration took to complete. This varied with the toolkit but was a difference of many hours depending on if ran locally on a desktop or run on a remote access server cluster. In case of the desktop, this could range from 1 hour to 18 hours for a full set of consecutive registrations, compared to on a server cluster were it could range from several minutes to an hour reflecting the increased computational power that was available. So for this reason, a server cluster was used. It should be noted that between tests and data captures, there was variation in terms of the time taken to

process the data. The main balancing decision was to maximise accuracy while balancing computational cost and time to process the data.

During the optimisation, it was found that any value above 0.0015 for the penalty term greatly increased the computational cost for minimal to no gains in accuracy. For this reason, it was decided that for the following registrations, the penalty term value will be 0.0015. This provided consistent accuracy in tests and when compared using the similarity score and Medrinna to the registrations performed using higher penalty terms. The other registration parameters can be seen in Table 6-3. As with the previous chapter to investigate the use of image registration, both metrics will be applied to the experimental data which allows to further understand the difference in the response between the two metrics. However, due to poor SSD response here, it is expected that it will be ineffective at registering the actual data, but the information will aid in assessing the application of this toolkit.

## **6.6. Results**

### **6.6.1. Experimental results**

To understand and establish a base line for assessing the registration output, firstly, there is a need to assess the output of the experimental arrangement for the tests. This includes identifying the launch velocity that was achieved across all the tests and the penetration of the fragment for each test.

The mean velocity of the projectile at launch was found to be  $98.22 \pm 4.62$  m/s. This highlighted that the cannon was able to fire projectiles at a consistent velocity, with the mean velocity in line with the assessment of the possible impact velocity that was undertaken in Chapter 2 is analytical study and as stated in that chapter, the goal was to increase the velocity with a successful test. Due to this consistent launch velocity, it can be assumed that the checks and monitoring of the experimental rig aided in preventing an increased likelihood of variation.

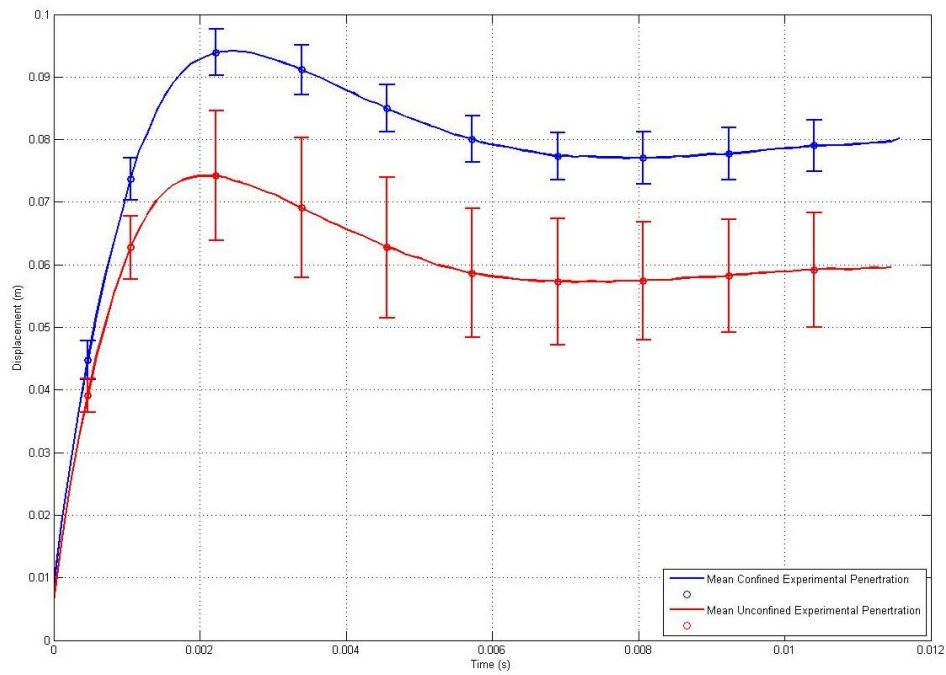


Fig: 6-11: The mean penetration for all confined and unconfined tests normalised to the experimental launch speed, with the standard deviation between the curves shown using error bars with the initial incline representing the initial penetration with the rebound and settling that was witnessed during the filming of the penetration impact.

As can be seen in Fig: 6-11, the general responses for all tests show a similar shape with the key steps in the penetration visible in the plot. The three key steps are the initial penetration, the rebound and the settling. The steep incline represents the penetration of the tissue surrogate and the reduction of gradient to the peak which represents the slowing of the projectile as it loses the energy needed to penetrate the tissue and begins to compress the material ahead of it until all its kinetic energy is converted to potential energy. Once all the kinetic energy has been expended, the potential elastic energy is released and the projectile rebounds along the cavity and settles until equilibrium is reached as this energy is dissipated. The region beyond where the projectile comes to rest does not show the same permanent damage that can be seen in the permanent cavity. By this component of the penetration process, the cavity has collapsed as all the kinetic energy has expanded the material during penetration and has been converted into potential energy. This in turn is released during settling, so the sample has reached equilibrium. It was not possible with the current experimental arrangement but it is logical to assume that a portion of the kinetic energy is released as heat through friction between the projectile and the material and sound generated. In this work, the focus resides on the physical

movement of the projectile and sample which is centred on the kinetic energy from the mass and launch velocity of the projectile.

An interesting result is the consistency of the two distinct mounting arrangements in relation to the curve shape but varied magnitude of penetration which is logical as when the sample is unconfined, the sample will move differently as it has greater freedom to absorb the impact and small changes in impact position will result in unique response. Compared to when the surrogate is confined, it limits the sample motion and will mean the surrogate responds in a much more consistent manner. The difference in magnitude also relates to this difference in freedom of motion as this impacts the absorption of the kinetic energy as a confined arrangement means that as the material has a reduced ability to move and deform its ability to absorb and store the kinetic energy of the projectile as elastic potential energy is limited meaning that more energy is dispersed by the gel rupturing leading to a deeper penetration. The unconfined material's ability to move freely means more of the energy is absorbed by the material moving, increasing the amount energy absorbed and reducing depth of the penetration as this reduces the amount of energy that is available to rupture the gel.

### **6.6.2.Registration Output**

The assessment initially started by identifying the best data captures that showed the greatest contrast and clarity for both the confined and unconfined tests. As with the previous chapter, a qualitative and quantitative analysis of the registration output was completed which followed the same approach that was used in Chapter 5. In line with previous work, the use of the similarity metric was not undertaken. It was previously identified that it did not provide an effective method of assessment. The pair-wise registration and the composition of the resulting pair-wise transformations were undertaken as described in Chapter 5.

As with the previous method, the pair-wise registration images were compared by overlaying the registered and reference images using the MedInria software. It was apparent that in the registered images, where the cavity crossed the grid pattern, an unusual transformation could be identified. Instead of a bisection of the grid which would occur due the failure of the material along the region where the permanent cavity is located, it instead deforms continuously with the front of the cavity where the projectile is located. This immediately showed that the registration was performing inherently inaccurately as these results assume the deformation is continuous, when in truth it is discontinuous as can be seen by the material failure

along the permanent cavity. This suggests that the material does not fail but rather compresses continuously ahead of the projectile. This means that when the pair-wise registration transformation are composed, it will produce strain values that are far above what can be considered mechanically possible, also meaning that the deformation in the direction of the penetration would not be accurate.

The two composed responses are shown in Fig: 6-12 and Fig: 6-13. It can be seen that in both figures, that the curves share the same general shape. However, as expected from the assessment of the pair-wise registration in both cases, there is a large difference between the registered penetrations and the experimental penetration. In both cases, the curve shape is extended and does not have the same magnitude. This clearly shows the image registration is unable to effectively capture the projectile motion over the course of the penetration. An investigation into the relationship was undertaken to identify if there was a scaling factor or other methods that could signify if a correction could be applied to produce a better outcome, but it was found that this was not possible which further reinforces that the registration in this case is flawed and does not effectively capture the motion of the surrogate.

Please see overleaf for figure Fig: 6-12 and Fig: 6-13.

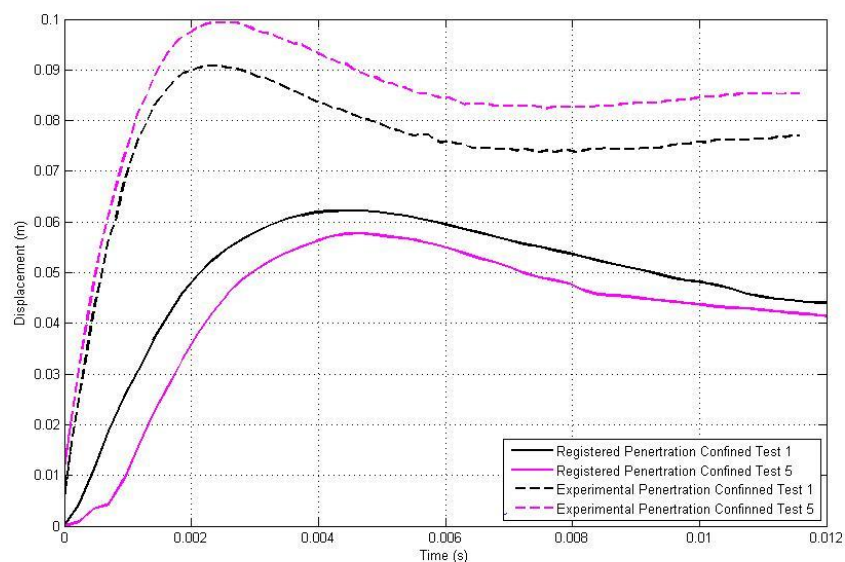


Fig: 6-12: Shows the comparison of the measured penetration and the registered penetration, for the confined mounting arrangement. There is a clear difference in the two responses both in magnitude and curve shape.

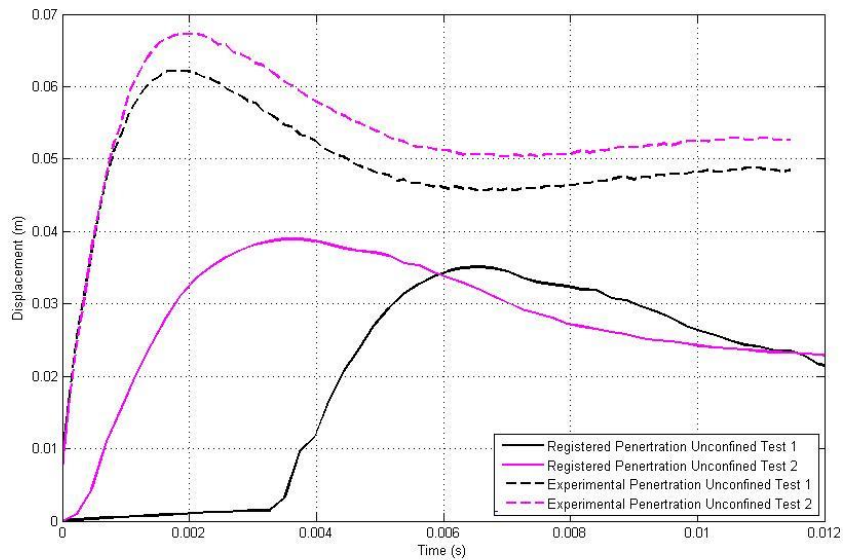


Fig: 6-13: This figure shows the comparison off the registered and measured penetration for the unconfined impacts. Again there is a clear distinction between the two responses. The second set of registration is a result of anomaly at impact due to the failure of the sabot which resulted in the projectile impact and launch speed varying as seen by the difference in the curves.

When assessing the images, there are two identifiable reasons for the registration performing inadequately: The first there is clear evidence of multi-planar motion with different components of the grid pattern moving in different planes and directions. As the registration attempts to track motion, this results in an integral of the motion across the grid pattern visible in the images. This multi-planar motion is further complicated by the discontinuous nature of the deformation, which results from the failure of the surrogate along the permanent cavity. The use of a dual camera arrangement was investigated; however, two cameras of the same specification were not available and to use two different cameras with different specifications would have greatly complicated the experimental arrangement and computational costs for both the registration and pre-processing, by needing to synchronise two different camera specifications and by needing large amount of pre-processing to ensure that images were capable of being registered simultaneously. Hence, it was not considered to be beneficial for the current testing as this would have changed the focus of the project from identifying if image registration can be used to quantify the deformation form the penetrating impact. However, this should be first area of investigation for further work as it is also a logical progression from the 2D arrangement as two cameras would allow a 3D registration to be performed.

In some cases, marks on the surrogate or localised material failure or defects added to the error in the registration arising from experimental variation or anomalies. This would inherently point to the one of the compounding reasons why the registration is incapable of capturing the motion, being the method for the inclusion of the grid pattern into the sample. This in turn highlights that the use of a needle to inject the grid pattern does not provide the necessary accuracy and stability to place markers in the desired plane while also ensuring the most efficient distribution of the pattern across the sample that is possible. However, as explored in Chapter 5, the use of other methods have their limitations which is further complicated due to the velocity that results from the penetrating impact. The primary limiting factor in this method is the accuracy of the injection process and the flexibility of the needle itself. This is a limitation that can only be partially overcome with the current equipment available.

The author proposes two possible methods to address this short coming: The first would be to use a mount or guide to ensure the accuracy and position of grid pattern insertion while also ensuring the flex of the needle is minimised. The second would be to increase the diameter and strength of the needle to reduce the possible flex during the injection. However, the thicker the needle, the more likely that the injection process will cause failure or damage during the insertion of the grid pattern. In any work, it is highly likely initial marker insertion will be a main focus of the revised experimental method.

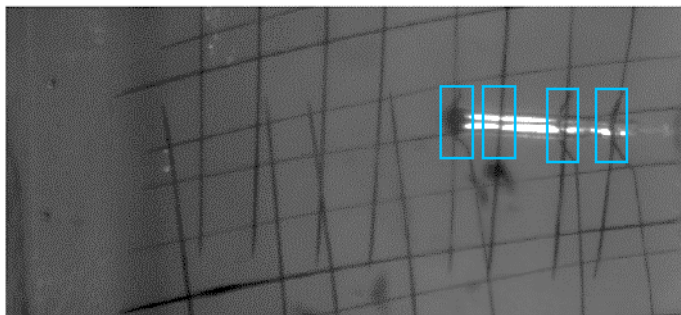
Examples of the issue can be seen in Fig: 6-14 and Fig: 6-15, specifically the multi-planar motion and the continuous nature of the registration. In both figures, the grid pattern is highlighted by the blue boxes. This demonstrates that in some cases, the cavity passes in front or behind the grid lines and in some cases bisected them all together. This means that the registration will track these grid lines as they move creating an integral of all these motions which does not represent the deformation in the intended plane being investigated. Then looking at the registered image, it can be seen that the registration has assumed continuous deformation by the over exaggerated stretching of the grid lines that the cavity has passed through highlighted in the distorted line in the red box. This also reinforces the impact of the integral registration as all the grid lines the cavity passes through can be seen to be stretched with the cavity. One of the possible ways that this could be achieved is through exploring the use of 3D image registration in future work. As by catching the impact in 3D would greatly aid reducing this integral effect as the composed images would allow tracking of both the grid pattern and cavity in multiple plane.

Please see overleaf for Fig: 6-14.



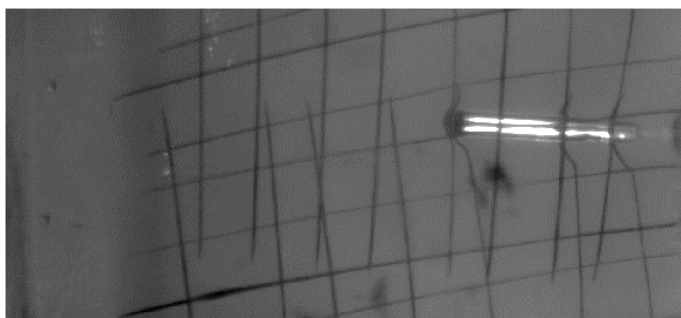
---

**Experimental  
Data**



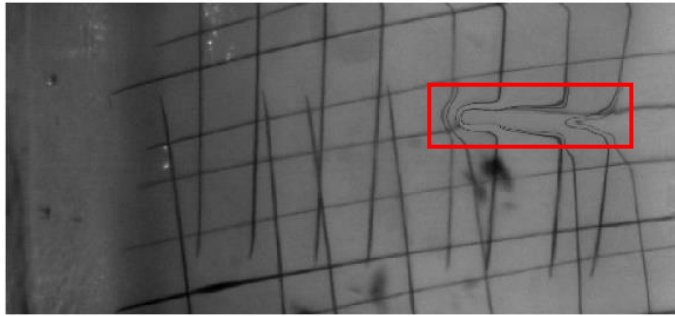
---

**Registered  
Image**



---

**Applied  
Composed  
Transform**

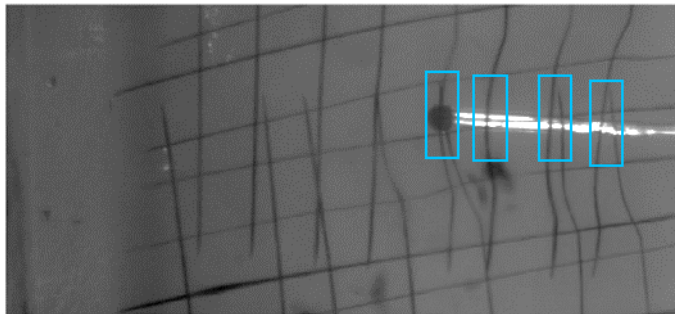


---

Fig: 6-14: Demonstrates the experimental output for 22<sup>nd</sup> frame of an unconfined impact test. The blue box highlights the multi-planner motion with two grid lines clearly moving different directions or with the cavity passing in front or behind them. The registered image shows that the pair-wise registration again performs as expected tracking the cavity and the grid line motion. However, the failure of the composed transformations can be seen in the lower image, with the red rectangle highlighting the error caused by the continuous transformation assumption.

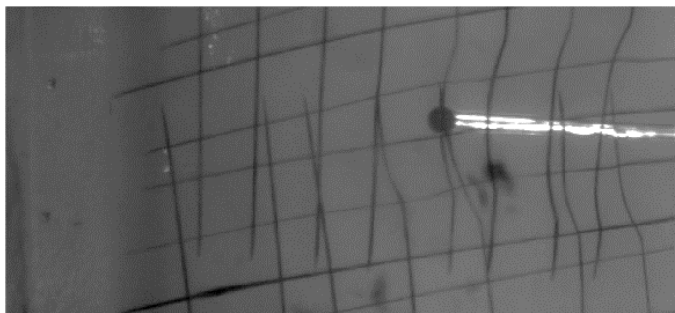
---

**Experimental  
Data**



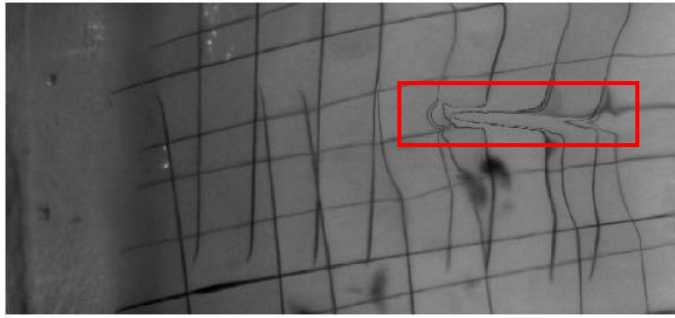
---

**Registered  
Image**



---

**Applied  
Composed  
Transform**



---

Fig: 6-15: Shows the results for the registered output for the 42<sup>nd</sup> frame of the same experiment. Both boxes show the multi-planar motion of the grid pattern throughout the length of the cavity alongside the increasing error due to the assumption of continuous displacement as seen in Fig: 6-14.

## **6.7. Discussion**

The results demonstrated that image registration is unable to quantify the displacement over the penetrating impact. The evidence above highlights that the main source of error relates to the experimental arrangement, specifically, the method for the inclusion of the grid pattern. As described in 6.4, the method is in line with that used in Chapter 5 while also expanding the method to account for the errors that were encountered in that Chapter. However, from the results that were recorded from the experimental arrangement in terms of consistency of both launch speed and the penetration response, the rig is capable of performing with a high degree of repeatability for both mounting arrangements with minor experimental variation. This further highlights that the experimental error that impacted the registration was the method for including the grid pattern.

Experimental variation was defined by the launch speed and the sample mounting arrangement. The first is due to the arrangement relying on pneumatic air-cannon, with the minor amount of variation seen in the launch speed over the course of all the experiments. This was largely due to the wear that was incurred on the sabot and the shock absorbing shield ring as this changed the launch velocity and flight path which was anticipated and multiple sabots and shock rings were produced using the same template and when wear became noticeable, the parts were replaced to ensure that the consistency of the cannon's firing was maintained. This wear was due to the forces and shock of the firing which wear the foam from which the sabot was made of, inducing localised failures which in turn reduce the pressure seal meaning some of the propellant is vented and not used to provide motive force. The variation within the sample mounting tests have already been discussed in the results. However, it is important to note that sample variance can be induced due to the material properties

differing. In this Chapter, the sample monitoring was expanded and when considering the experimental result. This inspires confidence in the manufacturing method (excluding the inclusion of grid pattern), able to account for the possible temperature variation and to produce consistent samples. This will also have a high degree of flexibility in terms of applicability to produce a range of sample concentration and shape. This highlights that this method of manufacturing could be applied for a range of different experiments that use ballistic gelatine as the specific tissue surrogate.

The previous chapter discussed both the camera arrangement and the possible optical distortion that can be induced. In these experiments, it was possible to establish an effective camera arrangement that allows for accurate capture of the impact. The key difference to Chapter 5 was the use of back light and camera settings to account for specific tests and environmental conditions. This included adjusting the aperture and more detailed use of the focus of the lens. This allowed a quantitative analysis of the effectiveness of the image registration. By backlighting, the cavity had a very high intensity; this is due to the light entering the cavity and being reflected within the cavity producing the high intensity. This meant that any similarity metric that could be dominated by regions of high intensity could limit the achievable accuracy. As this was expected, similarity metrics were selected to be robust against such regions of high intensity, but this will impact how the registration is processed, which extends the computational cost as a finer B-spline grid and penalty term was required to further ensure this was mitigated, which needs to be accounted for when applying the image registration toolkits and methods described in this Chapter.

The results achieved show that there are several limitations that effect the use of image registration as a method to quantification of displacement for penetrating impact. This results from two factors: The first is a result of the addition of the grid pattern in the sample which results in the grid pattern lines being in multiple planes in front and behind the expected plane of impact. This differs from the issues identified in Chapter 5 as a more evenly dispersed grid pattern was achieved in these experiments due to the lessons learned. Using a more controlled insertion method to generate an un-even pattern which aimed to provide as many distinct arrangements and hence unique points of reference did not result in an accurate registration. So in this work a uniform method was proposed to address this issue. However, due to the size of the samples, when the grid pattern was injected, three separate injection processes had to be performed: one vertical oriented and two horizontal opposite faces of the sample. Due to the depth of the grid pattern that was required, it resulted in the grid pattern consisting of overlapping lines which resulted in a variation in the

planes. This is due to the needle flexing and curving during the injection process even with the method's measures to ensure accuracy of placement in the expected plane of impact. This resulted in the projectile travelling between the grid lines which resulted in the multi-planar motion further compounded by lines moving in differing directions separate to the projectile and cavity motion. As highlighted in the discussion in Chapter 3, the integral effect that can be seen in some cases of photoelasticity is due to the imaging through the sample which is why for most 3D cases, two methods are mainly used which is reflection or using the sliced method to image through the multiple planes to avoid the integral effect with a similar effect having been induced in the images taken from the experiments. This first occurred in the pair-wise registration and then compounded in the composition of the transformation rendering the registration output incorrect and unusable.

A further limitation of the image registration framework was identified. The registration approach is based on the assumption that the deformation during the penetration was continuous. This means that all deformations are linked and that there are no boundaries or separation of the material over the course of the registration. In this case, there is material failure that changes over the course of the penetration resulting in a changing discontinuous deformation as the cavity extends with the material failure alongside expanding and collapsing. This adds a greater complexity to the process and limits the effectiveness of the registration toolkits as it will be able to track the projectile but assumes that the failure of the sample does not occur combined with the integral effect that is caused by multi-planar motion, meaning that the registration cannot effectively capture the deformation over the penetration. This is seen in the very high deformations in localised areas that would not reflect material failure along the cavity and means that the current registration approach used is incompatible with any experiment where failure is expected to be a large component of the experimental response.

The conclusion of this chapter is that image registration is not an effective method for the quantification of displacement for penetrating impact in the current arrangement that is being employed, due to an ineffective experimental method for the application of the grid pattern resulting in multi-planar motion. Alongside this, the discontinuous nature of the penetration process for this specific application of continuous deformation based image registration toolkits means that this method is intrinsically incapable of capturing the penetration process.

## **Chapter 7. Thesis conclusion**

This thesis has explored if image registration could be applied as a method for the quantification of deformation for penetrating projectile impact tests, using ballistic gelatine as a soft tissue surrogate. Throughout this project, the author aimed to achieve several aims which were defined in Section III. The results obtained in this thesis indicate image registration is unable to quantify the displacement for the given experiments undertaken. However, as highlighted by the pair-wise registration, the actual image registration methodology functioned correctly, but the experimental arrangement lead to the method and composition not being able to capture deformation over the captured impact and indentation tests. This chapter aims to accurately and concisely summarise the findings of this thesis and the results that pertain to each aim while also presenting the final conclusion that can be drawn from the thesis, followed by suggested avenues for future work if it was to be undertaken.

### **7.1. Meeting the aims of the project**

### **7.1.1. Define experimental conditions**

Even with the limitations of an analytical study, it was possible to establish an effective justification for the experimental boundary conditions. In line with the literature, the rising use of explosives devices against both military and civilian targets and the advances in the associated technology mean that the ability to study penetrating impacts and understand the mechanics is pressing. Not just the acute high speed regions, but also the longer time frame would beneficially increase the knowledge of both the mechanical and biological response to penetrating impacts. Furthermore, increasing technology and the use of explosives and improvised devices against large numbers of targets mean that medical personnel are being put under increasing pressure to deal with such injuries which are often highly varied and complex. This highlighted that the work this thesis proposed has the possibility to aid in further developing defensive technology and increasing the wider mechanical understanding of such impacts. This can then be used to help understand the biological responses and aid in developing new medical technologies or knowledge.

### **7.1.2. Confirm that image registration can be used as a method for quantifying displacement.**

In establishing whether image registration could be used for the quantification of displacement in high speed penetration experiments, the previous literature was consulted. As an initial starting point, the plausibility of the method and the previous experimental arrangements used was established. From this review, it was made clear that from previous usage in the field of medical imaging, image registration has been clearly established as a method for tracking the wider motion of organs and anatomical sites in the body and hence deriving deformation in real terms while also identifying the similarity of the tracking process and generation of the transformations between image registration and other established optical measuring methods that currently see regular usage in mechanical engineering experimental assessment. The main difference between current medical uses of image registration and those proposed in this work is centred on the image collection method and greater complexity of the implementation. In medical usage, the methodology and algorithms are tailored to a specific imaging modality and uses a range of other techniques such as segmentation and initialisation to aid in specifically identifying the region of interest, as well as applying a large range of different transformation and optimisation frameworks. The method that was proposed in this work was specifically selected for being accessible and its general formulation which allow

greater flexibility and use with a wider range of different software packages, in particular, the similarity between DIC and image registration. Both employ the use of similarity metrics to assess and define the optimisation of the transformation algorithm. However, this main difference in the methods is that DIC mainly focus on identifying the mechanical motion on the surface or the integral motion throughout the sample. Even though the core principals may be similar, the ability of image registration to be selectively tailored to work in a particular plane of the sample with minimal sample set up or specialised equipment is a large advantage. This was a significant reason why the image registration was highlighted as a method to be explored for the use of quantification the deformation during penetrating impact tests.

With the plausibility of the application of image registration established from the literature, it was then possible to define and describe a method to achieve a pair-wise registration using established image registration theory that could be applied to a range of toolkits or registration programs. At the same time, this thesis aimed to expand the method to allow composition of the pair-wise transformation to generate a dynamic displacement over multiple consecutive images from a single experiment was explored while also discussing the accessibility and adaptability of the image registration toolkits that are available and the open source software that has been used to the support the toolkits. From this, it can clearly be stated that image registration has the possibility to be applied as a method to quantify deformation over mechanical experimental data. The extensive usage in the medical field supports the potential suitability image registration. However, as highlighted by the results of this thesis, the experimental arrangement and setting have a significant effect on the output which will be discussed later in this chapter.

### **7.1.3.Characterise the tissue surrogate mechanical material properties.**

A review of the surrogates that have seen previous usage was conducted and the most appropriate material was found to be ballistic gelatine. As ballistic gelatine has been one of the most used ballistic surrogates in similar penetration experiments, this was not unexpected, but the literature review confirmed that this was a logical selection. In particular, the transparent properties of the material and ease of creation were the main factors in the selection of the surrogate. The specific type of ballistic gelatine was outlined in the Chapter 3 with the final selection being produced by the company GELITA, as this was both available and cost effective. The company produced several types of gelatine and for this work, type 3 scientific gelatine was chosen. This is produced to maximise the consistency of the final material and allow clear imaging with a high degree of transparency. It should be noted that bloom, which is



mentioned in the material specifications, is a standardised measure of strength with this gelatine being classified as a high bloom (250) or high strength gelatine. However, these values are only guides as the actual mechanical strength of the gelatine is decided by the specific concentration and manufacturing method that is used, hence the need to characterise the material and not solely rely on the specific bloom value.

A characterisation of GELITA type 3 ballistic gelatine was undertaken. This was specifically done to allow the validation of image registration results. It was performed over a slower speed than that of penetration to allow deeper analysis of the registration outputs and allow for its use in a validation test. The characterisation was partially successful with only one loading regime producing material parameters across all the compression speeds tested. However the testing and research allowed a good understanding of the material and key experimental considerations to account for when using ballistic gelatine. A review of previous literature included its previous usage, while also highlighting its applicability to a wider range of tests. This includes use as a medical imaging and surgical phantom, suggesting the wider application of the material characterisation beyond the validation test undertaken in this thesis.

In line with the previous literature, it was decided to investigate the characterisation of ballistic gelatine at quasi-static loading rates which allowed greater control and simplification of possible experimental arrangements. The selection of this speed was based on two key points: Firstly, the planned validation tests which, for ease of experimental setup and accuracy, were performed at comparable speeds to quasi-static strain rates. Secondly, the previous work undertaken by N.Ravikumar provided an initial base to build and compare the outcome of the material characterisation [113]. This is an area of penetrating impact that has not been heavily investigated but is an integral part of the wider penetration process. Specifically, uniaxial compression tests alongside hysteresis and stress relaxation tests over multiple loading rates were completed. It was possible to achieve optimised parameters for the uniaxial compression tests at loading rates of 0.02 mm/s, 0.2 mm/s and 2 mm/s fitted simultaneously. While in the case of the hysteresis and relaxation tests, the optimisations had difficulty fitting the material parameters simultaneously and when fitted individually, there were multiple errors. These were either produced by experimental rig limitations or identifiable slippage that varied between samples. This places limitation on the assumption used in the fitting FEA model which uses fixed boundary conditions which is unable to capture the sample slippage and erroneous motion induced by the experimental rig limitations.

The conclusion established for the visco-hyperelastic formulation is that only the uni-axial compression fitting was successful. However, the parameters for that loading regime the material parameters could be applied to the computational model used to validate the response of image registration output for the indentation tests. From the finding of the characterisation, it would be recommended that if any researcher would use the same methodology for the characterisation, an analysis of the surface interaction and the frictional response to loading should be undertaken. This was the greatest source of uncertainty encountered during the characterisation method used in this thesis.

#### **7.1.4. Apply image registration method to mechanical tests**

In this thesis, it was not possible to fully investigate the ability of image registration to be applied as a method for the quantification of deformation for experimental mechanical tests. The initial test investigated was a uniaxial indentation where an imbedded grid pattern was added to aid in the registration of the motion. The dye had minimal affect the surrogate material or the mechanical response as during testing, the gelatine did not fail or show erroneous deformation. However, the injection process could damage the gelatine as was seen in some samples and necessitated the removal of this damage or to not use samples that showed damage from the injection process. This would occur if there was too much pressure in the injection process, which could rupture the surrogate around the injection site. Another source of damage is in the flex or force of the injection. This is why the experimental methodology accounted for this by monitoring the sample during the creation and testing. If any damage or failure were identified that could have resulted from the manufacturing or the dye injection, these samples were removed or not used in this work and this aided in maximizing the consistency of the samples tested.

Tests were conducted at comparable loading speed to the characterisation compression speeds. This allowed the material model to be used to validate the image registration output. The results showed that image registration was ineffective at estimating the motion over the experimental data. This inaccuracy stemmed from experimental limitation that directly impacted the image registration output with the greatest limitation being the method for the inclusion of the markers in the sample and the image recording arrangement. The use of the injected grid pattern was in theory a sound approach. As identified in the literature, similar approaches have been used in other optical measuring techniques such as DIC and motion/marker capture alongside the focus of image registration in the tracking of objects in the medical field. All of this lends support to the method being sound, but as identified in this thesis, the implementation of the grid pattern presents several challenges. During the

indentation tests, the qualitative assessment highlighted that the registration approach was able to track where objects were present in the data showing that the pair-wise image registration was operating as expected. However, the registration was unable to estimate the motion in the areas of the image in which there were no objects (such as the indenter or grid lines) resulting in an inherent error when the transformation was composed. This was further hindered by optical distortion, identified from the indentation tests which resulted in refraction and reflection that was visible in the captured images. This was not due to insufficient light or from a particular light source but the size and shape of the sample itself which resulted in the visible distortions due to the changing surface geometry. This was mitigated in the following tests with careful camera arrangement and increasing the size of the sample to minimise the possibility of the surface motion that resulted in the reflection and refraction.

When considering the established usage and success in the medical imaging field, it would indicate with confidence that the registration method is performing as expected and the error being focused on the experimental limitation mentioned above. The two greatest limitations being the sample deformation impacting the way light travels in the sample which distorts the recorded image and the implementation of the grid pattern which means that the image registration is unable to capture the motion of the region without markers. This meant that in the penetrating impact tests, particular consideration needed to ensure the size of the samples were large enough so the sample surface changes would be minimal and minimise the optical distortions seen in the indentation tests images. Alongside this, refining the insertion of the grid pattern would address the limitations that have been identified specifically the distribution of the grid pattern.

#### **7.1.5. Apply image registration to penetration tests on the defined tissue surrogate.**

The penetration tests were conducted using a vertically orientated air-cannon and a sample arrangement aimed to address the limitations of the indentation test. From a purely experimental results assessment, the arrangement was able to produce consistent results over the two mounting arrangements used. As with the previous experiments, it was found the image registration method used was unable to estimate the motion over the course of the penetration. This clearly demonstrated that the current marker method requires further development in relation to its implementation specifically, the depth required to inject the markers, which was needed due to the

increasing in sample size to avoid the impact of surface motion as identified in 7.1.4. This depth meant an increased likelihood of inducing flex in the needle during insertion and producing a possible multi-planar grid pattern. The methodology followed used a graduated needle and careful insertion, which accounted for this possibility by assessing the produced sample to ensure that those samples with grid patterns that were out of plane were not used. It was not possible to completely mitigate small out of plane variation. This multi-plannar positioning of the grid and the penetration process cutting through the grid lines (alongside the image registration using a continuous deformation assumption) means that the registration of the penetration produced an integral effect Further compounded by the discontinuous nature of the deformation which relates to the failure along the cavity. This added an inherent error into any attempt to estimate the motion. This means that the image registration method worked as it was designed to, but for use in the assessment of penetrating impacts, the method needs to be expanded to account for the discontinuous deformation.

Discontinuous registration is an area that is currently being investigated for use in medical usage of image registration which lends support to the further development of this method [228]. Alongside this, the implementation of the grid pattern has benefits but requires further work in the implementation. However, the most significant finding of the work undertaken in this thesis has been that for any test with the likelihood of multi-planar motion or sample failure the use of 2D image capture and continuous deformation based image registration is susceptible to errors due to motion outside the image plane being investigated and the inherent error in the continuous deformation assumption that the image registration uses. However, a 3D registration would be able to account for this multi-planar motion and (when combined with discontinuous image registration) would minimise the errors and limitations encountered during the work undertaken in this thesis.

## **7.2. Conclusion**

To conclude, the research that has been undertaken in this thesis has highlighted two key findings: one in relation to the characterisation work that was undertaken and two that specifically relate to the use of image registration and the experimental arrangement used to capture the penetrating impact and indentation tests. The characterisation of the ballistic gelatine surrogate for uniaxial compression loading at quasi-static loading rate (0.02 mm/s, 0.2 mm/s and 2.0 mm/s) using a visco-

hyperelastic model was a partial success, with the model able to optimise the material model for uni-axial compression tests. However, the experimental arrangement and material model did not have the flexibility to optimise the material parameters for the stress relaxation and hysteresis tests. The second key finding is that image registration could plausibly be used as a method to quantify deformation as it is well established in medical imaging field. However, more work is needed to develop the method to account for the discontinuity in the penetrating impact, which results from the failure of the material along the cavity. If the mechanical tests do not include any discontinuous deformation, the current method could be applied. However, more research is needed to further develop its application to test using transparent tissue surrogates as the reflection and refraction distortions intensified during the indentation tests change the sample's surface geometry. The final key finding is that the method for the inclusion of fiducial markers (grid pattern) and the need to account for multi-planar motion need further work, either by expanding data capture methods or increasing the accuracy or placement of the grid pattern itself. To conclude, the use of image registration methodology proposed is not currently capable of assessing penetrating impact without further work to address the limitations that have been identified.

### **7.3. Future work to address limitations identified**

If further research was to be undertaken, the short comings that were identified in this thesis would need to be overcome. This focuses on two key components: (1) Investigating the use of a discontinuous transformation algorithm, (2) Expanding the experimental arrangement to allow for 3D imaging of the impact and an improved method for the inclusion of grid pattern. A proposal of how this could be achieved is given below.

As identified in the work undertaken in this thesis for the specific case of the penetrating impact, it is not possible to consider continuous deformation due to the failure of the sample along the cavity which is discontinuous nature. So a primary point of further investigation is the application for discontinuous transformation that can be applied to the pair-wise image registration method that this thesis proposed to account for the material failure along the cavity. This is an area that is currently being investigated in relation to medical image registration for the complex deformation that occurs at organ boundaries where the organ can move freely in relation to the surrounding tissue or bone structure [228]. This method is also a non-

rigid method that uses free-form deformation with a B-spline grid as used in this thesis. This B-spline grid is then enriched to account for the discontinuity with extra refinement and control points. This method does add several steps that would need to be incorporated into the methodology. This would include the definition of the discontinuity caused by the cavity which in this case changes over time. One method could be through segmenting the permanent cavity in relation to time. This would be undertaken using a similar approach to that used in Chapter 5 used to segment out the indenter making use of the ITKSnap or similar program to perform the segmentation. This would increase the work load as the discontinuity change is dependent on time and would require either manual segmentation or the development of an automatic approach.

As mentioned in 7.2, the image registration method would also be expanded to be performed in 3D, which would double the computational cost and work load as two sets of input images would need to be synchronised. All pre-processing would be doubled for the two sets of input image, alongside combining the two inputs to produce a 3D representation of the deformation over the course of the impact. This means that for any future development, the following development steps would need to be incorporated into the planned work: 1) The implementation of a discontinuous image registration methodology, 2) An automatic or manual segmentation method to define the cavity and 3) The application and visualisation of the results using 3D image registration to support application the of a new discontinuous image registration and to address the limitations that were identified in (2). This is centred on the production of the sample, the sample mounting arrangement and the filming arrangement to allow 3D imaging. As in this, the sample production method was effective at producing samples that were homogenous and consistent across the testing that was undertaken. However, the method for grid pattern insertion needs to be investigated further, as any future work would be expanded to be performed in 3D and due to the limitations that have been identified, a more accurate method to insert the grid pattern would need to be developed.

The author proposes the use a rig which is designed to minimise needle flex and ensure that the grid patterns are injected in the correct pattern in the two planes that are required for the 3D imaging. A series of tests are also recommended to identify the effects of increasing the needle rigidity to minimise the possible flex and to identify the optimal positioning of the grid pattern itself, since the issue of the permanent cavity bisecting the grid pattern and inducing multi-planer motion have clearly been seen. It may be more useful for the grid pattern to be positioned so it will still enable the wider sample motion to be captured but away from where the

permanent cavity will occur to avoid the permanent cavity bisecting the grid pattern. As the cavity is a distinct object, this should have minimal impact on the registration being able to capture the cavity motion but this will require investigation. However, this will need to be tested to determine the best ratio and position, this can be undertaken through a range of explorative tests.

The ability to directly measure the velocity of the launch would greatly benefit the accuracy of the experiments. This would require modifying the sample mounting to allow for a chronograph to be included. Alongside this, altering the mounting arrangement to allow 3D imaging and removing the Perspex screen to aid the clarity of the images would be beneficial. This also means imaging the unconfined mounting arrangement only. However, as the results showed, the penetration process showed comparable curve shape and consistency across the tests performed. This will not impact investigating if the new image registration formulation is viable and reduces the number of tests being performed, allowing the focus to be on the implementation of the method itself.

Finally, the positioning of the camera to collect two sets of images needs to be investigated. This will require two cameras of equal specification to be synchronized to capture at the same frames per second so the collected images between the two cameras initialize and capture at the same time. This will present several challenges such as lighting the samples which will double the amount of lighting and hence, increase the likelihood of sample heating. However, the current imaging method was repeatable and captured images of sufficient clarity were produced while also minimising possible sample warming. It would be logical to use this thesis method as an initial starting point and modifying it as required.

By performing the work that has been suggested above, it should allow for further investigation of the image registration method proposed in this thesis while exploring ways to address the limitations that were identified allowing image registration to develop further as a method for the quantification of deformation for mechanical engineering tests.

## Chapter 8. Bibliography

- [1] a Scope, U. Farkash, M. Lynn, a Abargel, and a Eldad, “Mortality epidemiology in low-intensity warfare: Israel Defense Forces’ experience.,” *Injury*, vol. 32, no. 1, pp. 1–3, Jan. 2001.
- [2] C. Wilson, “CRS Report for Congress Improvised Explosive Devices (IEDs) in Iraq and Afghanistan: Effects and Countermeasures,” Washington, 2007.
- [3] B. Adini, R. Cohen, A. Givon, I. Radomislensky, M. Wiener, and K. Peleg, “Do modern conflicts create different medical needs?,” *Am. J. Emerg. Med.*, vol. 29, no. 9, pp. 965–71, Nov. 2011.
- [4] W. Chin, “British Counter-Insurgency in Afghanistan,” *Def. Secur. Anal.*, vol. 23, no. 2, pp. 201–225, Jun. 2007.
- [5] C. Willy, T. Hauer, N. Huschitt, and H.-G. Palm, “‘Einsatzchirurgie’--experiences of German military surgeons in Afghanistan.,” *Langenbecks. Arch. Surg.*, vol. 396, no. 4, pp. 507–22, Apr. 2011.
- [6] A. J. Schoenfeld, “The combat experience of military surgical assets in Iraq and Afghanistan: a historical review.,” *Am. J. Surg.*, vol. 204, no. 3, pp. 377–



383, Sep. 2012.

- [7] N. Jacobs, D. M. Taylor, and P. J. Parker, “Changes in surgical workload at the JF Med Gp Role 3 Hospital, Camp Bastion, Afghanistan, November 2008-November 2010.,” *Injury*, vol. 43, no. 7, pp. 1037–1040, Jul. 2012.
- [8] G. Almogy and A. I. Rivkind, “Surgical lessons learned from suicide bombing attacks.,” *J. Am. Coll. Surg.*, vol. 202, no. 2, pp. 313–319, Feb. 2006.
- [9] J. Salomone, P. Pons, and N. McSwain, *PHTLS Prehospital Trauma Life Support*, Seventh Ed. Saint Louis: Mosby Jems ELSEVIER, 2011.
- [10] P. Lichte, R. Oberbeck, M. Binnebösel, R. Wildenauer, H.-C. Pape, and P. Kobbe, “A civilian perspective on ballistic trauma and gunshot injuries.,” *Scand. J. Trauma. Resusc. Emerg. Med.*, vol. 18–35, p. 35, Jan. 2010.
- [11] S. Bonnet, F. Gonzalez, a Poichotte, V. Duverger, and F. Pons, “Lessons learned from the experience of visceral military surgeons in the French role 3 Medical Treatment Facility of Kabul (Afghanistan): an extended skill mix required.,” *Injury*, vol. 43, no. 8, pp. 1301–6, Aug. 2012.
- [12] R. McGuigan, P. C. Spinella, A. Beekley, J. Sebesta, J. Perkins, K. Grathwohl, and K. Azarow, “Pediatric trauma: experience of a combat support hospital in Iraq.,” *J. Pediatr. Surg.*, vol. 42, no. 1, pp. 207–210, Jan. 2007.
- [13] B. a Johnson, D. Carmack, M. Neary, J. Tenuta, and J. Chen, “Operation Iraqi Freedom: the Landstuhl Regional Medical Center experience.,” *J. Foot Ankle Surg.*, vol. 44, no. 3, pp. 177–183, 2005.
- [14] S. L. Eskridge, C. a Macera, M. R. Galarneau, T. L. Holbrook, S. I. Woodruff, A. J. MacGregor, D. J. Morton, and R. a Shaffer, “Injuries from combat explosions in Iraq: injury type, location, and severity.,” *Injury*, vol. 43, no. 10, pp. 1678–1682, Oct. 2012.
- [15] M. H.-R. Hicks, H. Dardagan, P. M. Bagnall, M. Spagat, and J. a Sloboda, “Casualties in civilians and coalition soldiers from suicide bombings in Iraq, 2003-10: a descriptive study.,” *Lancet*, vol. 378, no. 9794, pp. 906–914, Sep. 2011.
- [16] J. J. Morrison, N. Hunt, M. Midwinter, and J. Jansen, “Associated injuries in casualties with traumatic lower extremity amputations caused by improvised

- explosive devices.," *Br. J. Surg.*, vol. 99, no. 3, pp. 362–366, Mar. 2012.
- [17] N. Boonthep, S. Intharachat, and T. Iemsomboon, "Factors influencing injury severity score regarding Thai military personnel injured in mass casualty incident April 10, 2010: lessons learned from armed conflict casualties: a retrospective study.," *BMC Emerg. Med.*, vol. 12, no. 1, pp. 1–7, Jan. 2012.
- [18] K. Peleg, L. Aharonson-daniel, M. Michael, S. C. Shapira, T. H. E. Israel, and T. Group, "Patterns of Injury in Hospitalized Terrorist Victims," *Am. J. Emerg. Med.*, vol. 21, no. 4, pp. 258–262, 2003.
- [19] A. Papy, C. Robbe, and N. Nsiampa, "Definition of a standardized skin penetration surrogate for blunt impacts," in *IRCOBI Conference*, 2012, pp. 486–493.
- [20] V. R. Hallikeri, H. S. Gouda, and S. a Kadagoudar, "Country made scare gun vs. air gun--a comparative study of terminal ballistics using gelatine blocks.," *Forensic Sci. Int.*, vol. 214, no. 1–3, pp. 148–151, Jan. 2012.
- [21] F. Bresson and O. Franck, "Comparing ballistic wounds with experiments on body simulator.," *Forensic Sci. Int.*, vol. 198, no. 1–3, pp. e23–e27, May 2010.
- [22] K. Whittle, J. Kieser, I. Ichim, M. Swain, N. Waddell, V. Livingstone, and M. Taylor, "The biomechanical modelling of non-ballistic skin wounding: blunt-force injury.," *Forensic Sci. Med. Pathol.*, vol. 4, no. 1, pp. 33–39, Jan. 2008.
- [23] Y. Wen, C. Xu, H. Wang, A. Chen, and R. C. Batra, "Impact of steel spheres on ballistic gelatin at moderate velocities," *Int. J. Impact Eng.*, vol. 62, pp. 142–151, Dec. 2013.
- [24] R. A. Ryckman, D. A. Powell, and A. Lew, "Ballistic penetration of Perma-Gel," in *AIP Conference Proceedings*, 2012, vol. 143, no. 1, pp. 143–148.
- [25] Y. Chen, Y. Miao, C. Xu, G. Zhang, T. Lei, and Y. Tan, "Wound ballistics of the pig mandibular angle: a preliminary finite element analysis and experimental study.," *J. Biomech.*, vol. 43, no. 6, pp. 1131–1137, Apr. 2010.
- [26] G. H. Yoon, J. S. Mo, K. H. Kim, C. H. Yoon, and N. H. Lim, "Investigation of bullet penetration in ballistic gelatin via finite element simulation and experiment," *J. Mech. Sci. Technol.*, vol. 29, no. 9, pp. 3747–3759, 2015.
- [27] R. a. Mrozek, B. Leighliter, C. S. Gold, I. R. Beringer, J. H. Yu, M. R.

- VanLandingham, P. Moy, M. H. Foster, and J. L. Lenhart, "The relationship between mechanical properties and ballistic penetration depth in a viscoelastic gel," *J. Mech. Behav. Biomed. Mater.*, vol. 44, pp. 109–120, 2015.
- [28] S. Sakaguchi, D. Carr, I. Horsfall, and L. Girvan, "Protecting the extremities of military personnel: fragment protective performance of one- and two-layer ensembles," *Text. Res. J.*, vol. 82, no. 12, pp. 1295–1303, Mar. 2012.
- [29] M. S. Chafi, G. Karami, and M. Ziejewski, "Biomechanical assessment of brain dynamic responses due to blast pressure waves.," *Ann. Biomed. Eng.*, vol. 38, no. 2, pp. 490–504, Mar. 2010.
- [30] G. T. Desmoulin and J.-P. Dionne, "Blast-induced neurotrauma: surrogate use, loading mechanisms, and cellular responses.," *J. Trauma*, vol. 67, no. 5, pp. 1113–1122, Nov. 2009.
- [31] NATO Research and Technology, "Test Methodology for Protection of Vehicle Occupants against Anti-Vehicular Landmine Effects ( Méthodologie d ' essais pour la protection des," North Atlantic Treaty Organisation, 2007.
- [32] S. a. Formby and R. K. Wharton, "Blast characteristics and TNT equivalence values for some commercial explosives detonated at ground level," *J. Hazard. Mater.*, vol. 50, no. 2–3, pp. 183–198, Oct. 1996.
- [33] G. F. Kinney, R. G. S. Sewell, and K. J. Graham, "Peak Overpressures For Internal Blasts," China Lake, 1979.
- [34] E. Stark and C. O'Connor, "Using Calculations to Determine Internal Residual in Explosive Overpressures Breaching Applications," *The Denator*, vol. 37, no. 6, pp. 55–57, 2010.
- [35] T. Ngo, P. Mendis, A. Gupta, and J. Ramsay, "Blast loading and blast effects on structures—an overview," *EJSE Spec. Issue Load. Struct.*, vol. 7, pp. 76–91, 2007.
- [36] T. Norman, "Building Security Design Considerations : The Effects of Bomb Blasts," 2007.
- [37] N. Yoganandan, B. D. Stemper, F. a Pintar, and D. J. Maiman, "Use of postmortem human subjects to describe injury responses and tolerances.," *Clin. Anat.*, vol. 24, no. 3, pp. 282–293, Apr. 2011.
- [38] R. Radovitzky and S. Socrate, "Investigation of tissue-level mechanism of

primary blast injury through modelling, simulation, neuroimaging and neuropathological studies,” Cambridge,MA, 2012.

- [39] S. J. Wolf, V. S. Bebarta, C. J. Bonnett, P. T. Pons, and S. V Cantrill, “Blast injuries.,” *Lancet*, vol. 374, no. 9687, pp. 405–415, Aug. 2009.
- [40] A. Andronache, M. von Siebenthal, G. Székely, and P. Cattin, “Non-rigid registration of multi-modal images using both mutual information and cross-correlation.,” *Med. Image Anal.*, vol. 12, no. 1, pp. 3–15, Feb. 2008.
- [41] G. P. Penney, J. Weese, J. a Little, P. Desmedt, D. L. Hill, and D. J. Hawkes, “A comparison of similarity measures for use in 2-D-3-D medical image registration.,” *IEEE Trans. Med. Imaging*, vol. 17, no. 4, pp. 586–595, Aug. 1998.
- [42] W. R. Crum, T. Hartkens, and D. L. G. Hill, “Non-rigid image registration: theory and practice,” *Br. J. Radiol.*, vol. 77, no. suppl\_2, pp. S140–S153, Dec. 2004.
- [43] S.-Y. Chien, Y.-W. Huang, B.-Y. Hsieh, S.-Y. Ma, and L.-G. Chen, “Fast Video Segmentation Algorithm With Shadow Cancellation, Global Motion Compensation, and Adaptive Threshold Techniques,” *IEEE Trans. Multimed.*, vol. 6, no. 5, pp. 732–748, Oct. 2004.
- [44] B. M. You, P. Siy, W. Anderst, and S. Tashman, “In vivo measurement of 3-D skeletal kinematics from sequences of biplane radiographs: application to knee kinematics.,” *IEEE Trans. Med. Imaging*, vol. 20, no. 6, pp. 514–525, Jun. 2001.
- [45] W. Liu and E. Ribeiro, “A survey on image-based continuum-body motion estimation,” *Image Vis. Comput.*, vol. 29, no. 8, pp. 509–523, 2011.
- [46] M. V Wyawahare, P. M. Patil, and H. K. Abhyankar, “Image Registration Techniques : An overview,” *Int. J. Signal Process. Image Process. Pattern Recognit.*, vol. 2, no. 3, pp. 11–28, 2009.
- [47] D. Robinson, S. Member, P. Milanfar, and S. Member, “in Image Registration,” *IEEE Trans. IMAGE Process.*, vol. 13, no. 9, pp. 1185–1199, 2004.
- [48] G. E. Christensen and H. J. Johnson, “Consistent image registration,” *IEEE Trans. Med. Imaging*, vol. 20, no. 7, pp. 568–582, 2001.
- [49] S. E. A. Muenzing, B. Van Ginneken, and J. P. W. Pluim, “On combining

- algorithms for deformable image registration,” *Lect. Notes Comput. Sci. (including Subser. Lect. Notes Artif. Intell. Lect. Notes Bioinformatics)*, vol. 7359 LNCS, pp. 256–265, 2012.
- [50] D. Rueckert, P. Aljabar, R. a Heckemann, J. V Hajnal, and A. Hammers, “Diffeomorphic registration using B-splines,” *Med. Image Comput. Comput. Assist. Interv.*, vol. 9, pp. 702–709, 2006.
- [51] P. D. Kotsas and T. Dodd, “A Review of Methods for 2D / 3D Registration,” *Int. J. Medical, Heal. Biomed. Bioeng. Pharm. Eng.*, vol. 5, no. 11, pp. 606–609, 2011.
- [52] R. Veltkamp, “Shape matching: Similarity measures and algorithms,” in *SMI '01 Proceedings of the International Conference on Shape Modeling & Applications*, 2001, pp. 188–197.
- [53] M. Yigitsoy, C. Wachinger, and N. Navab, “Temporal groupwise registration for motion modeling,” *Inf. Process. Med. Imaging*, vol. 22, pp. 648–659, 2011.
- [54] P. L. Reu and T. J. Miller, “The application of high-speed digital image correlation,” *J. Strain Anal. Eng. Des.*, vol. 43, no. 8, pp. 673–688, Aug. 2008.
- [55] K. Du, “Regional pulmonary function analysis using image registration and 4DCT,” University of Iwoa, 2013.
- [56] G. J. Wen, J. J. Lv, and W. X. Yu, “A high-performance feature-matching method for image registration by combining spatial and similarity information,” *IEEE Trans. Geosci. Remote Sens.*, vol. 46, no. 4, pp. 1266–1277, 2008.
- [57] M. J. Ledesma-carbayo, J. Kybic, M. Desco, A. Santos, S. Member, M. Sühling, S. Member, P. Hunziker, and M. Unser, “Spatio-Temporal Nonrigid Registration for Ultrasound Cardiac Motion Estimation,” *Trans. Med. Imaging*, vol. 24, no. 9, pp. 1113–1126, 2005.
- [58] H. Sundar, H. Litt, and D. Shen, “Estimating Myocardial Motion by 4D Image Warping,” *Pattern Recognit.*, vol. 42, no. 11, pp. 2514–2526, Nov. 2009.
- [59] E. Golkar, A. Aizzuddin, and A. Rahni, “Comparison of Intensity Based Deformable Registration Methods for Respiratory Motion Modelling from

- 4D MRI,” in *IEEE International Conference on Signal and Image Processing Applications (ICSIPA)*, 2015, pp. 439–442.
- [60] X. Mei and F. Porikli, “Fast Image Registration via Joint Gradient Maximization: Application to Multimodal Data.,” *Proc. SPIE Electro-Optical Infrared Syst.*, vol. 6395, p. 63950P, 2006.
- [61] N. Cahill, “Normalized measures of mutual information with general definitions of entropy for multimodal image registration,” *Biomed. Image Regist.*, no. 8, pp. 258–268, 2010.
- [62] T. S. Hamburg and L. Bridge, “2D / 3D Registration and Motion Tracking Surgical Interventions,” *Philips J. Res.*, vol. 51, no. 2, pp. 299–316, 1998.
- [63] Z. a Taylor, M. Cheng, and S. Ourselin, “Real-time nonlinear finite element analysis for surgical simulation using graphics processing units.,” *Med. Image Comput. Comput. Assist. Interv.*, vol. 10, no. 1, pp. 701–708, Jan. 2007.
- [64] W. P. M. Mercx and a. C. van den Berg, “The explosion blast prediction model in the revised CPR 14E(yellow book),” *Process Saf. Prog.*, vol. 16, no. 3, pp. 152–159, 1997.
- [65] J. Yang, “An Improved Analytical Approach to Determine the Explosive Effects of Flammable Gas-Air Mixtures,” Livermore, CA, 2005.
- [66] S. Dorofeev, “Evaluation of safety distances related to unconfined hydrogen explosions,” *Int. J. Hydrogen Energy*, vol. 32, no. 13, pp. 2118–2124, Sep. 2007.
- [67] US Department of Defence, “Explosives and Demolitions US Army Field Manual,” vol. 214, no. July. pp. 1–2, 2007.
- [68] J. Kress and S. Grogger, “The domestic IED threat,” *JFQ*, no. 48, pp. 66–69, 2008.
- [69] W. Keenan and J. E. Tancreto, “Blast environment from fully and partially vented explosions in cubicles,” Port Hueneme, 1975.
- [70] U. D. of Energy, “Excerpted from ‘A Manual for the Prediction of Blast and Fragment Loadings on Structures,’ US Department of Energy, August 1981. <http://www.osti.gov/bridge/servlets/purl/5892901-5PuqGG/> (775pp, 34MB),” in *A Manual for the Prediction of Blast and Fragement Loading on Structures*, no. August, US Department of Energy, 1981, p. 21.

- [71] M. D. Hutchinson, "The escape of blast from fragmenting munitions casings," *Int. J. Impact Eng.*, vol. 36, no. 2, pp. 185–192, Feb. 2009.
- [72] M. D. Hutchinson and D. W. Price, "On the continued acceleration of bomb casing fragments following casing fracture," *Def. Technol.*, vol. 10, no. 2, pp. 211–218, 2014.
- [73] U. S. Department of Energy, "A MANUAL FOR THE PREDICTION OF BLAST FRAGMENT LOADINGS ON STRUCTURE," Amarillo, 1981.
- [74] M. M. Crull, "PREDICTION OF PRIMARY FRAGMENTATION CHARACTERISTICS OF CASED MUNITIONS," Huntsville, 1998.
- [75] R. W. Gurney, "The Initial Velocities of Fragments From Bombs, Shells and Grenades," Maryland, Aberdeen Proving Ground, 1943.
- [76] P. W. Cooper, "Acceleration, formation, and flight of fragments," in *Explosives Engineering*, 1st ed., Wiley-VCH, 1996, pp. 385–394.
- [77] World Heritage Encyclopedia, "Relative Explosive Factor," *Explosives Engineering, Scales*. [Online]. Available: [http://www.gutenberg.cc/articles/Relative\\_effectiveness\\_factor](http://www.gutenberg.cc/articles/Relative_effectiveness_factor). [Accessed: 12-Oct-2017].
- [78] R. Jeremić, Z. Bajić, O. R. Statutes, A. Rules, P. Explosives, M. Meel, T. Whyte, R. Kaswa, H. Hao, Y. Hao, J. Li, W. Chen, P. Pavlidis, V. Karakasi, T. A. Birbilis, M. Meel, T. Whyte, and R. Kaswa, "An approach to determining the TNT equivalent of high explosives," *South African Fam. Pract.*, vol. 19, no. 3, pp. 23–26, 2016.
- [79] H. Hao, Y. Hao, J. Li, and W. Chen, "Review of the current practices in blast-resistant analysis and design of concrete structures," *Adv. Struct. Eng.*, vol. 19, no. 8, pp. 1193–1223, 2016.
- [80] C. Vijayaraghavan, D. Thirumalaivasan, and R. Venkatesan, "A study on nuclear blast overpressure on buildings and other infrastructures using geospatial technology," *J. Comput. Sci.*, vol. 8, no. 9, pp. 1520–1530, 2012.
- [81] M. D. Hutchinson, "With-Fracture Gurney Model to Estimate both Fragment and Blast Impulses," *Cent. Eur. J. Energ. Mater.*, vol. 7, no. 2, pp. 175–186, 2010.
- [82] A. Washburn and L. L. Ewing, "Allocation of clearance assets in IED warfare," *Nav. Res. Logist.*, vol. 58, no. 3, pp. 180–187, 2011.

- [83] C. Kopp, "Technology of improvised explosive devices," *Def. Today*, vol. 4649, pp. 46–48, 2008.
- [84] C. A. Alderson, "The Validity of British Army Counterinsurgency Doctrine After The War in Iraq 2003-2009," Cranfield University, 2009.
- [85] N. Aylwin-Foster, "Changing the Army for Counterinsurgency Operations," *Mil. Rev.*, vol. 86, no. 1, pp. 27–42, 2006.
- [86] D. Marston, "Adaptation in the Field: The British Army's Difficult Campaign in Iraq," *Secur. Challenges*, vol. 6, no. 1, pp. 71–84, 2010.
- [87] P. Gill, J. Horgan, and J. Lovelace, "Improvised Explosive Device: The Problem of Definition," *Stud. Confl. Terror.*, vol. 34, no. 9, pp. 732–748, Sep. 2011.
- [88] A. L. Wolfe and H. Arrow, "Military influence tactics: Lessons learned in Iraq and Afghanistan.," *Mil. Psychol.*, vol. 25, no. 5, pp. 428–437, 2013.
- [89] W. Chin, "Colonial Warfare in a Post-Colonial State: British Military Operations in Helmand Province, Afghanistan," *Def. Stud.*, vol. 10, no. 1–2, pp. 215–247, Mar. 2010.
- [90] E. Savage, C. Forestier, N. Withers, H. Tien, and D. Pannell, "Tactical combat casualty care in the Canadian Forces: lessons learned from the Afghan war.," *Can. J. Surg.*, vol. 54, no. 6, pp. S118–S123, Dec. 2011.
- [91] A. Ramasamy, S. D. Masouros, N. Newell, A. M. Hill, W. G. Proud, K. a Brown, A. M. J. Bull, and J. C. Clasper, "In-vehicle extremity injuries from improvised explosive devices: current and future foci.," *Philos. Trans. R. Soc. Lond. B. Biol. Sci.*, vol. 366, no. 1562, pp. 160–170, Jan. 2011.
- [92] S. T. Shuker, "Management of penetrating medial and retro-bulbar orbital shrapnel/bullet injuries.," *J. Craniomaxillofac. Surg.*, vol. 40, no. 8, pp. e261–e267, Dec. 2012.
- [93] Gryphon Security, "IEDAP-Photo-1," *www.gryphonsecurity.com*. [Online]. Available: <http://www.gryphonsecurity.com/images/content/IEDAP-Photo-1.jpg>. [Accessed: 16-Feb-2016].
- [94] Military Factory, "M67 (Grenade) Detonation," *www.militaryfactory.com*. [Online]. Available: [http://www.militaryfactory.com/smallarms/imgs/m67-grenade\\_6.jpg](http://www.militaryfactory.com/smallarms/imgs/m67-grenade_6.jpg). [Accessed: 16-Feb-2016].



- [95] C. R. Bass, M. B. Panzer, K. a. Rafaels, G. Wood, J. Shridharani, and B. Capehart, "Brain injuries from blast.," *Ann. Biomed. Eng.*, vol. 40, no. 1, pp. 185–202, Jan. 2012.
- [96] L. a. Santiago, B. C. Oh, P. K. Dash, J. B. Holcomb, and C. E. Wade, "A clinical comparison of penetrating and blunt traumatic brain injuries.," *Brain Inj.*, vol. 26, no. 2, pp. 107–125, Jan. 2012.
- [97] D. J. Englot, M. S. Laurans, K. Abbed, and K. R. Bulsara, "Removal of nail penetrating the basilar artery.," *Neurosurg. Rev.*, vol. 33, no. 4, pp. 501–504, Oct. 2010.
- [98] C. a. Bir, M. Ressler, and S. Stewart, "Skin penetration surrogate for the evaluation of less lethal kinetic energy munitions.," *Forensic Sci. Int.*, vol. 220, no. 1–3, pp. 126–129, Jul. 2012.
- [99] N. Maiden, "Ballistics reviews: mechanisms of bullet wound trauma.," *Forensic Sci. Med. Pathol.*, vol. 5, no. 3, pp. 204–9, Jan. 2009.
- [100] J. E. Field, S. M. Walley, W. G. Proud, H. T. Goldrein, and C. R. Siviour, "Review of experimental techniques for high rate deformation and shock studies," *Int. J. Impact Eng.*, vol. 30, no. 7, pp. 725–775, 2004.
- [101] E. Cramphorn, M. Carre, and Z. A. Taylor, "Image Registration for Quantifying Deformation in Penetrating Ballistic Impacts," in *10th International Conference on Advances In Experimental Mechanics*, 2015, no. 1, pp. 1–2.
- [102] United States Department of Defence, "Types of hand grenades," in *Field Manual 3-23.30*, 1st ed., no. June, United States Department of Defence, Ed. Amherst: University of Massachusetts Army ROTC, 2005, pp. 1–13.
- [103] B. Mckay, "Development of lower extremity injury criteria and biomechanical surrogate to evaluate military vehicle occupant injury during an explosive blast event," Wayne State University, 2010.
- [104] H. Department of the Army, *Army Ammunition Data Sheets For Grenades*, 1st ed. US Department of Defence, 1991.
- [105] B. Gulenc, "Investigation of interface properties and weldability of aluminum and copper plates by explosive welding method," *Mater. Des.*, vol. 29, no. 1, pp. 275–278, Jan. 2008.
- [106] Formula SAE, "Anthropometric Reference Data 5th Percentile Female &

95th Percentile Male.” Formula SAE, pp. 8–9, 2016.

- [107] R. J. Kuczmarski, C. L. Ogden, L. M. Grummer-Strawn, K. M. Flegal, S. S. Guo, R. Wei, Z. Mei, L. R. Curtin, A. F. Roche, and C. L. Johnson, “CDC growth charts: United States.,” *Adv. Data*, vol. 314, pp. 1–27, 2000.
- [108] M. J. Carre, S. J. Haake, T. Asai, and T. Akatsuka, “The curve kick of a football 2: flight through the air,” *Sport. Eng.*, vol. 1, no. 5, pp. 193–200, 2002.
- [109] D. Miller and A. Bailey, “Sphere drag at Mach numbers from 0.3 to 2.0 at Reynolds numbers approaching 107,” *J. Fluid Mech.*, vol. 93, no. 3, pp. 449–464, 1979.
- [110] A. Bailey and J. Hiatt, “Free-flight measurements of sphere drag at subsonic, transonic, supersonic, and hypersonic speeds for continuum, transition, and near-free-molecular flow conditions,” Tennessee, 1971.
- [111] D. Lyon, C. Bir, and B. Patton, “Injury Evaluation Techniques for Non-Lethal Kinetic Energy Munitions,” Arberdeen, 1999.
- [112] G. H. Sakorafas and G. Peros, “Principles of war surgery: current concepts and future perspectives.,” *Am. J. Emerg. Med.*, vol. 26, no. 4, pp. 480–489, May 2008.
- [113] N. Ravikumar, C. Noble, E. Cramphorn, and Z. a. Taylor, “A constitutive model for ballistic gelatin at surgical strain rates,” *J. Mech. Behav. Biomed. Mater.*, vol. 47, pp. 87–94, 2015.
- [114] L. Liu, Y. Fan, and W. Li, “Viscoelastic shock wave in ballistic gelatin behind soft body armor.,” *J. Mech. Behav. Biomed. Mater.*, vol. 34, pp. 199–207, Jun. 2014.
- [115] E. Amborn, K. Muchi-Kuchler, and B. Hinz, “Experimental Validation Technique for Constitutive Models Describing Behavior of Soft Tissue Surrogates During Projectile Penetration,” *ASME 2010 Int. Mech. Eng. Congr. Expo.*, vol. 9, pp. 1–10, 2010.
- [116] D. Cronin and M. Worswick, “Behind Armour Blunt Trauma for ballistic impacts on rigid body armour,” in *19th International Symposium of Ballistics*, 2001, pp. 7–11.
- [117] C. P. Salisbury and D. S. Cronin, “Mechanical Properties of Ballistic Gelatin at High Deformation Rates,” *Exp. Mech.*, vol. 49, no. 6, pp. 829–840, Jan.

2009.

- [118] A. Bouamoul and D. Cronin, “Bullets Behaviour in Ballistic Simulants Defence Academy of the United Kingdom.” Defence Academy of the United Kingdom, Shrivenham, pp. 1–11, 2012.
- [119] C. E. Mendez-Probst, M. Vanjecek, H. Razvi, and P. a Cadieux, “Ordnance gelatine as an in vitro tissue simulation scaffold for extracorporeal shock wave lithotripsy.,” *Urol. Res.*, vol. 38, no. 6, pp. 497–503, Dec. 2010.
- [120] J. Breeze, N. Hunt, I. Gibb, G. James, A. Hepper, and J. Clasper, “Experimental penetration of fragment simulating projectiles into porcine tissues compared with simulants,” *J. Forensic Leg. Med.*, vol. 20, no. 4, pp. 296–299, 2013.
- [121] T. Payne, S. Mitchell, R. Bibb, and M. Waters, “The evaluation of new multi-material Human soft tissue simulants for Sports impact surrogates,” *J. Mech. Behav. Biomed. Mater.*, vol. 41, pp. 336–356, Sep. 2015.
- [122] J. Jussila, “Preparing ballistic gelatine--review and proposal for a standard method.,” *Forensic Sci. Int.*, vol. 141, no. 2–3, pp. 91–98, May 2004.
- [123] C. J. Shepherd, G. J. Appleby-Thomas, P. J. Hazell, D. F. Allsop, M. Elert, M. D. Furnish, W. W. Anderson, W. G. Proud, and W. T. Butler, “The Dynamic Behaviour of Ballistic Gelatin,” in *AIP Conference Proceedings*, 2009, pp. 1399–1402.
- [124] M. V Swain, D. C. Kieser, S. Shah, and J. a Kieser, “Projectile penetration into ballistic gelatin.,” *J. Mech. Behav. Biomed. Mater.*, vol. 29, pp. 385–392, Jan. 2014.
- [125] C. Schyma, “Wounding capacity of muzzle-gas pressure.,” *Int. J. Legal Med.*, vol. 126, no. 3, pp. 371–376, May 2012.
- [126] G. J. Appleby-Thomas, P. J. Hazell, J. M. Wilgeroth, C. J. Shepherd, D. C. Wood, and A. Roberts, “On the dynamic behavior of three readily available soft tissue simulants,” *J. Appl. Phys.*, vol. 109, no. 8, pp. 1–6, 2011.
- [127] D. S. Cronin, “Material Properties for Numerical Simulations for Human, Ballistic Soap and Gelatin,” Valcartier, 2010.
- [128] R. a. Tomlinson and Z. a. Taylor, “Photoelastic materials and methods for tissue biomechanics applications,” *Opt. Eng.*, vol. 54, no. 8, pp. 1–9, 2015.

- [129] T. F. Juliano, A. M. Forster, P. L. Drzal, T. Weerasooriya, P. Moy, and M. R. VanLandingham, "Multiscale mechanical characterisation of biomimetic physically associating gels," *J. Mater. Res.*, vol. 21, no. 08, pp. 2084–2092, Mar. 2011.
- [130] L. Cannon, "Behind Armour Blunt Trauma - an emerging problem," *J. R. Army Med. Corps*, vol. 147, no. 1, pp. 87–96, Feb. 2001.
- [131] J. F. Greenleaf, M. Fatemi, and M. Insana, "Selected methods for imaging elastic properties of biological tissues.," *Annu. Rev. Biomed. Eng.*, vol. 5, pp. 57–78, Jan. 2003.
- [132] C. Schyma, S. Greschus, H. Urbach, and B. Madea, "Combined radio-colour contrast in the examination of ballistic head models.," *Int. J. Legal Med.*, vol. 126, no. 4, pp. 607–613, Jul. 2012.
- [133] Z. Kalcioğlu, M. Qu, K. J. Van Vliet, K. E. Strawhecker, and M. R. VanLandingham, "Multiscale characterisation of relaxation times of tissue surrogate gels and soft tissues," in *27th Army Conference*, 2010, pp. 1–7.
- [134] A. E. Kerdok, S. M. Cotin, M. P. Ottensmeyer, A. M. Galea, R. D. Howe, and S. L. Dawson, "Truth cube: Establishing physical standards for soft tissue simulation," *Med. Image Anal.*, vol. 7, no. 3, pp. 283–291, 2003.
- [135] S. G. Kroeker, P. L. Morley, C. F. Jones, L. E. Bilston, and P. a Cripton, "The development of an improved physical surrogate model of the human spinal cord--tension and transverse compression.," *J. Biomech.*, vol. 42, no. 7, pp. 878–883, May 2009.
- [136] J. a Kluge, N. C. Rosiello, G. G. Leisk, D. L. Kaplan, and a L. Dorfmann, "The consolidation behavior of silk hydrogels.," *J. Mech. Behav. Biomed. Mater.*, vol. 3, no. 3, pp. 278–289, Apr. 2010.
- [137] C. X. Wang, C. Cowen, Z. Zhang, and C. R. Thomas, "High-speed compression of single alginate microspheres," *Chem. Eng. Sci.*, vol. 60, no. 23, pp. 6649–6657, Dec. 2005.
- [138] Z. I. Kalcioğlu, M. Qu, K. E. Strawhecker, T. Shazly, E. Edelman, M. R. VanLandingham, J. F. Smith, and K. J. Van Vliet, "Dynamic impact indentation of hydrated biological tissues and tissue surrogate gels," *Philos. Mag.*, vol. 91, no. 7–9, pp. 1339–1355, 2011.
- [139] T. Juliano and P. Moy, "Compression and instrumented indentation

- measurements on biomimetic polymers,” in *Proceedings of the Society for Experimental Mechanics Conference*, 2006, no. September, pp. 1–14.
- [140] P. Moy and T. Weerasooriya, “Dynamic response of an alternative tissue simulant, physically associating gels (PAG),” in *Proceedings of the Society for Experimental Mechanics Conference*, 2006, no. September, pp. 1–14.
- [141] J. Hipwell, G. Penney, T. Cox, J. Byrne, and D. Hawkes, “2D-3D Intensity Based Registration of DSA and MRA - A Comparison of Similarity Measures.,” pp. 501–508, 2002.
- [142] K. Z. Abd-Elmoniem, M. Stuber, and J. L. Prince, “NIH Public Access,” *Med. Image Anal.*, vol. 12, no. 6, pp. 778–786, 2008.
- [143] M. a. Howard, M. Utz, T. J. Brennan, B. D. Dalm, S. Viljoen, J. K. Kanwal, and G. T. Gillies, “Biophysical attributes of an in vitro spinal cord surrogate for use in developing an intradural neuromodulation system,” *J. Appl. Phys.*, vol. 110, no. 7, pp. 074701-3–5, 2011.
- [144] A. Bartsch, E. Benzel, V. Miele, D. Morr, and V. Prakash, “Hybrid III anthropomorphic test device (ATD) response to head impacts and potential implications for athletic headgear testing.,” *Accid. Anal. Prev.*, vol. 48, pp. 285–291, Sep. 2012.
- [145] J. G. Snedeker, M. Barbezat, P. Niederer, F. R. Schmidlin, and M. Farshad, “Strain energy density as a rupture criterion for the kidney: impact tests on porcine organs, finite element simulation, and a baseline comparison between human and porcine tissues.,” *J. Biomech.*, vol. 38, no. 5, pp. 993–1001, May 2005.
- [146] S. Nicolle, L. Noguier, and J.-F. Paliere, “Shear mechanical properties of the spleen: experiment and analytical modelling.,” *J. Mech. Behav. Biomed. Mater.*, vol. 9, pp. 130–136, May 2012.
- [147] P. J. Thurner, B. Erickson, R. Jungmann, Z. Schriock, J. C. Weaver, G. E. Fantner, G. Schitter, D. E. Morse, and P. K. Hansma, “High-speed photography of compressed human trabecular bone correlates whitening to microscopic damage,” *Eng. Fract. Mech.*, vol. 74, no. 12, pp. 1928–1941, Aug. 2007.
- [148] S. Duenwald-Kuehl, R. Lakes, and R. Vanderby, “Strain-induced damage reduces echo intensity changes in tendon during loading.,” *J. Biomech.*, vol. 45, no. 9, pp. 1607–1611, Jun. 2012.

- [149] H. Mehmanparast, J. Mac-Thiong, and Y. Petit, “Compressive properties of a synthetic bone substitute for vertebral cancellous bone,” *Int J Med Biol Sci*, vol. 6, pp. 452–455, 2012.
- [150] B. Lundeland, Y. Gundersen, P.-K. Opstad, I. Thrane, Y. Zhang, R. W. Olaussen, and P. Vaagenes, “Severe gunshot injuries in a porcine model: impact on central markers of innate immunity.,” *Acta Anaesthesiol. Scand.*, vol. 55, no. 1, pp. 28–34, Jan. 2011.
- [151] S. Robinovitch, “Energy-shunting hip padding system attenuates femoral impact force in a simulated fall,” *J. Biomech. Eng.*, vol. 117, pp. 9–13, 1995.
- [152] C. von See, M. Rana, M. Stoetzer, H. Kokemueller, M. Ruecker, and N.-C. Gellrich, “Designing the ideal model for assessment of wound contamination after gunshot injuries: a comparative experimental study.,” *BMC Surg.*, vol. 12, no. 6, Jan. 2012.
- [153] S. Robinovitch, “Force attenuation in trochanteric soft tissues during impact from a fall,” *J. Orthop. Res.*, vol. 13, no. 6, pp. 956–962, 1995.
- [154] G. Wightman, J. Beard, and R. Allison, “An investigation into the behaviour of air rifle pellets in ballistic gel and their interaction with bone.,” *Forensic Sci. Int.*, vol. 200, no. 1–3, pp. 41–49, Jul. 2010.
- [155] L. Liu, Z. Jia, X. Ma, Y. Fan, W. Li, and H. Liu, “A spherical cavity expansion model of large elastic deformation and its application to ballistic gelatin penetration problems,” *Int. J. Impact Eng.*, vol. 71, pp. 106–116, Sep. 2014.
- [156] J. Kwon and G. Subhash, “Compressive strain rate sensitivity of ballistic gelatin.,” *J. Biomech.*, vol. 43, no. 3, pp. 420–425, Feb. 2010.
- [157] D. S. Cronin and C. Falzon, “Characterisation of 10% Ballistic Gelatin to Evaluate Temperature, Aging and Strain Rate Effects,” *Exp. Mech.*, vol. 51, no. 7, pp. 1197–1206, Nov. 2010.
- [158] GELITA, “GELITA Deutschland.” GELITA, Eberach Germany.
- [159] C. Basdogan, S. De, J. Kim, M. Muniyandi, H. Kim, and M. A. Srinivasan, “Haptics in Minimally Invasive Surgical Simulation,” *IEEE Comput. Soc.*, no. April, pp. 56–64, 2004.
- [160] D. Hutchison and J. C. Mitchell, “Lecture Notes in Computer Science,” in *MICCAI*, 2002, pp. 219–226.

- [161] E. Peña, “A rate dependent directional damage model for fibred materials: application to soft biological tissues,” *Comput. Mech.*, vol. 48, no. 4, pp. 407–420, Apr. 2011.
- [162] A. Horton, A. Wittek, and K. Miller, “Subject-specific biomechanical simulation of brain indentation using a meshless method.,” *Med. Image Comput. Comput. Assist. Interv.*, vol. 10, no. 1, pp. 541–548, Jan. 2007.
- [163] T. El Sayed, A. Mota, F. Fraternali, and M. Ortiz, “A variational constitutive model for soft biological tissues.,” *J. Biomech.*, vol. 41, no. 7, pp. 1458–1466, Jan. 2008.
- [164] D. Cronin and C. Falzon, “Dynamic characterisation and simulation of ballistic gelatin,” in *2009 SEM Annual Conference*, 2009.
- [165] D. Cronin, C. Salisbury, and C. Horst, “High rate characterisation of low impedance materials using a polymeric split Hopkinson pressure bar,” in *2006 SEM Annual Conference & Exposition on Experimental and Applied Mechanics*, 2006.
- [166] G. Subhash, J. Kwon, R. Mei, and D. F. Moore, “Non-Newtonian Behavior of Ballistic Gelatin at High Shear Rates,” *Exp. Mech.*, vol. 52, no. 6, pp. 551–560, 2012.
- [167] A. Awoukeng-Goumtcha, L. Taddei, F. Tostain, and S. Roth, “Investigations of impact biomechanics for penetrating ballistic cases.,” *Biomed. Mater. Eng.*, vol. 24, no. 6, pp. 2331–2339, Jan. 2014.
- [168] C. A. Jr and S. Bodner, “Ballistic impact: the status of analytical and numerical modeling,” *Int. J. Impact Eng.*, vol. 7, no. 1, pp. 9–35, 1988.
- [169] B. Wolfrum, “Cavitation and shock wave effects on biological systems,” Georg-August-Universität zu Göttingen, 2004.
- [170] L. Liu, Z. Jia, X. L. Ma, and Y. R. Fan, “Analytical and experimental studies on the strain rate effects in penetration of 10wt % ballistic gelatin,” in *Journal of Physics: Conference Series*, 2013, vol. 451, pp. 012035-1–7.
- [171] P. Moy, T. Weerasooriya, and C. A. Gunnarsson, “Tensile deformation of ballistic gelatin as a function of loading rate,” in *Proceedings of the XIth International Congress and Exposition Society for Experimental Mechanics*, 2008.
- [172] J. a Kieser, J. Tahere, C. Agnew, D. C. Kieser, W. Duncan, M. V Swain, and

- M. T. Reeves, "Morphoscopic analysis of experimentally produced bony wounds from low-velocity ballistic impact.," *Forensic Sci. Med. Pathol.*, vol. 7, no. 4, pp. 322–332, Dec. 2011.
- [173] T. Juliano and A. Forster, "Multiscale mechanical characterisation of biomimetic physically associating gels," *J. Mater. ....*, 2006.
- [174] M. Bornert, F. Brémand, P. Doumalin, J. C. Dupré, M. Fazzini, M. Grédiac, F. Hild, S. Mistou, J. Molimard, J. J. Orteu, L. Robert, Y. Surrél, P. Vacher, and B. Wattrisse, "Assessment of digital image correlation measurement errors: Methodology and results," *Exp. Mech.*, vol. 49, no. 3, pp. 353–370, 2009.
- [175] D. Lee, H. Tippur, M. Kirugulige, and P. Bogert, "Experimental Study of Dynamic Crack Growth in Unidirectional Graphite/Epoxy Composites using Digital Image Correlation Method and High-speed Photography," *J. Compos. Mater.*, vol. 43, no. 19, pp. 2081–2108, Jul. 2009.
- [176] F. Hild and S. Roux, "Digital Image Correlation: From Displacement Measurement to Identification of Elastic Properties," *Strain*, vol. 42, no. 2, pp. 69–80, 2005.
- [177] M. a. Sutton, J. H. Yan, V. Tiwari, H. W. Schreier, and J. J. Orteu, "The effect of out-of-plane motion on 2D and 3D digital image correlation measurements," *Opt. Lasers Eng.*, vol. 46, no. 10, pp. 746–757, Oct. 2008.
- [178] D. Zhang and D. D. Arola, "Applications of digital image correlation to biological tissues.," *J. Biomed. Opt.*, vol. 9, no. 4, pp. 691–699, 2004.
- [179] B. Pan, H. Xie, Z. Wang, K. Qian, and Z. Wang, "Study on subset size selection in digital image correlation for speckle patterns.," *Opt. Express*, vol. 16, no. 10, pp. 7037–7048, 2008.
- [180] B. Pan, A. Asundi, H. Xie, and J. Gao, "Digital image correlation using iterative least squares and pointwise least squares for displacement field and strain field measurements," *Opt. Lasers Eng.*, vol. 47, no. 7–8, pp. 865–874, 2009.
- [181] L. Wittevrongel, P. Lava, S. V. Lomov, and D. Debruyne, "A Self Adaptive Global Digital Image Correlation Algorithm," *Exp. Mech.*, no. April 2014, pp. 361–378, 2014.
- [182] M. Bornert, N. Lenoir, P. Bésuelle, Y. Pannier, S. a. Hall, G. Viggiani, and J.



- Desrues, “Discrete and continuum analysis of localised deformation in sand using X-ray  $\mu$ CT and volumetric digital image correlation,” *Géotechnique*, vol. 60, no. 5, pp. 315–322, 2010.
- [183] P. Lall, D. Panchagade, D. Iyengar, S. Shantaram, J. Suhling, and H. Schrier, “High Speed Digital Image Correlation for Transient-Shock Reliability of Electronics,” in *2007 Proceedings 57th Electronic Components and Technology Conference*, 2007, pp. 924–939.
- [184] V. Tiwari and S. Williams, “Application of digital image correlation in impact testing,” in *SEM Annual Conference & Exposition on Experimental and Applied Mechanics*, 2005, pp. 2–3.
- [185] P. Moy, C. A. Gunnarsson, and T. Weerasooriya, “Tensile deformation and fracture of ballistic gelatin as a function of loading rate,” in *Proceedings of the SEM Annual Conference*, 2009, pp. 1–8.
- [186] A. Ajovalasit, G. Petrucci, and M. Scafidi, “Review of RGB photoelasticity,” *Opt. Lasers Eng.*, vol. 68, pp. 58–73, 2015.
- [187] L. R. Xu and A. J. Rosakis, “An experimental study of impact-induced failure events in homogeneous layered materials using dynamic photoelasticity and high-speed photography,” *Opt. Lasers Eng.*, vol. 40, no. 4, pp. 263–288, Oct. 2003.
- [188] D. Donadio, M. Bernasconi, and F. Tassone, “Photoelasticity of sodium silicate glass from first principles,” *Phys. Rev. B - Condens. Matter Mater. Phys.*, vol. 70, no. 21, pp. 1–9, 2004.
- [189] H. Aben, J. Anton, and A. Errapart, “Modern Photoelasticity for Residual Stress Measurement in Glass,” *Strain*, vol. 44, no. 1, pp. 40–48, 2008.
- [190] a Shukla, “High-speed fracture studies on bimaterial interfaces using photoelasticity—a review,” *J. Strain Anal. Eng. Des.*, vol. 36, no. 2, pp. 119–142, Jan. 2001.
- [191] K. Green and P. L. Pratt, “MEASUREMENT OF THE DYNAMIC FRACTURE TOUGHNESS OF POLYMETHYLMETHACRYLATE BY HIGH-SPEED PHOTOGRAPHY,” *Eng. Fract. Mech.*, vol. 6, pp. 71–80, 1974.
- [192] V. Mishra and K. Ranjan, “Tracking of Ballistic Missiles and Velocity Measurement using Frame Distance Manipulation,” in *Conference on*

*Advances in Communication and Control Systems*, 2013, pp. 526–529.

- [193] V. Ganapathi, C. Plagemann, D. Koller, and S. Thrun, “Real time motion capture using a single time-of-flight camera,” in *2010 IEEE Computer Society Conference on Computer Vision and Pattern Recognition (CVPR2010)*, 2010, pp. 755–762.
- [194] M.-C. Silaghi, R. Plankers, R. Boulic, P. Fua, and D. Thalmann, “Local and Global Skeleton Fitting Techniques for Optical Motion Capture,” *IFIP CapTech 98, Geneva*, vol. 1537, pp. 26–40, 1998.
- [195] C. Theobalt, I. Albrecht, and J. Haber, “Pitching a baseball: tracking high-speed motion with multi-exposure images,” *ACM Trans. Graph.*, vol. 23, no. 3, pp. 540–547, 2004.
- [196] T. Payne, S. Mitchell, R. Bibb, and M. Waters, “Development of novel synthetic muscle tissues for sports impact surrogates,” *J. Mech. Behav. Biomed. Mater.*, vol. 41, pp. 336–356, Aug. 2014.
- [197] L. Sigal, A. O. Balan, and M. J. Black, “HumanEva: Synchronized video and motion capture dataset and baseline algorithm for evaluation of articulated human motion,” *Int. J. Comput. Vis.*, vol. 87, no. 1–2, pp. 4–27, 2010.
- [198] C. Bir, “The evaluation of blunt ballistic impacts of the thorax,” Wayne State University, 2000.
- [199] D. Rueckert, P. Aljabar, R. a Heckemann, J. V Hajnal, and A. Hammers, “Diffeomorphic registration using B-splines,” *Med. Image Comput. Comput. Assist. Interv.*, vol. 9, no. Pt 2, pp. 702–709, Jan. 2006.
- [200] L. Schwarz, “Non-rigid registration using free-form deformations,” Technische Universitat at Munchen, 2007.
- [201] B. F. Hutton and M. Braun, “Software for image registration: Algorithms, accuracy, efficacy,” *Semin. Nucl. Med.*, vol. 33, no. 3, pp. 180–192, 2003.
- [202] J. Ashburner and K. J. Friston, “Spatial Transformation of Images,” London, 1997.
- [203] M. Modat, J. McClelland, and S. Ourselin, “Lung registration using the NiftyReg package,” in *Medical Image Analysis for the Clinic: A Grand Challenge, Workshop from MICCAI 2010*, 2010, pp. 33–42.
- [204] M. Modat, G. Ridgway, Z. Taylor, M. Lehmann, J. Barnes, D. Hawkes, N.

- Fox, and S. Ourselin, “Fast free-form deformation using graphics processing units,” *Comput. Methods Programs Biomed.*, vol. 98, no. 3, pp. 278–284, 2010.
- [205] M. Staring, S. Klein, and J. P. W. Pluim, “A rigidity penalty term for nonrigid registration,” *Med. Phys.*, vol. 34, pp. 4098–4108, 2007.
- [206] D. Rueckert, L. I. Sonoda, C. Hayes, D. L. Hill, M. O. Leach, and D. J. Hawkes, “Nonrigid registration using free-form deformations: application to breast MR images,” *IEEE Trans. Med. Imaging*, vol. 18, no. 8, pp. 712–721, Aug. 1999.
- [207] S. Klein, M. Staring, and J. P. W. Pluim, “Evaluation of optimization methods for nonrigid medical image registration using mutual information and B-splines,” *IEEE Trans. Image Process.*, vol. 16, no. 12, pp. 2879–2890, 2007.
- [208] Z. Xie and G. Farin, “Image registration using hierarchical B-splines,” *IEEE Trans. Vis. Comput. Graph.*, vol. 10, no. 1, pp. 85–94, 2004.
- [209] M. De Craene, G. Piella, O. Camara, N. Duchateau, E. Silva, A. Doltra, J. D’hooge, J. Brugada, M. Sitges, and A. F. Frangi, “Temporal diffeomorphic free-form deformation: application to motion and strain estimation from 3D echocardiography,” *Med. Image Anal.*, vol. 16, no. 2, pp. 427–50, Mar. 2012.
- [210] B. Pan, K. Qian, H. Xie, and A. Asundi, “Two-dimensional digital image correlation for in-plane displacement and strain measurement: a review,” *Meas. Sci. Technol.*, vol. 20, no. 6, p. 062001, Jun. 2009.
- [211] B. Zitová and J. Flusser, “Image registration methods: a survey,” *Image Vis. Comput.*, vol. 21, no. 11, pp. 977–1000, Oct. 2003.
- [212] D. J. Kroon, “B-spline Grid, Image and Point based Registration.” Dr Kroon, MATLAB Central, Twente, 2010.
- [213] R. D. Eisler, A. K. Chatterjee, G. H. Burghart, and P. Loan, “Simulate the Tissue Damage from Small Arms Projectiles and Fragments Penetrating the Musculoskeletal System,” Fountain Valley California, 1998.
- [214] A. Courtney and M. Courtney, “Physical Mechanisms of Soft Tissue Injury from Penetrating Ballistic Impact,” 2012.
- [215] R. Schestowitz and C. Twining, “Assessing the accuracy of non-rigid registration with and without ground truth,” in *3rd IEEE International Symposium on Biomedical Imaging: Nano to Macro.*, 2006, no. 1, pp. 836–

- [216] R. Chisu, “Techniques for accelerating intensity-based rigid image registration,” Technische Universitat Munchen, 2005.
- [217] L. Zollei, E. Grimson, A. Norbash, and W. Wells, “2D-3D rigid registration of X-ray fluoroscopy and CT images using mutual information and sparsely sampled histogram estimators,” in *Proceedings of the 2001 IEEE Computer Society Conference on Computer Vision and Pattern Recognition*, 2001, vol. 2, pp. 696–703.
- [218] D. B. Russakoff, T. Rohlfing, A. Ho, D. H. Kim, R. Shahidi, J. R. Adler, and C. R. Maurer, “Evaluation of Intensity-Based 2D-3D Spine Image Registration Using Clinical Gold-Standard Data,” *Image Regist.*, no. Wbir, pp. 151–160, 2003.
- [219] J. H. Hipwell, G. P. Penney, R. A. McLaughlin, K. Rhode, P. Summers, T. C. Cox, J. V. Byrne, J. A. Noble, and D. J. Hawkes, “Intensity-based 2-D-3-D registration of cerebral angiograms,” *IEEE Trans Med Imaging*, vol. 22, no. 11, pp. 1417–1426, 2003.
- [220] I. M. J. van der Bom, S. Klein, M. Staring, R. Homan, L. W. Bartels, and J. P. W. Pluim, “Evaluation of optimization methods for intensity-based 2D-3D registration in x-ray guided interventions,” *Proc. SPIE*, vol. 7962, no. 1, pp. 796223-1–15, 2011.
- [221] F. P. M. M. Oliveira and J. M. R. S. S. Tavares, “Medical image registration: a review.,” *Comput. Methods Biomech. Biomed. Engin.*, vol. 17, no. 2, pp. 73–93, 2014.
- [222] E. Aybar, “Sobel edge detection method for MatLab,” Eskişehir, 2006.
- [223] T. S. Y. Tang, N. J. MacIntyre, H. S. Gill, R. a. Fellows, N. a. Hill, D. R. Wilson, and R. E. Ellis, “Accurate assessment of patellar tracking using fiducial and intensity-based fluoroscopic techniques,” *Med. Image Anal.*, vol. 8, no. 3, pp. 343–351, 2004.
- [224] F. Ino, K. Ooyama, and K. Hagihara, “A data distributed parallel algorithm for nonrigid image registration,” *Parallel Comput.*, vol. 31, no. 1, pp. 19–43, 2005.
- [225] A. B. Holley, S. Petteys, J. D. Mitchell, P. R. Holley, and J. F. Collen, “Thromboprophylaxis and VTE rates in soldiers wounded in Operation

- Enduring Freedom and Operation Iraqi Freedom.,” *Chest*, vol. 144, no. 3, pp. 966–973, Sep. 2013.
- [226] J. Peyrat and H. Delingette, “Registration of 4D cardiac CT sequences under trajectory constraints with multichannel diffeomorphic demons,” *IEEE Trans. Med. Imaging*, vol. 29, no. 7, pp. 1351–1368, 2010.
- [227] A. Sotiras, C. Davatzikos, and N. Paragios, “Deformable medical image registration: A survey,” *IEEE Trans. Med. Imaging*, vol. 32, no. 7, pp. 1153–1190, 2013.
- [228] R. Hua, J. M. Pozo, Z. A. Taylor, and A. F. Frangi, “Discontinuous non-rigid registration using extended free-form deformations,” in *SPIE. Medical Imaging Conference 2015*, 2015.
- [229] G. Holzapfel, “Nonlinear solid mechanics: a continuum approach for engineering science,” *Meccanica*, vol. 37, no. 4–5, pp. 489–490, 2002.
- [230] MathWorks Inc., “MATLAB&SIMULINK.” MathWorks Inc., Massachusetts, USA.
- [231] Center for Computational Image and Simulation Technologies in Biomedicine (CISTIB), “GIMIAS.” Center for Computational Image and Simulation Technologies in Biomedicine (CISTIB), Sheffield, UK.
- [232] A. Eloyan, S. Li, J. Muschelli, J. J. Pekar, S. H. Mostofsky, and B. S. Caffo, “Analytic programming with fMRI data: A quick-start guide for statisticians using R,” *PLoS One*, vol. 9, no. 2, pp. e89470-1–13, 2014.
- [233] Vision Research, “Phantom Cine Viewer.” AMETEK MATERIALS ANALYSIS DIVISION, Wayne, USA, 2014.
- [234] W. T. Neale, D. Hessel, and T. Terpstra, “Photogrammetric Measurement Error Associated with Lens Distortion,” *SAE Tech. Pap. 2011-01-0286*, pp. 1–54, Apr. 2011.
- [235] T. Rahman and N. Krouglicof, “An efficient camera calibration technique offering robustness and accuracy over a wide range of lens distortion.,” *IEEE Trans. Image Process.*, vol. 21, no. 2, pp. 626–637, Feb. 2012.
- [236] S. Shih, “When should we consider lens distortion in camera calibration,” *Pattern Recognit.*, vol. 28, no. 3, pp. 447–461, Mar. 1995.
- [237] V. Tiwari, M. a. Sutton, and S. R. McNeill, “Assessment of High Speed

Imaging Systems for 2D and 3D Deformation Measurements: Methodology Development and Validation,” *Exp. Mech.*, vol. 47, no. 4, pp. 561–579, Jan. 2007.

- [238] T. Whitmarsh, L. Humbert, M. de Craene, L. M. del Río Barquero, and A. F. Frangi, “Reconstructing the 3D shape and bone mineral density distribution of the proximal femur from dual-energy x-ray absorptiometry,” *IEEE Trans. Med. Imaging*, vol. 30, no. 12, pp. 2101–2114, 2011.
- [239] A. Mahajna, N. Aboud, I. Harbaji, A. Agbaria, Z. Lankovsky, M. Michaelson, D. Fisher, and M. M. Krausz, “Blunt and penetrating injuries caused by rubber bullets during the Israeli-Arab conflict in October, 2000: a retrospective study,” *Lancet*, vol. 359, pp. 1795–800, May 2002.
- [240] T. Børvik, L. Olovsson, S. Dey, and M. Langseth, “Normal and oblique impact of small arms bullets on AA6082-T4 aluminium protective plates,” *Int. J. Impact Eng.*, vol. 38, no. 7, pp. 577–589, Jul. 2011.
- [241] J. D. Hrubes, “High-speed imaging of supercavitating underwater projectiles,” *Exp. Fluids*, vol. 30, no. 1, pp. 57–64, Jan. 2001.
- [242] B. Akers and A. Belmonte, “Impact dynamics of a solid sphere falling into a viscoelastic micellar fluid,” *J. Nonnewton. Fluid Mech.*, vol. 135, pp. 97–108, 2006.
- [243] L. Labous, A. Rosato, and R. Dave, “Measurements of collisional properties of spheres using high-speed video analysis,” *Phys. Rev. E*, vol. 56, no. 5, pp. 5717–5725, Nov. 1997.
- [244] J. Komenda, P. Hejna, M. Rydlo, M. Novák, J. Krajsa, F. Racek, P. Rejtar, and L. Jedlička, “Forensic and clinical issues in the use of frangible projectile,” *J. Forensic Leg. Med.*, vol. 20, no. 6, pp. 697–702, Aug. 2013.

## Chapter 9. Appendix

### 9.1. Registration Toolkit Parameters

Table 9-1: Shows all the options that can be used for the Matlab based toolkit. In the case of the toolkit only one option can be applied from each option class if defined, if not toolkit will use its default options [212].

Option Class	Option	Description
<b>Similarity</b>	'sd'	Sum of Squared Difference Metric (Auto Detect Default)
	'mi'	Mutual Information Metric (Auto Detect Default)
	'd'	Image Difference Metric
	'gd'	Gradient Difference Metric
	'gc'	Gradient Correlation Metric
	'pi'	Pattern Intensity Metric
	'ld'	Log Difference Metric
	'cc'	Cross Correlation Metric
<b>Registration</b>	'Rigid'	Transformation defined by Translation and Rotation
	'Affine'	Transformation defined by Translation, Rotation, Shear and Resize
	'NonRigid'	Transformation defined by local B-spline grid base

	'Both'		Transformation defined by NonRigid and Affine (Default)
<b>Penalty</b>	Value between '0-1'		Thin sheet of metal smoothness penalty term (Default 2D 1e-3, 3D 1e-5)
<b>Interpolation</b>	'Linear'		Linearly interpolate new pixel intensities (Default)
	'Cubic'		Cubically interpolate new pixel intensities
<b>Grid</b>	Initial Coordinates	Grid	Defines the initial custom coordinates that will be used for the initial registration.
<b>Spacing</b>	'[sx sy sz]'		Defines the grid point spacing that will be used for the process of image registration.
<b>Masks</b>	'MaskMoving'		Binary image that defines the mask that will be applied to the moving image.
	'MaskStatic'		Binary image that defines the mask that will be applied to the static image.
<b>Verbose</b>	'1', '2' or '3'		Displays the Debug information.

Table 9-2: Shows all the options that can be used for the nifti\_reg toolkit. In the case of this toolkit in some case multiple options can be applied to achieve a combination effect, if not toolkit will use its default options

<b>Option Class</b>	<b>Option</b>	<b>Description</b>
<b>Initial Transformation</b>	'-aff'	Variable that holds the affine transformation that will be used to initialise registration
	'-incpp'	File defines the initial transformation applied to the control points
<b>Output</b>	'-cpp'	Output file containing the control point transformation output (Default)
	'-res'	Output file containing resampled/registered image (Default)
<b>Input Image</b>	'-rmask'	Binary image that will be applied to the static image as a mask
<b>Spline</b>	'-sx'	Defines final grid point spacing in x [5]
	'-sy'	Defines final grid point spacing in y [5]
	'-sz'	Defines final grid point spacing in z [5]
<b>Regularisation or Penalty</b>	'-be'	Bending energy penalty term [0.005]
	'-le'	Linear elasticity penalty term [0.0 0.0]
	'-l2'	L2 norm displacement penalty term [0.0]
	'-jl'	Log of the Jacobean determinant penalty term [0.0]
<b>Similarity</b>	'-nmi'	Normalised Mutual Information metric (Default)
	'-ssd'	Sum of squared difference metric
	'-kld'	Kernel log difference metric
<b>Optimisation</b>	'-maxit'	Maximum number of iterations [300]



---

	'-ln'	Number of levels to perform [3]
	'-lp'	Only perform the first level [ln]
	'-nopy'	Do not apply pyramidal approach
<b>F3D2</b>	'-vel'	Use the velocity field integration to generate the deformation
	'-fmask'	Binary image that will be applied to the static image as a mask

---